SLAC-R-984

STUDY OF CP VIOLATION IN DALITZ-PLOT ANALYSES OF B-MESON DECAYS TO THREE KAONS

A DISSERTATION
SUBMITTED TO THE DEPARTMENT OF PHYSICS
AND THE COMMITTEE ON GRADUATE STUDIES
OF STANFORD UNIVERSITY
IN PARTIAL FULFILLMENT OF THE REQUIREMENTS
FOR THE DEGREE OF
DOCTOR OF PHILOSOPHY

Brian Lindquist
January 2012

SLAC-Report-984
Work supported by Department of Energy contract DE-AC02-76SF00515

SLAC National Accelerator Laboratory, 2575 Sand Hill Road, Menlo Park, CA 94025

I certify that I have read this dissertation and that, in my opinion, it is fully adequate in scope and quality as a dissertation for the degree of Doctor of Philosophy.

(Aaron Roodman) Principal Adviser

I certify that I have read this dissertation and that, in my opinion, it is fully adequate in scope and quality as a dissertation for the degree of Doctor of Philosophy.

(Vera Lüth)

I certify that I have read this dissertation and that, in my opinion, it is fully adequate in scope and quality as a dissertation for the degree of Doctor of Philosophy.

(Lance Dixon)

I certify that I have read this dissertation and that, in my opinion, it is fully adequate in scope and quality as a dissertation for the degree of Doctor of Philosophy.

(Stanley Wojcicki)

Approved for the University Committee on Graduate Studies

Abstract

The Standard Model (SM) explains *CP* violation in terms of the CKM matrix. The *BABAR* experiment was designed mainly to test the CKM model in B decays. B decays that proceed through $b \to s$ loop diagrams, of which $B \to KKK$ decays are an example, are sensitive to new physics effects that could lead to deviations from the CKM predictions for *CP* violation.

We present studies of *CP* violation in the decays $B^+ \to K^+K^-K^+$, $B^+ \to K^0_S K^0_S K^+$, and $B^0 \to K^+K^-K^0_S$, using a Dalitz plot amplitude analysis. These studies are based on approximately 470 million $B\overline{B}$ decays collected by *BABAR* at the PEP-II collider at SLAC. We perform measurements of time-dependent *CP* violation in $B^0 \to K^+K^-K^0_S$, including $B^0 \to \phi K^0_S$. We measure a *CP*-violating phase $\beta_{\text{eff}}(\phi K^0_S) = 0.36 \pm 0.11 \pm 0.04$ rad., in agreement with the SM. This is the world's most precise measurement of this quantity. We also measure direct *CP* asymmetries in all three decay modes, including the direct *CP* asymmetry $A_{CP}(\phi K^+) = (12.8 \pm 4.4 \pm 1.3)\%$, which is 2.8 sigma away from zero. This measurement is in tension with the SM, which predicts an asymmetry of a few percent.

We also study the resonant and nonresonant features in the $B \to KKK$ Dalitz plots. We find that the hypothetical scalar $f_X(1500)$ resonance, introduced by prior analyses to explain an unknown peak in the m_{KK} spectrum, cannot adequately describe the data. We conclude instead that the $f_X(1500)$ can be explained as the sum of the $f_0(1500)$, $f'_2(1525)$, and $f_0(1710)$ resonances, removing the need for the hypothetical $f_X(1500)$. We also find that an exponential nonresonant model, used by previous analyses to describe the broad nonresonant feature seen in $B \to KKK$ decays, cannot fully model the data. We introduce a new nonresonant model that

contains more free parameters, allows for phase motion, and contains both S-wave and P-wave components.

Acknowledgment

I would first like to thank my mom and dad, Kathleen and Randall Lindquist, for all the countless things they have done for me. Thanks also to my siblings, Scott, Craig, and Kara. I also owe thanks to Irene Onyeneho, Michael Kozina, George Vidal, José Bento, Dave and Vida Hansen, George and Charlie Capps, and the rest of the Catholic Community at Stanford. Thanks also to the many members of the Stanford Quiz Bowl Club, with whom I have shared hours and hours of friendly competition.

A huge debt of gratitude is owed to my advisor, Aaron Roodman, who has mentored me and helped guide me through this seemingly interminable period known as grad school. I also owe many thanks to two individuals, Mathew Graham and Josh Thompson, who helped me a lot on the work that went into this thesis.

I would like to thank several grad students on *BABAR*: Mark Allen, Wells Wulsin, Manuel Franco Sevilla, Andrew Wagner, and Kyle Knoepfel. Thanks also to Vera Lüth, Hojeong Kim, Ingrid Ofte, Arafat Gabareen Mokhtar, Michael Kelsey, Art Snyder, Jim McDonald, Natasha Haulman, and the rest of Group C. In addition, I should thank Judy Meo, Chris O'Grady, Matt Weaver, Witold Kozanecki, Alan Fisher, Wolfgang Gradl, and Jim Smith. I also thank Su Dong, Philippe Grenier, Martin Kocian, and Pelle Hansson for introducing me to the world of ATLAS. I am especially grateful for all the hard work of Jacques Chauveau, Deborah Bard, and Claudia Patrignani.

Finally, I would like to thank Stanley Wojcicki and Lance Dixon for serving on my thesis committee, and Jun Li for chairing my thesis defense.

Contents

List of Tables

List of Figures

Chapter 1

Introduction

> *Physics of heavy quark flavors is a subject for botanists and, if I only could, I would never mention it on this blog. Indeed, a mere thought of the humongous number of b- and c-hadrons and of their possible decay chains gives me migraines.*
>
> "Jester" [1]

The *BABAR* experiment, situated at the PEP-II collider at SLAC, collected data from 1999-2008. PEP-II collides electrons and positrons with asymmetric energies, with center-of-mass energy at the $\Upsilon(4S)$ resonance, which decays almost entirely to $B\overline{B}$ pairs. Due to the unprecedented quantities of B mesons produced at *BABAR* and its friendly rival experiment Belle, these experiments have appropriately been called "B-factories." The main goal of the B-factories is to study CP violation in B mesons. In the Standard Model (SM), CP violation is governed by the Cabibbo-Kobayashi-Maskawa (CKM) matrix. Before *BABAR* and Belle, the CKM picture was merely a hypothesis, but thanks to precise measurements at the B-factories, the CKM matrix has been shown to give a good description of CP-violation, for which Kobayashi and Maskawa received the 2008 Nobel Prize in Physics.

Despite the success of the SM, there are reasons to think there are other sources of CP violation in nature, which, if we are lucky, may be visible at the B-factories, or at future "Super" B-factories. The SM makes quite precise predictions for the CP violation in many different B meson decay modes, and by comparing experimental measurements of these decay modes to theory and to each other, one can test the consistency of the CKM picture.

One particularly powerful way of testing the SM is to measure the CP-violating angle β in $B^0 \to \phi(1020)K_S^0$ decays, and then to compare this with the value of β measured in $B^0 \to J/\psi K_S^0$ decays. Any large discrepancy between the two β measurements could signal a breakdown in the SM. $B^0 \to \phi K_S^0$ decays are dominated by loop diagrams, and so are sensitive to new virtual particles (such as squarks) that can appear in the loops. This makes them a good place to look for deviations from the SM. Similarly, $B^+ \to \phi K^+$ decays [1] are expected to have a small amount of CP violation in the SM, so a large amount could signal new physics.

The ϕ decays to KK, so other $B \to KKK$ decays, such as $B \to f_0(980)K$, can quantum mechanically interfere with $B \to \phi K$. This interference can be properly handled by accounting for all the resonances and nonresonant decays that contribute to the three-body phasespace of $B \to KKK$ decays. By studying the entire $B \to KKK$ phasespace, one also has more opportunities to look for CP violation than just $B \to \phi K$ decays. Since a plot of three-body phasespace is known as a "Dalitz plot," this type of analysis is called a Dalitz plot analysis. If B physics is capable of causing migraines, Dalitz plot analyses are liable to give someone a stroke.

The $B \to KKK$ decays have interesting Dalitz plots, dominated by prominent features that have not been well understood. One such feature is a large peak that has been called the $f_X(1500)$, and has been modeled by previous analyses as a scalar. However, its properties are not consistent with any known particle. A large fraction of $B \to KKK$ decays are "nonresonant," and the theoretical understanding of them is poor. We will spend considerable time in this analysis studying these features in detail.

These two areas of study – CP violation and Dalitz plot features – are not completely orthogonal, since measurements of CP violation can be affected if the Dalitz plot is incorrectly modeled. In this analysis, we will perform Dalitz plot analyses

---

[1] Charge conjugation is implied throughout this thesis, unless otherwise indicated.

of $B^+ \to K^+K^-K^+$, $B^+ \to K^0_S K^0_S K^+$, and $B^0 \to K^+K^-K^0_S$, extracting many *CP* violating measurements, including the angle β in $B^0 \to \phi K^0_S$ and the direct *CP* asymmetry in $B^+ \to \phi K^+$. The analysis in this thesis is based on the full $\Upsilon(4S)$ dataset collected over *BABAR*'s lifetime, and therefore represents *BABAR*'s final word on these decay modes.

In Chapter 2, we will give a theoretical introduction to *CP* violation and Dalitz plot analyses. In Chapter 3, we will give an overview of the PEP-II collider and the *BABAR* detector. Chapter 4 will then summarize the criteria we use to select events. The maximum likelihood fit and our method of modeling signal and background events is described in Chapter 5. In Chapter 6, we present our studies of the $B \to KKK$ Dalitz plots, in which we test various resonances and nonresonant models in order to decide how best to describe the Dalitz plot features. Having determined a Dalitz plot model for the $B \to KKK$ decays, we will then measure the *CP*-violating parameters and present the final results in Chapter 7. Finally, Chapter 8 will summarize the results and give some conclusions.

Chapter 2

Theory

2.1 *CP* Violation

Prior to the mid-1950's, physicists widely thought that the laws of physics were invariant under the parity transformation, i.e., the transformation $\vec{x} \rightarrow -\vec{x}$. However, this assumption was refuted in 1957, when Wu *et al.* [2] showed experimental evidence for parity violation in Cobalt-60 beta decay. In response, it was theorized that the charge conjugation transformation (i.e., the transformation of particles to their anti-particles) may be violated in exactly the right way so that the laws of physics would be invariant under the *combination* of charge conjugation and parity, abbreviated *CP*. However, in 1964, Cronin and Fitch [3] discovered that *CP* was violated in neutral kaons, albeit by a small amount. Since then, understanding *CP* violation (CPV) has been one of the key issues in particle physics.

CP violation is of more than just academic interest. Models of cosmology suggest that we wouldn't be here without it. Observations show that the visible universe consists essentially entirely of matter, rather than anti-matter. Logically, this so-called baryon asymmetry of the universe (BAU) must either be due to an initial condition, or have arisen dynamically in the past. The initial condition approach is generally rejected, [1] leaving us to explain how the BAU arose dynamically (so-called

---

[1] The initial condition hypothesis will not work in inflationary models, because inflation would wash-out to zero any pre-inflation asymmetry.

baryogenesis).

In 1967, Andrei Sakharov [4] gave three conditions necessary for baryogenesis:

- Baryon number violation.
- *C* and *CP* violation.
- A deviation from thermal equilibrium.

In principle, the Standard Model (SM) of particle physics can accommodate all three of these conditions. We will show how CPV is accounted for in the SM in Section 2.3, and even baryon number is violated non-perturbatively in the SM through so-called sphaleron transitions. However, quantitatively, the experimentally observed BAU (often specified as the baryon-to-photon ratio in the universe, $(N_B - N_{\bar{B}})/N_\gamma \approx 6 \times 10^{-10}$) is much too large to be explained by the SM. The amount of CPV in the SM is roughly 10 orders of magnitude too small to explain the observed BAU! [2] This is a clear indication that there are non-SM sources of CPV in nature. Although there is no guarantee that any non-SM sources will be observable at colliders, there are plausible scenarios in which they may be, an example of which will be shown in Section 2.4. This gives a strong motivation to studying CPV experimentally.

2.2 *CP* Violation in *B* Mesons

Although CPV was first discovered in kaons, B mesons have proven to be a better place to study CPV, for reasons that will become clearer in Section 2.3. At *BABAR*, we study two types of B mesons: neutral ($\overset{(-)}{B}{}^0$) and charged ($B^\pm$).

The neutral B flavor eigenstates B^0 (consisting of a $\bar{b}$ and d) and $\overline{B}^0$ (consisting of a b and $\bar{d}$) can oscillate into one another. This oscillation is mediated by the box diagrams shown in Fig. 2.1. The mass eigenstates are then linear combinations of B^0 and $\overline{B}^0$:

---

[2] The insufficient amount of CPV is not the only problem the SM has in explaining baryogenesis. In the SM, the third Sakharov condition is provided by an electroweak phase-transition, but this phase-transition would need to be strongly first-order in order to produce a large BAU. However, experimental constraints on the Higgs mass rule this out.

$$
\begin{aligned}
B_L &= pB^0 + q\overline{B}^0 \\
B_H &= pB^0 - q\overline{B}^0 \, ,
\end{aligned} \tag{2.1}
$$

where B_L is the lighter, and B_H the heavier mass eigenstate. This mixture of the flavor eigenstates in the mass eigenstates is known as B *mixing*. The coefficients p and q are complex numbers, normalized to $|p|^2 + |q|^2 = 1$, and which can in principle be computed in the SM. The $B^0 - \overline{B}^0$ oscillations occur at a frequency $\Delta m_d = m_{B_H} - m_{B_L}$. We will ignore the difference in the decay widths of the B_L and B_H.

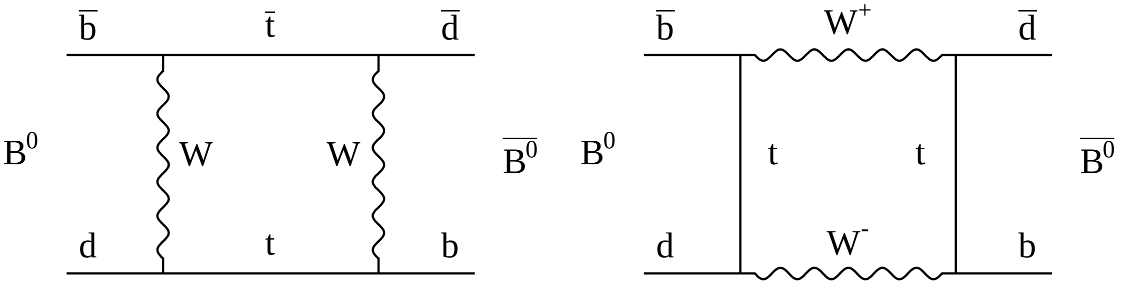

Figure 2.1: Box diagrams responsible for $B^0 - \overline{B}^0$ oscillations.

At *BABAR*, $\overset{(-)}{B^0}$ are produced in the decay $\Upsilon(4S) \rightarrow B^0\overline{B}^0$. This produces the $B^0\overline{B}^0$ in a coherent, entangled state, which means that as they oscillate, if at any point in time the first meson is known to be a B^0 ($\overline{B}^0$), then the second meson is guaranteed to be a $\overline{B}^0$ (B^0).

Assume we are interested in studying the decay of a B to a specific final state f. Then denote the amplitude for $B^0 \rightarrow f$ as $\mathcal{A}_f$, and the amplitude for $\overline{B}^0 \rightarrow f$ as $\overline{\mathcal{A}}_f$. Assume we identify ("tag") the flavor of one B (which we will call B^0_{tag}) at proper time t_{tag}. Assume also that the other B (B^0_{sig}) decays to f at proper time t_{sig}, where t_{sig} could be greater than or less than t_{tag}. Define $\Delta t \equiv t_{\text{sig}} - t_{\text{tag}}$. Then, the time-dependent decay rate for $B^0_{\rm sig} \to f$ is

$$\begin{aligned}\frac{d\Gamma}{d\Delta t} \;\propto\;& e^{-|\Delta t|/\tau_{B^0}}|\mathcal{A}|^2\Big[1+|\lambda_f|^2 \\ & -q_{tag}(1-|\lambda_f|^2)\cos\Delta m_d\Delta t + q_{tag}\; 2\;{\rm Im}(\lambda_f)\sin\Delta m_d\Delta t\Big]\,, \end{aligned} \tag{2.2}$$

where τ_{B^0} is the B^0 lifetime, $q_{tag} = +1(-1)$ when $B^0_{\rm tag}$ is tagged as a B^0 ($\overline{B}^0$), and

$$\lambda_f \equiv \frac{q}{p}\frac{\overline{\mathcal{A}}_f}{\mathcal{A}_f}\,. \tag{2.3}$$

This expression is general, but often we are interested in the case where f is a *CP*-eigenstate with eigenvalue η_{CP}. In this case, $\overline{\mathcal{A}}_{\bar f} = \eta_{CP}\overline{\mathcal{A}}_f$, and so

$$\lambda_f = \eta_{CP}\frac{q}{p}\frac{\overline{\mathcal{A}}_{\bar f}}{\mathcal{A}_f}\,. \tag{2.4}$$

The time-dependent *CP*-asymmetry is then

$$a_{CP}(\Delta t) \;\equiv\; \frac{\Gamma(q_{tag}=+1)-\Gamma(q_{tag}=-1)}{\Gamma(q_{tag}=+1)+\Gamma(q_{tag}=-1)} \tag{2.5}$$

$$= \frac{-(1-|\lambda_f|^2)}{1+|\lambda_f|^2}\cos\Delta m_d\Delta t + \frac{2\;{\rm Im}(\lambda_f)}{1+|\lambda_f|^2}\sin\Delta m_d\Delta t\,, \tag{2.6}$$

which is sometimes written as

$$a_{CP}(\Delta t) = -C\cos\Delta m_d\Delta t + S\sin\Delta m_d\Delta t\,. \tag{2.7}$$

One of the major focuses of *BABAR* is to measure the C and S coefficients for many different *CP*-eigenstates f, and to compare these measurements to SM predictions. In the absence of CPV, $C = S = 0$.

In addition to the time-dependent *CP*-asymmetry of Eq. 2.5, we can also define a time-integrated *CP*-asymmetry, A_{CP}, by integrating Eq. 2.2 over Δt. Performing the integration, we find $A_{CP} = -C$. We will often use A_{CP} and $-C$ interchangeably in this thesis. We can similarly define a time-integrated *CP*-asymmetry for B^+ decays:

$$A_{CP} \equiv \frac{\Gamma^- - \Gamma^+}{\Gamma^- + \Gamma^+} = \frac{|\overline{\mathcal{A}}_{\bar{f}}|^2 - |\mathcal{A}_f|^2}{|\overline{\mathcal{A}}_{\bar{f}}|^2 + |\mathcal{A}_f|^2}\,, \tag{2.8}$$

where $\Gamma^+ \equiv \Gamma(B^+ \to f)$ and $\Gamma^- \equiv \Gamma(B^- \to \bar{f})$.

CPV in B mesons is typically classified into three different categories: CPV in mixing, CPV in decay, and CPV in the interference between decay and mixing. This thesis involves searches for the second and third categories of CPV.

2.2.1 CPV in Mixing

This occurs if $|q/p| \neq 1$, and is also known as "indirect" CPV. In the SM, this form of CPV is expected to be very small for B^0 mesons, $\mathcal{O}(0.001)$. However, CPV in $K^0 - \overline{K}^0$ mixing was the first form of CPV to be discovered, in the Cronin and Fitch experiment [3].

2.2.2 CPV in Decay

This occurs if $\overline{\mathcal{A}}_{\bar{f}}/\mathcal{A}_f \neq 1$, and is also known as "direct" CPV. It is possible in both $\overset{(-)}{B^0}$ and $B^\pm$ decays. Direct CPV results in a value of the time-integrated asymmetry A_{CP} that is non-zero. In order for direct CPV to occur, there must be at least two amplitudes contributing to the process $B \to f$, and these amplitudes must differ in both their *weak* phases and their *strong* phases. Here, a weak phase refers to a phase that flips sign under *CP*. In the SM, weak phases only arise from the CKM matrix describing the weak interaction (Sec. 2.3). Strong phases are phases that stay the same under *CP*. They arise mainly from QCD.

To illustrate direct CPV, assume we have two amplitudes, a_1 and a_2, contributing to $B \to f$. Then,

$$\begin{aligned}\mathcal{A}_f &= |a_1|e^{i(\phi_1+\delta_1)} + |a_2|e^{i(\phi_2+\delta_2)}\\ \overline{\mathcal{A}}_{\bar{f}} &= |a_1|e^{i(\phi_1-\delta_1)} + |a_2|e^{i(\phi_2-\delta_2)}\,,\end{aligned} \tag{2.9}$$

where ϕ_j are strong phases and δ_j are weak phases. Then, using Eq. 2.8, we find

$$A_{CP} = \frac{2|a_1||a_2|\sin(\delta_1 - \delta_2)\sin(\phi_1 - \phi_2)}{|a_1|^2 + |a_2|^2 + 2|a_1||a_2|\cos(\delta_1 - \delta_2)\cos(\phi_1 - \phi_2)}\,, \tag{2.10}$$

which shows that the weak phases and strong phases must both differ in order to get $A_{CP} \neq 0$.

Direct CPV is very small in kaon decays, $\mathcal{O}(10^{-6})$, but can be much larger in certain B decays such as $B^0 \to K^+\pi^-$ [5, 6], where it is $\mathcal{O}(0.1)$.

2.2.3 CPV in the Interference between Decay and Mixing

This occurs if $\mathrm{Im}(\lambda_f) \neq 0$. Physically, it results from interference between the processes $B^0 \to f$ and $B^0 \to \overline{B}^0 \to f$. It leads to a non-zero S coefficient in Eq. 2.7, and so measuring it experimentally requires a time-dependent analysis. Measurement of this type of CPV is central to *BABAR*. We will go through a SM calculation of it in Section 2.3.

2.3 The CKM Matrix

The SM provides a very economical explanation of CPV, encoding it in the Cabibbo-Kobayashi-Maskawa (CKM) matrix [7, 8], V:

$$V = \begin{pmatrix} V_{ud} & V_{us} & V_{ub} \\ V_{cd} & V_{cs} & V_{cb} \\ V_{td} & V_{ts} & V_{tb} \end{pmatrix} \tag{2.11}$$

This 3×3 complex unitary matrix describes how the different quark flavors couple to the $W^{\pm}$ bosons. An up-type quark i and down-type quark j couple to the W with strength proportional to V_{ij} (or V_{ij}^*, depending on whether the W^- is going out of or into the vertex). The CKM matrix provides *CP* violation if $V^* \neq V$ after eliminating all removable phases.

A useful way of parameterizing the CKM matrix is the so-called Wolfenstein approximation:

$$V = \begin{pmatrix} 1-\lambda^2/2 & \lambda & A\lambda^3(\rho - i\eta) \\ -\lambda & 1-\lambda^2/2 & A\lambda^2 \\ A\lambda^3(1-\rho-i\eta) & -A\lambda^2 & 1 \end{pmatrix} + \mathcal{O}(\lambda^4)\,, \tag{2.12}$$

which is written as an expansion in the small parameter $\lambda \approx 0.23$. The other parameters are: $A \approx 0.81$, $\bar{\rho} \approx 0.13$, $\bar{\eta} \approx 0.34$ [9], where $\bar{\rho} \approx \rho(1-\lambda^2/2)$ and $\bar{\eta} \approx \eta(1-\lambda^2/2)$. In this parameterization, CPV is accounted for by the single parameter η. The fact that a single parameter is responsible for all CPV in the SM makes this a highly predictive model, providing many consistency checks.

Because the CKM matrix is unitary, it satisfies:

$$V_{ud}V_{ub}^* + V_{cd}V_{cb}^* + V_{td}V_{tb}^* = 0\,. \tag{2.13}$$

This equation can be represented in the complex plane as a triangle. Usually, one rotates the triangle and rescales it so one point is at $(0,0)$, another at $(1,0)$, and then the third point is at $(\bar{\rho}, \bar{\eta})$, as shown in Fig. 2.2. This is known as the unitarity triangle (UT). The three angles can be defined as

$$\begin{aligned} \alpha &\equiv arg\left(-\frac{V_{td}V_{tb}^*}{V_{ud}V_{ub}^*}\right) \\ \beta &\equiv arg\left(-\frac{V_{cd}V_{cb}^*}{V_{td}V_{tb}^*}\right) \\ \gamma &\equiv \pi - \alpha - \beta\,. \end{aligned} \tag{2.14}$$

To a good approximation, $V_{td} = |V_{td}|e^{-i\beta}$, $V_{ub} = |V_{ub}|e^{-i\gamma}$, and the other elements of the CKM matrix are purely real.

There are many ways to measure experimentally the sides and angles of the UT. By checking the consistency of the various side and angle measurements, one can test whether the CKM matrix gives a complete description of all CPV phenomena. To illustrate such a measurement, let's take a look at the decay mode $B^0 \to J/\psi\, K_S^0$,

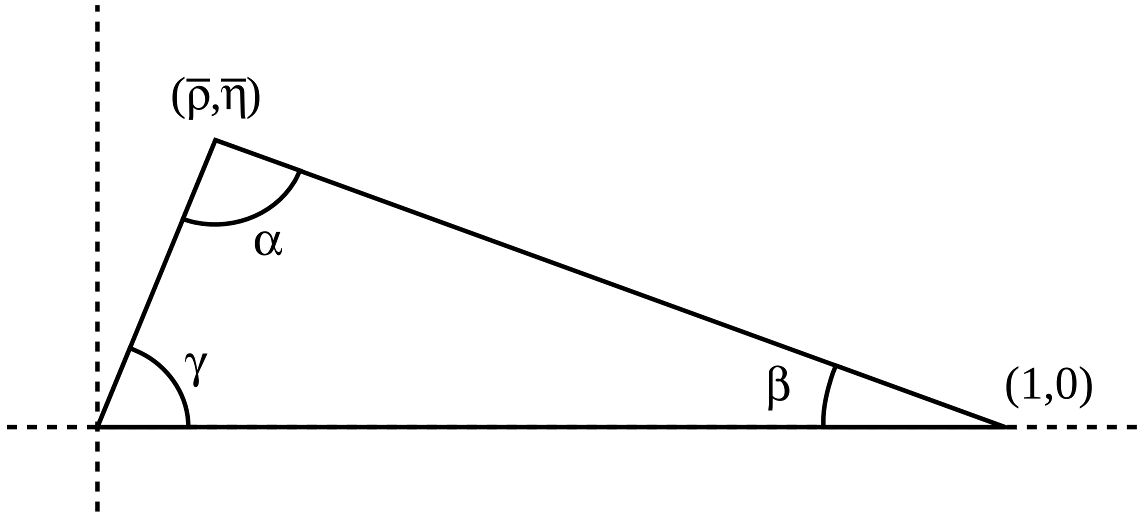

Figure 2.2: The unitarity triangle.

often called the "golden mode" for measuring CPV at *BABAR*.

$B^0 \rightarrow J/\psi K_S^0$ is dominated by a single decay amplitude, the tree diagram shown in Fig. 2.3. Because a single decay amplitude dominates, we know that direct CPV will be small in this mode. However, there can still be time-dependent CPV, in the form of a non-zero S coefficient. From Eq. 2.5, $S = (2\,\mathrm{Im}(\lambda_f))/(1 + |\lambda_f|^2) \approx \mathrm{Im}(\lambda_f)$. We can calculate λ_f to be

$$\lambda_f = \eta_f \left(\frac{V_{tb}^* V_{td}}{V_{tb} V_{td}^*}\right) \left(\frac{V_{cb} V_{cs}^*}{V_{cb}^* V_{cs}}\right) \left(\frac{V_{cs} V_{cd}^*}{V_{cs}^* V_{cd}}\right) \tag{2.15}$$

where the first term in parentheses is (q/p), the second comes from the decay diagram shown in Fig. 2.3, and the third comes from $K^0 - \overline{K}^0$ mixing. Making use of Eq. 2.14, it is straightforward to show that

$$\mathrm{Im}(\lambda_f) = -\eta_f \sin(2\beta) = \sin(2\beta)\,, \tag{2.16}$$

where we make use of the fact that $J/\psi K_S^0$ has a CP eigenvalue $\eta = -1$. So, $S = \sin(2\beta)$ in this mode. This is a theoretically very clean measurement, accurate to $\mathcal{O}(0.001)$.

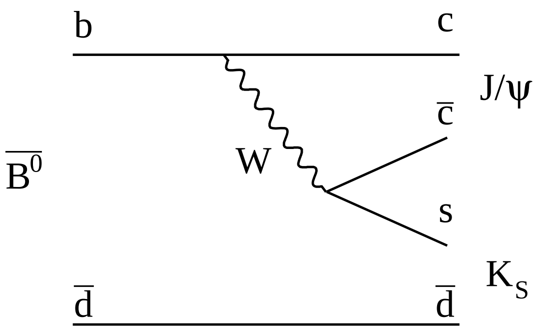

Figure 2.3: The dominant Feynman diagram for $\overline{B}^0 \to J/\psi K_S^0$.

2.4 $b \to s$ Penguins

One interesting class of B decay channels are the so-called $b \to s$ penguin decays. These decays are dominated by the loop diagrams (affectionately known as "penguin" diagrams [10]) shown in Fig. 2.4, where $q = (u, d, s$, or $c)$. The most important aspect of these decays is their potential sensitivity to new physics (NP). This sensitivity comes from the possibility of new particles appearing in the loops of the penguin diagrams. For example, Fig. 2.4 shows a potential contribution to these decays from a SUSY diagram. Of particular interest is the possibility that the NP carries a new CP-violating phase, which could then impact the observed CP violation.

In this thesis, we will be specifically interested in penguins with $q = u$ or s, which we will call $u\bar{u}s$ and $s\bar{s}s$ penguins. If we consider the amplitudes that can contribute to these decays, we have three penguin amplitudes (corresponding to possible u, c, or t quarks in the loop). In the case of $u\bar{u}s$, there is also a possible tree amplitude that can contribute, shown in Fig. 2.5. Calling the penguin amplitudes P_u,P_c, and P_t, and calling the tree amplitude T, and explicitly factoring out the CKM factors, we can write the total decay amplitudes as

$$\begin{aligned} A(u\bar{u}s) &= V_{tb}V_{ts}^*P_t + V_{cb}V_{cs}^*P_c + V_{ub}V_{us}^*(T + P_u) \\ A(s\bar{s}s) &= V_{tb}V_{ts}^*P_t + V_{cb}V_{cs}^*P_c + V_{ub}V_{us}^*P_u \end{aligned} \tag{2.17}$$

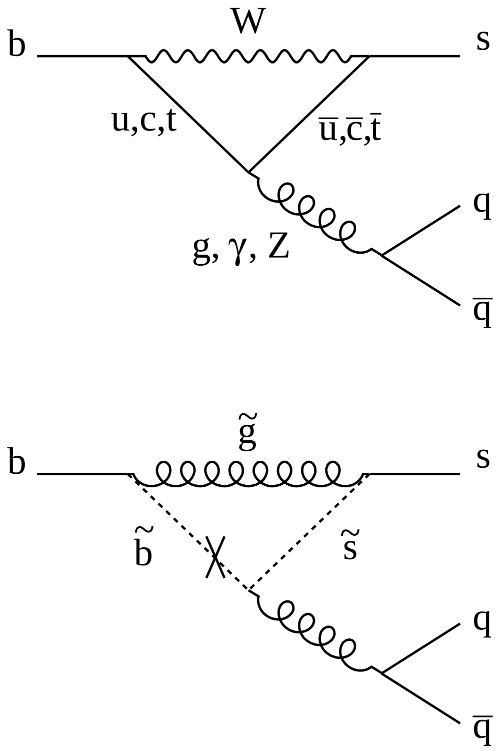

Figure 2.4: Top: $b \to s$ penguin diagram in SM. Bottom: example SUSY contribution to the same process. The "X" represents a mass-insertion.

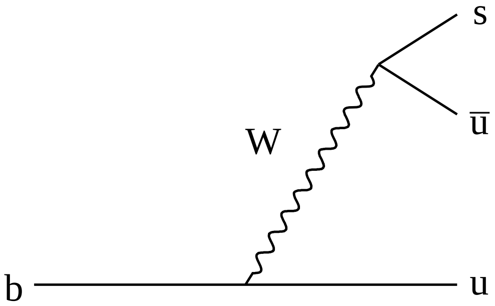

Figure 2.5: Tree diagram that can contribute to the same final state as $b \to u\bar{u}s$ penguin.

Then, by invoking the unitarity of the CKM matrix, this can be rewritten as

$$\begin{aligned} A(u\bar{u}s) &= V_{cb}V_{cs}^*(P_c - P_t) + V_{ub}V_{us}^*(T + P_u - P_t) \\ A(s\bar{s}s) &= V_{cb}V_{cs}^*(P_c - P_t) + V_{ub}V_{us}^*(P_u - P_t) \end{aligned} \tag{2.18}$$

The $(P_u - P_t)$ term will be called the "u-penguin" and the $(P_c - P_t)$ term will be called the "c-penguin." Note that the u-penguin/tree term is CKM suppressed relative to the c-penguin term by a factor of ≈ 0.02. Since the u-penguin and c-penguin terms should be similar except for the CKM factors, we can usually ignore the u-penguins. However, the tree amplitude is generally enhanced relative to the penguins, so depending on the enhancement, it could be very important. It is important to note that the tree amplitude does not contribute to $s\bar{s}s$.

Many $b \to s$ penguins involve decays to CP eigenstates, and thus provide an opportunity to measure time-dependent CPV. If we can ignore the tree and u-penguin terms that are proportional to $V_{ub}V_{us}^*$, then we can observe that the CKM factor for the c-penguin is the same as the CKM factor in the tree diagram for $B^0 \to J/\psi K_S^0$. This means that if we measure time-dependent CPV in a $b \to s$ penguin decay channel, we should measure $S = -\eta_f \sin(2\beta)$. However, if we include the CKM-suppressed terms, this prediction no longer holds. The CKM-suppressed amplitudes carry an extra weak phase factor of $e^{-i\gamma}$, so their presence will cause S to deviate from $\eta_f \sin(2\beta)$. This is known as SM "pollution." The most useful $b \to s$ penguin modes to study are those with small SM pollution. In those cases, a measurement of S that deviates from $\eta_f \sin(2\beta)$ can be attributed to new physics. Some of the best modes for this purpose are $B^0 \to \eta' K_S^0$, $B^0 \to K_S^0 K_S^0 K_S^0$, and $B^0 \to \phi(1020) K_S^0$.

2.5 $B \to KKK$ Decays

2.5.1 Overview

The focus of this thesis is on the $b \to s$ penguin-dominated decays $B^0 \to K^+K^-K_S^0$, $B^+ \to K^+K^-K^+$, and $B^+ \to K_S^0 K_S^0 K^+$. The first two of these decay modes are particularly interesting, because they contain the sub-modes $B^0 \to \phi(1020)K_S^0, \phi(1020) \to K^+K^-$ and $B^+ \to \phi(1020)K^+, \phi(1020) \to K^+K^-$, respectively. As already mentioned, $B^0 \to \phi K_S^0$ is one of the best $b \to s$ penguin modes for looking for NP in time-dependent CPV. It is easy to see why this is so: the ϕ is an $s\bar{s}$ resonance, so this is a $b \to s\bar{s}s$ transition, which we already showed does not have a tree contribution, so the SM pollution should be small. For the same reason, $B^+ \to \phi K^+$ does not have a tree contribution, [3] so we should expect the direct CPV in this mode to be small, since direct CPV requires two interfering amplitudes with different weak phases.

So, two important measurements for NP searches are $S(\phi K_S^0)$ and $A_{CP}(\phi K^+)$. ($A_{CP}(\phi K_S^0)$ should be similarly theoretically clean, but since we expect $A_{CP}(\phi K_S^0) \approx A_{CP}(\phi K^+)$, and $A_{CP}(\phi K^+)$ is much easier to measure experimentally, we do not expect $A_{CP}(\phi K_S^0)$ to be as useful.) There are numerous SM theoretical predictions for $\Delta S \equiv (-\eta_f S - \sin(2\beta))$ for ϕK_S^0, using both QCD factorization (QCDF) [11] and perturbative QCD (PQCD) [12]. Another paper [13] also accounts for long-distance effects from final-state interactions. For example, final-state interactions can allow $B^0 \to K^{*+}\pi^-$ to rescatter into ϕK_S^0. This allows ϕK_S^0 to receive tree contributions, albeit indirectly. The theoretical predictions give ΔS in the range $(-0.01 - 0.04)$.

---

[3] At least as far as short-distance diagrams are concerned. Long-distance effects will be discussed in the next paragraph.

There are similar predictions for $A_{CP}(\phi K^+)$ using QCDF [14] and PQCD [12], which give A_{CP} in the range $(0.0-4.7)\%$. Neither of these predictions include long-distance effects.

Only a small fraction ($\sim 10\%$) of all $B^0 \to K^+K^-K^0_S$ decays come from ϕK^0_S, and similar fraction of $B^+ \to K^+K^-K^+$ decays come from ϕK^+. These non-ϕ decays can also be useful in looking for CPV and possible NP, although they suffer from larger SM uncertainties. Another reason to study the non-ϕ decays is that they can overlap with the ϕ resonance, so any measurement of CPV in ϕK that doesn't account for the non-ϕ decays may be biased. Our approach is to model all of the resonant and nonresonant features in $B \to KKK$, and account properly for their interference with the ϕK decays. Since a plot of three-body phase-space is known as a Dalitz plot (DP), we will refer to the resonant and nonresonant structures as DP structures.

Measuring CPV using the entire $B^0 \to K^+K^-K^0_S$ DP is complicated due to the fact that $K^+K^-K^0_S$ is not a pure *CP* eigenstate. $CP(K^+K^-K^0_S) = (-1)^L$ when the K^+K^- system has orbital angular momentum L. Clearly, then, measuring CPV properly in $B^0 \to K^+K^-K^0_S$ depends on knowing the spins of the DP structures. Since the DP structures in $B^0 \to K^+K^-K^0_S$, $B^+ \to K^+K^-K^+$, and $B^+ \to K^0_S K^0_S K^+$ should be similar, we benefit from studying all three modes together. Understanding the DP structures is not only important for CPV, it is also of interest in its own right. There are two strange features seen in $B \to KKK$ Dalitz plots. First, a large contribution from a resonance that has been dubbed the $f_X(1500)$ has been seen in both $B^+ \to K^+K^-K^+$ and $B^0 \to K^+K^-K^0_S$. The nature of this resonance has been poorly understood. Second, an uncommonly large contribution from "nonresonant" decays is seen in $B^+ \to K^+K^-K^+$ and $B^0 \to K^+K^-K^0_S$. A simple phase-space model is inadequate to describe these decays. There has never been a published DP analysis of $B^+ \to K^0_S K^0_S K^+$, so doing such an analysis may help elucidate these DP features. One special feature of $B^+ \to K^0_S K^0_S K^+$ is that the $K^0_S K^0_S$ system is forbidden to be in an odd-L state (due to Bose-Einstein statistics), so this makes studying spin easier. For example, if $f_X(1500) \to K^0_S K^0_S$ were to be seen in $B^+ \to K^0_S K^0_S K^+$, this would show that the $f_X(1500)$ must have even spin.

2.5.2 Dalitz Plot Analysis

In the case of three-body decays, the decay rate can be a function of location on the DP. We define the DP as follows. For a decay $B \to K_1 K_2 K_3$, with p_1, p_2 and p_3 the four-momenta of the respective kaons, we define $s_{ij} \equiv m_{ij}^2 \equiv (p_i + p_j)^2$. The s_{ij} are the DP coordinates. In this thesis, we will use the following convention for labeling the kaons:

- For $B^\pm \to K^\pm K^\mp K^\pm$, $K_1 = K^\pm$, $K_2 = K^\mp$, and $K_3 = K^\pm$. To distinguish between the two same-charge kaons, we choose the indices so that $s_{12} \leq s_{23}$.
- For $B^\pm \to K^0_S K^0_S K^\pm$, $K_1 = K^0_S$, $K_2 = K^0_S$, and $K_3 = K^\pm$. To distinguish between the two K^0_S, we choose the indices so that $s_{13} \leq s_{23}$.
- For $\overset{(-)}{B^0} \to K^+ K^- K^0_S$, $K_1 = K^+$, $K_2 = K^-$, and $K_3 = K^0_S$.

Note that the three s_{ij} are not mutually independent, because four-momentum conservation leads to

$$s_{12} + s_{13} + s_{23} = m_B^2 + m_{K_1}^2 + m_{K_2}^2 + m_{K_3}^2 \,. \tag{2.19}$$

So, the DP location can be fully specified in terms of two s_{ij}.

For the B^+ decay modes, the DP-dependent decay rate is

$$\frac{d\Gamma}{ds_{12}ds_{23}} \propto |\overset{(-)}{\mathcal{A}}|^2 \,, \tag{2.20}$$

where $\mathcal{A}$ and $\overline{\mathcal{A}}$ apply to B^+ and B^- decays, respectively, and are now functions of DP location: $\overset{(-)}{\mathcal{A}} = \overset{(-)}{\mathcal{A}}(s_{12}, s_{23})$.

The time-dependent and DP-dependent decay rate for $B^0 \to K^+ K^- K^0_S$ is a modified form of Eq. 2.2:

$$\begin{aligned} \frac{d\Gamma}{ds_{12}ds_{23}d\Delta t} \propto \; & e^{-|\Delta t|/\tau_{B^0}} \Big[\left(1 - q_{tag}\Delta w\right) \left(|\mathcal{A}|^2 + |\overline{\mathcal{A}}|^2 \right) \\ & - q_{tag}\, (1 - 2w) \, \left(|\mathcal{A}|^2 - |\overline{\mathcal{A}}|^2 \right) \cos \Delta m_d \Delta t \\ & + q_{tag}\, (1 - 2w) \; 2 \, \mathrm{Im} \left[e^{-2i\cdot\beta} \overline{\mathcal{A}} \mathcal{A}^* \right] \sin \Delta m_d \Delta t \Big] \,, \end{aligned} \tag{2.21}$$

where $\mathcal{A}$ and $\overline{\mathcal{A}}$ apply to B^0 and $\overline{B}^0$ decays, respectively, and are functions of DP location. We have made use of $q/p \approx e^{-2i\cdot\beta}$, and have introduced the experimental quantity w, the *mistag rate*, which is the fraction of events in which the $B^0_{\rm tag}$ is tagged with the incorrect flavor [15]. Δw is the difference in w for B^0 and $\overline{B}^0$ tags, and is typically very small, so we will suppress it throughout the rest of this thesis, even though we still do account for it in our fit model. We assume that the efficiency for B^0 and $\overline{B}^0$ tags is the same.

2.5.3 Isobar Model

We study decays using an amplitude analysis, which accounts for multiple amplitudes contributing to a three-body final state. We use the so-called isobar model [16, 17, 18], which describes the overall decay amplitude as a linear coherent sum of individual amplitudes (or "isobars"):

$$\mathcal{A}(s_{12}, s_{23}) = \sum_j \mathcal{A}_j(s_{12}, s_{23}) \tag{2.22}$$

$$\overline{\mathcal{A}}(s_{12}, s_{23}) = \sum_j \overline{\mathcal{A}}_j(s_{12}, s_{23})\,. \tag{2.23}$$

where

$$\mathcal{A}_j \equiv a_j F_j(s_{12}, s_{23}) \tag{2.24}$$

and

$$\bar{\mathcal{A}}_j \equiv \bar{a_j} \bar{F}_j(s_{12}, s_{23})\,. \tag{2.25}$$

The isobar coefficients a_j and $\bar{a_j}$ are complex numbers that describe the relative magnitudes and phases of the particular decay channels. All of the weak phases of the decay are contained in a_j and $\bar{a_j}$.

The quantities $F_j(s_{12}, s_{23})$ and $\bar{F}_j(s_{12}, s_{23})$ describe the decay dynamics of the individual decay channels, and do not include any weak phases. Since the overall decay amplitudes for $B^+ \to K^+K^-K^+$ must be symmetric under exchange of identical bosons, $F_j(s_{12}, s_{23})$ must be replaced with $F_j(s_{12}, s_{23}) + F_j(s_{23}, s_{12})$. Likewise, for $B^+ \to K^0_S K^0_S K^+$, $F_j(s_{12}, s_{23})$ must be replaced with $F_j(s_{12}, s_{23}) + F_j(s_{12}, s_{13})$. Since the F_j do not contain any weak phases, in the B^+ modes $F_j = \bar{F}_j$. However, in $B^0 \to K^+K^-K^0_S$,

$$F_j = (-1)^L \bar{F}_j \, , \tag{2.26}$$

where L is the orbital angular momentum of K_3 in the K_1K_2 frame. The reason is that we use the definitions $K_1 = K^+$ and $K_2 = K^-$ for both B^0 and $\overline{B}^0$ decays. However, if *CP* is conserved, then we should have $\mathcal{A}(B^0 \to K^+K^-K^0_S) = \overline{\mathcal{A}}(\overline{B}^0 \to K^-K^+K^0_S)$, so $\mathcal{A}(s_{12}, s_{23}) = \overline{\mathcal{A}}(s_{12}, s_{13})$. When we exchange K_1 and K_2, this introduces a factor of $(-1)^L$. We will describe the exact Dalitz plot dependence of the amplitudes $F_j(s_{12}, s_{23})$ in Sections 2.5.4 and 2.5.5.

We use the following parameterization for the isobar coefficients:

$$\begin{aligned} a_j &= c_j(1 + b_j)e^{i(\phi_j + \delta_j)} \\ \bar{a}_j &= c_j(1 - b_j)e^{i(\phi_j - \delta_j)} \end{aligned} \tag{2.27}$$

where c_j, ϕ_j, b_j, and δ_j are real numbers. The parameters b_j and δ_j describe *CP* asymmetry for the component j. Specifically, the direct *CP* asymmetry $A_{CP}(j)$ for a particular isobar is given by

$$A_{CP}(j) = \frac{-2b_j}{1 + b_j^2} \, . \tag{2.28}$$

For the B^+ modes, one can define the *CP*-violating phase difference

$$\Delta\phi(j) \equiv arg(a_j \bar{a}_j^*) = 2\delta_j \, , \tag{2.29}$$

which is a form of direct CPV. In $B^0 \to K^+K^-K^0_S$, we can express the CPV due to interference between decay and mixing in terms of the "effective" β for the component j:

$$\beta_{\text{eff}}(j) \equiv \frac{1}{2} arg(e^{2i \cdot \beta} a_j \bar{a}_j{}^*) = \beta + \delta_j \, . \tag{2.30}$$

As an example to illustrate the power of a DP amplitude analysis, assume we have only two isobars contributing to $B^0 \to K^+K^-K^0_S$, an even-spin resonance $\mathcal{A}_1$ and an odd-spin resonance $\mathcal{A}_2$. Assume they have $b_1 = b_2 = 0$, and $\delta_1 = \delta_2 = \delta$. Then,

$$\begin{aligned} \mathcal{A} &= c_1 e^{i(\phi_1+\delta)} F_1 + c_2 e^{i(\phi_2+\delta)} F_2 & (2.31) \\ \overline{\mathcal{A}} &= c_1 e^{i(\phi_1-\delta)} F_1 - c_2 e^{i(\phi_2-\delta)} F_2\,, & (2.32) \end{aligned}$$

where we used $\bar{F}_2 = -F_2$ because it is odd-spin. Plugging these expressions into Eq. 2.21, and calculating only the $\sin(\Delta m_d \Delta t)$ coefficient, we get:

$$\begin{aligned} 2\ \mathrm{Im}\left[e^{-2i\cdot\beta}\overline{\mathcal{A}}\mathcal{A}^*\right] &= -(2c_1^2|F_1|^2 - 2c_2^2|F_2|^2)\sin(2\beta_{\text{eff}}) \\ &+ 4c_1c_2\ \mathrm{Im}(F_1F_2^* e^{i(\phi_1-\phi_2)})\cos(2\beta_{\text{eff}})\,, \qquad (2.33) \end{aligned}$$

where $\beta_{\text{eff}} = \beta + \delta$. As we can see, the interference term between the two resonances is proportional to $\cos(2\beta_{\text{eff}})$. [4] This is quite significant, because the standard way of measuring β, in $B^0 \to J/\psi K^0$ decays, is only sensitive to $\sin 2\beta$, so it has a "trigonometric ambiguity" between β and $\pi/2 - \beta$. By measuring $\cos(2\beta_{\text{eff}})$, we can remove this ambiguity, assuming $\beta_{\text{eff}} \approx \beta$. This is not just an academic example: in reality, the odd-spin $\phi(1020)$ does interfere with the even-spin $f_0(980)$ (as well as even-spin nonresonant decays), so we are sensitive to $\cos(2\beta_{\text{eff}})$. This gives another motivation for performing a DP analysis of $B^0 \to K^+K^-K^0_S$!

It is difficult to directly compare the values for a_j to results from other experiments, since the values of a_j depend on normalization and phase convention. However, there are other more meaningful quantities that we can define, which will allow for direct comparisons to other experiments. The fit fraction FF_j for a component is defined as:

$$FF_j = \frac{\int(|\mathcal{A}_j|^2 + |\bar{\mathcal{A}}_j|^2)\ ds_{12}ds_{23}}{\int(|\mathcal{A}|^2 + |\overline{\mathcal{A}}|^2)\ ds_{12}ds_{23}}. \qquad (2.34)$$

Note that the fit fractions do not necessarily add up to one. The reason for this is interference effects between the different resonances. We can quantify this interference

---

[4] If both resonances had been even-spin, or both odd-spin, then this interference term would have been proportional to $\sin(2\beta_{\text{eff}})$.

by defining interference fit fractions for $i \neq j$:

$$FF_{ij} \;=\; 2\ \mathrm{Re}\frac{\int(\mathcal{A}_i\mathcal{A}_j^* + \bar{\mathcal{A}}_i\bar{\mathcal{A}_j}^*)\ ds_{12}ds_{23}}{\int(|\mathcal{A}|^2 + |\overline{\mathcal{A}}|^2)\ ds_{12}ds_{23}}. \tag{2.35}$$

The fit fractions satisfy the relation

$$\sum_j FF_j + \sum_{i<j} FF_{ij} = 1\,. \tag{2.36}$$

The partial branching fraction for an individual isobar component is defined as the fit fraction for the component times the total $B \to KKK$ branching fraction:

$$\mathcal{B}_j \equiv FF_j \times \mathcal{B}\,. \tag{2.37}$$

2.5.4 Resonant Amplitudes

Table 2.1 gives the resonances studied in this analysis. Note that not all these resonances end up the in the final nominal models. In Chapter 6, we will present the studies that help us determine which resonances to include in the nominal fit models. Not included in this table are contributions from D meson and J/ψ decays. Those particles are long enough lived that they do not interfere significantly, so they are effectively treated as backgrounds. They are discussed in Section 5.4.

The decay dynamics of a process $B \to rK_c, r \to K_aK_b$, where r is an intermediate resonance, can be described by the complex amplitude F_r, which can be written as

$$F_r(m_{12}, m_{23}) = Z_L(\vec{p}, \vec{q})B_L^B(|\vec{p^*}|R')B_L^r(|\vec{q}|R)T_r(m_{ab}), \tag{2.38}$$

where:

- $\vec{p}$ and $\vec{q}$ are the momenta of c and a, respectively, both calculated in the rest frame of r.
- $\vec{p^*}$ is the momentum of c in the rest frame of the B.
- L is the spin of the resonance r.

Table 2.1: List of resonances used in this analysis. Not all of these resonances end up in the nominal fit models. "Source" indicates the source for the parameters. Resonances without errors on their parameters are only used as systematics, not as part of the nominal fit model. "RBW" means Relativistic Breit-Wigner.

Resonance	Lineshape	Mass (MeV/c^2)	Width (MeV)	Source
$\phi(1020)$	RBW	1019.455 ± 0.020	4.26 ± 0.04	[9]
$f_0(980)$	Flatté	see text	see text	[19]
$f_X(1500)$	RBW	floated	floated	n.a.
$f_0(1500)$	RBW	1505 ± 6	109 ± 7	[9]
$f_0(1710)$	RBW	1720 ± 6	135 ± 8	[9]
$f_2'(1525)$	RBW	1525 ± 5	73^{+6}_{-5}	[9]
χ_{c0}	RBW	3414.75 ± 0.31	10.3 ± 0.6	[9]
$f_0(1370)$	RBW	1400	300	[20]
$a_0^0(1450)$	RBW	1474	265	[9]
$a_0^-(1450)$	RBW	1474	265	[9]
$a_0^-(980)$	Flatté	see text	see text	[21]
$\phi(1680)$	RBW	1680	150	[9]
$f_2(1270)$	RBW	1275	185	[9]
$f_2(2010)$	RBW	2011	202	[9]
$f_2(2300)$	RBW	2297	149	[9]

- $Z_L(\vec{p}, \vec{q})$ is the Zemach tensor, describing the angular distribution of the decay. It will be described in detail below.
- $B_L^B(|\vec{p^*}|R')$ and $B_L^r(|\vec{q}|R)$ are the Blatt-Weisskopf barrier factors, with a radius parameter R' and R. These factors will be described in detail below.
- $T_r(m_{ab})$ is the lineshape (e.g. Relativistic Breit-Wigner) specific to a particular resonance. This factor will be described in detail below.

Zemach Tensors

The angular distributions of the decay products are described by Zemach tensors Z_L [22], which depend on the spin L of the intermediate resonance. The Zemach tensors are given by the expressions

$$Z_0(\vec{p}, \vec{q}) = 1 \tag{2.39}$$

$$Z_1(\vec{p}, \vec{q}) = 4\vec{p} \cdot \vec{q} \tag{2.40}$$

$$Z_2(\vec{p}, \vec{q}) = \frac{16}{3}\left[3(\vec{p} \cdot \vec{q})^2 - (|\vec{p}||\vec{q}|)^2\right]. \tag{2.41}$$

Helicity Angles

The Zemach tensors depend on both $\vec{p}$ and $\vec{q}$. There is no ambiguity about what $\vec{p}$ is, but we must decide on a convention to specify which particle $\vec{q}$ refers to for a $r \to K\bar{K}$ decay. Depending on which particle we choose, $\vec{q}$ will flip sign. As can be seen from Sec. 2.5.4, this will only affect odd-spin isobars. In this analysis, we decide to use the convention that for a $B \to rK_3, r \to K_1K_2$ decay, $\vec{q}$ will refer to the momentum of the K_1. For a $B \to rK_1, r \to K_2K_3$ decay, $\vec{q}$ will refer to the momentum of the K_3. There are no odd-spin (K_1K_3) isobars in any of the decay modes, so we do not set a convention for this case.

Note that this convention is the same as what was used in BABAR's previous $B^0 \to K^+K^-K^0_S$ analysis [23], but opposite the convention used in BABAR's previous

$B^+ \to K^+K^-K^+$ analysis [24]. The result of this change in convention is that the phases of any P-wave isobars will be shifted by π radians, *i.e.*, the signs of these isobars will be flipped.

This convention for $\vec{q}$ translates into a convention for *helicity angles.* We define the cosine of the helicity angle for an isobar as $\frac{\vec{p}\cdot\vec{q}}{|\vec{p}||\vec{q}|}$. We will use the following notation:

- For a $B \to rK_3, r \to K_1K_2$ decay, θ_3 is the helicity angle. In other words, θ_3 is the angle between K_1 and K_3, measured in the K_1K_2 frame.
- For a $B \to rK_1, r \to K_2K_3$ decay, θ_1 is the helicity angle. In other words, θ_1 is the angle between K_1 and K_3, measured in the K_2K_3 frame.

In terms of helicity angles, the Zemach tensors have the dependence $Z_1 \propto \cos(\theta)$ and $Z_2 \propto 3\cos^2(\theta) - 1$, i.e., they are proportional to the first and second Legendre polynomials.

Blatt-Weisskopf Factors

Blatt-Weisskopf barrier factors [25] are used to take into account the finite sizes of the decaying resonances. They only affect non-scalar resonances. The Blatt-Weisskopf factors can be written as a function of $z = |\vec{q}|R$ or $z = |\vec{p^*}|R'$, where R is the radius of the $K\bar{K}$ resonance, and R' is the radius of the B meson.

The Blatt-Weisskopf factors $B_L(z)$ for $L = 0$, $L = 1$, and $L = 2$ resonances are

$$B_{L=0}(z) = 1 \tag{2.42}$$

$$B_{L=1}(z) = \sqrt{\frac{1+z_0^2}{1+z^2}} \tag{2.43}$$

$$B_{L=2}(z) = \sqrt{\frac{9+3z_0^2+z_0^4}{9+3z^2+z^4}}, \tag{2.44}$$

where z_0 is the value that z has when the invariant mass of the pair of daughter particles is equal to the mass of the parent resonance. The $B_L(z)$ are normalized so that $B_L(z_0) = 1$.

The Blatt-Weisskopf radii are not measured in the PDG, and different analyses have used different guesses for their values. For example, [23] used $R = 1.5\ (\text{GeV}/c)^{-1}$ for the $\phi(1020)$, while [24] used $R = 4.0\ (\text{GeV}/c)^{-1}$. In this analysis, we take R to be $4.0\ (\text{GeV}/c)^{-1} \approx 0.8$ fm for all $K\bar{K}$ resonances. We will vary R by $\pm 2.5\ (\text{GeV}/c)^{-1}$ as a systematic.

In this analysis, we will normally ignore the Blatt-Weisskopf factor $B^B_L(|\vec{p^*}|R')$ that comes from the B decay (i.e., we set $B^B_L(|\vec{p^*}|R') = 1$, equivalent to $R' = 0$). However, as a systematic, we will include a $B^B_L(|\vec{p^*}|R')$ term with $R' = 1.5\ (\text{GeV}/c)^{-1}$.

Lineshapes

Most of the resonances in this analysis use a Relativistic Breit-Wigner (RBW) function for $T_r(m_{ab})$. The RBW has the functional form

$$T_r(m_{ab}) = \frac{1}{m_r^2 - m_{ab}^2 - i m_r \Gamma_r(m_{ab})}, \tag{2.45}$$

where $\Gamma_r(m_{ab})$ is the resonance width with the following dependence on m_{ab}:

$$\Gamma_r(m_{ab}) = \Gamma_r \left(\frac{q}{q_0}\right)^{2L+1} \left(\frac{m_r}{m_{ab}}\right) B^r_L(|\vec{q}|R)^2. \tag{2.46}$$

In the preceding equations, m_r and Γ_r are the pole mass and width of the resonance r. q_0 is the value that q has when $m_{ab} = m_r$.

We describe the $f_0(980)$ resonance using the coupled-channel (Flatté) function [26], which has the form

$$T_r(m_{ab}) = \frac{1}{m_r^2 - m_{ab}^2 - i(\Gamma_{KK}(m_{ab}) + \Gamma_{\pi\pi}(m_{ab}))}, \tag{2.47}$$

where

$$\Gamma_{KK}(m_{ab}) = g_K \sqrt{1 - 4m_K^2/m_{ab}^2} \tag{2.48}$$

and

$$\Gamma_{\pi\pi}(m_{ab}) = g_\pi \sqrt{1 - 4m_{\pi^\pm}^2/m_{ab}^2}\,, \tag{2.49}$$

where m_K is the average of m_{K^+} and $m_{K^0_S}$. The parameters g_K and g_π are coupling constants that we take from the BES experiment [19]:

$$\begin{aligned} g_\pi &= 0.165 \pm 0.010 \pm 0.015\,\mathrm{GeV}^2/c^4 \\ \frac{g_K}{g_\pi} &= 4.21 \pm 0.25 \pm 0.21 \end{aligned}$$

The $a_0^+(980)$ resonance is similarly described with a Flatté function, with

$$T_r(m_{ab}) = \frac{1}{m_r^2 - m_{ab}^2 - i(\Gamma_{KK}(m_{ab}) + \Gamma_{\pi\eta}(m_{ab}))}, \tag{2.50}$$

where

$$\Gamma_{\pi\eta}(m_{ab}) = g_{\pi\eta}\sqrt{\left(1 - \frac{(m_{\pi^\pm} + m_\eta)^2}{m_{ab}^2}\right)\left(1 - \frac{(m_{\pi^\pm} - m_\eta)^2}{m_{ab}^2}\right)}\,. \tag{2.51}$$

We take the parameters from Crystal Ball [21], [5] which found:

$$\begin{aligned} \sqrt{g_{\pi\eta}} &= 0.324 \pm 0.015\,\mathrm{GeV}/c^2 \\ \frac{g_K}{g_{\pi\eta}} &= 1.03 \pm 0.14\,. \end{aligned}$$

2.5.5 Nonresonant Amplitudes

Not all $B \to KKK$ decays can be ascribed to a particular two-body resonance, and instead are referred to as nonresonant (NR) decays. Previous analyses of $B^+ \to K^+K^-K^+$ [27, 24] and $B^0 \to K^+K^-K^0_S$ [23, 28] have found large fractions of nonresonant decays. To account for this nonresonant component, we include a nonresonant amplitude $F_{NR}(s_{12}, s_{23})$ in the isobar model. Since nonresonant decays are poorly understood, we test a number of different empirical parameterizations.

The *BABAR* and Belle DP analyses of $B^+ \to K^+K^-K^+$ both used an exponential

---

[5] Technically, we used $\sqrt{g_K/g_{\pi\eta}} = 1.03$ instead, but this difference is completely negligible, considering that this resonance is not used in our nominal fit model, but rather is only used as a systematic.

model for nonresonant decays:

$$F_{NR}(s_{12}, s_{23}) = e^{\alpha s_{12}} + e^{\alpha s_{23}} \tag{2.52}$$

That model only contains K^+K^- S-wave terms. In this analysis, we also test for a K^+K^+ S-wave nonresonant term in $B^+ \to K^+K^-K^+$:

$$F_{NR}(s_{12}, s_{23}) = e^{\alpha_{13} s_{13}} \tag{2.53}$$

Thus, the overall, symmetrized, nonresonant amplitude becomes:

$$\mathcal{A}_{NR}(s_{12}, s_{23}) = a_{12}\left(e^{\alpha s_{12}} + e^{\alpha s_{23}}\right) + a_{13} e^{\alpha_{13} s_{13}} \tag{2.54}$$

The previous *BABAR* and Belle analyses of $B^0 \to K^+K^-K^0_S$ have used a similar exponential NR model, but with $K^+K^0_S$ and $K^-K^0_S$ S-wave terms:

$$\mathcal{A}_{NR}(s_{12}, s_{23}) = e^{\alpha s_{12}} + a_{13} e^{\alpha s_{13}} + a_{23} e^{\alpha s_{23}} \tag{2.55}$$

Note that the $(K^+K^0_S)$ and $(K^-K^0_S)$ terms are S-wave in the $(K^+K^0_S)$ and $(K^-K^0_S)$ systems, respectively. However, they are *not* purely S-wave in the (K^+K^-) system, and that is what is crucial for determining whether they are *CP*-even or *CP*-odd. Thus, these terms contain both *CP*-even and *CP*-odd contributions.

We also test a nonresonant parameterization that is the sum of an S-wave (spin-0) and P-wave (spin-1) term, with both terms having a polynomial mass dependence, like this:

$$\mathcal{A}_{NR} = \left(a_{S0} + a_{S1}x + a_{S2}x^2\right) + \left(a_{P0} + a_{P1}x + a_{P2}x^2\right) P_1(\cos\theta_3)\,, \tag{2.56}$$

where $x \equiv m_{12} - m_0$, and m_0 is an offset that we define as

$$m_0 \equiv \frac{1}{2}\left(m_B + \frac{1}{3}(m_{K_1} + m_{K_2} + m_{K_3})\right)\,. \tag{2.57}$$

$\cos\theta_3$ is the cosine of θ_3, defined in Sec. 2.5.4. $P_1(\cos\theta_3)$ indicates the 1st-order

Legendre polynomial. [6] In the case of $B^+ \to K^0_S K^0_S K^+$, the P-wave term is forbidden by Bose-symmetry. In the case of $B^+ \to K^+K^-K^+$, both the S-wave and P-wave terms must be symmetrized under $\{1 \leftrightarrow 3\}$, so we add a copy of Eq. 2.56 with x changed to $y \equiv m_{23} - m_0$ and $\cos\theta_3$ changed to $\cos\theta_1$, defined in Sec. 2.5.4.

As a cross-check, we can also add a D-wave (spin-2) term to the previous NR model, so the following model results:

$$\begin{aligned}\mathcal{A}_{NR} = \left(a_{S0} + a_{S1}x + a_{S2}x^2\right) + \left(a_{P0} + a_{P1}x + a_{P2}x^2\right) P_1(\cos\theta_3) \\ + \left(a_{D0} + a_{D1}x + a_{D2}x^2\right) P_2(\cos\theta_3)\,,\end{aligned} \tag{2.58}$$

plus a symmetric term in the case of $B^+ \to K^+K^-K^+$.

In $B^+ \to K^+K^-K^+$, we also test the following 2D-polynomial nonresonant parameterization:

$$\begin{aligned}\mathcal{A}_{NR} &= a_{00} + a_{10}(x+y) + a_{20}(x^2+y^2) + a_{11}(xy) + \\ &\quad a_{30}(x^3+y^3) + a_{21}(x^2y + xy^2)\,.\end{aligned} \tag{2.59}$$

This model doesn't have a simple physical interpretation in terms of S-wave and P-wave, etc., components. However, the a_{11} and a_{21} terms may be viewed as combinations of S-wave and higher-wave components, while the other terms in the parameterization may be thought of as S-wave terms.

---

[6] We use the following non-standard normalization convention for the Legendre polynomials: $\int_{-1}^{1} P_l(\cos\theta_3) P_k(\cos\theta_3) d\cos\theta_3 = \delta_{lk}$. This will be convenient for certain calculations in Sec. 6.1.

Chapter 3

BABAR and PEP-II

The design of the *BABAR* experiment is heavily influenced by the physics goal of measuring time-dependent CP violation in B decays. Colliding e^+e^- at the $\Upsilon(4S)$ resonance is a natural choice for such an experiment, as it provides a good signal to background ratio. Furthermore, the $B\overline{B}$ pairs from the $\Upsilon(4S)$ decay are created in a well-defined initial state, and one can use this kinematic information to achieve excellent background suppression. However, the B mesons are created with very low momenta in the $\Upsilon(4S)$ frame, which would normally make a time-dependent measurement of their decays unfeasible. *BABAR* solves this problem by using asymmetric energies for the e^+ and e^- beams, thus producing an $\Upsilon(4S)$ that is highly boosted ($\beta\gamma \approx 0.56$) in the lab frame. This allows the longitudinal distance between the B decays to be converted into a Δt measurement.

In this chapter, we will give a brief overview of the *BABAR* detector and the PEP-II asymmetric e^+e^- collider.

3.1 PEP-II

PEP-II, situated at SLAC, consists of two intersecting storage rings, one each for the e^+ and e^- beams. The e^- bunches are generated by thermionic emission at the start of SLAC's 3.2km linac. After having their emittance reduced in a damping ring, the e^- bunches are accelerated to 9.0 GeV and injected into the "high-energy ring" (HER) of PEP-II. The e^+ bunches are generated by firing high-energy e^- at a tungsten target, which produces e^+ through pair-production. The e^+ are then sent to a damping ring, and then accelerated to 3.1 GeV and injected into the "low-energy ring" (LER).

The HER and LER intersect at the interaction region (IR), and here the e^+ and e^- beams collide. Strong quadrupole magnets are used to focus the beams at the collision point, in order to maximize luminosity. Performance parameters achieved by PEP-II, taken from [29], are given in Table 3.1. PEP-II was able to reach a peak luminosity of $1.2\times10^{34}\ cm^{-2}s^{-1}$, which surpassed its design luminosity [30] by a factor of four. A critical factor in achieving such a high luminosity is the large number of bunches that circulate at once. This is made possible due to the two-ring design.

Table 3.1: Machine parameters for PEP-II. Parameters are from during 2006.

Parameter	LER	HER
Energy (GeV)	3.1	9.0
$\varepsilon_x/\varepsilon_y$ (nm · rad)	36/1	73/1
β_x^*/β_y^* (cm)	21/1.0	74/1.1
N(bunches)	1730	1730
I (A)	3.0	1.9
$\mathcal{L}$ ($cm^{-2}s^{-1}$)	1.2×10^{34}	

Between 1999 and 2008, about 430 fb^{-1} of data were recorded by *BABAR* at the $\Upsilon(4S)$ resonance ("onpeak" data). In addition, about one-tenth this much data were collected at an energy 40 MeV below the $\Upsilon(4S)$ ("offpeak"). The offpeak data is useful for understanding backgrounds to $\Upsilon(4S)$ decays. PEP-II also produced smaller datasets at the $\Upsilon(3S)$ and $\Upsilon(2S)$, but those datasets are irrelevant for this analysis.

3.2 The *BABAR* Detector

A sketch of the *BABAR* detector is shown in Fig. 3.1. This sketch also shows the *BABAR* coordinate system, with the e^- traveling in the $+z$ direction, and the x and y axes in the horizontal and vertical directions, respectively. *BABAR* consists of the following subdetectors, moving outwards from the collision point:

- **Silicon Vertex Tracker (SVT).** It is crucial for measuring the positions of the B decay vertices, and is also important for low-momentum tracking. Additionally, $\mathrm{d}E/\mathrm{d}x$ measurements here help with particle identification (PID) of low-momentum charged hadrons.
- **Drift Chamber (DCH).** The main tracking subdetector, it gives the momenta of charged particles. Also, $\mathrm{d}E/\mathrm{d}x$ measurements here help with PID.
- **Detector of Internally Reflected Cherenkov Light (DIRC).** This subdetector contributes to charged hadron PID.
- **Electromagnetic Calorimeter (EMC).** This is used for measurements of photons and π^0's. It is also used for $e^{\pm}$ identification.
- **Instrumented Flux Return (IFR).** This subdetector is used for muon identification, and for measuring K_L^0's.

The first four of these subdetectors are inside a 1.5T magnetic field generated by a superconducting solenoid. This analysis makes use of all five subdetectors, but it depends more on the first three subdetectors than the last two. We will now give a brief overview of the subdetectors, with an emphasis on their relevance to the $B \to KKK$ analysis. Much of the information in this section is taken from [31]; more details about the *BABAR* detector can be found there. [1]

3.2.1 Silicon Vertex Tracker

The SVT is a five-layer silicon tracker, designed especially for precise vertexing of B decays. Radial and side views of the SVT are shown in Figs. 3.2 and 3.3, respectively. The first three layers are just outside the beampipe, and are most important for measuring impact parameters. The fourth and fifth layers are farther out, and help SVT tracks to be linked up with DCH tracks, and also allow for tracking of charged

---

[1] Figs. 3.1, 3.2, 3.3, 3.4, 3.6, and 3.7 are taken from [31]. Reprinted from Nucl. Instrum. Meth. **A479**, B. Aubert *et al.*, *The BABAR detector*, 1, Copyright 2002, with permission from Elsevier.

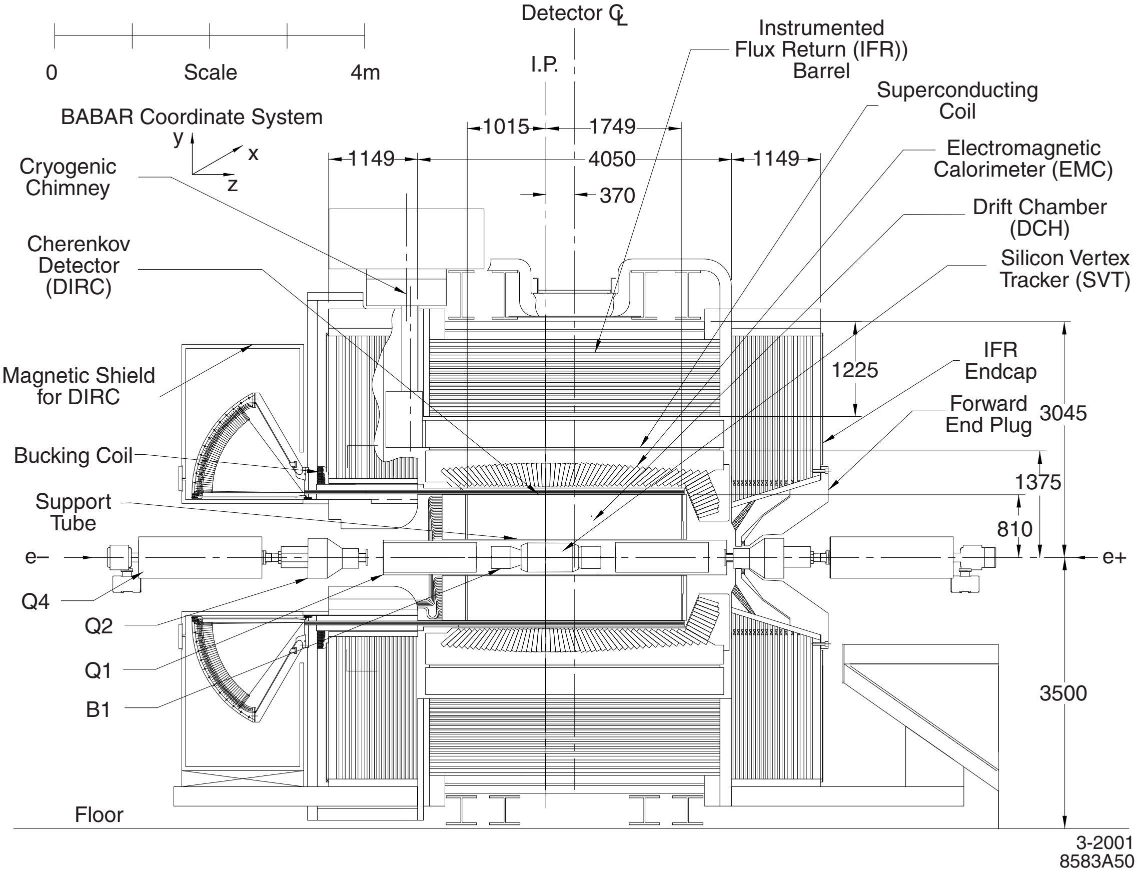

Figure 3.1: Sketch of the *BABAR* detector. Dimensions are given in mm.

particles with transverse momenta (p_T) below 120 MeV, which are too low momentum to be tracked by the DCH.

Each layer of the SVT consists of between six and eighteen modules, with each module consisting of many detectors. The detectors are double-sided silicon strip detectors. On one side, the strips run in the azimuthal direction, and are used to measure the z-coordinate ("z"-strips), and on the other side, the strips run in the longitudinal direction, and are used to measure the ϕ-coordinate ("ϕ"-strips). The radii of the layers and readout pitches of the strips are given in Table 3.2. The outer two layers have an arched shape, as can be seen in 3.3, so their radii are not constant. The readout pitches are often larger than the actual physical pitches, because some of the strips are not read out ("floating strips"), in order to reduce the number of readout channels. In total, the SVT has about 150, 000 readout channels.

Table 3.2: Radii and readout pitches for each of the SVT layers.

Layer	radius (mm)	readout pitch (μm)	
		z	ϕ
1	32	100	50-100
2	40	100	55-110
3	54	100	110
4	91-127	210	100
5	114-144	210	100

The silicon strip sensors are 300 μm thick, with an n-type bulk, with orthogonal n^+ and p^+ strips on either side of the bulk. The sensors are reverse biased so that they are fully depleted. Charged particles traversing the sensors generate electron-hole pairs in the bulk, and the electrons and holes propagate under influence of the applied voltage to opposite strips. The induced signals are then sent via fanout circuits to custom-built frontend electronics. The strength of the signal pulses can be used to measure dE/dx, which allows for 2σ $K-\pi$ separation below 500 MeV.

The mean B^0 flight distance is $\beta\gamma c\tau \approx 250\,\mu$m, and the time-dependent CPV oscillations peak at around $\Delta z = 500\,\mu$m, so this sets the scale for the desired Δz resolution. The actual Δz resolution has a core width of about $100\,\mu$m, with long tails resulting in an overall width of about 190 μm. The Δz resolution is mainly due to the B^0_{tag} vertex resolution.

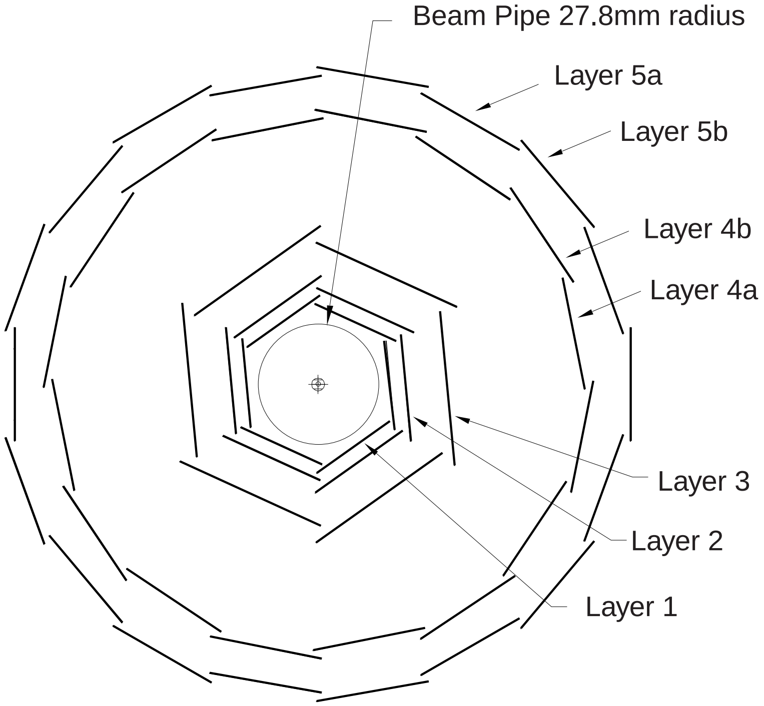

Figure 3.2: Radial view of the SVT.

3.2.2 Drift Chamber

The DCH is the main tracking device in *BABAR*, used for identifying charged tracks and measuring their momenta. It also measures $\mathrm{d}E/\mathrm{d}x$, which allows for PID at low momenta. The DCH is shown in Fig. 3.4.

The DCH is a cylindrical detector filled with a gas mixture of 80% helium and 20% isobutane. The detector is strung longitudinally with 40 layers of wires. The wires are arranged into 7104 hexagonal "cells," with six "field wires" surrounding a "sense wire." The field wires are held at ground potential, while 1900-1960 V are applied to the sense wires. When a charged particle passes through the detector, it ionizes the gas, which causes an avalanche of ionization to drift to the nearest sense wires. The

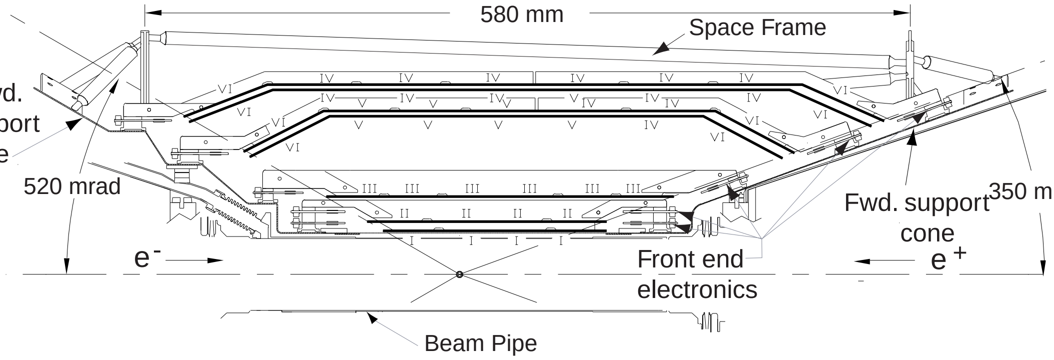

Figure 3.3: Longitudinal view of the SVT.

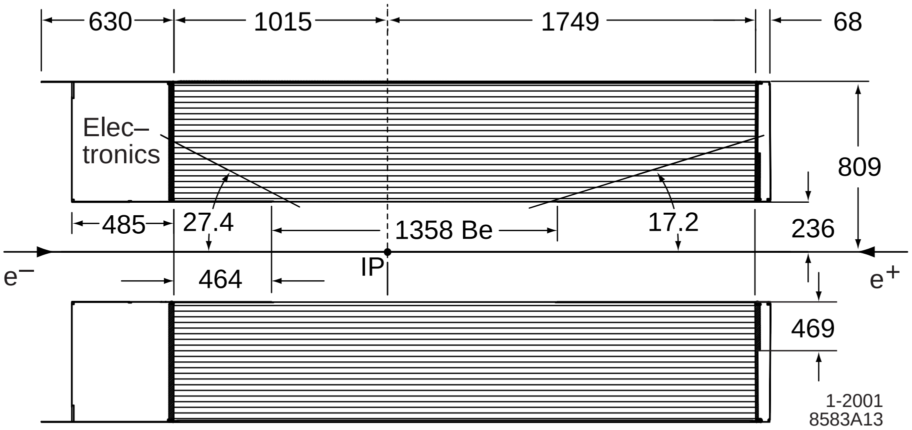

Figure 3.4: Longitudinal view of the DCH. Dimensions are in mm; angles are in degrees.

drift time can be used to measure the particle's position. The 40 layers are organized into 10 superlayers, the wires within each superlayer being oriented at the same angle. Some superlayers are oriented in the z-direction, while others are oriented at small (45-76 mrad) stereo angles, which allows for z-position measurements.

The DCH provides a hit resolution between $100\,\mu$m and $400\,\mu$m, depending on the drift distance. The p_T for charged particles, which is measured mainly by the DCH, has a measured resolution of

$$\frac{\sigma_{p_T}}{p_T} = (0.13 \pm 0.01)\% \cdot p_T + (0.45 \pm 0.03)\% \,. \tag{3.1}$$

In $B \to KKK$ decays, the $K^{\pm}$ typically have p_T in the range 200 MeV/c to 2.5 GeV/c, with an average of about 1 GeV/c. An important parameter for $B \to KKK$ decays is the resolution on the KK invariant mass. This is particularly important for narrow resonances like the $\phi(1020)$ and χ_{c0}. Fig. 3.5 shows the $m_{K^+K^-}$ resolution in simulation for $B^0 \to K^+K^-K^0_S$ decays, as a function of $m_{K^+K^-}$.

The DCH can also measure $\mathrm{d}E/\mathrm{d}x$ for charged particles, which allows for PID. Fig. 3.6 shows $\mathrm{d}E/\mathrm{d}x$ measurements in the DCH for various charged particles, as a function of momentum. Good K/π separation is possible below 700 MeV. This is highly complementary to the PID information from the DIRC, which is strong for momenta $\gtrsim 700$ MeV.

The DCH also helps in reconstructing K^0_S that decay outside of the SVT. In $B^0 \to K^+K^-K^0_S$, these long-lived K^0_S account for about one-fifth of all reconstructed K^0_S decays.

3.2.3 Detector of Internally Reflected Cherenkov Light

The DIRC system is dedicated to PID by detecting Cherenkov light emitted by charged particles. It is important for momenta above 700 MeV/c, where the $\mathrm{d}E/\mathrm{d}x$ measurements become less useful. The momenta of the $K^{\pm}$ in $B \to KKK$ decays have a broad distribution, with almost all between 0.5 GeV/c and 3.5 GeV/c. This means the DIRC is mainly responsible for PID in this analysis.

The DIRC contains 144 fused silica bars, each 4.9m long, arranged in a barrel

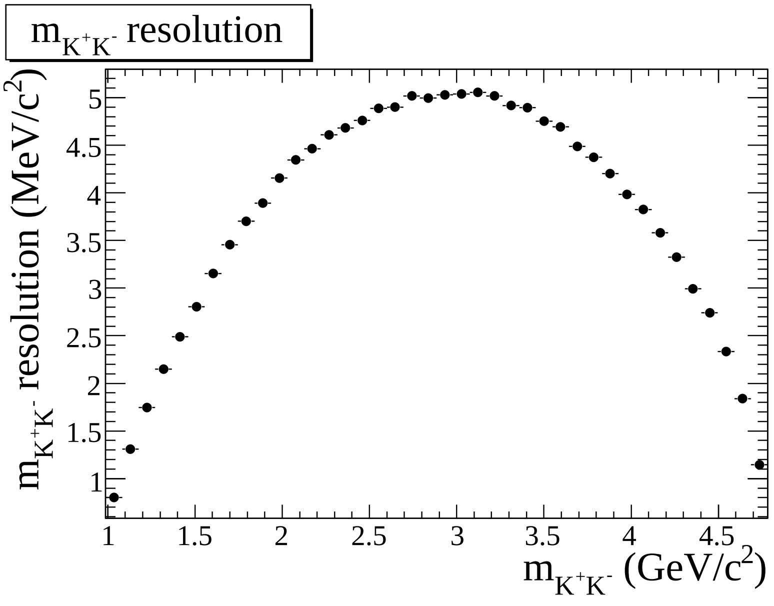

Figure 3.5: The simulated $m_{K^+K^-}$ resolution for $B^0 \rightarrow K^+K^-K^0_S$ ($K^0_S \rightarrow \pi^+\pi^-$) decays, as a function of $m_{K^+K^-}$. Resolution is calculated from a Gaussian fit to the core of the resolution, ignoring the tails of the distribution. The reason the resolution improves at high $m_{K^+K^-}$ is that the kinematic fit constrains the $K^+K^-K^0_S$ invariant mass to the true B^0 mass, and so a good K^0_S measurement is able to reduce the error on $m_{K^+K^-}$.

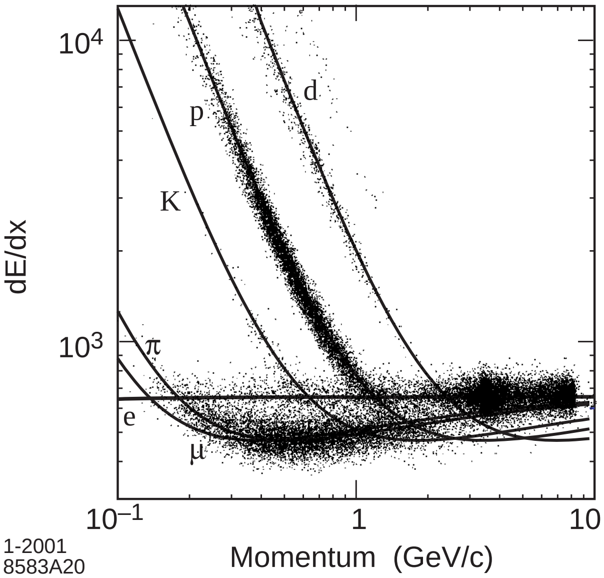

Figure 3.6: dE/dx from data, as measured in the DCH.

shape. Groups of 12 bars are each enclosed in a *bar box*. The operation of the DIRC is illustrated in Fig. 3.7. When a charged particle passes through one of the bars (index of fraction $n = 1.473$), it emits Cherenkov light at an angle θ_C, where $\cos\theta_C = 1/n\beta$. Some of this light is internally reflected along the bar. A mirror is placed on one end of the bar to reflect the light, while the light is allowed to escape out the other end of the bar into a *standoff box*. The standoff box is filled with water ($n \approx 1.346$) and its surface is covered by an array of 10,752 photomultiplier tubes (PMT's) for detecting the light. By measuring the photon angle with the PMT array, and combining this with the charged particle's track (calculated from the SVT and DCH), one can infer θ_C, up to some geometric ambiguities. Timing information is used to reduce the number of these ambiguities.

The θ_C resolution has been measured in $\mu^+\mu^-$ events to be about 2.5 mrad per track. Fig. 3.8 shows θ_C for different particle types, as a function of momentum. By combining the θ_C measurement with the momentum measurement from the DCH and SVT, one can infer the particle type.

The main importance of PID in $B \to KKK$ is to distinguish $K^\pm$ from $\pi^\pm$. We

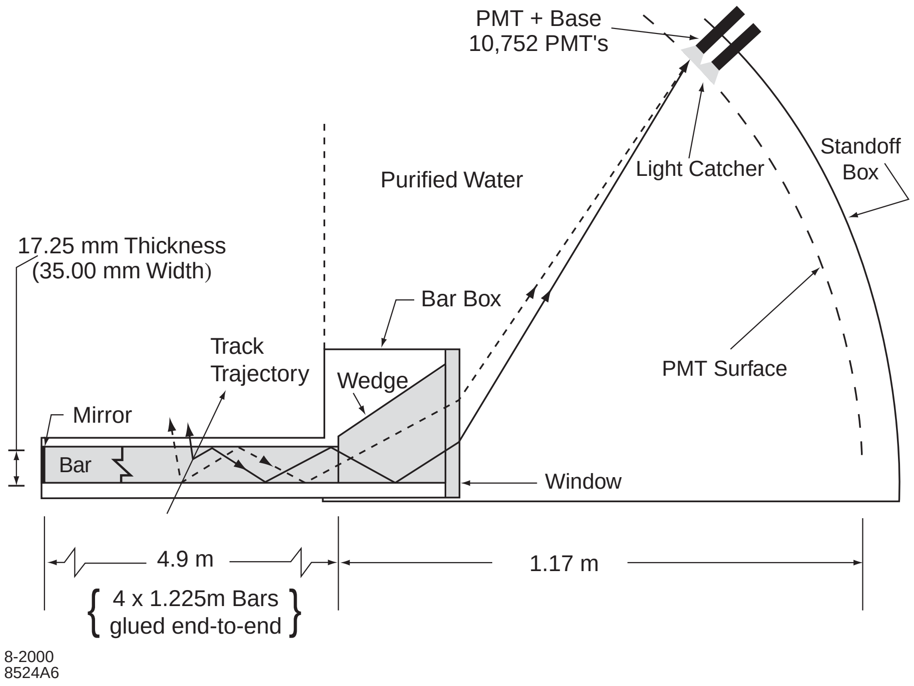

Figure 3.7: Illustration of the DIRC. Shown are the trajectories of two Cherenkov photons down one of the bars and into the water-filled standoff box.

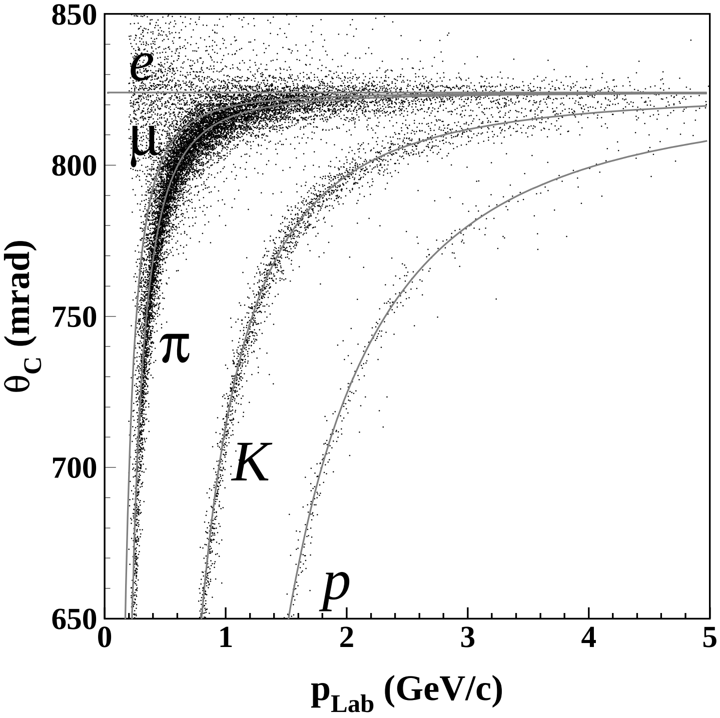

Figure 3.8: The Cherenkov angle θ_C measured in the DIRC, as a function of momentum. Events are from a multi-hadron data sample. Figure is from [32]. Reprinted from Nucl. Instrum. Meth. **A538**, I. Adam *et al.*, *The DIRC particle identification system for the BABAR experiment*, 281, Copyright 2005, with permission from Elsevier.

combine information from the DIRC with PID information from the other subdetectors to distinguish between particle types. We use a variety of PID selection criteria in the different $B \to KKK$ analyses (see Chapter 4). Generally, tighter PID requirements result in a kaon efficiency of $\gtrsim 80\%$ and a pion-as-kaon misidentification rate $\lesssim 3\%$ for most of the momentum range. Meanwhile, looser PID criteria typically give a kaon efficiency $\approx 90\%$ and a pion-as-kaon misidentification rate $\lesssim 5\%$ for most of the momentum range. However, for $p > 3\,\text{GeV}$ the performance can be somewhat worse than this.

3.2.4 Electromagnetic Calorimeter

The EMC is a homogeneous calorimeter that measures electromagnetic showers generated by photons and $e^\pm$. It is designed to measure photons over a wide range of energies, from $20\,\text{MeV}$ to $9\,\text{GeV}$. It can also be used to distinguish $e^\pm$, which shower heavily, from $\pi^\pm$ and $\mu^\pm$.

The EMC has two sections, a barrel and a forward endcap, and contains 6580 individual crystals arranged in rings. It covers polar angles from 15.8° to 141.8°. This results in a 90% solid angle coverage in the $\Upsilon(4S)$ frame.

The crystals are made of thallium-doped cesium iodide (CsI(Tl)). It has good scintillation properties, with a high light yield, short radiation length (1.85 cm), and small Moliére radius (3.8 cm). The thickness of the EMC varies between 16 and 17.5 radiation-lengths. The scintillation light is measured by silicon PIN diodes connected to the backs of the crystals. The energy resolution of the EMC can be parameterized as

$$\frac{\sigma_E}{E} = \frac{(2.32 \pm 0.30)\%}{\sqrt[4]{E(\,\text{GeV})}} \oplus (1.85 \pm 0.12)\%\,, \tag{3.2}$$

while the angular resolution is

$$\sigma_\theta = \sigma_\phi = \left(\frac{3.87 \pm 0.07}{\sqrt{E(\,\text{GeV})}} + 0.00 \pm 0.04\right)\,\text{mrad}\,. \tag{3.3}$$

The EMC is not particularly important for this analysis. It is mainly used in the $B^0 \to K^+K^-K^0_S$ mode, when we reconstruct $K^0_S \to \pi^0\pi^0$ (although almost all of our physics reach in $B^0 \to K^+K^-K^0_S$ comes from the $K^0_S \to \pi^+\pi^-$ mode). With our nominal selection criteria for the $B^0 \to K^+K^-K^0_S$ analysis, the $K^0_S \to \pi^0\pi^0$ reconstruction efficiency is around 20%. The resolution on the $K^0_S \to \pi^0\pi^0$ mass is about $12\,\mathrm{MeV}/c^2$, as determined from simulation. The EMC's ability to identify $e^\pm$ is also important for the $\overset{(-)}{B^0}$ flavor tagging, as one method of flavor tagging relies on identifying $e^\pm$ from semileptonic decays.

3.2.5 Instrumented Flux Return

The steel flux return of the 1.5T solenoid is instrumented, and used as a subdetector to identify muons and neutral hadrons, in particular K^0_L. The IFR's main importance to this analysis is in $B^0 \to K^+K^-K^0_S$, where it is used in $\overset{(-)}{B^0}$ flavor tagging by identifying $\mu^\pm$ from semileptonic decays.

The IFR consists of a hexagonal barrel section and two endcaps. The steel of the flux return is divided into 18 plates, with gaps between them. Originally, there were 19 layers of resistive plate chambers (RPC's) between the gaps in the barrel, and 18 layers of RPC's in the endcaps. Very early on, the performance of the RPC's began to degrade, result in a severe loss in muon efficiency. Between 2004 and 2006, twelve of the RPC's in the barrel were replaced by limited streamer tubes (LST's)[33], which have had fewer problems. Another six of the RPC's in the barrel were replaced by brass, in order to provide more absorption material.

The main muon identification purpose for the IFR is to distinguish muons from $\pi^\pm$. This is achieved by looking at the number of layers traversed by a particle, and the shape of the cluster of hits left by the particle. For momenta above $1.2\,\mathrm{GeV}/c$, muon efficiencies of $\sim 80\%$ with pion mis-ID rates $\sim 2\%$ are possible.

Chapter 4

Event Selection

4.1 Datasets

These analyses are based on *BABAR*'s full $\Upsilon(4S)$ data sample (onpeak data). The $B^+ \to K^+K^-K^+$ analysis uses data from *BABAR*'s R22 processing cycle, while $B^+ \to K^0_S K^0_S K^+$ and $B^0 \to K^+K^-K^0_S$ are based on the later R24 processing cycle. The integrated luminosity and number of $B\overline{B}$ pairs used in these analyses are shown in Table 4.1. In addition, we study backgrounds with about $44\,\mathrm{fb}^{-1}$ of offpeak data.

Table 4.1: Datasets used for these analyses. R22 is used for $B^+ \to K^+K^-K^+$; R24 is used for $B^+ \to K^0_S K^0_S K^+$ and $B^0 \to K^+K^-K^0_S$.

	R22		R24	
Run Period	Luminosity (fb^{-1})	$N_{B\overline{B}}$ ($\times 10^6$)	Luminosity (fb^{-1})	$N_{B\overline{B}}$ ($\times 10^6$)
Run 1	20.4	22.4	20.6	22.6
Run 2	61.1	67.4	62.1	68.4
Run 3	32.3	35.6	32.7	35.8
Run 4	100.3	110.5	100.8	111.4
Run 5	133.3	147.2	133.9	147.6
Run 6	78.4	84.4	79.0	85.2
Total	425.7	467.4	429.1	471.0

In addition to the real data collected by *BABAR*, we study simulated Monte Carlo (MC) signal and background events. These events are passed through a realistic GEANT4 simulation of the detector.

We use two classes of signal MC to describe $B \to KKK$ events. "Phasespace" MC is generated uniformly over the DP, while "Dalitz model" MC is generated with a more realistic DP distribution using an isobar model. We will sometimes refer to a particular MC sample by the "SP" (Simulated Production) number assigned to it in *BABAR*'s MC database. We use the following signal MC samples in this analysis:

$B^+ \to K^+K^-K^+$

- SP-1932 (Phasespace model): about 7.8 Million events,
- SP-6845 (Dalitz model based on *BABAR*'s previous $B^+ \to K^+K^-K^+$ analysis): 968,000 events.
- SP-9688 (Dalitz Model based on *BABAR*'s previous $B^+ \to K^+K^-K^+$ analysis, but with corrections): 4.296 Million events.

$B^+ \to K^0_S K^0_S K^+$

- SP-3915 (Phasespace model, $K^0_S \to \pi^+\pi^-$ only): about 4.272 Million events,
- SP-9000 (Phasespace model, both $K^0_S \to \pi^+\pi^-$ and $K^0_S \to \pi^0\pi^0$): about 427,000 events,
- SP-10338 (Dalitz model based on *BABAR*'s previous $B^0 \to K^+K^-K^0_S$ analysis, $K^0_S \to \pi^+\pi^-$ only): 1.706 Million events

$B^0 \to K^+K^-K^0_S$

- SP-1593 (Phasespace model, both $K^0_S \to \pi^+\pi^-$ and $K^0_S \to \pi^0\pi^0$): 6.397 Million events
- SP-7930 (Dalitz model based on *BABAR*'s previous $B^0 \to K^+K^-K^0_S$ analysis, $K^0_S \to \pi^+\pi^-$ only): 8.595 Million events
- SP-7931 (Dalitz model based on *BABAR*'s previous $B^0 \to K^+K^-K^0_S$ analysis, $K^0_S \to \pi^0\pi^0$ only): 8.587 Million events

We also study backgrounds using MC. Backgrounds in this analysis can be split into two basic categories: *continuum* background, originating from $e^+e^- \to q\bar{q}$ events, with $q = u, d, s, c$; and $B\overline{B}$ background, originating from $e^+e^- \to \Upsilon(4S) \to B\overline{B}$ events. Continuum background is mainly studied with offpeak data or onpeak sideband data, while $B\overline{B}$ background is studied with MC. Some background studies are done using "generic" MC that attempts to simulate a general background process with proper branching fractions and kinematic distributions. We use the following generic MC samples in this analysis:

- B^+B^- generic (Simulates $\Upsilon(4S) \to B^+B^-$ events): about 703 million events in R22, 709 million in R24.
- $B^0\overline{B}^0$ generic (Simulates $\Upsilon(4S) \to B^0\overline{B}^0$ events): about 685 million events in R22, 718 million in R24.
- *uds* (Simulates $e^+e^- \to q\bar{q}$ events, with $q = u, d, s$): about 900 million events in R22. Not used in R24.

We also study backgrounds from specific $B^\pm$ and $\overset{(-)}{B^0}$ decay modes using *exclusive MC* in which one of the B's from the $\Upsilon(4S)$ decays generically, while the other B decays through a specific decay channel of interest. These exclusive $B\overline{B}$ samples will be discussed in Sec. 5.4.

4.2 Event Preselection

In order to make the amount of data more manageable to analysts, *BABAR* data is *skimmed* into different categories. We then only need to look at data belonging to a particular skim category. In $B^+ \to K^+K^-K^+$, we use events that pass the `BToCCC` skim, while in $B^+ \to K^0_S K^0_S K^+$ and $B^0 \to K^+K^-K^0_S$, we use events passing the `BToCPP` skim. The skim criteria are very loose compared to our ultimate selection criteria, so we do not lose in signal efficiency.

$B \to KKK$ events are reconstructed by combining particle candidates belonging to various *lists*. In $B^+ \to K^+K^-K^+$, B candidates are formed by combining three charged tracks from the `GoodTracksLoose` list that pass a very loose kaon-PID criteria (`KLHNotPion`). The `GoodTracksLoose` list requires tracks to have $p_T > 50\,\mathrm{MeV}/c$, $p < 10\,\mathrm{GeV}$, and to have a distance-of-closest approach (DOCA) no greater than 1.5 cm in the xy plane, and no greater than 2.5 cm in z.

In $B^+ \to K^0_S K^0_S K^+$, a track from `GoodTracksLoose` passing a very loose kaon-PID criteria (`KCombinedSuperLoose`) is combined with two K^0_S candidates from the `KsDefault` list. The `KsDefault` list contains $K^0_S \to \pi^+\pi^-$ candidates formed from charged tracks having an invariant mass within $25\,\mathrm{MeV}/c^2$ of the K^0_S mass.

In $B^0 \to K^+K^-K^0_S$, we reconstruct B candidates in two decay channels: $K^0_S \to \pi^+\pi^-$ and $K^0_S \to \pi^0\pi^0$. We will abbreviate these two decay channels as $K^0_S \to \pi^+\pi^-$ and $K^0_S \to \pi^0\pi^0$, respectively. In $K^0_S \to \pi^+\pi^-$, the B is formed from two tracks from `GoodTracksLoose` (passing `KCombinedSuperLoose`) combined with a K^0_S from `KsDefault`. In $K^0_S \to \pi^0\pi^0$, meanwhile, the K^0_S is taken from the list `KsToPi0Pi0Default`. The `KsToPi0Pi0Default` candidates are formed from two π^0 candidates. The π^0 candidates are formed either from two photon candidates, or from a single EMC cluster whose shape is consistent with coming from a π^0 ("merged" π^0's).

The B candidates are formed using a fitting algorithm called `TreeFitter` which uses a Kalman Filter method. The fit is both geometric and kinematic, and constrains the B's production vertex to the beamspot. The fit is first performed without a constraint on the B mass. Afterwards, the fit is redone with the B candidate's mass constrained to the true B mass, and the result of this fit is used to get the DP coordinates for the candidate. The B mass constraint forces the DP coordinates to lie within the kinematically allowed region.

At this initial stage, events are required to pass the loose cuts $5.2 < m_{\mathrm{ES}} < 5.3\,\mathrm{GeV}/c^2$ and $|\Delta E| < 0.3\,\mathrm{GeV}$. m_{ES} is defined as $m_{\mathrm{ES}} \equiv \sqrt{(s/2 + \mathbf{p}_i \cdot \mathbf{p}_B)^2/E_i^2 - \mathbf{p}_B^2}$, where $\sqrt{s}$ is the total e^+e^- CM energy, and $(E_i, \mathbf{p}_i)$ is the four-momentum of the e^+e^- system and $\mathbf{p}_B$ is the B candidate momentum, both measured in the laboratory frame. ΔE is defined as $\Delta E \equiv E_B - \sqrt{s}/2$, where E_B is the B candidate energy in the CM frame. For signal events, m_{ES} peaks at $\mathrm{m}_B \approx 5.28\,\mathrm{GeV}/c^2$ and ΔE peaks at zero. After this initial selection stage, we transform m_{ES} as $5.29\,\mathrm{GeV}/c^2 + m_{\mathrm{ES}} - 0.5 \cdot \sqrt{s}$. From now on, this transformed m_{ES} will be simply referred to as m_{ES}.

4.3 Initial Cuts

BABAR has performed previous analyses of $B^+ \to K^+K^-K^+$ [24, 34], $B^+ \to K^0_S K^0_S K^+$ [35, 36], and $B^0 \to K^+K^-K^0_S$ [23, 37]. (In the case of $B^+ \to K^0_S K^0_S K^+$, however, it was not a DP analysis.) In many cases, we chose to use the same cuts as were chosen in those analyses, rather than doing our own optimization.

We make a few loose initial cuts in $B^+ \to K^+K^-K^+$ and $B^+ \to K^0_S K^0_S K^+$. They are not very important; we list them here mainly for thoroughness. In $B^+ \to K^+K^-K^+$ we apply the following cuts:

- The total energy of the event E_{tot} is less than 20 GeV.
- The difference between m_{ES} and the invariant mass of the B candidate is less than $0.1\,\text{GeV}/c^2$.
- The invariant masses of the K pairs, m_{ij}, satisfy $0 \leq m^2_{ij} \leq (m_B - m_K)^2 + 1.0\,\text{GeV}^2$. Note that $(m_B - m_K)^2$ is the theoretical kinematic limit for m^2_{ij}.
- The χ^2 of the B vertex fit is less than 200.
- There are at least four tracks in the `GoodTracksLoose` list for the event.

In $B^+ \to K^0_S K^0_S K^+$, we only apply the first of those cuts ($E_{tot} < 20\,\text{GeV}$).

More importantly, we make a cut on $\cos\theta_T$ in all three $B \to KKK$ modes, where θ_T is the angle between the thrust axis calculated with the B candidate's daughters and the thrust axis formed from the other charged and neutral particles in the event. This cut's purpose is to suppress continuum backgrounds, which peak at $|\cos\theta_T| = 1$. In $B^+ \to K^0_S K^0_S K^+$ and $B^0 \to K^+K^-K^0_S$, we require $|\cos\theta_T| < 0.9$, while in $B^+ \to K^+K^-K^+$, we require $|\cos\theta_T| < 0.95$.

4.4 K^0_S Selection

We apply the same K^0_S selection cuts that *BABAR*'s previous $B^+ \to K^0_S K^0_S K^+$ and $B^0 \to K^+K^-K^0_S$ analyses used. We require that each K^0_S pass the following selection criteria:

- The K_S^0 must have a flight significance ≥ 3, where the flight significance is the flight length divided by the error on the flight length.
- The K_S^0 flight direction must satisfy $\cos\alpha_{K_S} > 0.999$, where α_{K_S} is defined as the angle between the K_S^0 momentum vector and the vector that connects the B and K_S^0 decay vertices.

We also make a requirement on the reconstructed K_S^0 mass, $m_{\pi\pi}$, that depends on the decay mode:

- For $B^+ \to K_S^0 K_S^0 K^+$, $m_{\pi\pi}$ must be within 12 MeV/c^2 of the nominal K_S^0 mass ($m_{K_S^0}$).
- For $B^0 \to K^+K^-K_S^0$ ($K_S^0 \to \pi^+\pi^-$), $m_{\pi\pi}$ must be within 20 MeV/c^2 of $m_{K_S^0}$.
- For $B^0 \to K^+K^-K_S^0$ ($K_S^0 \to \pi^0\pi^0$), $m_{\pi\pi}$ must be in the range $(m_{K_S^0} - 20\,\text{MeV}/c^2) < m_{\pi\pi} < (m_{K_S^0} + 30\,\text{MeV}/c^2)$. This range was determined from an optimization study in a previous analysis.

4.5 Kaon PID Selection

BABAR has developed a number of different PID *selectors* that combine information from the DIRC, DCH, SVT, etc. to determine whether a charged track is consistent with a particular particle hypothesis. In $B^+ \to K^+K^-K^+$, we choose from a set of likelihood-ratio-based kaon selectors (`LH`). In terms of increasing tightness, the selectors are `KLHNotPion`, `KLHLoose`, `KLHTight`, and `KLHVeryTight`. In $B^+ \to K_S^0 K_S^0 K^+$ and $B^0 \to K^+K^-K_S^0$, we choose from a set of kaon selectors based on an Error Correcting Output Code technique (`KM`), which have similar performance to the `LH` selectors, but somewhat better.[1] In terms of increasing tightness, the selectors are `KKMSuperLoose`, `KKMVeryLoose`, `KKMLoose`, `KKMTight`, `KKMVeryTight` and `KKMSuperTight`.

---

[1] The `KM` selectors were not available in the R22 release, so that is why we do not use them in $B^+ \to K^+K^-K^+$.

In $B^+ \rightarrow K^+K^-K^+$ and $B^+ \rightarrow K^0_S K^0_S K^+$, we do an optimization procedure to decide what kaon PID selectors to use. For different PID selectors, we estimate how many signal events and background events would pass our selection in the region $m_{\rm ES} > 5.27\,{\rm GeV}/c^2, |\Delta E| < 0.1\,{\rm GeV}$ (for $B^+ \rightarrow K^+K^-K^+$) or $m_{\rm ES} > 5.275\,{\rm GeV}/c^2, |\Delta E| < 0.06\,{\rm GeV}$ (for $B^+ \rightarrow K^0_S K^0_S K^+$). The number of signal events is estimated using Dalitz model signal MC and previous measurements for the signal branching fractions. The number of background events is extrapolated from onpeak data outside of the signal region. Using these predictions for the number of signal events (S) and background events (B), we pick the kaon PID requirements that maximize the expected $S/\sqrt{S+B}$.

The optimization study for $B^+ \rightarrow K^+K^-K^+$ shows the same performance for two combinations:

- `KLHLoose-KLHLoose-KLHTight`
- `KLHLoose-KLHLoose-KLHVeryTight`.

We choose the latter option. It means that two of the three kaons should pass `KLHLoose` and the last kaon should pass `KLHVeryTight`. The efficiency of this PID cut is about 67% for signal MC, 17% for offpeak data, 16% for $B^0\overline{B}^0$ generic MC, and 15% for B^+B^- generic MC. (B^+B^- generic MC contains actual $B^+ \rightarrow K^+K^-K^+$ events, which we have removed.) These efficiencies are the relative efficiencies for the PID cut, after all of the already mentioned cuts have been applied.

Based on the optimization study for $B^+ \rightarrow K^0_S K^0_S K^+$, we decide to choose the `KKMVeryLoose` selector. The efficiency of this PID selector is about 94% for signal MC, 61% for offpeak data, 52% for $B^0\overline{B}^0$ generic MC, and 69% for B^+B^- generic MC.

For $B^0 \rightarrow K^+K^-K^0_S$, we do not do a separate PID optimization, but instead base our choices on *BABAR*'s previous analysis of this mode. If the K^+K^- invariant mass $m_{K^+K^-}$ is less than $1.1\,{\rm GeV}/c^2$, than we require one K to pass `KKMLoose` and the other K to pass `KKMSuperLoose`. If $m_{K^+K^-} > 1.1\,{\rm GeV}/c^2$, then we apply tighter PID requirements: both K are required to pass `KKMTight`. This is the same as what the previous analysis did, except they used the `LH` selectors instead of `KM`.

The `KM` selectors are very similar in performance to the `LH` selectors, but somewhat better. The argument made for different PID requirements in the different $m_{K^+K^-}$ regions was that the looser PID requirement increased the signal efficiency by 13% in the ϕ region, with no significant increase in $B\overline{B}$ background. Meanwhile, using the looser PID requirement for the entire DP would have significantly increased the $B\overline{B}$ backgrounds.

4.6 Event Shape

4.6.1 Training a Discriminator

We train multivariate methods to reject continuum background better, using the `TMVA` package [38]. For $B^+ \to K^+K^-K^+$, we train multivariate discriminators to discriminate between Dalitz model signal MC (SP-6845) and offpeak data. The input variables are $|\cos\theta_B|$, $|\cos\theta_T|$, $\mathcal{L}_2/\mathcal{L}_0$, $|\mathrm{TFlv}|$, and $|\Delta t/\sigma_{\Delta t}|$, where

- $\cos\theta_B$ is the cosine of the angle between the B meson direction and the z-direction.
- $\mathcal{L}_2/\mathcal{L}_0$ is the ratio of the 2nd and 0th order Legendre polynomial moments, defined as
$$\mathcal{L}_J = \sum_i |\vec{p_i}| P_J(\cos\theta_i) \tag{4.1}$$
where the sum is over the rest of the event, the angles are measured with respect to the thrust axis of the B-candidate, and all quantities are measured in the $\Upsilon(4S)$ frame.
- TFlv is the output of the neural network used for B flavor tagging.
- Δt is the measured time difference between the two B decays, and $\sigma_{\Delta t}$ is the error on Δt.

The input variable distributions are shown in Fig. 4.1. Four multivariate methods were tested: a Boosted Decision Tree (BDT), a Likelihood cut, a Fisher Discriminant, and a Multi-Layer Perceptron Neural Network (MLP).

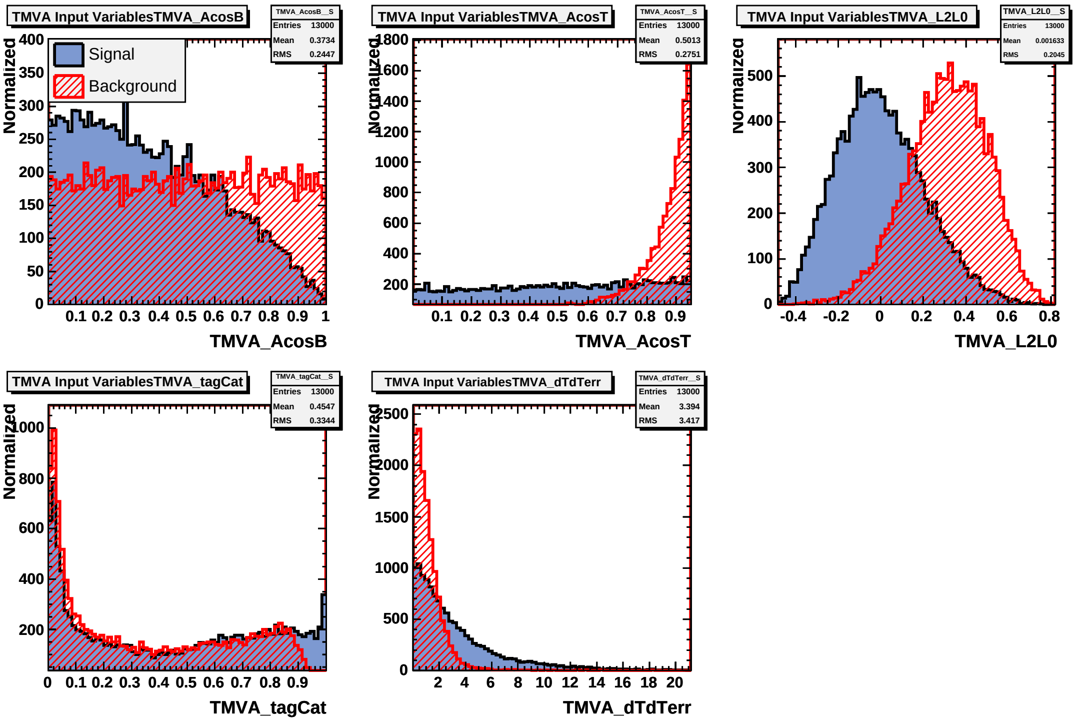

Figure 4.1: The TMVA input variable distributions for $B^+ \to K^+K^-K^+$.

Table 4.2: TMVA overtraining check. The table gives the relative signal efficiency of TMVA cuts that produce the specified relative background rejection. Numbers are given both for the test and training samples.

Background rejection	99%	90%	70%
Methods	Signal efficiency for test (training) sample		
MLP	0.436 (0.411)	0.788 (0.785)	0.931 (0.928)
BDT	0.380 (0.627)	0.765 (0.918)	0.924 (0.945)
Likelihood	0.382 (0.425)	0.752 (0.759)	0.923 (0.922)
Fisher	0.342 (0.328)	0.731 (0.733)	0.913 (0.909)

As shown in Fig. 4.2, the MLP neural network does the best job of discriminating between signal and background events. We also checked that the MLP does not suffer from overtraining. To do this, we split both the signal and background events into two independent samples, a “training” sample and a “test” sample. We train the MLP on the signal/background training sample. Then we look at what the relative signal efficiency is for an MLP cut that achieves 70%, 90%, and 99% relative background rejection. We look at this for both the “training” and “test” samples. If the MLP were overtrained, we would expect to see a better signal efficiency (for a given background rejection rate) for the training sample than for the test sample. The results of this overtraining test (done not only for the MLP method, but also for the BDT, Likelihood cut, and Fisher methods) can be seen in Table 4.2. The MLP method exhibits similar signal efficiencies for both the training and test samples, so there is no sign of overtraining, while the BDT method shows clear overtraining. So we choose to use the MLP neural network in our analysis. The MLP output distributions for offpeak and signal (SP-6845) events are shown in Fig. 4.3. To further reduce the number of continuum background events entering into the maximum-likelihood (ML) fit, we apply the cut $0.25 < MLP < 1.13$. The efficiency of this cut is 34.8% for offpeak data, and 93.3% for signal (SP-6845).

For $B^+ \to K^0_S K^0_S K^+$, instead of specifically training a new neural network, we simply use the exact same neural network as in $B^+ \to K^+ K^- K^+$. To further reduce the number of continuum background events entering into the ML fit, we apply the cut $0.25 < MLP < 1.12$. The efficiency of this cut is 50.9% for offpeak data, and

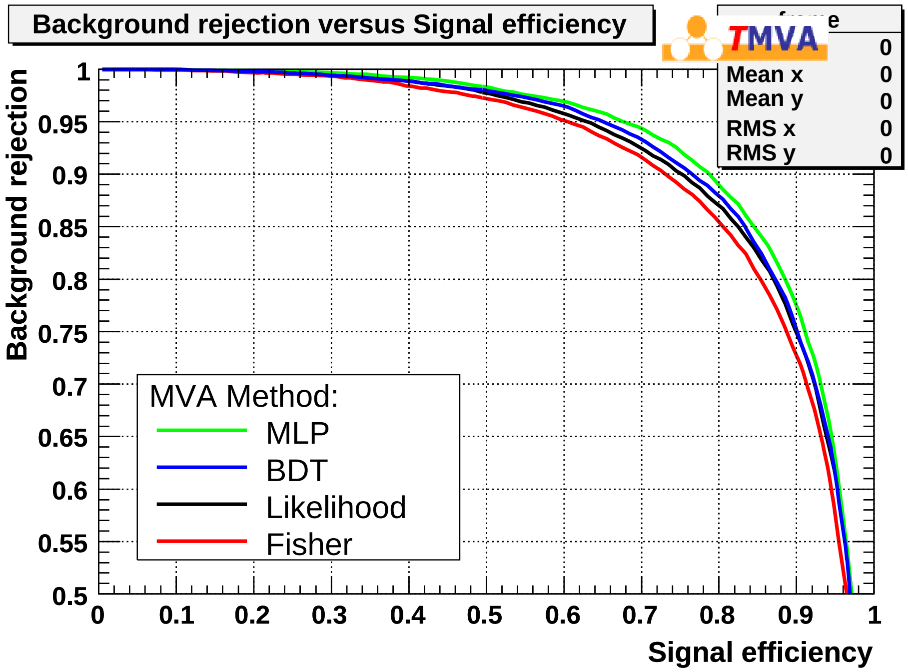

Figure 4.2: The TMVA performance plot for $B^+ \to K^+K^-K^+$.

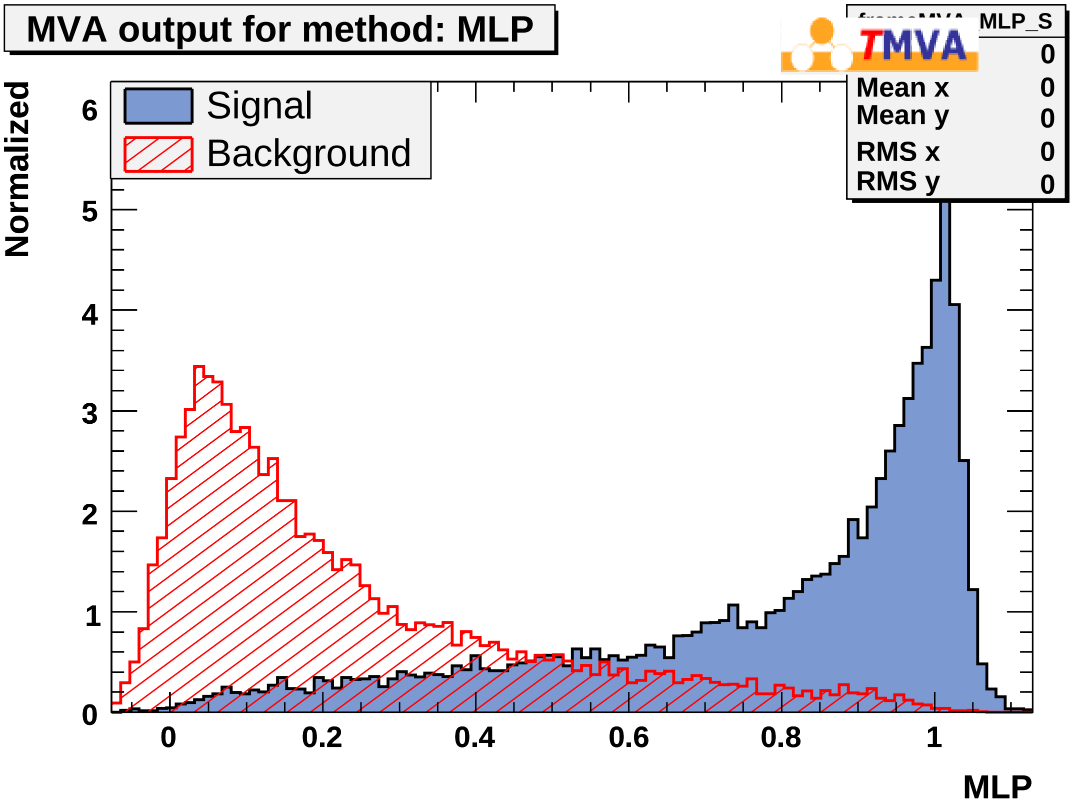

Figure 4.3: The MLP neural network distributions for background (offpeak) and signal (SP-6845), for $B^+ \to K^+K^-K^+$. Only events that pass the selection criterion $0.25 < MLP < 1.13$ enter into the ML fit.

95.8% for signal (SP-10338).

For $B^0 \to K^+K^-K^0_S$, we do not want to use a neural network containing TFlv or $|\Delta t/\sigma_{\Delta t}|$, since those variables will be correlated with the variables in our ML fit. So, we use `TMVA` to train new multivariate discriminators based only on $|\cos\theta_B|$, $|\cos\theta_T|$, and $\mathcal{L}_2/\mathcal{L}_0$. We train using $K^0_S \to \pi^+\pi^-$ Dalitz model signal MC (SP-7930) and $K^0_S \to \pi^+\pi^-$ offpeak data. We find that the four multivariate methods do a similarly good job of discriminating between signal and background. We decide to use the MLP, since that is the multivariate method used in $B^+ \to K^+K^-K^+$ and $B^+ \to K^0_S K^0_S K^+$. The MLP output distributions for offpeak and signal MC events are shown in Fig. 4.4, for both $K^0_S \to \pi^+\pi^-$ and $K^0_S \to \pi^0\pi^0$. To further reduce the number of continuum background events entering into the maximum-likelihood fit, we apply the cut $MLP > 0.11$. The efficiency of this cut is 74% (76%) for $K^0_S \to \pi^+\pi^-$ ($K^0_S \to \pi^0\pi^0$) offpeak data, and 98% (98%) for $K^0_S \to \pi^+\pi^-$ ($K^0_S \to \pi^0\pi^0$) DP-model signal MC. The performance of the MLP in this mode is substantially worse than in $B^+ \to K^+K^-K^+$, but this is not surprising, because it uses two fewer discriminating variables, and because a tighter $|\cos\theta_T|$ cut (0.9 instead of 0.95) is applied in this mode prior to training the MLP.

4.6.2 Correlation with Dalitz Plot

It is well established in three-body analyses that the event shape of continuum background events is correlated with DP position [39]. The basic reason is that continuum events with a “jettier” event shape tend to have two particles from one jet, so that pair of particles has a small invariant mass. So, continuum events that are more “continuum-like” are more likely to be close to the edge of the DP. To test how much the MLP output is correlated with the DP position, we divide the DP into 2 regions, based on the Dalitz distance Δ_{DP}. Δ_{DP} is defined as the minimum of the three invariant masses m_{12}, m_{23}, and m_{31}. The MLP distribution for offpeak data depends on the Δ_{DP} value, as shown in Fig. 4.5 for $B^+ \to K^+K^-K^+$. We will deal with this correlation in the ML fit, as explained in Sec. 5.3.3. A similar plot is also shown in Fig. 4.5, this time for $B^+ \to K^+K^-K^+$ signal MC (SP-6845). We can see that

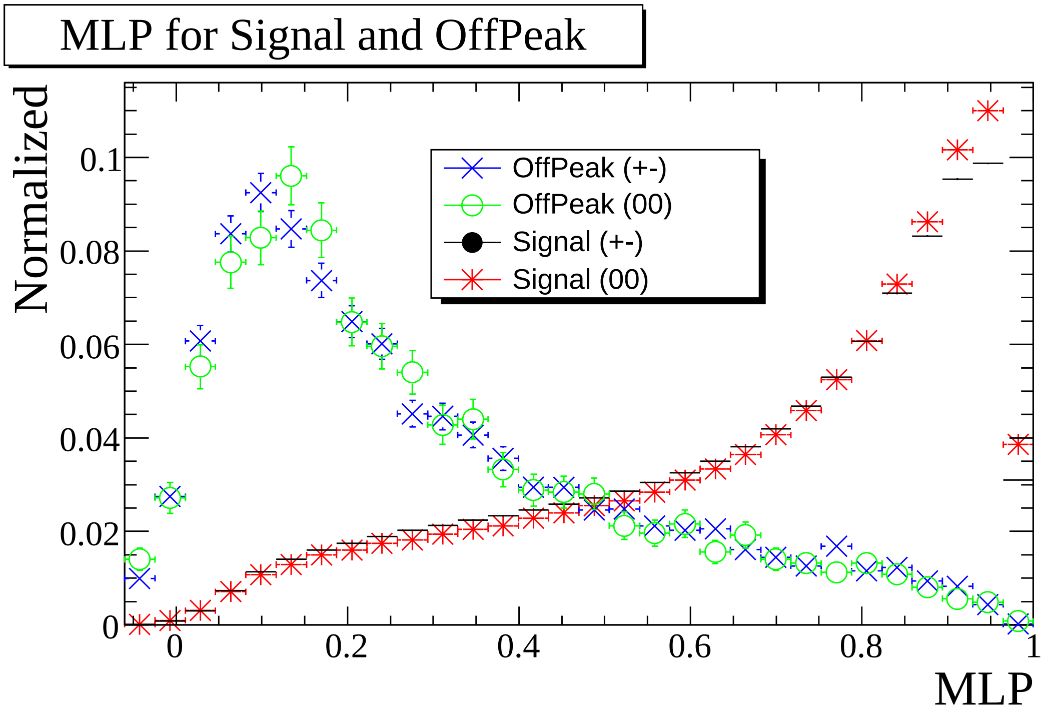

Figure 4.4: The MLP neural network distributions for $B^0 \rightarrow K^+K^-K^0_s$, for both background (offpeak) and signal MC (SP-7930 and SP-7931). Both the the $K^0_s \rightarrow \pi^+\pi^-$ and $K^0_s \rightarrow \pi^0\pi^0$ channels are shown. Only events that pass the selection criterion $MLP > 0.11$ enter into the ML fit.

NN value	MLP range	
	$B^+ \to K^+K^-K^+$,$B^+ \to K^0_S K^0_S K^+$	$B^0 \to K^+K^-K^0_S$
10	[0.25, 0.4737]	[0.11, 0.308]
9	[0.4737, 0.6365]	[0.308, 0.456]
8	[0.6365, 0.757]	[0.456, 0.577]
7	[0.757, 0.8427]	[0.577, 0.676]
6	[0.8427, 0.9035]	[0.676, 0.755]
5	[0.9035, 0.9468]	[0.755, 0.816]
4	[0.9468, 0.9787]	[0.816, 0.865]
3	[0.9787, 1.0035]	[0.865, 0.905]
2	[1.0035, 1.0222]	[0.905, 0.940]
1	[1.0222, 1.13]	[0.940, ∞]

Table 4.3: Bin ranges for MLP, and the NN value assigned for each bin. $B^+ \to K^+K^-K^+$ and $B^+ \to K^0_S K^0_S K^+$ use the same MLP binning, except that the maximum value of the MLP in $B^+ \to K^0_S K^0_S K^+$ is 1.12, instead of 1.13.

signal MC shows only a small dependency of the MLP output on Δ_{DP}. Similarly, in $B^+ \to K^0_S K^0_S K^+$ and $B^0 \to K^+K^-K^0_S$, the offpeak events show some correlation between MLP and Δ_{DP}, while the signal MC events show minimal correlation.

4.6.3 Binned Neural Network

The distribution of the MLP output has an unusual shape, which makes modeling it with a PDF difficult. Instead of trying to find a smooth function that models the distribution well, we bin the MLP output into 10 bins, and use the resulting *binned neural network* variable (hereafter simply NN) in the ML fit. The variable NN takes on the discrete values shown in Table 4.3. The bin ranges were chosen so that signal events have a roughly flat distribution in NN, and continuum events peak at large values of NN. The MLP bin ranges and the NN distributions are illustrated for the various $B \to KKK$ modes in Figs. 4.6-4.9. We then use a binned PDF known as a *Parametric Step Function* to model the NN distribution. The Parametric Step Function is essentially a 1D histogram with bin heights that may be either floated or fixed in the fit.

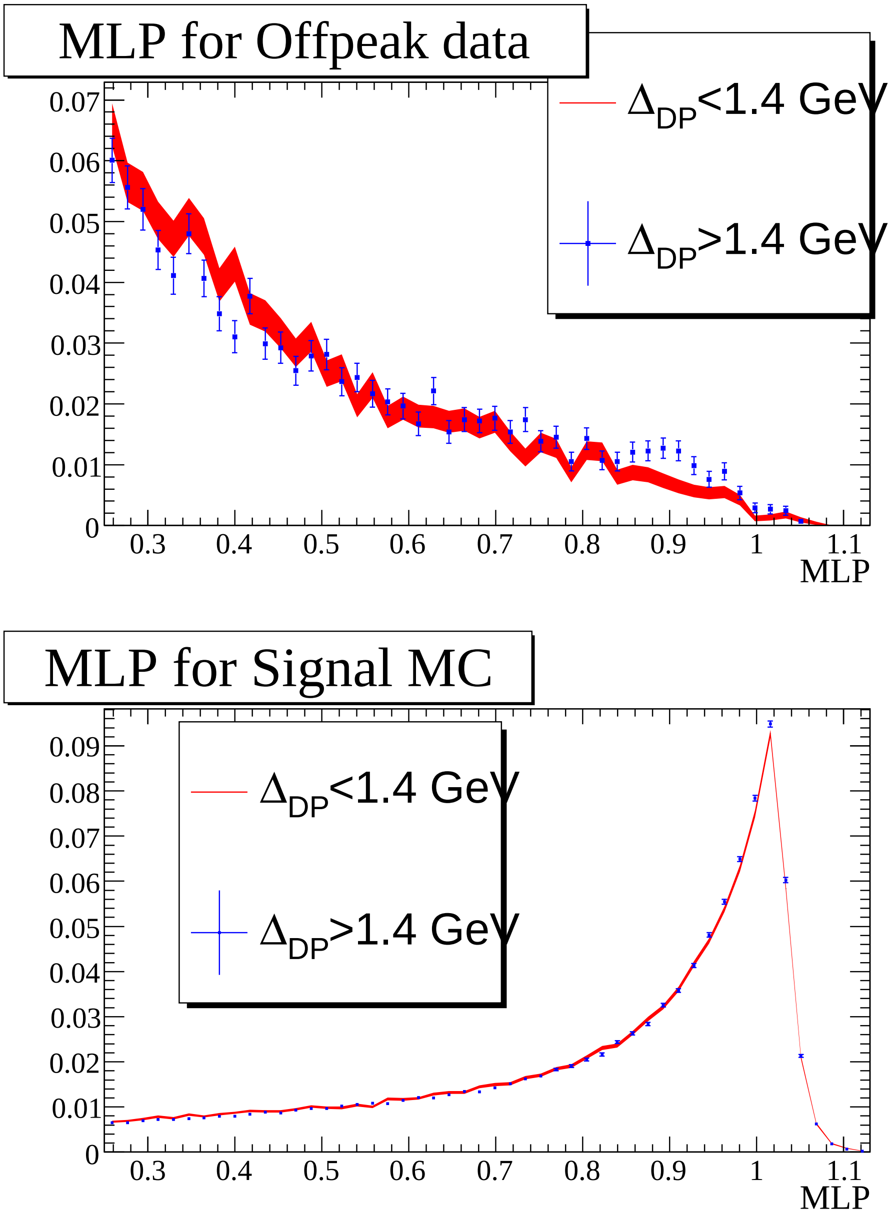

Figure 4.5: The MLP neural network distribution for $B^+ \to K^+K^-K^+$, for offpeak data and signal MC, plotted for different Δ_{DP} ranges. For the $\Delta_{DP} < 1.4\,\text{GeV}$ line, the thickness of the line indicates the error.

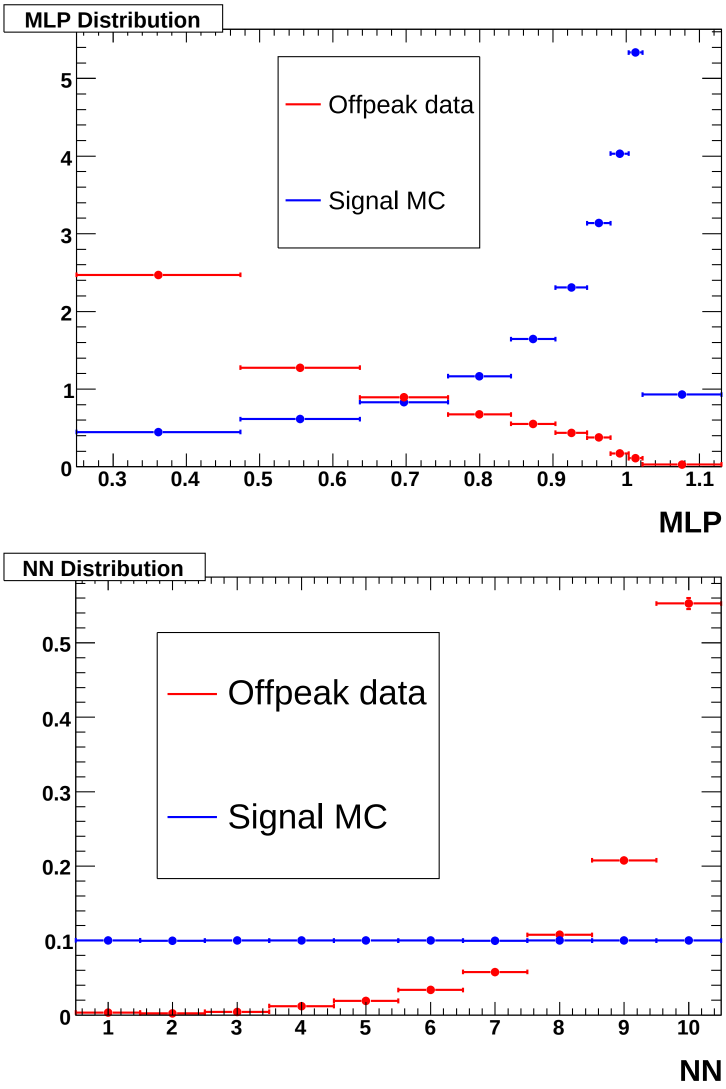

Figure 4.6: $B^+ \to K^+K^-K^+$ distributions of MLP (top) and NN (bottom), for offpeak and signal MC (SP-6845), illustrating the bin widths defined in Table 4.3. The height of each bin is proportional to the number of events in the bin divided by the bin width. The offpeak and signal distributions are normalized to equal areas.

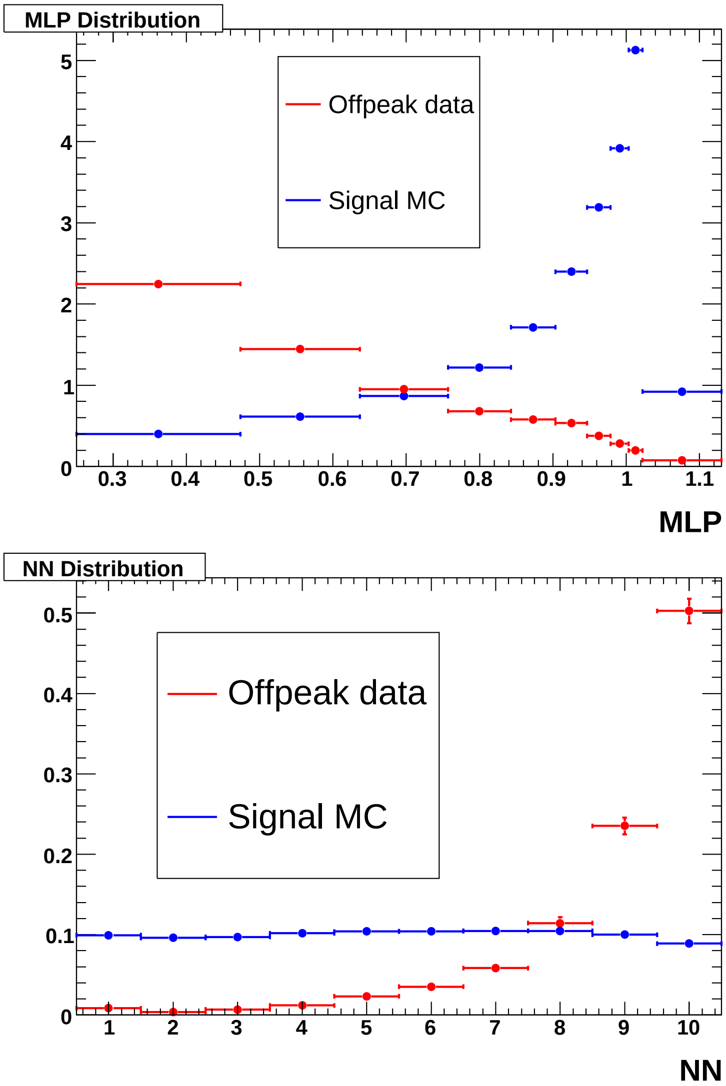

Figure 4.7: $B^+ \to K_S^0 K_S^0 K^+$ distributions of MLP (top) and NN (bottom), for offpeak and signal MC (SP-10338), illustrating the bin widths defined in Table 4.3.

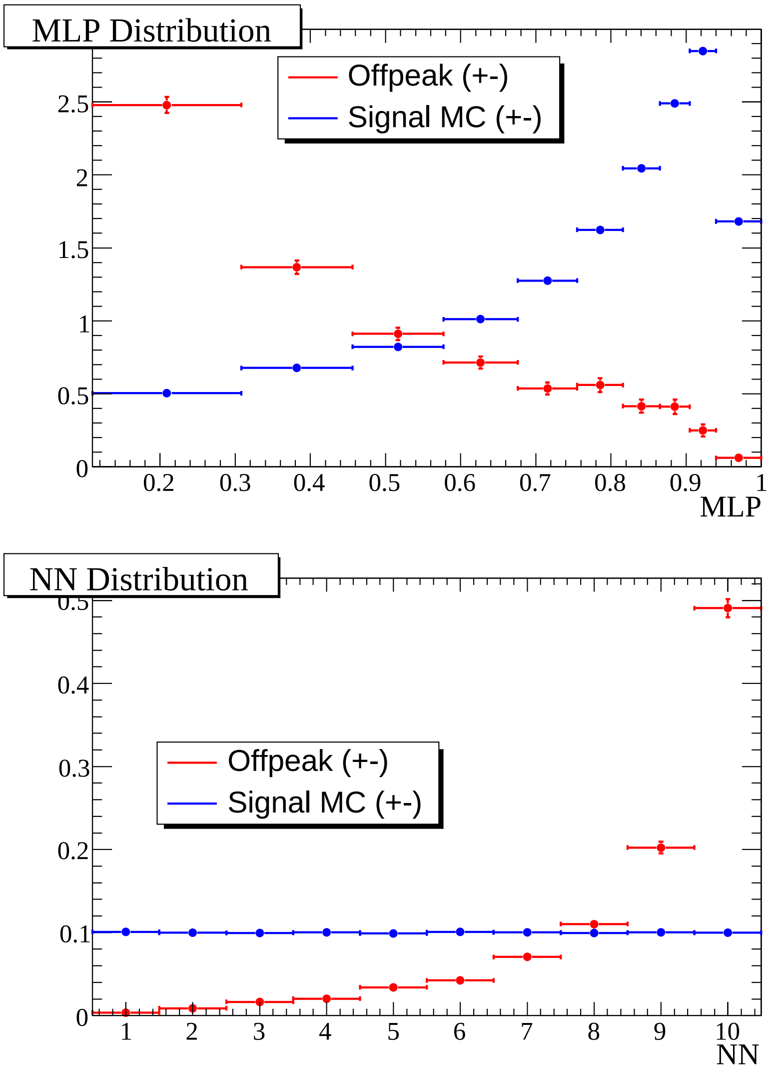

Figure 4.8: $B^0 \rightarrow K^+K^-K^0_S$ ($K^0_S \rightarrow \pi^+\pi^-$) distributions of MLP (top) and NN (bottom), for offpeak and signal MC (SP-7930), illustrating the bin widths defined in Table 4.3.

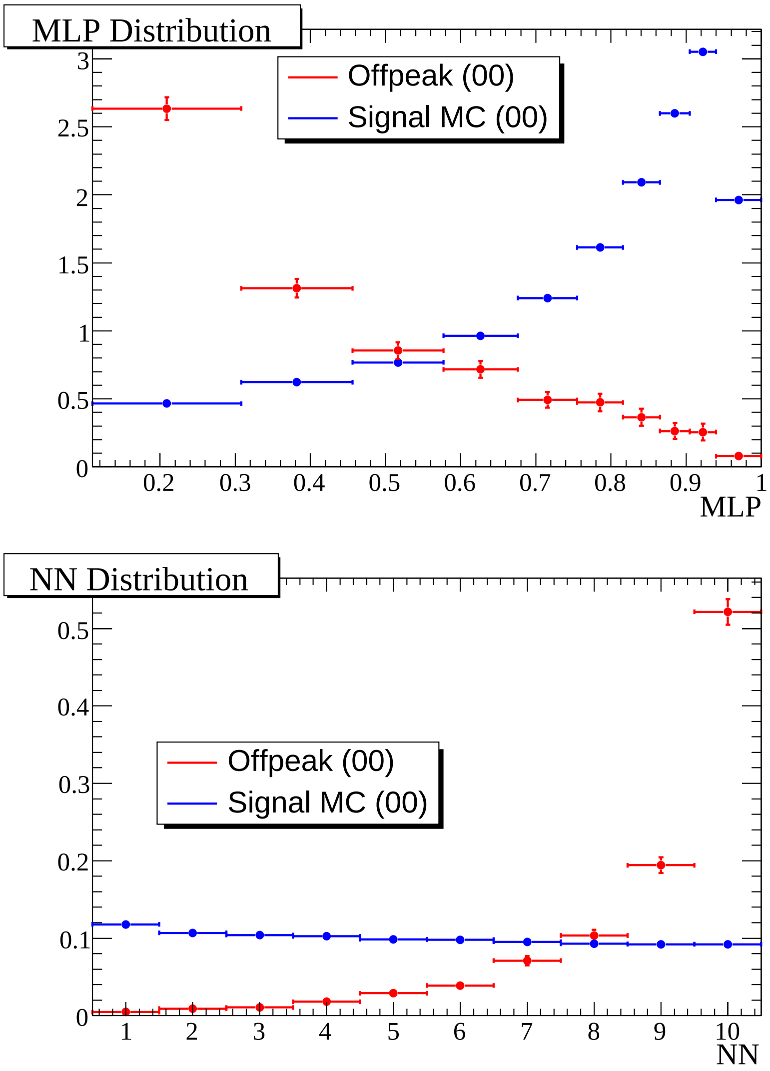

Figure 4.9: $B^0 \rightarrow K^+K^-K^0_S$ ($K^0_S \rightarrow \pi^0\pi^0$) distributions of MLP (top) and NN (bottom), for offpeak and signal MC (SP-7931), illustrating the bin widths defined in Table 4.3.

4.7 Multiple B Candidates

Sometimes, more than one B candidate per event pass all of our selection cuts. The average number of B candidates per event in signal MC is:

- $B^+ \to K^+K^-K^+$: 1.08 (92% of events have only one B candidate).
- $B^+ \to K^0_S K^0_S K^+$: 1.02 (98% of events have only one B candidate).
- $B^0 \to K^+K^-K^0_S$, $K^0_S \to \pi^+\pi^-$: 1.05 (96% of events have only one B candidate).
- $B^0 \to K^+K^-K^0_S$, $K^0_S \to \pi^+\pi^-$: 1.13 (90% of events have only one B candidate).

To avoid having multiple B candidates per event entering into our fit, we select a single, "best" B candidate from each event. For $B^+ \to K^+K^-K^+$ events with multiple B candidates, we choose the B candidate with the smallest χ^2 in the B meson vertex fit.

For $B^+ \to K^0_S K^0_S K^+$ events with multiple B candidates, we choose the best B candidate using the following procedure:

1. We choose the B candidate with the smallest value of $\Delta\ m_{K^0_S}$, defined as:

$$\Delta\ m_{K^0_S} = \sqrt{(\frac{m_{K^0_{S,1}} - m_{K^0_S,PDG}}{\sigma(m_{K^0_{S,1}})})^2 + (\frac{m_{K^0_{S,2}} - m_{K^0_S,PDG}}{\sigma(m_{K^0_{S,2}})})^2} \tag{4.2}$$

   This results in a single best B candidate in 96.2% of all signal events that contain multiple B candidates.

2. If multiple B candidates remain, we choose whichever one's $K^\pm$ candidate passes the tightest Kaon PID. This results in a single best B candidate in 1.3% of all signal events that contain multiple B candidates (*i.e.*, this is the absolute percentage, not the relative percentage, of events that are selected here).

3. If multiple B candidates still remain, we choose the one with the smallest χ^2 from the B vertex fit. This results in a single best B candidate in the remaining signal events (2.5% of all signal events that contain multiple B candidates).

For $B^0 \to K^+K^-K^0_S$ events with multiple B candidates, we choose the best B candidate using the following procedure:

1. We choose the B candidate with the smallest value of $|m_{K^0_S} - m_{K^0_S,PDG}|$. This results in a single best B candidate in 2.5% (63.5%) of all $K^0_S \to \pi^+\pi^-$ ($K^0_S \to \pi^0\pi^0$) signal events that contain multiple B candidates.
2. If multiple B candidates remain, we choose whichever one has a $K^\pm$ candidate passing the tightest Kaon PID. This results in a single best B candidate in 0.6% (0.2%) of all $K^0_S \to \pi^+\pi^-$ ($K^0_S \to \pi^0\pi^0$) signal events.
3. If multiple B candidates still remain, we choose the one with the smallest chi-squared from the B vertex fit. This results in a single best B candidate in all of the remaining signal events (96.9% (36.2%) of all $K^0_S \to \pi^+\pi^-$ ($K^0_S \to \pi^0\pi^0$) signal events that contain multiple B candidates).

4.8 Final Cuts

Events are required to lie in a *signal region* (SR) in the $m_{\rm ES}$-ΔE plane. Events outside the signal region ("sideband" events) will sometimes be used to study continuum backgrounds. The signal regions are:

- $B^+ \to K^+K^-K^+$: $m_{\rm ES} > 5.27\,{\rm GeV}/c^2$ and $|\Delta E| < 0.1\,{\rm GeV}$.
- $B^+ \to K^0_SK^0_SK^+$: $m_{\rm ES} > 5.26\,{\rm GeV}/c^2$ and $|\Delta E| < 0.1\,{\rm GeV}$.
- $B^0 \to K^+K^-K^0_S$, $K^0_S \to \pi^+\pi^-$: $m_{\rm ES} > 5.26\,{\rm GeV}/c^2$ and $|\Delta E| < 0.06\,{\rm GeV}$.
- $B^0 \to K^+K^-K^0_S$, $K^0_S \to \pi^0\pi^0$: $m_{\rm ES} > 5.26\,{\rm GeV}/c^2$ and $-0.12\,{\rm GeV} < \Delta E < 0.06\,{\rm GeV}$.

The asymmetric ΔE cut for $K^0_S \to \pi^0\pi^0$ is motivated by the asymmetric ΔE distribution for signal events in this mode. See Sec. 5.2.1 for the $m_{\rm ES}$ and ΔE distributions of signal events. The signal regions are not optimized to maximize $S/\sqrt{S+B}$, since we will be performing a ML in the signal region that accounts for the signal and background shapes.

To avoid problems related to rounding, we exclude events that are extremely close to the boundary of the DP from the fit. Specifically, we exclude events that are within 10^{-6} of the edge of the square Dalitz plot (for explanation of the square Dalitz plot, see Sec. 5.2.3). For example, in $B^+ \to K^+K^-K^+$, in terms of the square Dalitz plot variables m_{13} and y_{sq} (see Sec. 5.2.3), we make the following requirements on DP position:

1. $m_{min} + 10^{-6}\,\mathrm{GeV} < m_{13} < m_{max} - 10^{-6}\,\mathrm{GeV}$
2. $10^{-6} < y_{sq} < 1 - 10^{-6}$

Here, $m_{min} = 2m_{K^+}$ and $m_{max} = m_{B^+} - m_{K^+}$ are the lower and upper kinematic limits of m_{13}, respectively. Analogous cuts are made in $B^+ \to K^0_S K^0_S K^+$ and $B^0 \to K^+K^-K^0_S$. Greater than 99.9% of signal MC events pass these cuts.

For $B^0 \to K^+K^-K^0_S$, we are doing a time-dependent analysis, so we will be using Δt in the fit. We require $|\Delta t| < 20$ ps and $\sigma_{\Delta t} < 2.5$ ps, where $\sigma_{\Delta t}$ is the per-event uncertainty on Δt. These are the same requirements used in BABAR's $J/\psi K^0$ sin2β analysis [15].

4.9 Signal Efficiency

The signal efficiency is calculated from Dalitz model signal MC. The efficiencies for $B^+ \to K^+K^-K^+$, $B^+ \to K^0_S K^0_S K^+$, $B^0 \to K^+K^-K^0_S$ ($K^0_S \to \pi^+\pi^-$), and $B^0 \to K^+K^-K^0_S$ ($K^0_S \to \pi^0\pi^0$) are summarized in Tables 4.4, 4.5, 4.6, and 4.7, respectively. The average efficiencies ε for the different modes are:

- $B^+ \to K^+K^-K^+$: $\varepsilon = 33.7\%$.
- $B^+ \to K^0_S K^0_S K^+$: $\varepsilon = 27.1\%$.
- $B^0 \to K^+K^-K^0_S$ ($K^0_S \to \pi^+\pi^-$): $\varepsilon = 33.3\%$.
- $B^0 \to K^+K^-K^0_S$ ($K^0_S \to \pi^0\pi^0$): $\varepsilon = 7.9\%$.

Table 4.4: Signal efficiency for $B^+ \to K^+K^-K^+$, calculated from Dalitz model signal MC (SP-9688). The cuts are listed in the order that they are applied.

Cut	Events Passing Cut	Total Efficiency (%)	Relative Efficiency (%)
Signal B reconstructed	2752744	64.077 ± 0.048	64.077 ± 0.048
Loose ΔE & m_{ES} Cut	2752738	64.077 ± 0.023	100.000 ± 0.000
Invariant mass Sanity Check	2752702	64.076 ± 0.023	99.999 ± 0.000
$E_{Tot} < 20\,\mathrm{GeV}$	2723678	63.400 ± 0.023	98.946 ± 0.006
$\lvert\cos\theta_T\rvert < 0.95$	2566614	59.744 ± 0.024	94.233 ± 0.014
$\lvert m_{\mathrm{ES}} - m_B\rvert < 0.1\,\mathrm{GeV}/c^2$	2566515	59.742 ± 0.024	99.996 ± 0.000
Vertex $\chi^2 < 200$	2517914	58.611 ± 0.024	98.106 ± 0.009
$N_{GTL} \geq 4$	2497071	58.125 ± 0.024	99.172 ± 0.006
Kaon PID	1678857	39.080 ± 0.024	67.233 ± 0.030
TMVA	1576706	36.702 ± 0.023	93.915 ± 0.018
Best B cand	1576706	36.702 ± 0.023	100.000 ± 0.000
Inside Signal Box	1446720	33.676 ± 0.023	91.756 ± 0.022
Dalitz Plot Check	1446547	33.672 ± 0.023	99.988 ± 0.001

Note that the efficiency for $B^+ \to K^0_S K^0_S K^+$ is only calculated for decays where both K^0_S decay to $\pi^+\pi^-$, so the efficiency for all $B^+ \to K^0_S K^0_S K^+$ decays would be worse by a factor of $(0.692)^2$. Similar statements hold for the $B^0 \to K^+K^-K^0_S$ ($K^0_S \to \pi^+\pi^-$) and $B^0 \to K^+K^-K^0_S$ ($K^0_S \to \pi^0\pi^0$) efficiencies.

Table 4.5: Signal efficiency for $B^+ \to K^0_S K^0_S K^+$, calculated from Dalitz model signal MC (SP-10338). The cuts are listed in the order that they are applied.

Cut	Events Passing Cut	Total Efficiency (%)	Relative Efficiency (%)
Signal B reconstructed	859579	50.386 ± 0.077	50.386 ± 0.077
Loose ΔE & m_{ES} Cut	859572	50.385 ± 0.038	99.999 ± 0.000
$E_{Tot} < 20\,\text{GeV}$	858966	50.350 ± 0.038	99.929 ± 0.003
$\lvert\cos\theta_T\rvert < 0.90$	758444	44.457 ± 0.038	88.297 ± 0.035
K^0_S Cuts	534205	31.313 ± 0.036	70.434 ± 0.052
Kaon PID	503985	29.542 ± 0.035	94.343 ± 0.032
TMVA	482887	28.305 ± 0.034	95.814 ± 0.028
Best B cand	482887	28.305 ± 0.034	100.000 ± 0.000
Inside Signal Box	462514	27.111 ± 0.034	95.781 ± 0.029
Dalitz Plot Check	462497	27.110 ± 0.034	99.996 ± 0.001

Table 4.6: Signal efficiency for $B^0 \to K^+K^-K^0_S$ ($K^0_S \to \pi^+\pi^-$), calculated from Dalitz model signal MC (SP-7930). The cuts are listed in the order that they are applied.

Cut	Events Passing Cut	Total Efficiency (%)	Relative Efficiency (%)
Signal B reconstructed	5181029	60.280 ± 0.034	60.280 ± 0.034
$\lvert\cos\theta_T\rvert < 0.9$	4534466	52.757 ± 0.017	87.521 ± 0.015
K^0_S cuts	4322679	50.293 ± 0.017	95.329 ± 0.010
Kaon PID	3264709	37.984 ± 0.017	75.525 ± 0.021
TMVA	3196872	37.195 ± 0.016	97.922 ± 0.008
Best B cand	3196872	37.195 ± 0.016	100.000 ± 0.000
Inside Signal Box	2956663	34.400 ± 0.016	92.486 ± 0.015
Dalitz Plot Check	2955538	34.387 ± 0.016	99.962 ± 0.001
$\lvert\Delta t\rvert < 20\,\text{ps}$	2919302	33.965 ± 0.016	98.774 ± 0.006
$\sigma_{\Delta t}$	2863565	33.317 ± 0.016	98.091 ± 0.008

Table 4.7: Signal efficiency for $B^0 \to K^+K^-K^0_S$ ($K^0_S \to \pi^0\pi^0$), calculated from Dalitz model signal MC (SP-7931). The cuts are listed in the order that they are applied.

Cut	Events Passing Cut	Total Efficiency (%)	Relative Efficiency (%)
Signal B reconstructed	2804824	32.664 ± 0.034	32.664 ± 0.034
$\lvert\cos\theta_T\rvert < 0.9$	2493486	29.038 ± 0.015	88.900 ± 0.019
Photon Cuts	2074901	24.163 ± 0.015	83.213 ± 0.024
K^0_S Cuts	1231448	14.341 ± 0.012	59.350 ± 0.034
Kaon PID	943348	10.986 ± 0.011	76.605 ± 0.038
TMVA	923853	10.759 ± 0.011	97.933 ± 0.015
Best B cand	923853	10.759 ± 0.011	100.000 ± 0.000
Inside Signal Box	695367	8.098 ± 0.009	75.268 ± 0.045
Dalitz Plot Check	695117	8.095 ± 0.009	99.964 ± 0.002
$\lvert\Delta t\rvert < 20\,\mathrm{ps}$	688448	8.017 ± 0.009	99.041 ± 0.012
$\sigma_{\Delta t}$	674210	7.852 ± 0.009	97.932 ± 0.017

Chapter 5

Maximum Likelihood Fit

5.1 Likelihood Function

We extract signal parameters by performing a maximum-likelihood (ML) fit to data. The ML fits are performed using `Minuit` [40]. The $B^+ \to K^+K^-K^+$, $B^+ \to K^0_S K^0_S K^+$, and $B^0 \to K^+K^-K^0_S$ fits are performed separately. In $B^+ \to K^+K^-K^+$ and $B^+ \to K^0_S K^0_S K^+$, the likelihood function that is maximized in the fit has the form:

$$\mathcal{L} \propto \exp\left(-\sum_k N_k\right) \prod_{i=1}^{n} \mathcal{P}_i \tag{5.1}$$

where i indicates the number of the event in the dataset, and n is the total number of events in the dataset. The index k is the signal or background category (there are multiple background categories, including one continuum and several different $B\overline{B}$ categories), and N_k is the expected number of events in category k. $\mathcal{P}_i$ is the PDF evaluated for the i-th event, and has the general form:

$$\mathcal{P}_i = \sum_k N_k \mathcal{P}_{k,i}\,, \tag{5.2}$$

where $\mathcal{P}_{k,i}$ is the PDF for category k, evaluated for event i, and has the general form:

$$\mathcal{P}_{k,i} \equiv \mathcal{P}_k(m_{\mathrm{ES}}, \Delta E, \mathrm{NN}, x_{sq}, y_{sq}, q)$$

$$= \mathcal{P}_k(m_{\mathrm{ES}})\mathcal{P}_k(\Delta E)\mathcal{P}_k(\mathrm{NN}, x_{sq}, y_{sq})\mathcal{P}_k(x_{sq}, y_{sq}, q_{tag})\,, \tag{5.3}$$

where the square DP variables x_{sq} and y_{sq} are defined in Sec. 5.2.3, and $q = \pm 1$ is the charge of the signal B.

In $B^0 \to K^+K^-K^0_S$, the likelihood function is somewhat different. It is split up by *tagging category* c. *BABAR* tags the flavor (B^0 or $\overline{B}^0$) of the B^0_{tag} using an algorithm that categorizes events into six different categories: Lepton, KaonI, KaonII, KaonPion, Pion, and Other. See [15] for details. Some PDF's depend on tagging category. Especially important is that the mistag rate w (see Eq. 2.21) differs by tagging category. We also retain events with no tagging information ($w = 0.5$) in a seventh tagging category, since these events still help us measure DP parameters.

The likelihood function in $B^0 \to K^+K^-K^0_S$ is

$$\mathcal{L} \propto \prod_{c=1}^{7} \exp\left(-\sum_k N_k^c\right) \prod_{i=1}^{n^c} \mathcal{P}_i^c\,, \tag{5.4}$$

where n^c is the number of events in tagging category c, and N_k^c is the expected number of events in c and in signal or background category k. $\mathcal{P}_i^c$ is the PDF for c, evaluated for event i:

$$\mathcal{P}_i^c = \sum_k N_k^c \mathcal{P}_{k,i}^c\,, \tag{5.5}$$

where $\mathcal{P}_{k,i}^c$ is the PDF for tagging category c and signal/background category k, evaluated for event i, and has the general form:

$$\begin{aligned}\mathcal{P}_{k,i}^c &\equiv \mathcal{P}_k^c(m_{\mathrm{ES}}, \Delta E, \mathrm{NN}, x_{sq}, y_{sq}, \Delta t, \sigma_{\Delta t}, q_{tag}) \\ &= \mathcal{P}_k^c(m_{\mathrm{ES}})\mathcal{P}_k^c(\Delta E)\mathcal{P}_k^c(\mathrm{NN}, x_{sq}, y_{sq})\mathcal{P}_k^c(x_{sq}, y_{sq}, \Delta t, \sigma_{\Delta t}, q_{tag})\,. \end{aligned} \tag{5.6}$$

The $B^0 \to K^+K^-K^0_S$ ($K^0_S \to \pi^+\pi^-$) and $B^0 \to K^+K^-K^0_S$ ($K^0_S \to \pi^0\pi^0$) fits are performed simultaneously, with different PDF's for each K^0_S decay mode.

In the remainder of this chapter, we will discuss the individual PDF's in detail, and show validation studies of the ML fits.

5.2 Signal Model

5.2.1 m_{ES} and ΔE and Self-Crossfeed

We study the signal m_{ES} and ΔE distributions with MC. An important consideration is the fraction of signal events that are incorrectly reconstructed. We refer to these events as self-crossfeed (SCF). Note that these are *true* $B \to KKK$ events that are reconstructed as $B \to KKK$, but in an incorrect fashion. An example would be a true $B^+ \to K^+K^-K^+$ event in which the B^+ is reconstructed by combining two K^+'s from the actual $B^+ \to K^+K^-K^+$ decay with a K^- coming from the B^- decay (the "other B"). Events that are correctly reconstructed (not SCF) are called "truth-matched." We will also use the term "truth-matching" in a slightly different sense, to refer to the actual (generated MC) particle that a particle candidate is reconstructed from. For example, if a K^+ candidate is reconstructed from a π^+ in MC, then we will say that the K^+ is "truth-matched" to the π^+.

Based on the studies discussed next, we decide that it is not necessary to separate SCF events into a separate category from truth-matched signal events.

$B^+ \to K^+K^-K^+$

We perform a study of SCF using signal MC. For the purpose of this study, we assign reconstructed signal events to one of four categories:

- **TM** These are $B^+ \to K^+K^-K^+$ events that are truth-matched. This means that the $K^\pm$ are all truth-matched to MC $K^\pm$ particles, and that the MC particles to which they are truth-matched all come from a single $B^+ \to K^+K^-K^+$ decay.
- **Rad** These are $B^+ \to K^+K^-K^+$ (+ one or more photons) events that are truth-matched. *BABAR*'s MC generator has a routine called PHOTOS that adds radiative photons to some of the $B^+ \to K^+K^-K^+$ events. We exclude such events from the TM category, even if such events are truth-matched.

Table 5.1: The fractions of truth-matched (TM), radiative (Rad), combinatoric (Comb) and mis-identified (misPID) events for $B^+ \rightarrow K^+K^-K^+$ signal MC.

Monte Carlo Sample	TM (%)	Rad (%)	misPID (%)	Comb (%)
Signal MC (SP-9688)	85.63	13.69	0.04	0.64

- **misPID** These are events in which one or more of the reconstructed $K^\pm$ are truth-matched to a non-$K^\pm$ particle.

- **Comb** These are all other events that don't fit into the other categories. They are virtually all combinatoric events, in which the signal B is reconstructed from kaons that don't actually all originate from the same B.

The fraction of events in each of the signal categories is given for Dalitz model signal MC (SP-9688) in Table 5.1. As can be seen, almost all of the events are either (non-radiative) truth-matched or radiative truth-matched events, while less than 1% of events are in the SCF categories of misPID and Comb. Of the SCF events, almost all are of the combinatoric variety.

The signal MC distributions in m_{ES} and ΔE for each category are shown in Figs. 5.1 and 5.2. Since the shapes of TM and Rad are similar and the fractions of Comb and misPID are small, we do not separate the different signal categories in this analysis.

$B^+ \rightarrow K^0_s K^0_s K^+$

We place reconstructed signal events into one of four categories:

- **TM** These are $B^+ \rightarrow K^0_s K^0_s K^+$ events that are truth-matched.

- **Rad** These are $B^+ \rightarrow K^0_s K^0_s K^+$ (+ one or more photons) events that are truth-matched.

- **SCF 1** These are events in which one or both of the K^0_s are not truth-matched to any MC particle at all. This is quite common.

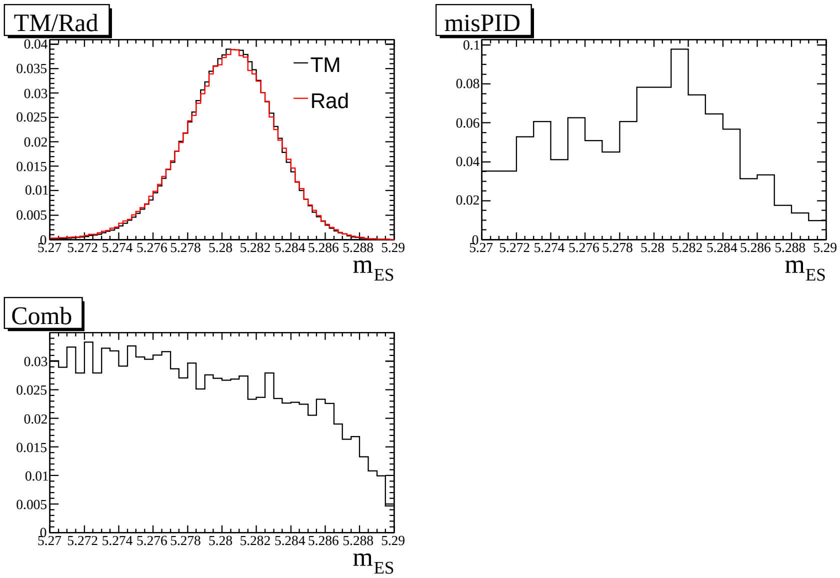

Figure 5.1: The signal m_{ES} distribution for each signal category, for $B^+ \to K^+K^-K^+$ Dalitz model signal MC (SP-9688). Distributions are normalized to one.

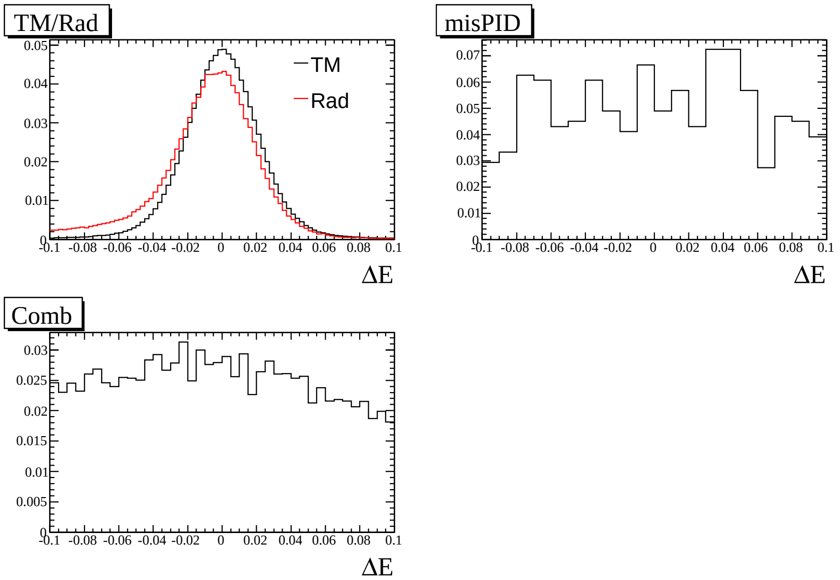

Figure 5.2: The signal ΔE distribution for each signal category, for $B^+ \to K^+K^-K^+$ Dalitz model signal MC (SP-9688). Distributions are normalized to one.

Table 5.2: The fractions of truth-matched (TM), radiative (Rad), SCF 1, SCF 2 events for $B^+ \to K^0_S K^0_S K^+$ signal MC (SP-10338).

Monte Carlo Sample	TM (%)	Rad (%)	SCF 1 (%)	SCF 2 (%)
Signal MC (Dalitz Model, SP-10338)	77.99	6.12	15.54	0.34

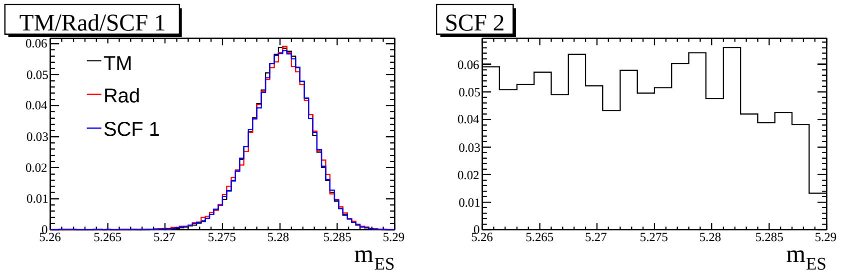

Figure 5.3: The signal $m_{\rm ES}$ distribution for each signal category, for $B^+ \to K^0_S K^0_S K^+$ Dalitz-model signal MC (SP-10338). Distributions are normalized to one.

- **SCF 2** These are all other mis-reconstructed events that don't fit into the other categories. Most of them are combinatoric events, in which the signal B is reconstructed from kaons that don't actually all originate from the same B.

Their fractions are given for signal MC in Table 5.2. The signal MC distributions in $m_{\rm ES}$ and ΔE for each category are shown in Figs. 5.3 and 5.4. The Rad and SCF 1 categories look fairly similar to TM events. The SCF 2 category looks like background events, but it represents only a small fraction of signal events, so we will not separate SCF and non-SCF events explicitly in this analysis.

$B^0 \to K^+K^-K^0_S$

We place reconstructed signal events into one of five categories:

- **TM** These are $B^0 \to K^+K^-K^0_S$ events that are truth-matched.
- **Rad** These are $B^0 \to K^+K^-K^0_S$ (+ one or more photons) events that are truth-matched.

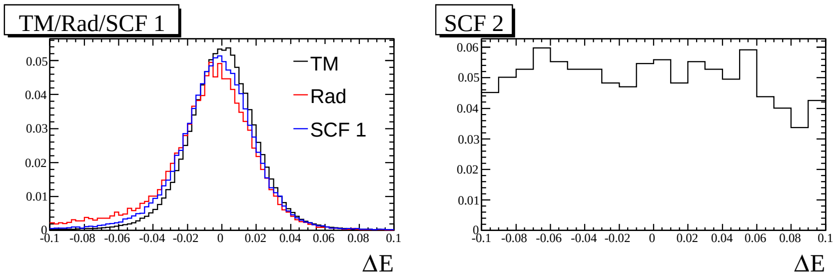

Figure 5.4: The signal ΔE distribution for each signal category, for $B^+ \to K^0_S K^0_S K^+$ Dalitz-model signal MC (SP-10338). Distributions are normalized to one.

Table 5.3: The fractions of truth-matched (TM), radiative (Rad), SCF 1, SCF 2, and SCF 3 events for $B^0 \to K^+K^-K^0_S$ signal MC.

Monte Carlo Sample	TM (%)	Rad (%)	SCF 1 (%)	SCF 2 (%)	SCF 3 (%)
$K^0_S \to \pi^+\pi^-$ Sig MC (DP Model, SP-7930)	86.1	5.2	8.1	0.4	0.3
$K^0_S \to \pi^0\pi^0$ Sig MC (DP Model, SP-7931)	84.7	5.0	8.0	1.8	0.5

- **SCF 1** These are events in which the K^0_S is not truth-matched to any MC particle at all. This is quite common.

- **SCF 2** These are events in which the K^0_S is reported as truth-matched to a MC K^0_S particle, but there is some problem with the K^0_S reconstruction. In $K^0_S \to \pi^+\pi^-$, this is mainly due to one or both of of the K^0_S daughter pions being truth-matched to a non-pion track (usually a muon). In $K^0_S \to \pi^0\pi^0$, this is mainly due to one of daughter photons being truth-matched to an electron or positron.

- **SCF 3** These are all other mis-reconstructed events that don't fit into the other categories. Most of them are combinatoric events, in which the signal B is reconstructed from kaons that don't actually all originate from the same B.

Their fractions are given for signal MC in Table 5.3. The $K^0_S \to \pi^+\pi^-$ signal MC distributions in $m_{\rm ES}$ and ΔE for each category are shown in Fig. 5.5 and 5.6. The

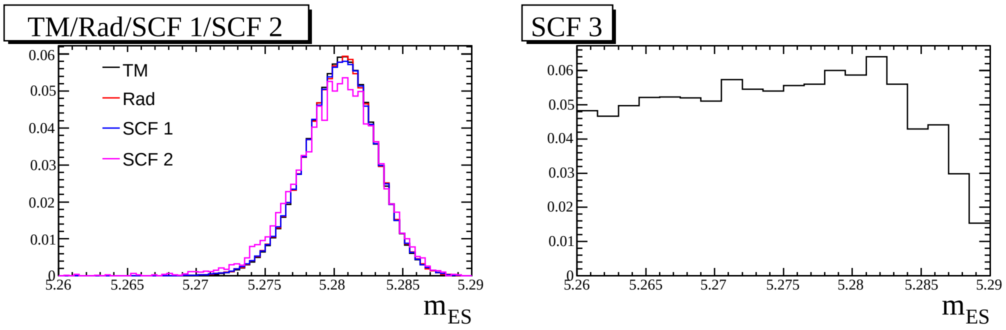

Figure 5.5: The signal m_{ES} distribution for each signal category, for $B^0 \rightarrow K^+K^-K^0_S$ ($K^0_S \rightarrow \pi^+\pi^-$) Dalitz-model signal MC (SP-7930). Distributions are normalized to one.

Rad and SCF 1 categories look very similar to TM events for m_{ES}, and are slightly shifted for ΔE. The SCF 2 and SCF 3 categories look more different, but together they represent less than 1% of signal events. The $K^0_S \rightarrow \pi^0\pi^0$ signal MC distributions in m_{ES} and ΔE for each category are shown in Fig. 5.7 and 5.8. The reconstruction effects are clearly worse in this mode than in $K^0_S \rightarrow \pi^+\pi^-$. In particular, the SCF 1 category, which represents about 8% of signal events, has significantly different m_{ES} and ΔE distributions than TM signal. However, the signal yield in $K^0_S \rightarrow \pi^0\pi^0$ is expected to be much smaller than in $K^0_S \rightarrow \pi^+\pi^-$, so the $K^0_S \rightarrow \pi^0\pi^0$ mode should not impact our combined measurement much. So, we will not separate SCF and non-SCF events explicitly.

In conclusion, we decide that the SCF events are a small enough issue that we can afford to group them together with signal events. In Sec. 5.2.5, we will show how we handle the effects of reconstruction on DP position. The impact of not separating out SCF events will ultimately be tested in our “embedded toy” studies (Sec. 5.5).

PDF Type

The m_{ES} and ΔE distributions for signal events are not perfectly Gaussian, especially because we have decided to group SCF events together with truth-matched

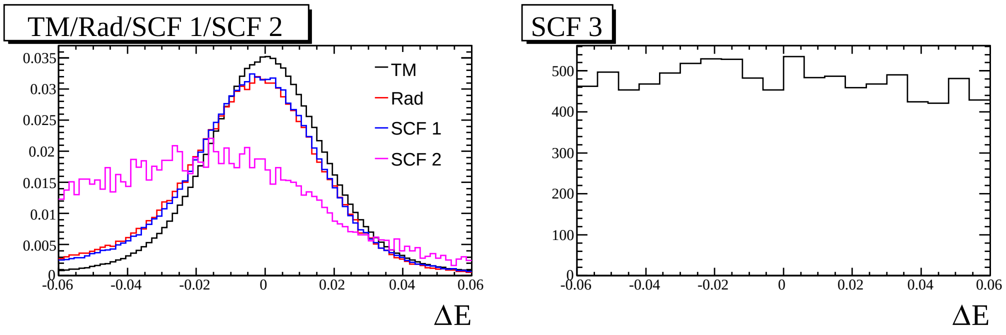

Figure 5.6: The signal ΔE distribution for each signal category, for $B^0 \to K^+K^-K^0_S$ ($K^0_S \to \pi^+\pi^-$) Dalitz-model signal MC (SP-7930). Distributions are normalized to one.

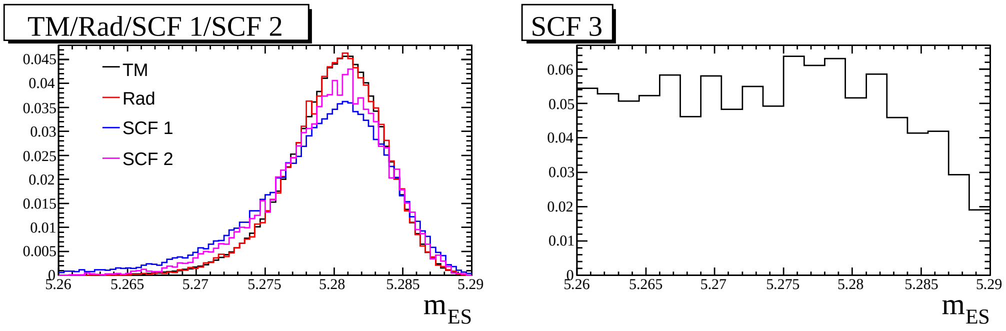

Figure 5.7: The signal m_{ES} distribution for each signal category, for $B^0 \to K^+K^-K^0_S$ ($K^0_S \to \pi^0\pi^0$) Dalitz-model signal MC (SP-7931). Distributions are normalized to one.

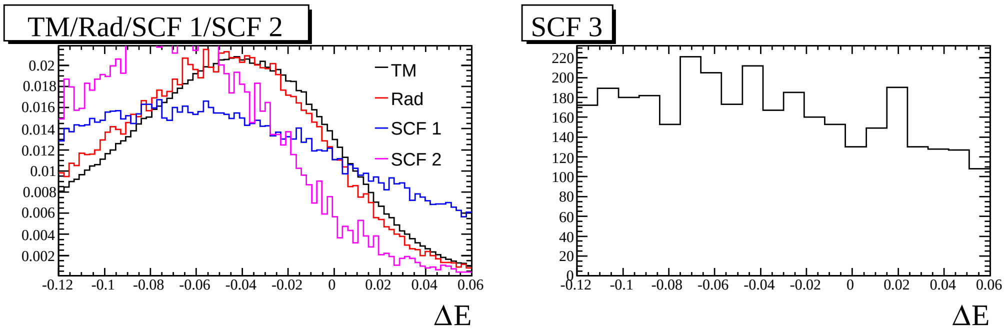

Figure 5.8: The signal ΔE distribution for each signal category, for $B^0 \to K^+K^-K^0_S$ ($K^0_S \to \pi^0\pi^0$) Dalitz-model signal MC (SP-7931). Distributions are normalized to one.

events. We model these distributions using a so-called "Cruijff" function, [1] which is an asymmetric Gaussian with non-Gaussian tails, defined as:

$$\mathcal{P}(x) = \exp\left(- \frac{(x-x_0)^2}{2\sigma_\pm^2 + \alpha_\pm (x-x_0)^2} \right), \tag{5.7}$$

where σ_+ and α_+ (σ_- and α_-) are used when $x > x_0$ ($x < x_0$). In most cases, we take these PDF parameters from fits to MC, but allow the means (x_0) to vary ("float") in the nominal fit to data. Exact lists of which parameters are floated in the nominal fits will be given in Chapter 7.

5.2.2 NN PDF

The NN PDF for signal events is a parametric step function, as already shown in Sec. 4.6.3. The parameters of the PDF are the bin heights. Since we use 10 bins, there are 9 free parameters (with one bin height being constrained by the normalization condition). The PDF parameters are generally taken from MC, but in the case of $B^+ \to K^+K^-K^+$, there are a sufficient number of events to obtain these parameters by floating them in fits to data, and a significant data-MC difference is observed. However, to limit the number of free parameters in the final nominal fit, we do not

---

[1] Named after the Dutch soccer player. Don't blame me.

float these parameters in the nominal $B^+ \to K^+K^-K^+$ fit. Instead, we float them in a separate *CP*-blind fit, and then fix them to those values in the nominal fit, and vary them as a systematic.

5.2.3 Dalitz Plot and Δt

The DP PDF for the B^+ modes is described by Eq. 2.20, while the Δt and DP PDF for $B^0 \to K^+K^-K^0_S$ is described by Eq. 2.21, where $\mathcal{A}$ and $\overline{\mathcal{A}}$ are described by an isobar model. In Chapter 6, we will study what terms to include in the isobar model. For now, we will discuss a few extra features that go into these PDF's.

Square Dalitz Plot

The traditional Dalitz plot uses the square of the invariant masses of two different particle pairs. For example, a traditional Dalitz plot might plot s_{12} vs. s_{23}. However, this results in events occupying an irregularly-shaped region. Computationally, it is easier to work with rectangular regions. We therefore transform to a set of variables that form a so-called *square Dalitz plot*. The square DP variables that we use are x_{sq} and y_{sq}, where

- $B^+ \to K^+K^-K^+$: $x_{sq} = m_{13}$ and $y_{sq} = |\cos\theta_H|$, where θ_H is the angle between K_2 and K_1, calculated in the K_1K_3 reference frame.
- $B^+ \to K^0_S K^0_S K^+$: $x_{sq} = m_{12}$ and $y_{sq} = |\cos\theta_3|$ (see Sec. 2.5.4).
- $B^0 \to K^+K^-K^0_S$: $x_{sq} = m_{12}$ and $y_{sq} = \cos\theta_3$.

In Figs. 5.9, 5.10, and 5.11, we show comparisons of the traditional Dalitz plot and the square DP for the three $B \to KKK$ modes.

We transform to the square DP variables before performing our ML fit. However, recall from Sec. 2.5.2 that the DP-dependent decay rates were defined with respect to the differential area $ds_{12}ds_{23}$. When doing the transformation of variables, this differential area changes to $|J|dx_{sq}dy_{sq}$, where J is the Jacobian of the transformation $(x_{sq}, y_{sq}) \to (s_{12}, s_{23})$.

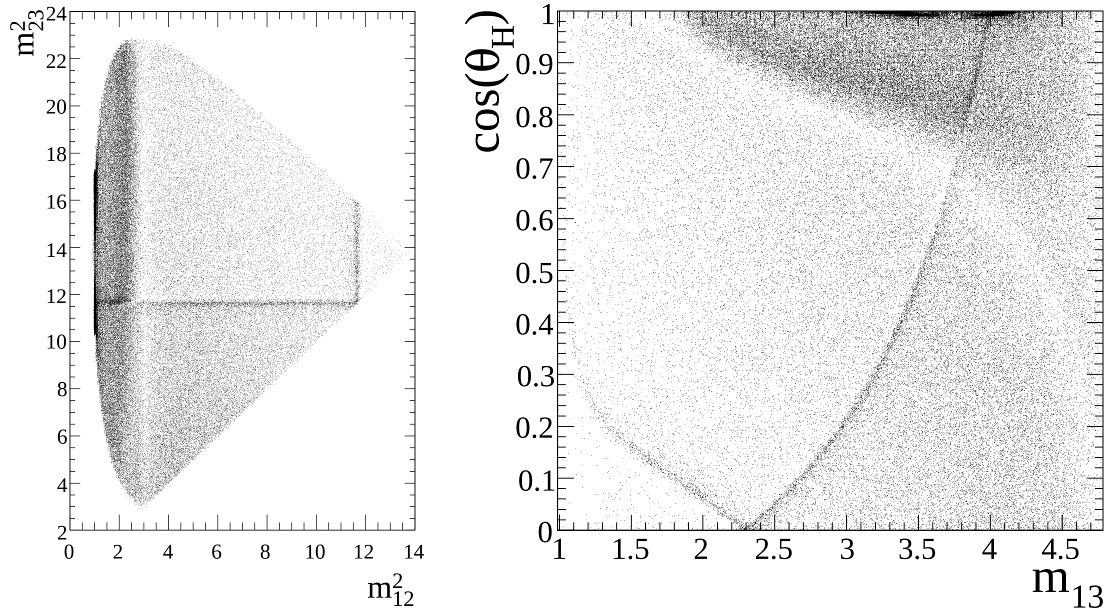

Figure 5.9: $B^+ \to K^+K^-K^+$ signal MC distributions for the standard DP (left) and square DP (right).

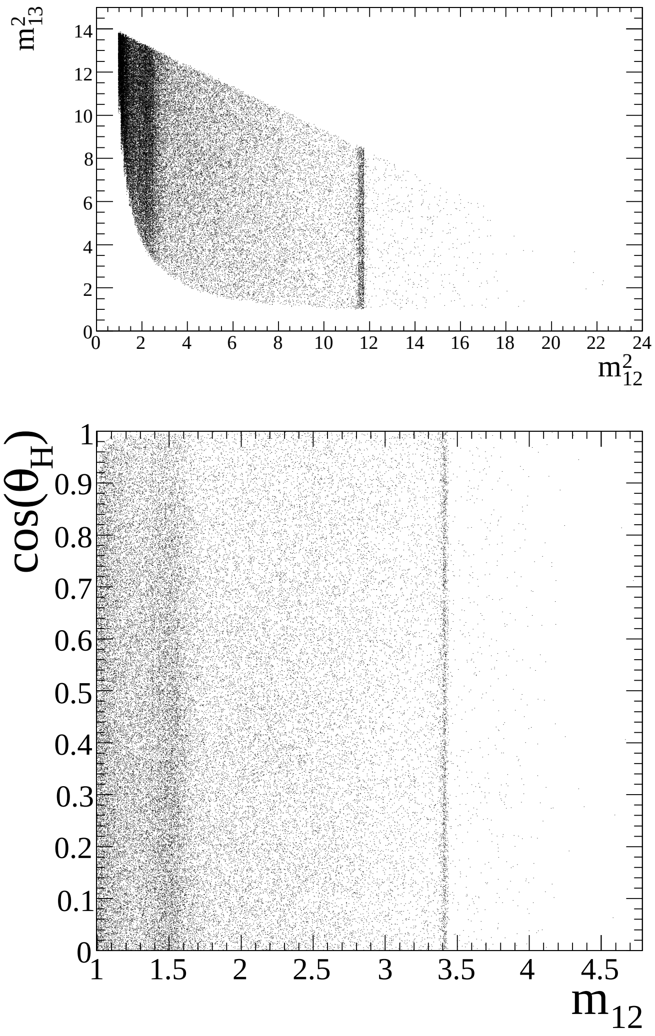

Figure 5.10: $B^+ \to K_S^0 K_S^0 K^+$ signal MC distributions for the standard DP (top) and square DP (bottom).

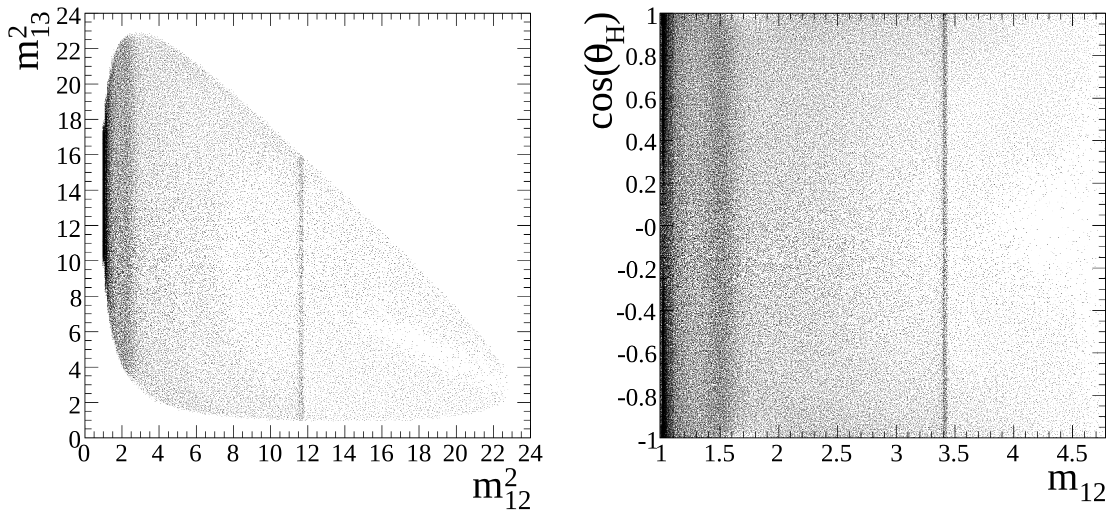

Figure 5.11: $B^0 \to K^+K^-K^0_S$ signal MC distributions for the standard DP (left) and square DP (right).

5.2.4 Efficiency Map

The efficiency map, i.e. the efficiency as a function of position on the square DP, is made from phase-space model signal MC. The efficiency map is split into a finite number of bins, with the number of bins chosen to be large enough to capture the efficiency variation adequately, while small enough so that there are enough MC events in each bin to limit the statistical uncertainties. The binning chosen (number of x_{sq} bins × number of y_{sq} bins) is 21×20 in $B^+ \to K^+K^-K^+$, 40×40 in $B^+ \to K^0_SK^0_SK^+$, 40×40 in $B^0 \to K^+K^-K^0_S$ ($K^0_S \to \pi^+\pi^-$), and 40×20 in $B^0 \to K^+K^-K^0_S$ ($K^0_S \to \pi^0\pi^0$). Data-MC PID corrections are applied to the efficiency map. The average PID correction is about 96.5%, 98.8%, and 95% in $B^+ \to K^+K^-K^+$, $B^+ \to K^0_SK^0_SK^+$, and $B^0 \to K^+K^-K^0_S$, respectively (data efficiency is less than MC). The efficiency maps for the various modes are shown in Figs. 5.12-5.14. Significant variations in efficiency are seen as a function of DP position. Areas of lower efficiency tend to be where one of the $K^\pm$ or one of the K^0_S has low momentum. For the B^+ modes, we show separate efficiency maps for B^+ and B^- decays. We decide to use the same efficiency map for B^+ and B^- decays, and will account for this approximation as a systematic (Sec. 7.4.9).

5.2.5 Dalitz Plot Resolution

We study the resolution of the Dalitz plot variables, x_{sq} and y_{sq}. The reconstructed values of these variables can differ from their "true" values due to tracking resolution, misreconstruction effects (SCF), or due to the $K^{\pm}$ radiating off photons, which alters the 4-vectors of the $K^{\pm}$. In MC, the radiation of photons is implemented through PHOTOS. To determine the true (pre-radiation) 4-vectors of the kaons, we add each MC photon to one of the $K^{\pm}$. In the case of $B^+ \to K^+K^-K^+$ and $B^0 \to K^+K^-K^0_S$, the MC does not indicate explicitly which $K^{\pm}$ each photon comes from, so we calculate the angle formed between the photon and each kaon, and assign the photon to whichever kaon forms the smallest angle.

Define x_r and x_t as the reconstructed and true x_{sq} values, respectively. Define y_r and y_t as the reconstructed and true y_{sq} values, respectively. If we plot the reconstructed minus true DP positions, $\Delta x_{sq} \equiv x_r - x_t$ and $\Delta y_{sq} \equiv y_r - y_t$, we find that the distributions are highly non-Gaussian, with long tails. These plots are shown for $B^+ \to K^+K^-K^+$ phase-space signal MC in Fig. 5.15, in log scale. The other $B \to KKK$ modes are qualitatively similar.

The DP resolution depends on location on the DP, so to account for the resolution in our fit, we convolve the signal DP PDF with a 2-dimensional resolution map. The signal DP PDF, $P(x_r, y_r)$, which is evaluated at the reconstructed DP position, then becomes:

$$P(x_r, y_r) = \int\int P(x_t, y_t)\mathcal{R}(x_t, y_t, x_r, y_r)dx_t dy_t \tag{5.8}$$

where $\mathcal{R}(x_t, y_t, x_r, y_r)$ is the 2D resolution map that indicates the probability that a true DP position (x_t, y_t) will be reconstructed at the DP position (x_r, y_r). We compute the resolution map by using phase-space signal MC.

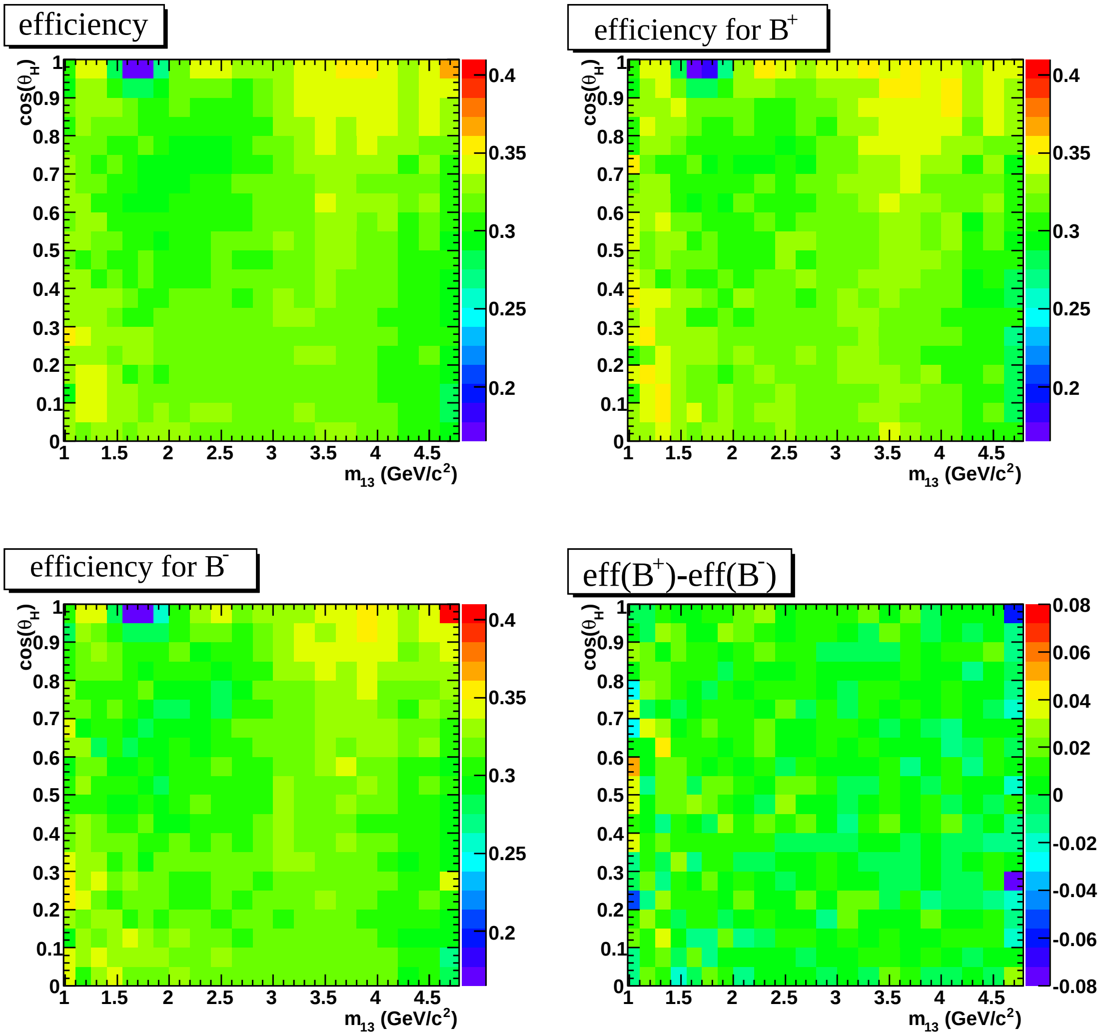

Figure 5.12: The $B^+ \to K^+K^-K^+$ efficiency map. Top left: for both B^+ and B^- decays. Top right: for B^+ decays only. Bottom left: for B^- decays only. Bottom right: difference in efficiency for B^+ and B^- decays.

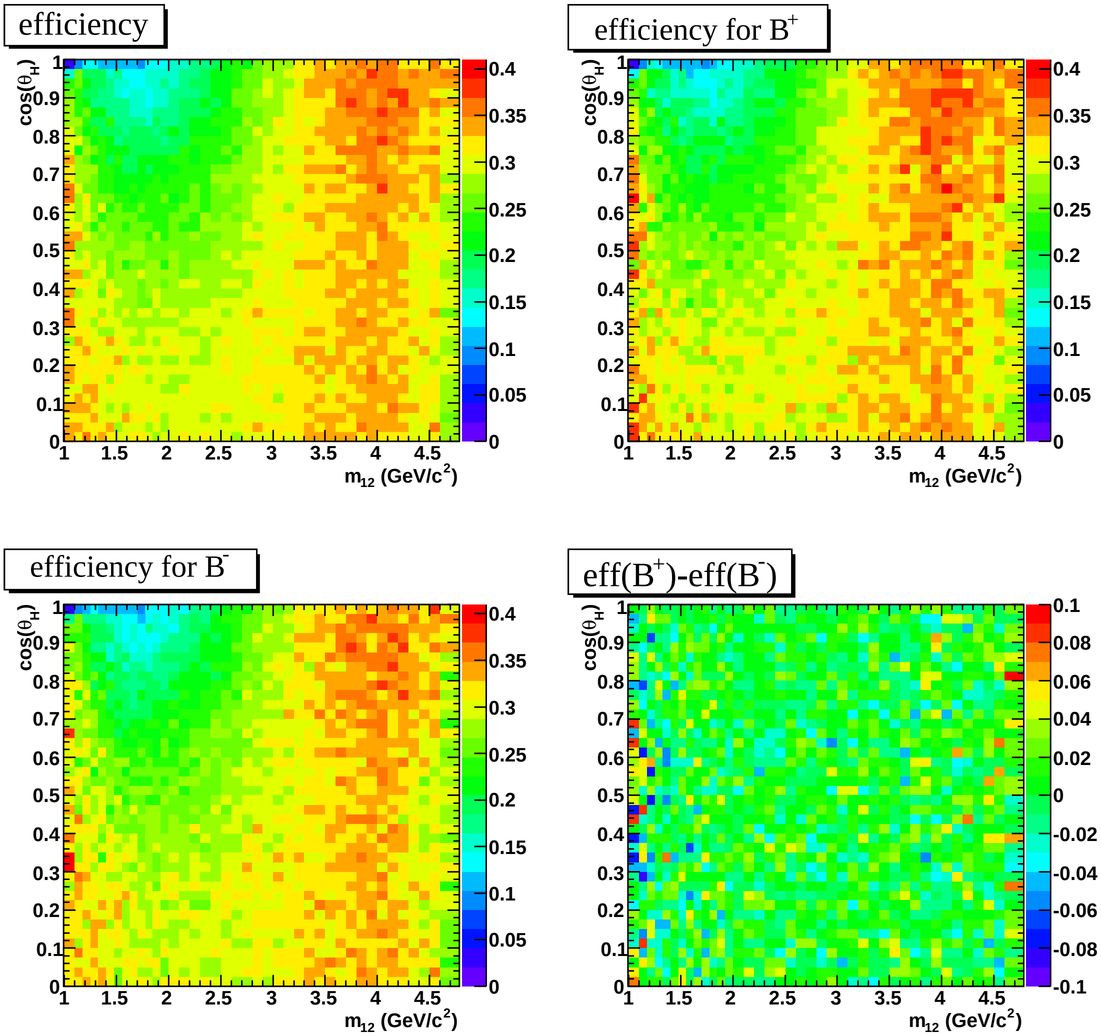

Figure 5.13: The $B^+ \to K_S^0 K_S^0 K^+$ efficiency map. Top left: for both B^+ and B^- decays. Top right: for B^+ decays only. Bottom left: for B^- decays only. Bottom right: difference in efficiency for B^+ and B^- decays.

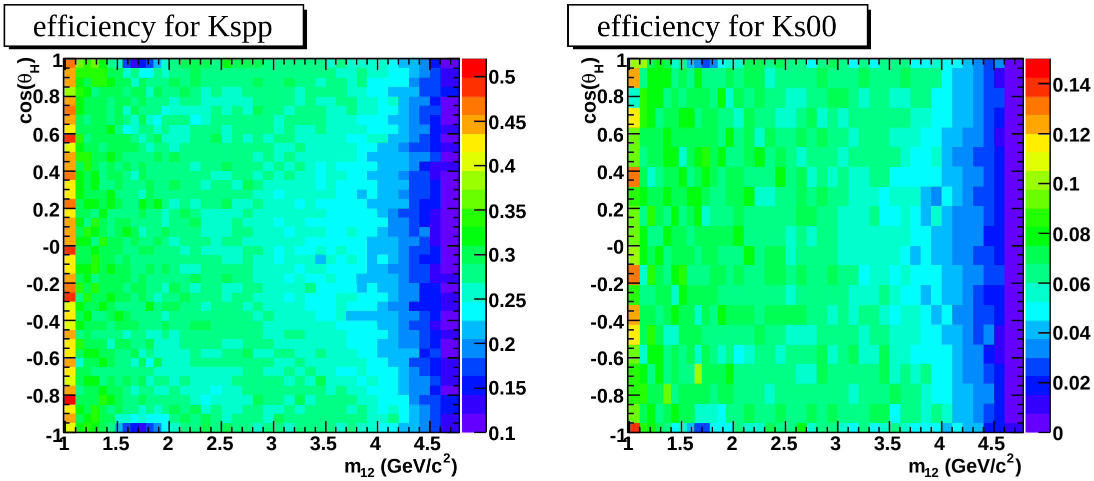

Figure 5.14: The $B^0 \to K^+K^-K^0_S$ efficiency map for $K^0_S \to \pi^+\pi^-$ (left) and $K^0_S \to \pi^0\pi^0$ (right).

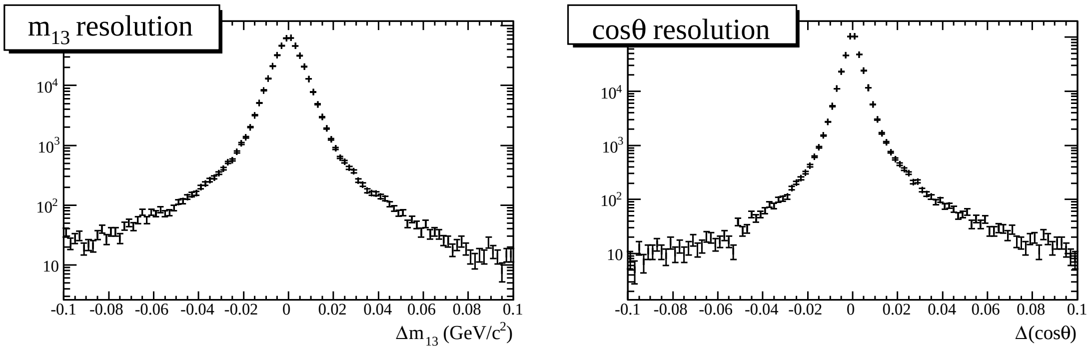

Figure 5.15: Plots of the differences between the reconstructed DP positions and the true DP positions. These plots show all events, but actually the resolution depends upon the DP location. Left: Δx_{sq}. Right: Δy_{sq}. Plots are shown in log-scale.

5.2.6 Δt Resolution

The time-dependence of the $B^0 \rightarrow K^+K^-K^0_S$ decay rate given in Eq. 2.21 assumes that Δt is perfectly known. To account for finite Δt resolution, the signal PDF is convolved with a Δt resolution function, $\mathcal{R}(\Delta t, \sigma_{\Delta t})$. The resolution function is given by a triple Gaussian:

$$\mathcal{R}(\Delta t, \sigma_{\Delta t}) = (1 - f_{tail} - f_{out})\mathcal{R}_{core}(\Delta t, \sigma_{\Delta t}) + f_{tail}\mathcal{R}_{tail}(\Delta t, \sigma_{\Delta t}) + f_{out}\mathcal{R}_{out}(\Delta t, \sigma_{\Delta t}) \tag{5.9}$$

with the core Gaussian given by

$$\mathcal{R}_{core}(\Delta t, \sigma_{\Delta t}) = \frac{1}{\sqrt{2\pi}\varSigma_{core}\sigma_{\Delta t}} \exp\left[-\frac{1}{2}\left(\frac{\Delta t - \mu_{core}\sigma_{\Delta t}}{\varSigma_{core}\sigma_{\Delta t}}\right)^2\right], \tag{5.10}$$

the tail Gaussian given by

$$\mathcal{R}_{tail}(\Delta t, \sigma_{\Delta t}) = \frac{1}{\sqrt{2\pi}\varSigma_{tail}\sigma_{\Delta t}} \exp\left[-\frac{1}{2}\left(\frac{\Delta t - \mu_{tail}\sigma_{\Delta t}}{\varSigma_{tail}\sigma_{\Delta t}}\right)^2\right], \tag{5.11}$$

with $\varSigma_{tail}$ fixed to 3.0, and the outlier given by

$$\mathcal{R}_{out}(\Delta t, \sigma_{\Delta t}) = \frac{1}{\sqrt{2\pi}\varSigma_{out}} \exp\left[-\frac{1}{2}\left(\frac{\Delta t}{\varSigma_{out}}\right)^2\right] \tag{5.12}$$

where $\varSigma_{out}$ is fixed to 8 ps.

The parameters f_{tail}, f_{out}, μ_{core}, μ_{tail}, and $\varSigma_{core}$ are taken from BABAR's B Tagging group [41], which obtained them from a fit to a data sample of B^0 decays to the flavor eigenstates $D^{(*)-}h^+$, with $h^+ = (\pi^+, \rho^+, a_1^+)$. The parameters μ_{core} and $\varSigma_{core}$ are split by tagging category, having one set of values for the Lepton category, and another set of values for all the other categories. The $K^0_S \rightarrow \pi^+\pi^-$ and $K^0_S \rightarrow \pi^0\pi^0$ modes both use the same Δt resolution function.

5.3 Continuum Background Model

Most of the background events in this analysis are expected to come from continuum $e^+e^- \to q\bar{q}, q = u, d, s, c$ decays. We will float the number of continuum background events in the nominal ML fit. We use both offpeak and onpeak sideband events to model the contribution from continuum events, as described below.

5.3.1 m_{ES} Distribution

We use an ARGUS function [42] of the form

$$\mathcal{P}(x) = x\sqrt{1 - \left(\frac{x}{x_0}\right)^2} e^{c\left(1-\left(\frac{x}{x_0}\right)^2\right)} \tag{5.13}$$

for the m_{ES} PDF for continuum events. We fix x_0 to the kinematic endpoint of $5.29\,\mathrm{GeV}/c^2$, while c is a free parameter. In the B^+ modes, we float the parameter c in our nominal fit to data.

In $B^0 \to K^+K^-K^0_S$, on the other hand, we allow c to be different for each tagging category, and obtain the c values by fitting to onpeak data in the sideband region $5.22 < m_{\mathrm{ES}} < 5.29$, $\Delta E > 0.1$. Separate parameters are used for $K^0_S \to \pi^+\pi^-$ and $K^0_S \to \pi^0\pi^0$ events. The results of these fits are shown in Fig. 5.16, projected over all tagging categories. The PDF parameters are fixed in the nominal fit to data, and we will vary them as a systematic. The continuum m_{ES} distributions for $B^+ \to K^+K^-K^+$ and $B^+ \to K^0_SK^0_SK^+$ look similar, so we do not show plots for them.

5.3.2 ΔE Distribution

We use linear PDF's (first-order polynomials) to describe the ΔE distribution of continuum events. The slopes the PDF's are floated in the nominal fit to data. As an illustration of the ΔE distribution for continuum events, we show a fit to $B^+ \to K^+K^-K^+$ offpeak data in Fig. 5.17. The $B^+ \to K^0_SK^0_SK^+$ and $B^0 \to K^+K^-K^0_S$ distributions look similar.

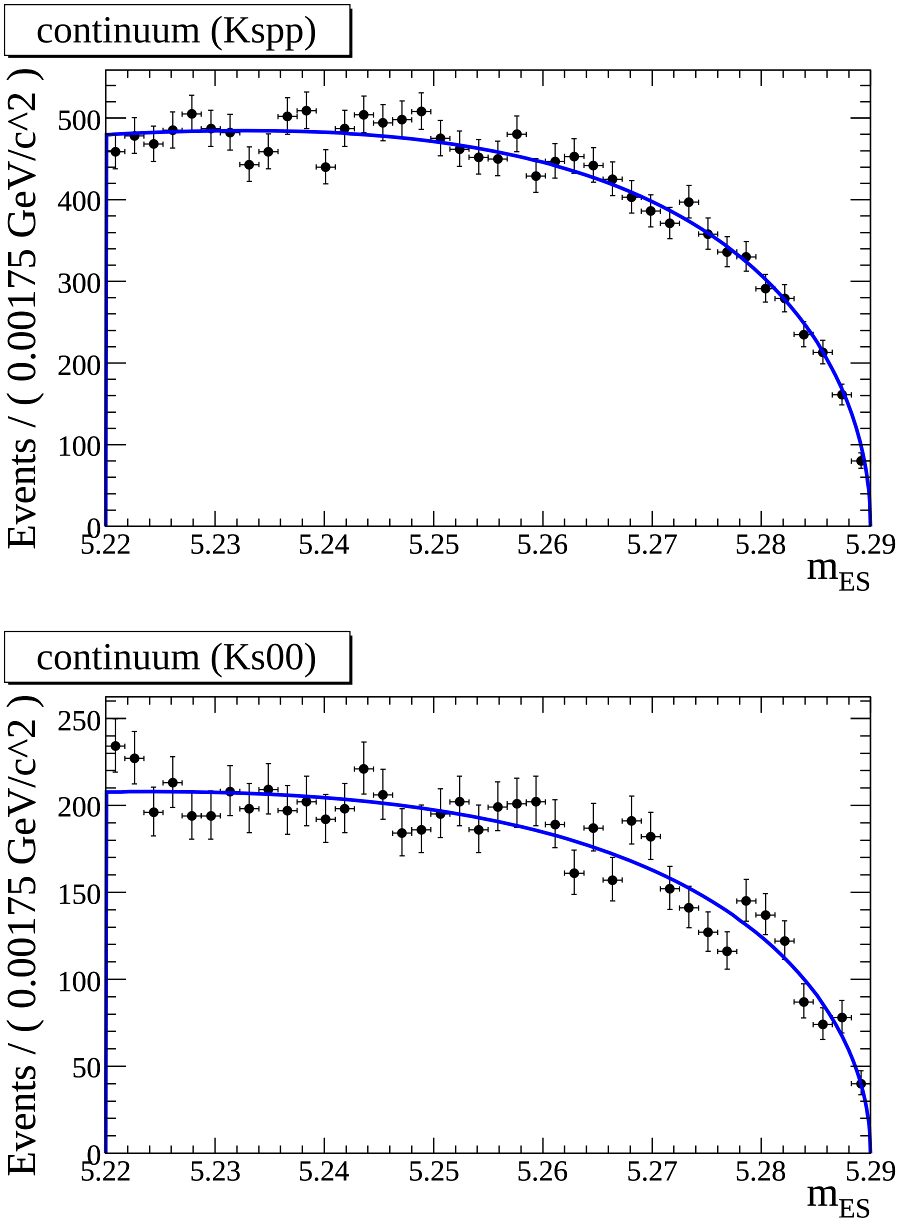

Figure 5.16: m_{ES} PDF's for $B^0 \rightarrow K^+K^-K^0_S$ continuum background events, for $K^0_S \rightarrow \pi^+\pi^-$ (top) and $K^0_S \rightarrow \pi^0\pi^0$ (bottom). The PDF's are shown fit to onpeak sideband events.

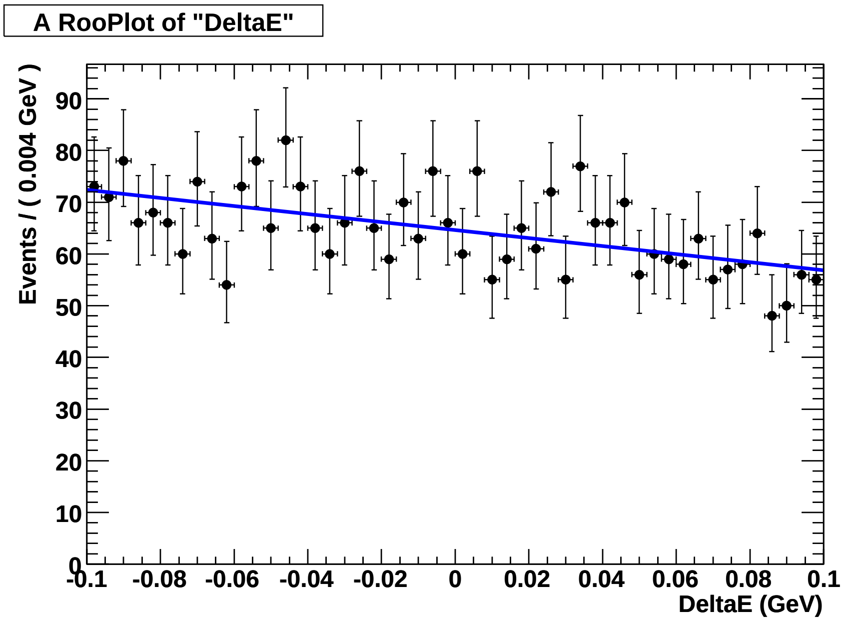

Figure 5.17: ΔE PDF for $B^+ \to K^+K^-K^+$ continuum events. The PDF (blue) is shown fit to offpeak events (black points).

5.3.3 NN Distribution

As explained in Sec. 4.6.2, the event shape variable that we use depends on DP position for continuum events. The DP-dependence of the unbinned event shape variable (MLP) was illustrated in Fig. 4.5. The PDF we use is a modified Parametric Step Function, with each bin height having a linear dependence on the Dalitz distance, Δ_{DP}. Explicitly, the PDF is:

$$P(i) = a_i + b_i\Delta_{DP} \tag{5.14}$$

where i is the number of the bin (an integer). A fit to $B^+ \to K^+K^-K^+$ offpeak events, with the parameters a_i and b_i floating, is shown in Fig. 5.18. Note that although we use 10 NN bins, only a_0 through a_8 and b_0 through b_8 are floating parameters, because the values of a_9 and b_9 are constrained by the requirement that the PDF be normalized to 1.

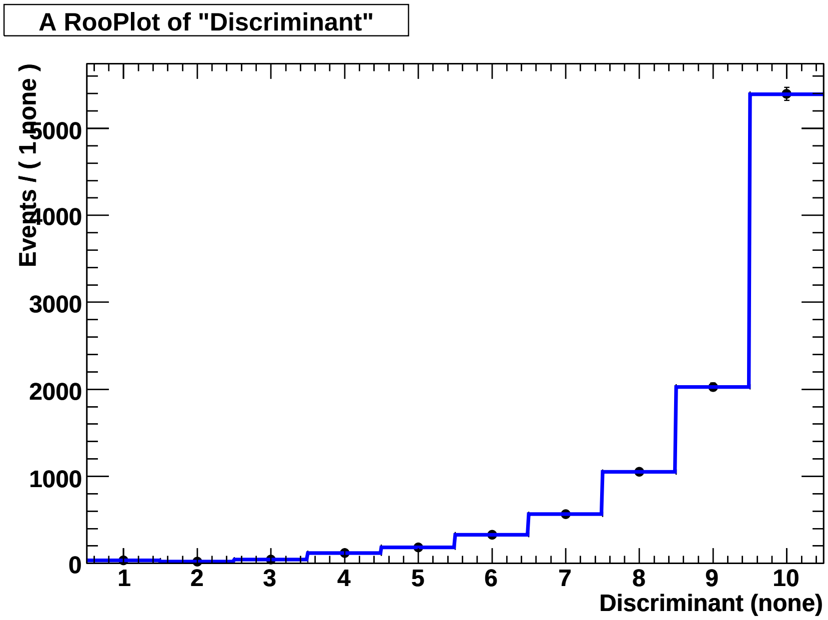

Figure 5.18: NN PDF for $B^+ \to K^+K^-K^+$ continuum background events. In this figure, the PDF (blue line) is shown fit to offpeak events (black points). Note that the PDF depends both on NN and Δ_{DP}, but this figure only shows the NN projection.

In $B^+ \to K^0_S K^0_S K^+$ and $B^0 \to K^+K^-K^0_S$, we will float these PDF parameters in our nominal data fits. In $B^+ \to K^+K^-K^+$, to keep the number of parameters low and improve fit stability, we we float them in a separate *CP*-blind fit to data, and then fix them to those values in the nominal fit, and vary them as a systematic.

5.3.4 Dalitz Plot Distribution

The continuum events have a highly non-uniform distribution on the DP. In $B^+ \to K^+K^-K^+$ and $B^0 \to K^+K^-K^0_S$, there are particularly strong peaks in the region of the $\phi(1020)$. We model the DP distribution with a special kind of histogram PDF that has variable bin size. The bin size is calculated in an adaptive manner that automatically uses small binning in areas of the DP containing many events, and large binning in areas of the DP containing few events. This is done so that the bin-size is small enough to capture narrow structures such as in the region of the $\phi(1020)$, but large in areas more sparsely populated with events, so that statistical fluctuations are not too large in these bins. More details about this procedure are given in Appendix B.

The PDF's are taken from onpeak events from the following m_{ES} sidebands:

- $B^+ \to K^+K^-K^+$: $5.2 < m_{\mathrm{ES}} < 5.27$, $-0.1 < \Delta E < 0.1$.
- $B^+ \to K^0_S K^0_S K^+$: $5.2 < m_{\mathrm{ES}} < 5.26$, $-0.1 < \Delta E < 0.1$.
- $B^0 \to K^+K^-K^0_S$: $m_{\mathrm{ES}} < 5.26$, $-0.06(-0.12) < \Delta E < 0.06$ for $K^0_S \to \pi^+\pi^-$ ($K^0_S \to \pi^0\pi^0$) events.

Since the onpeak sidebands contain $B\overline{B}$ events, we subtract off the $B\overline{B}$ events, by estimating their DP distribution from generic $B\overline{B}$ MC.

Projections of the 2-dimensional DP PDF for $B^+ \to K^+K^-K^+$ are shown in Fig. 5.19, overlaid with offpeak events. We plot offpeak events from the full m_{ES} and ΔE range, instead of just the signal region, in order to have a reasonable number of events. As can be seen, the PDF (taken from onpeak, with $B\overline{B}$ subtraction) agrees quite well with the offpeak distribution, which is a good cross-check. There is a small peak in the D^0-region in the PDF that is not seen in offpeak events, but the discrepancy is small. Further study of the events in the D^0 region shows that they are continuum events rather than $B\overline{B}$ events, so we believe this peak belongs in the PDF. In Fig. 5.20, we show the $B^+ \to K^+K^-K^+$ continuum PDF *without* $B\overline{B}$ subtraction, overlaid with the onpeak sideband events.

Similarly, in Figs. 5.21, 5.22, and 5.23, we show projections of the continuum DP PDF's for $B^+ \to K^0_S K^0_S K^+$, $B^0 \to K^+K^-K^0_S$ ($K^0_S \to \pi^+\pi^-$), and $B^0 \to K^+K^-K^0_S$ ($K^0_S \to \pi^0\pi^0$), respectively. The PDF projections are overlaid with offpeak events for comparison.

In $B^+ \to K^+K^-K^+$ and $B^+ \to K^0_S K^0_S K^+$, to account for possible charge asymmetries in continuum events, we give the PDF an A_{CP} parameter. We will float this asymmetry in the nominal ML fit. In $B^0 \to K^+K^-K^0_S$, we assume that the continuum events have no $B^0_{\rm tag}$-flavor-dependent asymmetry.

5.3.5 Δt Distribution

For $B^0 \to K^+K^-K^0_S$, the Δt distribution of continuum events is modeled by the sum of a "prompt" (zero-lifetime) component and a long-lived exponential decay, which is then convolved with a resolution function:

$$\mathcal{P}(\Delta t) \;=\; (f_{prompt}\;\delta(\Delta t) + (1 - f_{prompt})e^{-|\Delta t|/\tau}) \otimes \mathcal{R}(\Delta t, \sigma_{\Delta t}) \qquad (5.15)$$

where the fraction f_{prompt} is split by tagging category. The resolution function $\mathcal{R}$ is given by a double Gaussian,

$$\mathcal{R}(\Delta t, \sigma_{\Delta t}) = (1 - f_{out})\mathcal{R}_{core}(\Delta t, \sigma_{\Delta t}) + f_{out}\mathcal{R}_{out}(\Delta t, \sigma_{\Delta t}) \qquad (5.16)$$

with the core Gaussian given by

$$\mathcal{R}_{core}(\Delta t, \sigma_{\Delta t}) = \frac{1}{\sqrt{2\pi}\,\varSigma_{core}\sigma_{\Delta t}} \exp\left[-\frac{1}{2}\left(\frac{\Delta t - \mu_{core}\sigma_{\Delta t}}{\varSigma_{core}\sigma_{\Delta t}}\right)^2\right] \qquad (5.17)$$

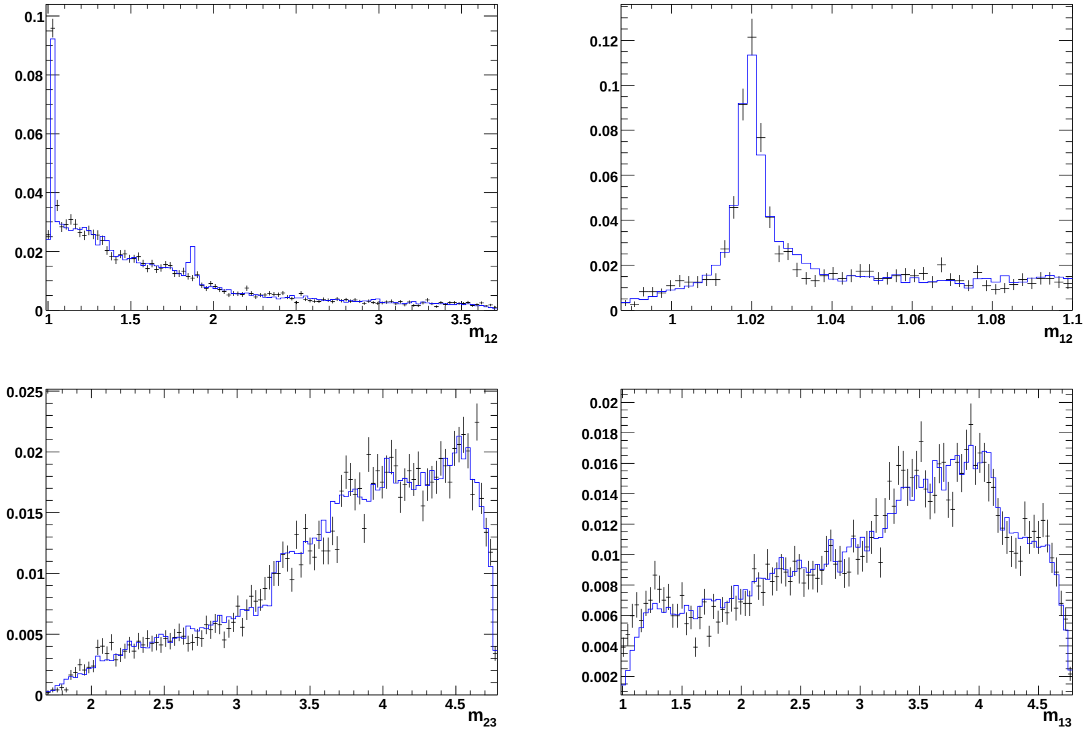

Figure 5.19: Projections of the 2-dimensional $B^+ \to K^+K^-K^+$ continuum DP PDF (blue lines), overlaid with offpeak events (black points).

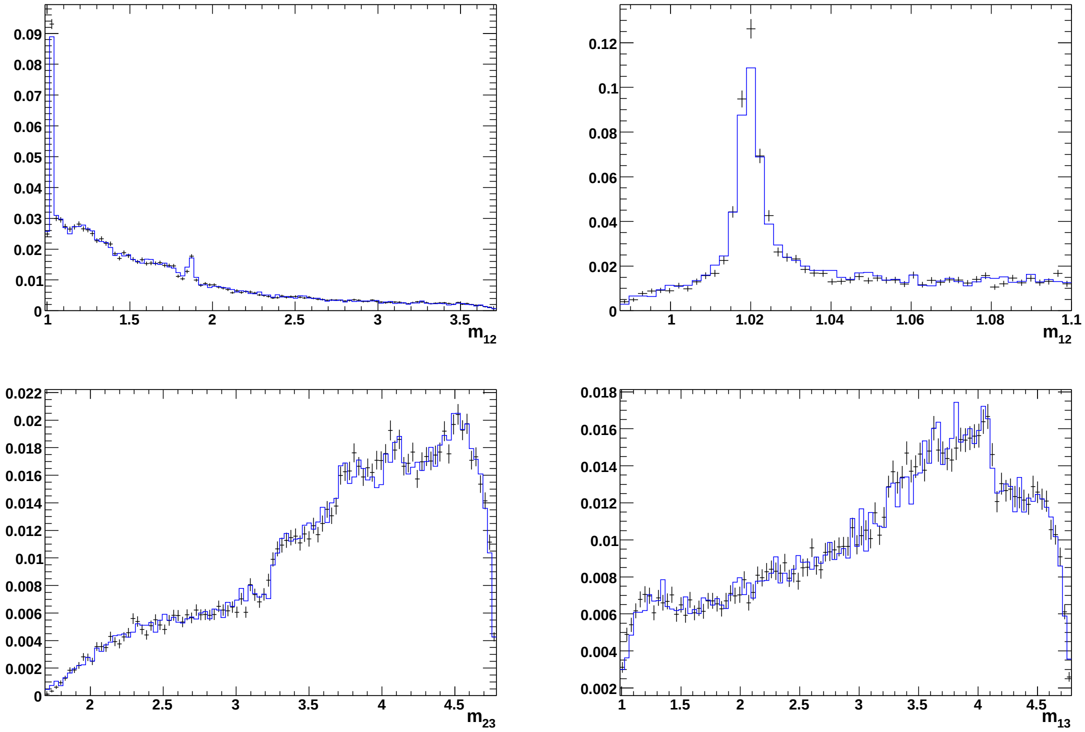

Figure 5.20: Projections of the 2-dimensional $B^+ \to K^+K^-K^+$ continuum DP PDF *without* $B\overline{B}$ subtraction (blue lines), overlaid with onpeak sideband events (black points).

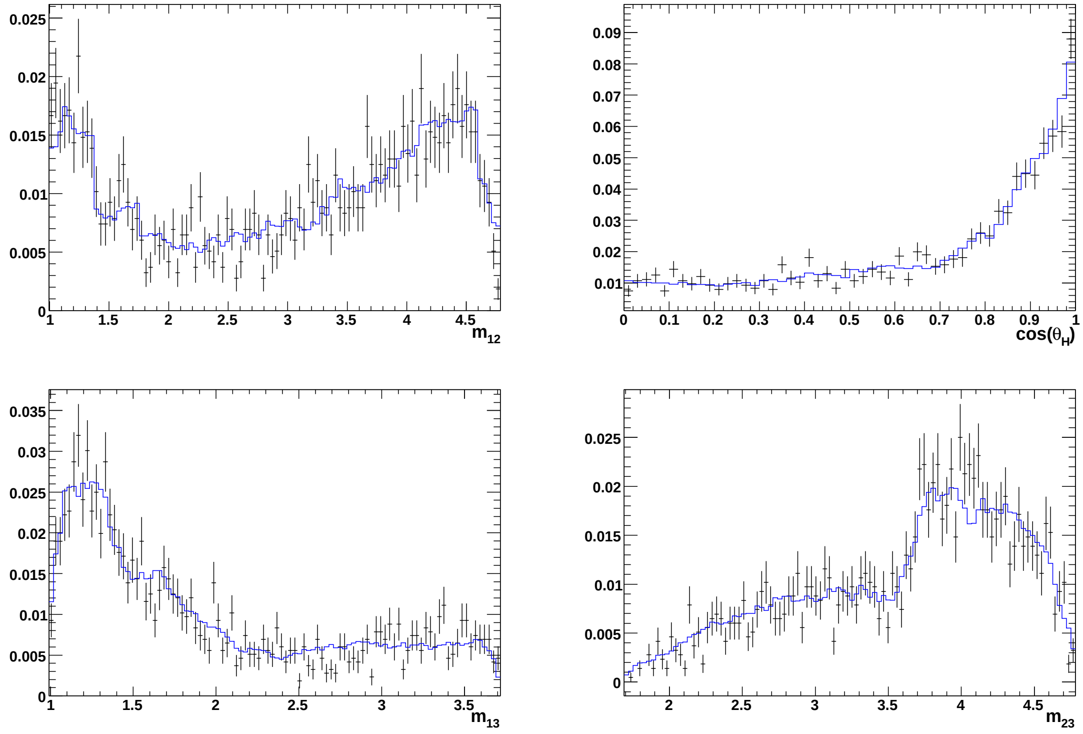

Figure 5.21: Projections of the 2-dimensional $B^+ \to K_S^0 K_S^0 K^+$ continuum DP PDF (blue lines), overlaid with offpeak events (black points).

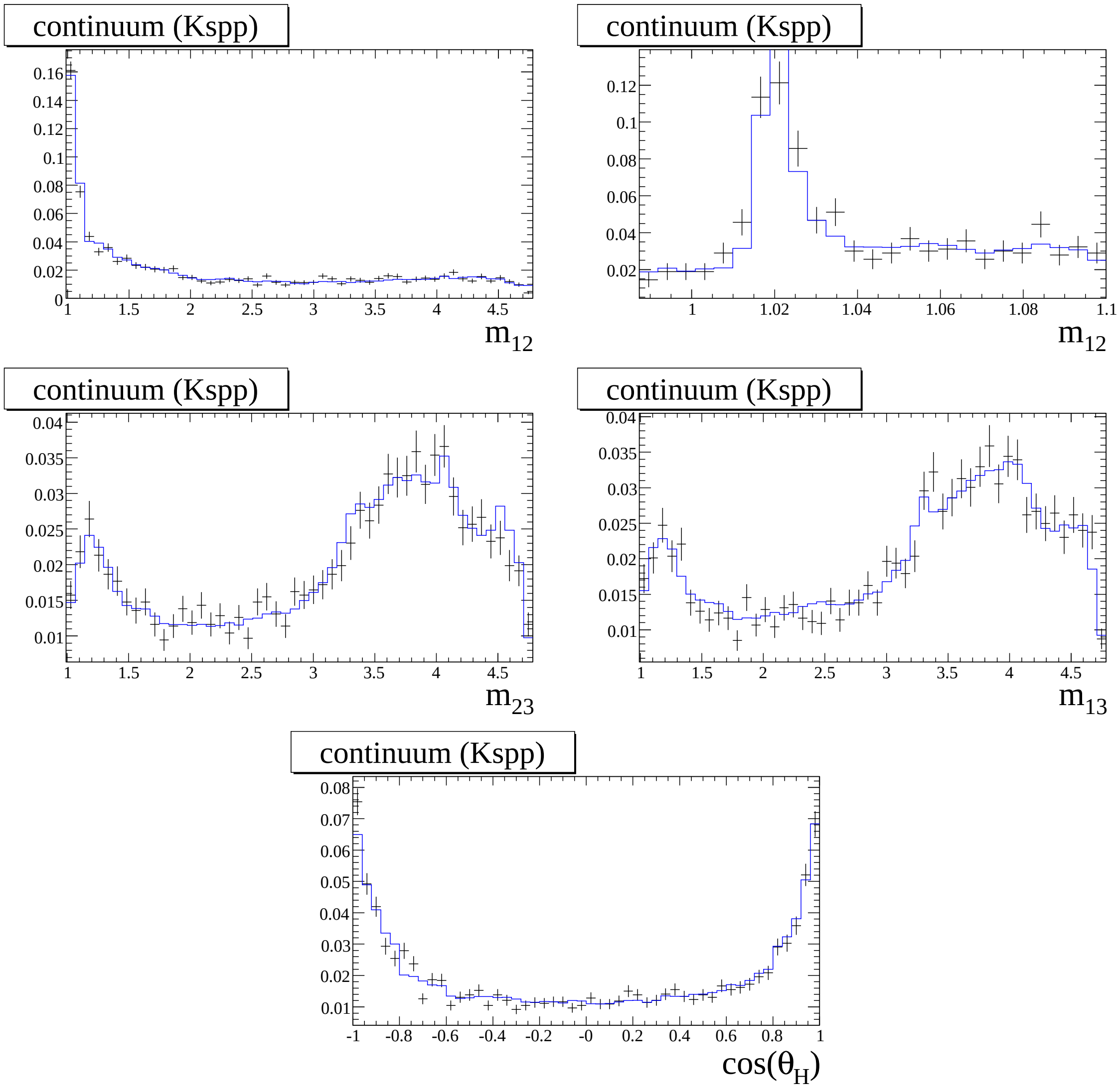

Figure 5.22: Projections of the 2-dimensional $B^0 \to K^+K^-K^0_S$ ($K^0_S \to \pi^+\pi^-$) continuum DP PDF (blue lines), overlaid with offpeak events (black points).

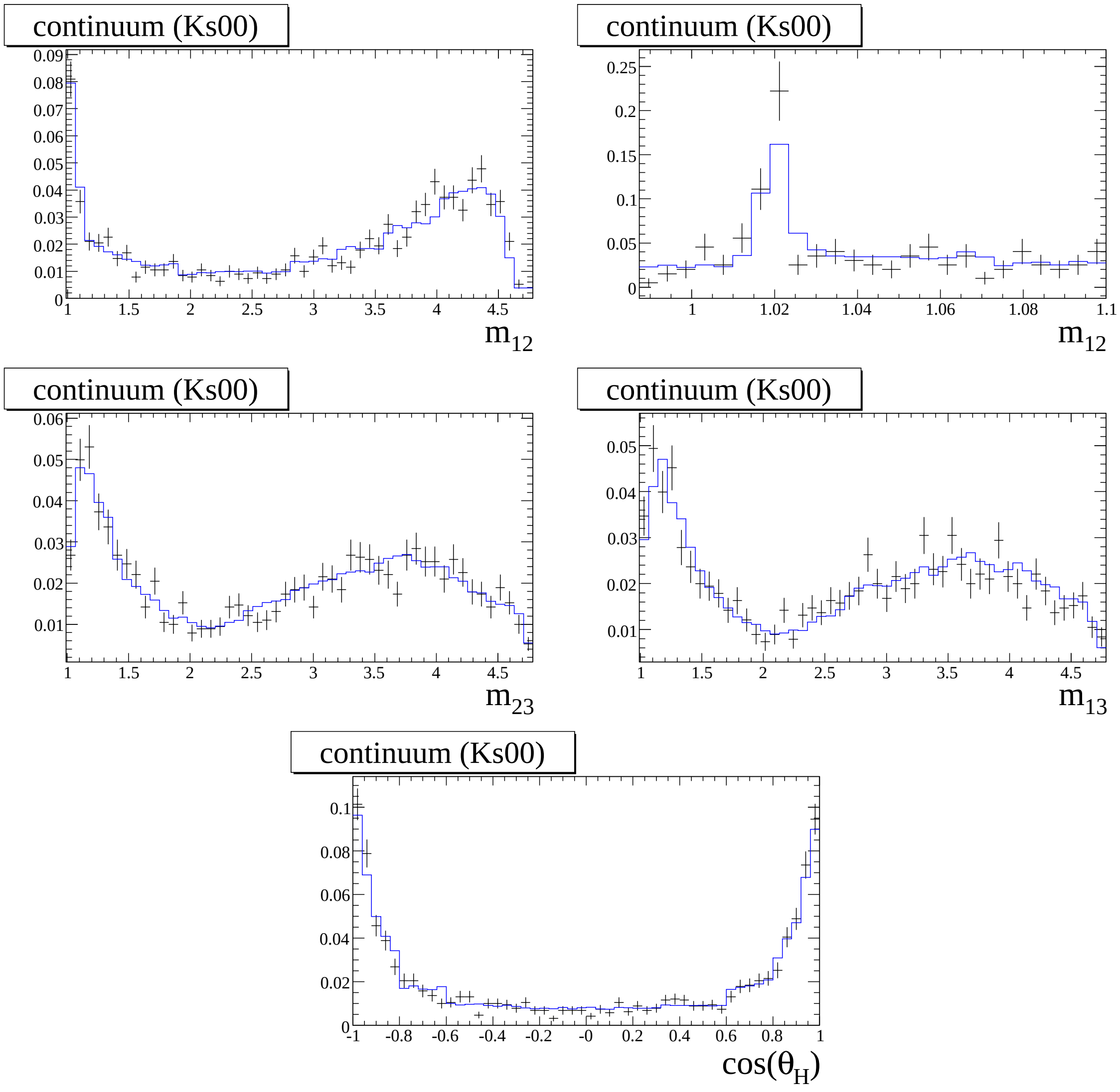

Figure 5.23: Projections of the 2-dimensional $B^0 \to K^+K^-K^0_S$ ($K^0_S \to \pi^0\pi^0$) continuum DP PDF (blue lines), overlaid with offpeak events (black points).

and the outlier given by

$$\mathcal{R}_{out}(\Delta t, \sigma_{\Delta t}) = \frac{1}{\sqrt{2\pi}\Sigma_{out}} \exp\left[-\frac{1}{2}\left(\frac{\Delta t}{\Sigma_{out}}\right)^2\right] \tag{5.18}$$

where Σ_{out} is fixed to 8 ps.

The parameters τ, f_{prompt}, f_{out}, μ_{core}, and Σ_{core} are obtained by fitting to onpeak data in the sideband region $5.2 < m_{\mathrm{ES}} < 5.26$, $-0.06(-0.12) < \Delta E < 0.06$ for $K_S^0 \to \pi^+\pi^-$ ($K_S^0 \to \pi^0\pi^0$) events. The results of these fits are shown in Fig. 5.24. The PDF parameters are fixed in the nominal fit to data.

5.4 $B\overline{B}$ Background Model

In order to estimate how many events from $B\overline{B}$ backgrounds we expect to pass our cuts, we look at "generic" MC samples of B^+B^- and $B^0\overline{B}^0$ events (SP-1235 and SP-1237, respectively). The generic MC attempts to model all known B decays, using either measured branching fractions or estimated branching fractions if no measurements are available. Based on the generic MC studies, we can determine what the largest and/or most dangerous $B\overline{B}$ backgrounds are, which we can then study using specific MC for those individual decay channels ("exclusive" MC).

The most dangerous $B\overline{B}$ backgrounds are those from $b \to c$ decays that have the same final state as signal. We call such backgrounds "peaking" backgrounds. For example, $B^+ \to \bar{D}^0 K^+, \bar{D}^0 \to K^+K^-$ is a peaking background for $B^+ \to K^+K^-K^+$. Whether to consider such decays as signal or background is to some extent a matter of semantics. Since we are trying to study charmless $b \to s$ transitions rather than $b \to c$ transitions, we will regard the latter as $B\overline{B}$ backgrounds. An exception to this is $B \to \chi_{c0}K$, which we will normally regard as signal, because the χ_{c0} has a wide enough decay width that it interferes (in the quantum mechanical sense) with the charmless signal. Therefore, we include the χ_{c0} in the signal isobar model. The peaking backgrounds come from J/ψ and various D resonances, which are too long-lived to interfere with the charmless signal in any significant way, so we can treat

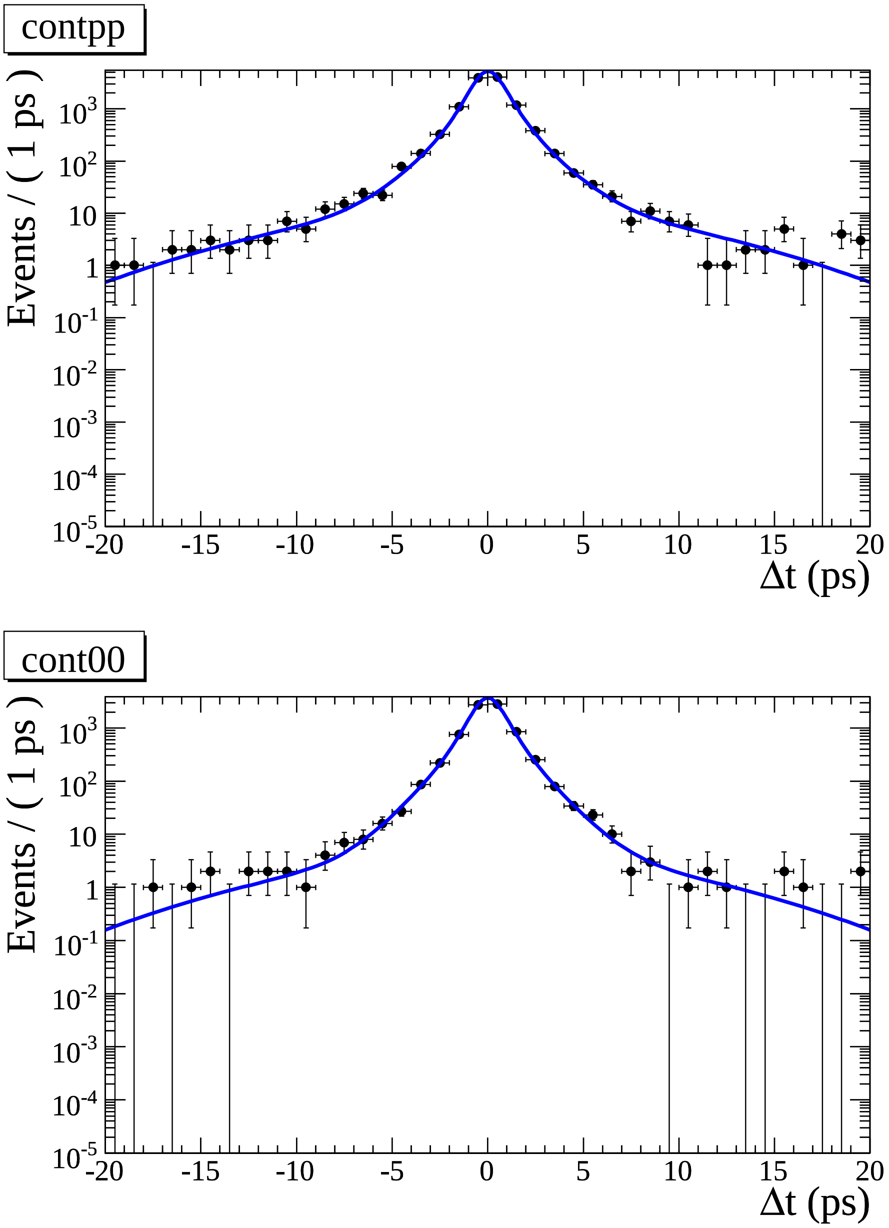

Figure 5.24: Δt PDF's for continuum events, for $K_S^0 \to \pi^+\pi^-$ (top) and $K_S^0 \to \pi^0\pi^0$ (bottom) events, plotted on a log scale. In this figure, the PDF's are shown fit to onpeak sideband events.

them as backgrounds.[2]

5.4.1 $B^+ \rightarrow K^+K^-K^+$

Based on generic MC, after scaling to the integrated luminosity of Runs 1-6, we expect roughly 660 B^+B^- background events and 120 $B^0\overline{B}^0$ background events to pass our cuts. Those numbers do not include the sizable contributions that are expected from the peaking backgrounds $B^+ \rightarrow \bar{D}^0K^+, \bar{D}^0 \rightarrow K^+K^-$ and $B^+ \rightarrow J/\psi K^+, J/\psi \rightarrow K^+K^-$ decays.

Since the amount of generic MC events is limited, in order to more reliably model the $B\overline{B}$ backgrounds, we use exclusive MC samples for 20 of the most common decay modes, all of which are from B^+ decays. We then split these 20 exclusive decay modes into six different categories:

- "BB charmless." This category contains the primary charmless $B\overline{B}$ background modes. The largest contribution is from $B^+ \rightarrow K^+K^-\pi^+$ decays, which can be misidentified as signal if the π is misidentified as a kaon.

- "BB charm 1." This category consists of various decay modes, which all contain a $\bar{D}^0 \rightarrow K^+K^-$ decay somewhere in their decay chain. By far the largest contribution is from $B^+ \rightarrow \bar{D}^0\pi^+, \bar{D}^0 \rightarrow K^+K^-$ decays, where the π is misidentified as a kaon. Events in this category are peaked sharply around the D^0-mass in the Dalitz plot. Most of these events are shifted to the right in ΔE, because of pions being misidentified as kaons.

- "BB charm 2." This category consists solely of the decay mode $B^+ \rightarrow \bar{D}^0K^+, \bar{D}^0 \rightarrow K^+\pi^-$. These events have a peaking structure in the Dalitz plot, but the peak is shifted to the right of the D^0-mass, because of the pion being misidentified as a kaon. This misidentification also causes these events to be shifted to the right in ΔE.

---

[2] A partial-exception to this is in $B^0 \rightarrow K^+K^-K^0_S$, where, from a technical standpoint, we decided to implement the peaking backgrounds as non-interfering isobars in the signal model. However, from the standpoint of the final results we quote, we will still regard them as backgrounds.

- "BB charm 3." This category consists of other decay modes that contain a $\bar{D}^0 \to K^+\pi^-$ decay somewhere in their decay chain. These decays are mainly four-body decay modes. Events in this category have m_{ES} and ΔE distributions that are more continuum-like than the previous three $B\overline{B}$ categories, although they still have some peaking structure in m_{ES}. This category has a peak in the Dalitz plot around the D^0-mass, but the peak is significantly broader than for BB charm 1 or BB charm2.

- "BB charm 5." This category consists entirely of the single decay mode $B^+ \to \bar{D}^0 K^+, \bar{D}^0 \to K^+K^-$. Although this decay mode has the same final state as signal events, we treat it as a $B\overline{B}$ background in the ML fit. However, it has virtually the same m_{ES}, ΔE, and NN distributions as signal events, so we use the signal m_{ES}, ΔE, and NN PDF's for this category. This category has a very narrow peak in the Dalitz plot around the D^0-mass.

- "BB charm 6." This category consists entirely of the single decay mode $B^+ \to J/\psi K^+, J/\psi \to K^+K^-$. This decay mode has the same final state as signal events, so we use the signal m_{ES}, ΔE, and NN PDF's for this category. This category has a very narrow peak in the Dalitz plot around the J/ψ-mass. We decided to include this component late in the analysis, so we do not have an exclusive MC sample for it. Instead, we created "toy" J/ψ events, by generating a narrow peak at the J/ψ mass, and then smearing this peak by the known resolutions. The DP PDF is then created from these toy events.

In Table 5.4, we list the exclusive decay modes that are in each of these categories. For each of these $B\overline{B}$ categories (except "BB charm 6"), we generate a MC "cocktail." The cocktail is generated by mixing together MC events from each of the decay modes in that particular category. The number of events to put into the cocktail from each decay mode is calculated using the branching fractions (taken from the PDG), and the selection efficiency (calculated by running our selection code over the exclusive MC events). This information is summarized in Table 5.4.

The exclusive modes in the five $B\overline{B}$ categories already mentioned only account for approximately two-thirds of the total number of $B\overline{B}$ background events expected.

To account for the remaining $B\overline{B}$ events, we form an additional $B\overline{B}$ category:

- "BB charm 4." This category consists of all remaining $B\overline{B}$ decays not included in any of the previous $B\overline{B}$ categories. These events are modeled with the $B\overline{B}$ generic MC (SP-1235 and SP-1237), where the 20 exclusive decay modes are explicitly removed. Almost all of the decay modes in this category involve D decays, with many-body final states. These events have m_{ES} and ΔE distributions similar to continuum events. They are very broadly peaked around the D^0-mass in the Dalitz plot.

We use different PDF's for each of the seven $B\overline{B}$ background categories. The PDF types used for each of the background categories are listed in Table 5.5. The PDF shapes for each of the $B\overline{B}$ categories are shown in Appendix A. The m_{ES}, ΔE, and NN PDF parameters are obtained by fitting to the MC cocktail samples, except for in the case of the "BB charm 5" and "BB charm 6" categories, in which case these PDF's are set equal to the signal PDF's. The DP PDF's are special histogram PDF's, using variable bin size, like what was used for the continuum DP distribution (see Sec. 5.3.4).

To account for possible charge asymmetries in the background, we give each background PDF a separate A_{CP} parameter. The A_{CP} is fixed to the value found in the MC cocktails (essentially zero). An exception to this is "BB charm 5," which we fix to the world average value of $A_{CP} = 0.24 \pm 0.08$. We will vary the A_{CP}'s as a systematic.

5.4.2 $B^+ \to K^0_S K^0_S K^+$

Based on generic MC, we expect roughly 60 B^+B^- events and 80 $B^0\overline{B}^0$ events to pass our cuts. This does not include a small number (~ 8) of peaking $B^+ \to K^+\bar{D}^0, \bar{D}^0 \to K^0_S K^0_S$ events that we also expect.

We use exclusive MC samples for 10 of the most common (or most signal-like) decay modes, which include both B^+ and B^0 modes. We then split these 10 exclusive decay modes into three different categories:

Table 5.4: Summary of $B\overline{B}$ backgrounds in $B^+ \rightarrow K^+K^-K^+$. "Mode #" is the SP number that BABAR has assigned to the MC sample. "MC ε" is the efficiency for background to pass all selection criteria, as determined from MC. "$\mathcal{B}$" is the top-level branching fraction for the background mode, and $\prod \mathcal{B}_i$ is the product of all the sub-branching fractions involved in the decay chain, so that the overall branching fraction is the product of $\mathcal{B}$ and $\prod \mathcal{B}_i$. "Exp. Yield" is the number of events expected in the full dataset of $\approx 470 MB\overline{B}$ pairs. "# in PDF Bkg. File" gives the number of MC events that are mixed into the cocktail used for forming the PDF's for a particular background category.

Bkg. channel	Mode #	MC ε (%)	$\mathcal{B}$ (10^{-6})	$\prod \mathcal{B}_i$	Exp. Yield	# in PDF Bkg. file
BB charmless						
$B^+ \rightarrow K^+K^-\pi^+$ (*Dalitz model*)	9755	1.417	$5.0^{+0.7}_{-0.7}$	1.0	33.1	1352
$B^+ \rightarrow K^+\pi^-\pi^+$ (*Dalitz model*)	9178	0.020	55^{+7}_{-7}	1.0	5.0	205
$B^+ \rightarrow K^+K^-K^{*+}_{K^+\pi^0}$ (*N.R.*)	2477	0.047	$31.0^{+4.9}_{-4.9}$	0.333	2.3	92
$B^+ \rightarrow \eta'_{\rho\gamma}K^+$	6748	0.016	$70.2^{+2.5}_{-2.5}$	0.294	1.5	62
$B^+ \rightarrow \phi_{K^+K^-}K^{*+}_{K^+\pi^0}$	4615	0.043	$10.5^{+1.5}_{-1.5}$	0.164	0.3	14
					42.3	1725
BB charm 1						
$B^+ \rightarrow \bar{D^0}\pi^+(\bar{D^0} \rightarrow K^+K^-)$	3021	1.799	4840^{+150}_{-150}	0.00393	160.1	5109
$B^+ \rightarrow \bar{D}^*(2007)^0_{\bar{D^0}\gamma}\pi^+(\bar{D^0} \rightarrow K^+K^-)$	3174	0.368	5190^{+260}_{-260}	0.00150	13.4	428
$B^+ \rightarrow \bar{D^0}_{K^+K^-}\rho^+_{\pi^+\pi^0}$	3028	0.034	13400^{+1800}_{-1800}	0.00393	8.5	270
$B^+ \rightarrow \bar{D}^*(2007)^0_{\bar{D^0}\pi^0}\pi^+(\bar{D^0} \rightarrow K^+K^-)$	3025	0.116	5190^{+260}_{-260}	0.00243	6.8	218
$B^+ \rightarrow \bar{D}^*(2007)^0_{\bar{D^0}\gamma}K^+(\bar{D^0} \rightarrow K^+K^-)$	3172	2.205	416^{+33}_{-33}	0.00150	6.4	205
					195.3	6230
BB charm 2						
$B^+ \rightarrow \bar{D^0}K^+(\bar{D^0} \rightarrow K^+\pi^-)$	2435	1.257	402^{+21}_{-21}	0.0389	92.0	4928
					92.0	4928
BB charm 3						
$B^+ \rightarrow \bar{D}^*(2007)^0_{\bar{D^0}\pi^0}K^+(\bar{D^0} \rightarrow K^+\pi^-)$	2420	0.477	416^{+33}_{-33}	0.0241	22.4	180
$B^+ \rightarrow \bar{D}^*(2007)^0_{\bar{D^0}\pi^0}\pi^+(\bar{D^0} \rightarrow K^+\pi^-)$	2421	0.037	5190^{+260}_{-260}	0.0241	21.4	172
$B^+ \rightarrow \bar{D^0}\pi^+(\bar{D^0} \rightarrow K^+\pi^-)$	2442	0.024	4840^{+150}_{-150}	0.0389	21.0	169
$B^+ \rightarrow \bar{D^0}_{K^+\pi^-}\rho^+_{\pi^+\pi^0}$	2436	0.007	13400^{+1800}_{-1800}	0.0389	18.2	146
$B^+ \rightarrow \bar{D}^*(2007)^0_{\bar{D^0}\gamma}K^+(\bar{D^0} \rightarrow K^+\pi^-)$	2626	0.581	416^{+33}_{-33}	0.0148	16.7	134
$B^+ \rightarrow \bar{D}^*(2007)^0_{\bar{D^0}\gamma}\pi^+(\bar{D^0} \rightarrow K^+\pi^-)$	2629	0.035	5190^{+260}_{-260}	0.0148	12.7	102
$B^+ \rightarrow \bar{D^0}_{K^+\pi^-}K^{*+}_{K^+\pi^0}$	4837	0.131	530^{+40}_{-40}	0.0130	4.2	34
					116.6	937
BB charm 4						
B^+B^- *generic*					265.0	776
$B^0\overline{B}^0$ *generic*					121.2	355
					386.2	1131
BB charm 5						
$B^+ \rightarrow \bar{D^0}K^+(\bar{D^0} \rightarrow K^+K^-)$	3018	31.588	402^{+21}_{-21}	0.00393	233.5	123825
					233.5	123825
BB charm 6						
$B^+ \rightarrow J/\psi\ K^+(J/\psi \rightarrow K^+K^-)$	-	-	1007^{+35}_{-35}	0.00024	~ 35	-
					~ 35	-

Table 5.5: PDF types used for each of the different $B\overline{B}$ categories in $B^+ \rightarrow K^+K^-K^+$, for $m_{\rm ES}$, ΔE, and NN. The "Histogram" PDF uses a histogram, but with interpolation so that the PDF is smooth. "PSF" stands for Parametric Step Function. BB charm5 and BB charm 6 share their $m_{\rm ES}$, ΔE, and NN PDF's with the signal.

$B\overline{B}$ category	$m_{\rm ES}$ PDF	ΔE PDF	NN PDF
BB charmless	Cruijff	Cruijff	PSF
BB charm 1	Cruijff	Histogram	PSF
BB charm 2	Cruijff	Cruijff	PSF
BB charm 3	Cruijff	First-order Polynomial	PSF
BB charm 4	ARGUS	First-order Polynomial	PSF
BB charm 5	Cruijff (signal)	Cruijff (signal)	PSF (signal)
BB charm 6	Cruijff (signal)	Cruijff (signal)	PSF (signal)

- "BB 1." This category contains a couple of $B\overline{B}$ decays with a $K^0_SK^0_S\pi^\pm$ final state. These events peak in $m_{\rm ES}$, and have a ΔE peak shifted to the right.
- "BB 2." This category contains an assortment of exclusive $B\overline{B}$ decays. The $m_{\rm ES}$ and ΔE shapes are similar to continuum events.
- "BB 4." This category contains the single decay $B^+ \rightarrow K^+\bar{D}^0, \bar{D}^0 \rightarrow K^0_SK^0_S$. It has virtually the same $m_{\rm ES}$, ΔE, and NN distributions as signal events, so we use the signal $m_{\rm ES}$, ΔE, and NN PDF's for this category. This category has a very narrow peak in the Dalitz plot around the D^0-mass.

In Table 5.6, we list the exclusive decay modes that are in each of these categories. For each of these $B\overline{B}$ categories, we generate a MC "cocktail," just like we did for $B^+ \rightarrow K^+K^-K^+$.

The exclusive modes in the 3 $B\overline{B}$ categories already mentioned only account for around one-fourth of the total number of $B\overline{B}$ background events expected. To account for the remaining $B\overline{B}$ events, we form an additional $B\overline{B}$ category:

- "BB 3." This category consists of all remaining $B\overline{B}$ decays not included in any of the previous $B\overline{B}$ categories. Most of the decay modes in this category involve

D decays. These events are modeled with the $B\overline{B}$ generic MC (SP-1235 and SP-1237), where the 10 exclusive decay modes are explicitly removed. These events have $m_{\rm ES}$ and ΔE distributions similar to continuum events.

We use different PDF's for each of the four $B\overline{B}$ background categories. The PDF types used for each of the background categories are listed in Table 5.7. The PDF shapes for each of the $B\overline{B}$ categories are shown in Appendix A. The $m_{\rm ES}$, ΔE, and NN PDF parameters are obtained by fitting to the MC cocktail samples, except for in the case of the "BB 4" category, in which case these PDF's are set equal to the signal PDF's. The DP PDF's are histogram PDF's with variable bin size.

5.4.3 $B^0 \to K^+K^-K^0_S$

Based on generic $B\overline{B}$ MC, we expect roughly 70 B^+B^- events and 70 $B^0\overline{B}^0$ events to pass our cuts for $K^0_S \to \pi^+\pi^-$. For $K^0_S \to \pi^0\pi^0$, we expect roughly 80 B^+B^- and 40 $B^0\overline{B}^0$ events. As in BABAR's previous $B^0 \to K^+K^-K^0_S$ analysis, we combine all B^+B^- events and $B^0\overline{B}^0$ events into a single $B\overline{B}$ background category. This doesn't include peaking $B\overline{B}$ backgrounds with a $K^+K^-K^0_S$ final state, which are handled separately, and are discussed later in this section.

We form the PDF's for the single $B\overline{B}$ background category using a combination of B^+B^- and $B^0\overline{B}^0$ generic MC. Separate PDF's are used for $K^0_S \to \pi^+\pi^-$ and $K^0_S \to \pi^0\pi^0$. For $K^0_S \to \pi^+\pi^-$, the $m_{\rm ES}$ distribution is first smoothed with KEYS, and then a histogram PDF is formed from the KEYS function. The histogram PDF uses interpolation between bins. The $K^0_S \to \pi^+\pi^-$ ΔE distribution is modeled with a linear polynomial. The $K^0_S \to \pi^+\pi^-$ PDF's are shown in Fig. 5.25.

For $K^0_S \to \pi^0\pi^0$, there is a slight correlation between $m_{\rm ES}$ and ΔE, so we use a 2D PDF for $m_{\rm ES}$ and ΔE. We first use a 2D KEYS function to smooth the MC, then we create a 2D histogram PDF from the KEYS function. The 2D histogram PDF uses interpolation between bins. This PDF and its projections are shown in Fig. 5.26.

The NN distributions are modeled with a Parametric Step Function, and the PDF's are shown in Figs. 5.25 and 5.26. For the DP PDF's, we use histograms with variable-size binning. The 1-D projections of these PDF's are shown in Figs. 5.27 and

Table 5.6: Summary of $B\overline{B}$ backgrounds in $B^+ \to K^0_S K^0_S K^+$. "Mode #" is the SP number that *BABAR* has assigned to the MC sample. "MC ε" is the efficiency for background to pass all selection criteria, as determined from MC. "$\mathcal{B}$" is the top-level branching fraction for the background mode, and $\prod \mathcal{B}_i$ is the product of all the sub-branching fractions involved in the decay chain, so that the overall branching fraction is the product of $\mathcal{B}$ and $\prod \mathcal{B}_i$. "Exp. Yield" is the number of events expected in the full dataset of $\approx 470 M B\overline{B}$ pairs. "# in PDF Bkg. File" gives the number of MC events that are mixed into the cocktail used for forming the PDF's for a particular background category.

Bkg. channel	Mode #	MC ε (%)	$\mathcal{B}$ (10^{-6})	$\prod \mathcal{B}_i$	Exp. Yield	# in PDF Bkg. file
BB 1						
$B^+ \to \bar{D}^0{}_{K^0_S K^0_S} \pi^+ (K^0_S \to \pi^+\pi^-)$	8438	1.361	4840^{+150}_{-150}	0.00018	5.6	2940
$B^+ \to K^0_S\ K^{*+}_{K^0_S \pi^+}$	1944	0.435	$0.38^{+0.39}_{-0.39}$	0.666	0.5	273
					6.1	3213
BB 2						
$B^0 \to K^0_S K^0_S K^0_S$	8996	0.291	$6.2^{+1.2}_{-1.1}$	1.0	8.5	469
$B^0 \to K^+ K^- K^0_S$	7930	0.168	$24.7^{+2.3}_{-2.3}$	0.346	6.8	373
$B^0 \to K^{*+}_{K^0_S \pi^+} K^- K^0_S (K^0_S \to \pi^+\pi^-)$	8192	0.322	10^{+10}_{-10}	0.318	4.8	266
$B^+ \to \bar{D}^0{}_{K^0_S \pi^+\pi^-} K^+ (K^0_S \to \pi^+\pi^-)$	5378	0.044	402^{+21}_{-21}	0.0207	1.7	96
$B^+ \to \bar{D}^0{}_{K^0_S \pi^0} \pi^+ (K^0_S \to \pi^+\pi^-)$	3549	0.004	4840^{+150}_{-150}	0.00844	0.8	45
$B^+ \to K^{*+}_{K^+ \pi^0} K^0_S K^0_S (K^0_S \to \pi^+\pi^-)$	8190	0.064	10^{+10}_{-10}	0.159	0.5	27
$B^+ \to K^{*0}_{K^0_S \pi^0} K^+ K^0_S (K^0_S \to \pi^+\pi^-)$	8191	0.046	10^{+10}_{-10}	0.159	0.3	19
					23.5	1295
BB 3						
B^+B^- *generic*					51.5	155
$B^0\overline{B}^0$ *generic*					66.6	200
					118.1	355
BB 4						
$B^+ \to K^+ \bar{D}^0{}_{K^0_S K^0_S} (K^0_S \to \pi^+\pi^-)$	10337	23.913	402^{+21}_{-21}	0.00018	8.1	51652
					8.1	51652

Table 5.7: PDF types used for each of the different $B\overline{B}$ categories in $B^+ \rightarrow K^0_S K^0_S K^+$, for m_{ES}, ΔE, and NN. The "Histogram" PDF uses a histogram, but with interpolation so that the PDF is smooth. "PSF" stands for Parametric Step Function. BB 4 shares its m_{ES}, ΔE, and NN PDF's with the signal.

$B\overline{B}$ category	m_{ES} PDF	ΔE PDF	NN PDF
BB 1	Cruijff	Cruijff	PSF
BB 2	Histogram	First-order Polynomial	PSF
BB 3	ARGUS	First-order Polynomial	PSF
BB 4	Cruijff (signal)	Cruijff (signal)	PSF (signal)

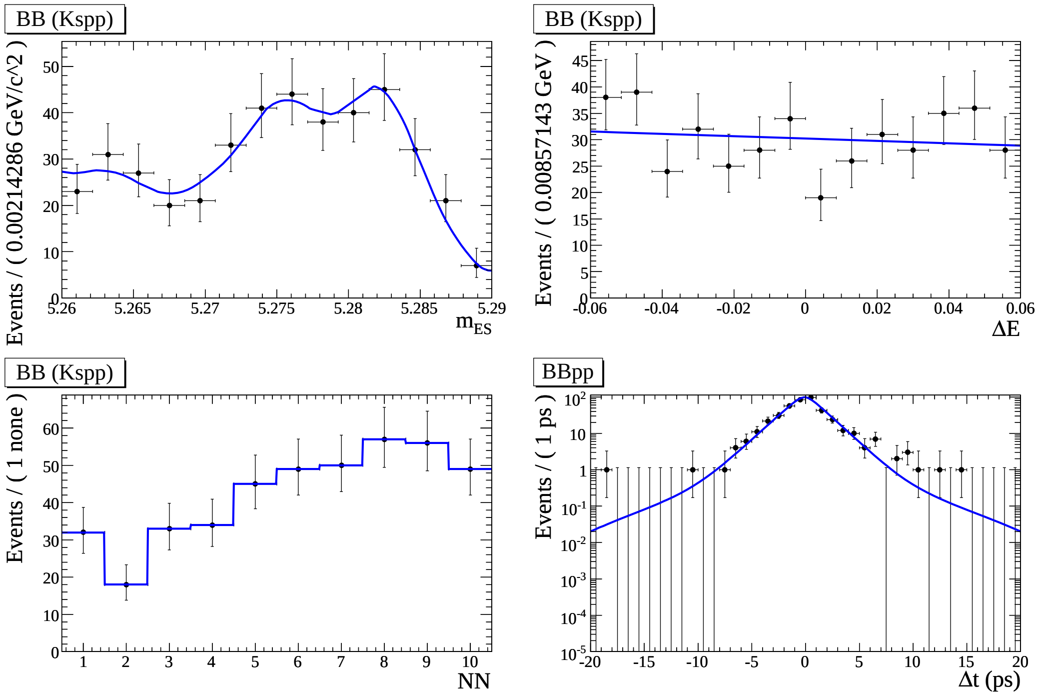

Figure 5.25: $B\overline{B}$ PDF's for $B^0 \rightarrow K^+K^-K^0_S$ ($K^0_S \rightarrow \pi^+\pi^-$). Top left: m_{ES}, top right: ΔE, bottom left: NN, bottom right: Δt. The PDF's are shown fit to $B\overline{B}$ generic MC. The Δt PDF is plotted on a log scale.

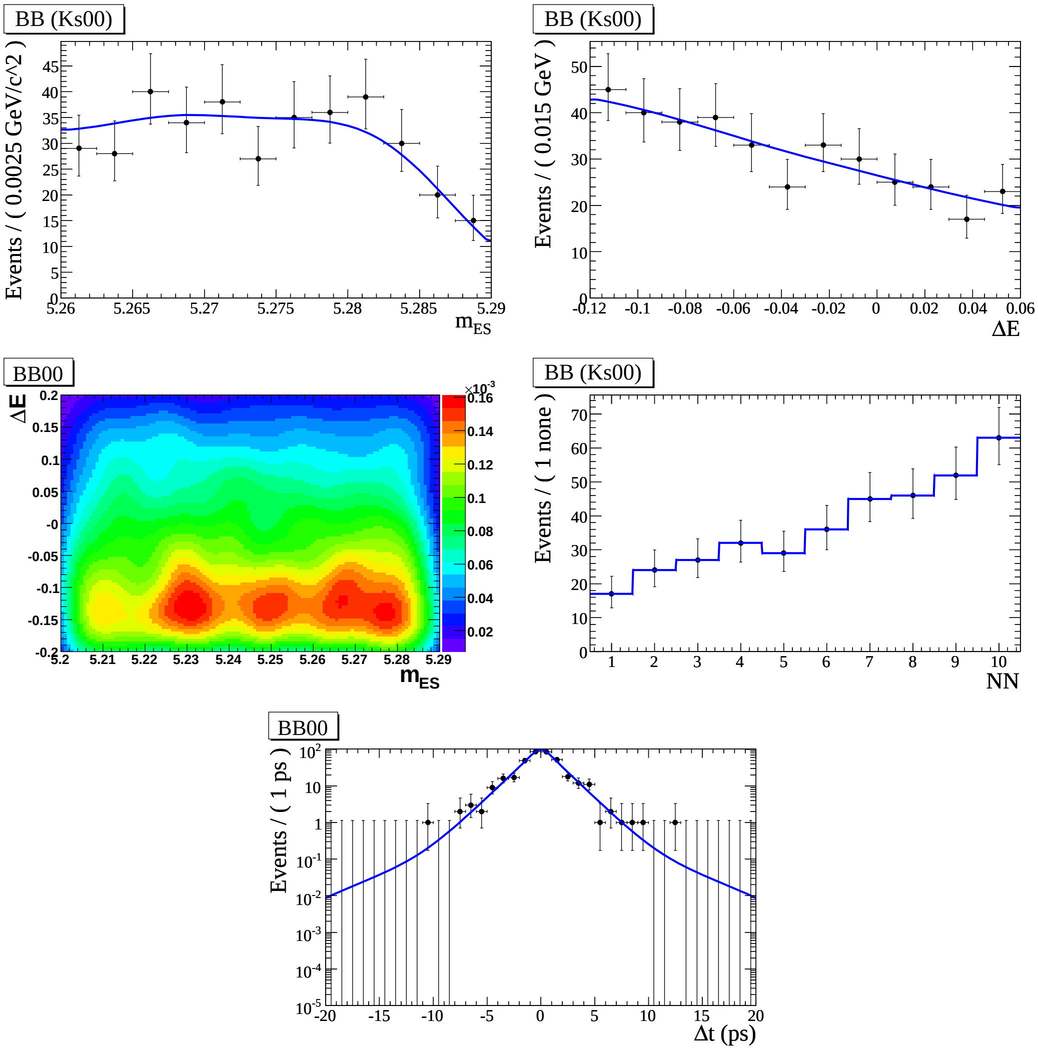

Figure 5.26: $B\overline{B}$ PDF's for $B^0 \to K^+K^-K^0_S$ ($K^0_S \to \pi^0\pi^0$). Top left: m_{ES} projection of the m_{ES}-ΔE PDF, top right: ΔE projection of the m_{ES}-ΔE PDF, middle left: The 2D KEYS function for m_{ES} and ΔE, middle right: NN, bottom: Δt. The PDF's are shown fit to $B\overline{B}$ generic MC. The Δt PDF is plotted on a log scale.

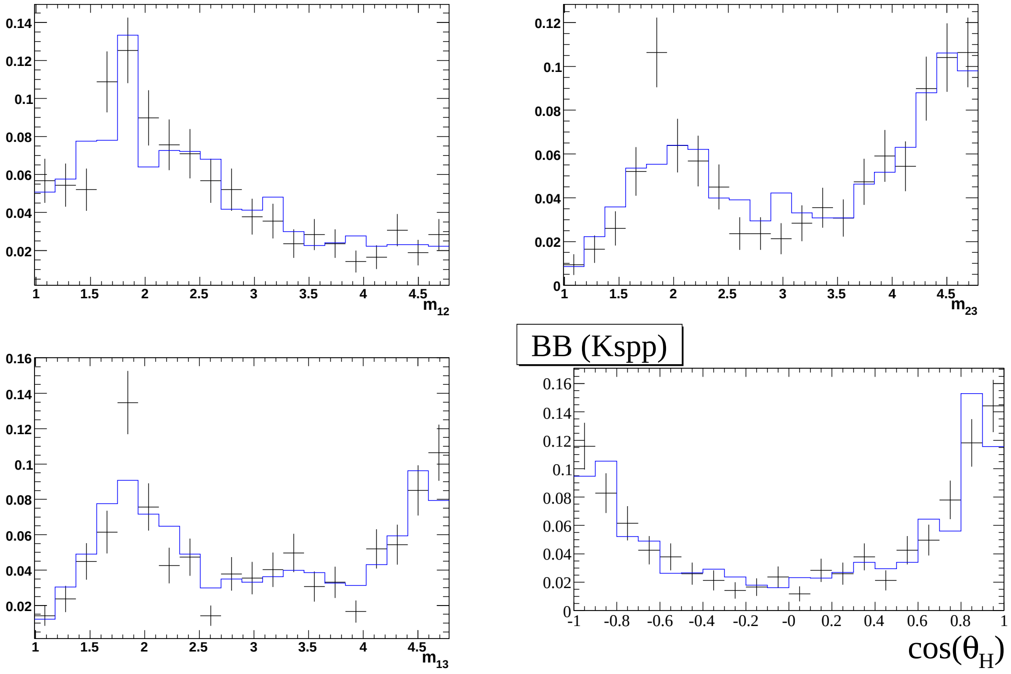

Figure 5.27: Projections of the 2-dimensional $B\overline{B}$ DP PDF (in blue), overlaid with $B\overline{B}$ generic MC events (black points). $K^0_S \to \pi^+\pi^-$ mode. Peaks can be seen from $B^0 \to D^-(K^-K^0_S)\pi^+$ events.

5.28.

The Δt distribution is modeled by the sum of a prompt component and a long-lived exponential decay, which is then convolved with a resolution function:

$$\begin{aligned}\mathcal{P}(\Delta t, \sigma_{\Delta t}, q_{tag}) &= [(1 - f_{prompt})e^{-|\Delta t|/\tau}(1 + q_{tag}S \sin \Delta m_d \Delta t - q_{tag}C \cos \Delta m_d \Delta t) \\ &\quad + f_{prompt}\ \delta(\Delta t)] \otimes \mathcal{R}(\Delta t, \sigma_{\Delta t}) \qquad (5.19)\end{aligned}$$

where the fraction f_{prompt} is split by tagging category. The CP-violating parameters S and C are fixed to zero in the nominal fit, and varied as a systematic. τ is taken to be the B^0 lifetime, 1.53 ps. Mistag rate w and mistag asymmetry Δw are also accounted for (but we have suppressed them in Eq. 5.19 for brevity), and these parameters are split by tagging category and set to be the same as for signal events.

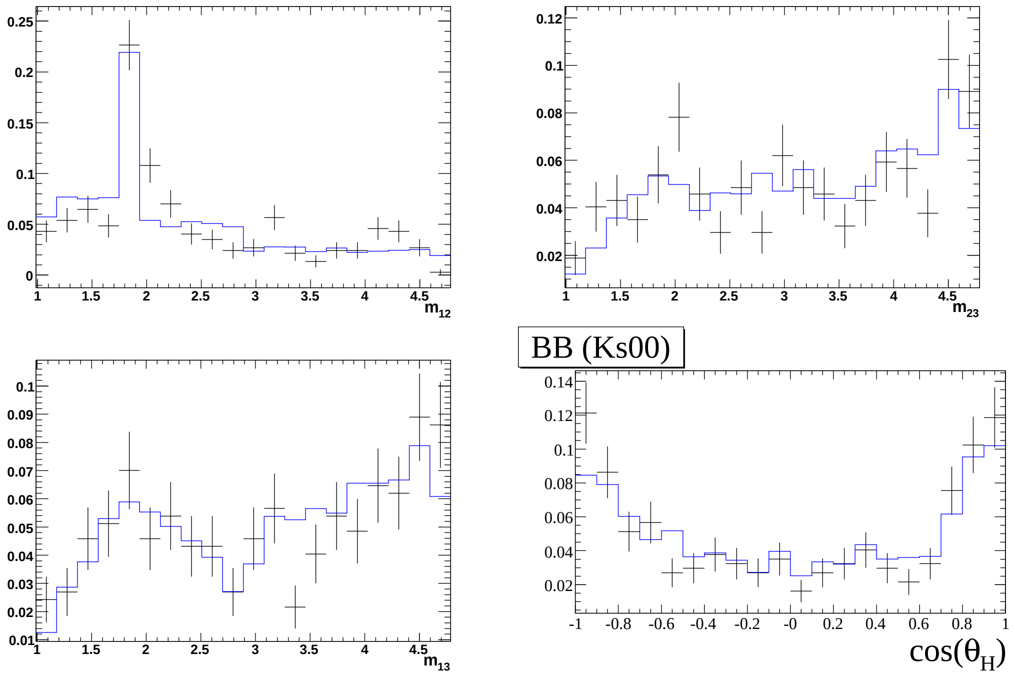

Figure 5.28: Projections of the 2-dimensional $B\overline{B}$ DP PDF (in blue), overlaid with $B\overline{B}$ generic MC events (black points). $K_S^0 \to \pi^0\pi^0$ mode. The peak in the x_{sq} plot is from $B^+ \to D^0\rho^+$ events, with $D^0 \to K^+K^-$ or $D^0 \to K^+\pi^-$.

The resolution function $\mathcal{R}$ has the same double Gaussian form as for continuum events (Eqs. 5.16-5.18). $\mathit{\Sigma}_{out}$ is fixed to 8 ps. The parameters f_{out} and $\mathit{\Sigma}_{core}$ are fixed to the values used in the continuum PDF's. The parameters f_{prompt} and μ_{core} are obtained by fitting to $B\overline{B}$ generic MC in the signal region. The results of these fits are shown in Figs. 5.25 and 5.26.

In addition to the $B\overline{B}$ backgrounds already discussed, we also expect peaking $B\overline{B}$ backgrounds from $b \to c$ decays that have a $K^+K^-K^0_S$ final state. The largest such backgrounds are $B^0 \to D^-(K^-K^0_S)K^+$, $B^0 \to D^-_s(K^-K^0_S)K^+$, $B^0 \to D^0(K^+K^-)K^0_S$, and $B^0 \to J/\psi(K^+K^-)K^0_S$. Unlike in the B^+ modes, where we treated peaking backgrounds as separate $B\overline{B}$ background categories, in $B^0 \to K^+K^-K^0_S$, we find it easier to treat the peaking backgrounds as non-interfering isobars (*i.e.*, signal) in the ML fit. Although formally we treat them as "signal" events, from a physics standpoint we still view them as backgrounds, and we will not consider them as signal when computing values like the inclusive $B^0 \to K^+K^-K^0_S$ branching fraction.

5.5 Fit Validation

Our ML fit procedure is very complex, so it is important that we verify that it works prior to fitting to data. We do this by running a series of pseudoexperiments designed to imitate the actual fit to data. We perform two types of pseudoexperiments: "pure toy" studies and "embedded toy" studies. In pure toys, we generate a number of datasets containing signal, continuum, and $B\overline{B}$ events by randomly sampling the PDF's. We then fit to these "toy" datasets. Pure toys help us study fit stability, whether the fit is biased, and whether the errors on fit parameters are properly estimated. In embedded toys, the continuum events are generated as in the pure toys, but signal events are taken ("embedded") from realistic MC passed through a full detector simulation. $B\overline{B}$ backgrounds are either generated from PDF or embedded from exclusive MC samples. Embedded toys are used to look for biases caused by imperfections in the fit model (e.g., neglecting correlations between variables or imperfectly modeling the DP resolution).

5.5.1 $B^+ \to K^+K^-K^+$

Pure Toy Studies

We generate 500 independent datasets, each toy dataset containing roughly the number of signal and background events that we expect in the Run1-6 dataset. The number of events in each signal and background category is fluctuated according to Poisson statistics.

The signal DP model used is the same as in SP-9688, which is based on the nominal fit result from *BABAR*'s previous Run1-4 analysis. The isobar model contains: $\phi(1020)$, $f_0(980)$, $f_X(1500)$, $f_0(1710)$, χ_{c0}, and NR. The NR component uses an exponential model, as given in Eq. 2.52. The signal is generated with no *CP*-violation. In the fit, we float the NR α parameter as well as the mass (m) and width (Γ) of the $f_X(1500)$. We float the *CP*-conserving and *CP*-violating isobar parameters c, ϕ, b, and δ for each isobar (see Eq. 2.28). We also float the yields for signal, continuum, and most of the $B\overline{B}$ categories. Finally, we float 21 continuum PDF parameters (mostly for the NN) and the means of the signal m_{ES} and ΔE shapes.

We perform a fit to each toy dataset. We only accept fits that converge with a full covariance matrix (covariance quality = 3 as reported by `Minuit`). The results of these toy fits are summarized in Table 5.8. We only show the isobar parameters, the mass and width of the $f_X(1500)$, and the signal yield, since these are the parameters of most interest. For each parameter in the table, we list the value it was generated with, its mean error, and the mean and width of its *pull* distribution. For a given parameter x, the pull of this parameter is defined as:

$$Pull(x) \equiv \frac{x_{fitted} - x_{generated}}{\sigma_x} \tag{5.20}$$

The mean and width of the pull distribution are determined by performing a Gaussian fit to it. For an ideal unbiased fit, the pull distribution of each parameter x should be a Gaussian distribution with mean 0 and width 1.

As can be seen from Table 5.8, none of the DP or *CP* parameters have large biases, with the worst pull having a mean of 0.17. The width of the pull distribution for the

$f_X(1500)$'s RBW width is rather large (1.23). This indicates that the error on this parameter is being underestimated by the fit. We consider this acceptable.

Table 5.8: Pure toy fit results for $B^+ \to K^+K^-K^+$. 425/500 fits converge with good covariance matrix quality.

Parameter	Value	Mean error	Pull mean	Pull width
$b[\ \chi_{c0}\ ]$	0	0.0549	0.09	0.92
$c[\ \chi_{c0}\ ]$	0.437	0.0389	-0.03	0.95
$\delta[\ \chi_{c0}\ ]$	0	0.1300	0.11	0.92
$\phi[\ \chi_{c0}\ ]$	-1.02	0.1430	0.05	0.95
$b[\ f_X(1500)\ ]$	0	0.0209	0.07	1.00
$c[\ f_X(1500)\ ]$	8.22	0.5954	-0.14	1.11
$\delta[\ f_X(1500)\ ]$	0	0.0443	0.06	0.95
$\phi[\ f_X(1500)\ ]$	1.29	0.0563	0.02	1.11
$\Gamma[\ f_X(1500)\ ]$	0.257	0.0180	-0.10	1.23
$m[\ f_X(1500)\ ]$	1.539	0.0101	-0.01	1.03
$b[\ f_0(1710)\ ]$	0	0.1364	0.10	0.95
$c[\ f_0(1710)\ ]$	1.24	0.1807	0.17	0.98
$\delta[\ f_0(1710)\ ]$	0	0.1157	0.05	0.99
$\phi[\ f_0(1710)\ ]$	-0.59	0.1548	0.12	1.07
$b[\ f_0(980)\ ]$	0	0.1044	-0.03	0.94
$c[\ f_0(980)\ ]$	5.28	0.4679	-0.01	1.10
$\delta[\ f_0(980)\ ]$	0	0.0496	-0.03	0.94
$\phi[\ f_0(980)\ ]$	0.48	0.0910	0.11	1.06
$b[$ NR $]$	0	0.0286	0.02	0.99
$\alpha[$ NR $]$	-0.152	0.008	-0.05	0.91
$b[\ \phi(1020)\ ]$	0	0.0235	-0.12	1.02
$c[\ \phi(1020)\ ]$	0.117	0.009	-0.12	0.96
$\delta[\ \phi(1020)\ ]$	0	0.0929	-0.05	0.98
$\phi[\ \phi(1020)\ ]$	-0.15	0.1153	-0.10	1.07
N(signal)	5300	85.2646	0.02	1.00

Embedded Toy Studies

In addition to pure toy studies, we also perform so-called "embedded toys." In these studies, we generate continuum and "BB charm 4" background events from the PDF, just like for the pure toy studies, but the signal events and other $B\overline{B}$ categories are taken from SP Monte Carlo samples. The signal events are taken from SP-9688, and the embedded $B\overline{B}$ events are taken from the exclusive $B\overline{B}$ cocktails described in Sec. 5.4. We have enough signal MC events to create 272 embedded toy datasets. We do not have enough MC events for all of the different $B\overline{B}$ SP modes, so some of the $B\overline{B}$ SP events are re-used among the toy datasets. No Poisson fluctuation is used when creating these datasets.

We also do similar fits to these datasets, but floating the NR α parameter and the RBW mass and width of the $f_X(1500)$. These fits are summarized in Table 5.9, only listing the DP and *CP* parameters, for the sake of brevity. As can be seen, the pulls for the DP and *CP* parameters are worse in the embedded toys than in the pure toys, but we consider these pulls acceptable. The biases in embedded toys will eventually be treated as systematic errors when we report our final result.

5.5.2 $B^+ \to K^0_S K^0_S K^+$

Pure Toy Studies

We generate 500 independent datasets, with Poisson fluctuations for the yields. Since we are doing the first ever DP analysis of $B^+ \to K^0_S K^0_S K^+$, we cannot rely on previous isobar models of this mode. Instead, we adapt our isobar model from BABAR's preliminary Run1-6 $B^0 \to K^+K^-K^0_S$ result [43]. It contains the $f_0(980)$, $f_X(1500)$, χ_{c0}, and an exponential NR model like that in Eq. 2.55, but symmetrized under exchange of the two K^0_S. The $NR(K^+K^0_S)$ term (*i.e.*, the $(e^{\alpha s_{13}} + e^{\alpha s_{23}})$ term) was guessed by averaging the isobar coefficients of the $NR(K^+K^0_S)$ and $NR(K^-K^0_S)$ terms in $B^0 \to K^+K^-K^0_S$. This is the same model as used in SP-10338 signal MC.

We perform a fit to each toy dataset. The number of signal events in this mode is small ($\sim$ 600), so, in order to reduce the number of parameters in the fit, we constrain the *CP*-violating parameters (b and δ) of all the charmless isobars to be the same. However, we allow for the χ_{c0} to have separate *CP*-violating parameters, since it comes from a $b \to c$ transition. We did studies that showed that if we attempted to measure separate *CP*-violating parameters for the different isobars, the errors on these

Table 5.9: Embedded toy fit results for $B^+ \to K^+K^-K^+$. 233/272 fits converge with good covariance matrix quality.

Parameter	Value	Mean error	Pull mean	Pull width
$b[\ \chi_{c0}\ ]$	0	0.0556	0.15	1.01
$c[\ \chi_{c0}\ ]$	0.437	0.0379	-0.21	0.95
$\delta[\ \chi_{c0}\ ]$	0	0.1270	0.03	1.03
$\phi[\ \chi_{c0}\ ]$	-1.02	0.1389	-0.05	0.98
$b[\ f_X(1500)\ ]$	0	0.0212	0.14	0.97
$c[\ f_X(1500)\ ]$	8.22	0.5744	-0.09	1.13
$\delta[\ f_X(1500)\ ]$	0	0.0442	0.04	0.98
$\phi[\ f_X(1500)\ ]$	1.29	0.0560	-0.18	1.23
$\Gamma[\ f_X(1500)\ ]$	0.257	0.0179	-0.07	1.35
$m[\ f_X(1500)\ ]$	1.539	0.0102	0.13	1.01
$b[\ f_0(1710)\ ]$	0	0.1348	-0.01	0.93
$c[\ f_0(1710)\ ]$	1.24	0.1804	0.28	0.96
$\delta[\ f_0(1710)\ ]$	0	0.1175	0.04	0.99
$\phi[\ f_0(1710)\ ]$	-0.59	0.1562	-0.30	1.13
$b[\ f_0(980)\ ]$	0	0.0986	0.04	0.90
$c[\ f_0(980)\ ]$	5.28	0.4591	0.30	1.01
$\delta[\ f_0(980)\ ]$	0	0.0478	-0.05	0.91
$\phi[\ f_0(980)\ ]$	0.48	0.0884	0.06	1.16
$b[$ NR $]$	0	0.0276	0.16	0.92
$\alpha[$ NR $]$	-0.152	0.007	0.34	0.99
$b[\ \phi(1020)\ ]$	0	0.0230	0.02	0.98
$c[\ \phi(1020)\ ]$	0.117	0.009	0.05	1.03
$\delta[\ \phi(1020)\ ]$	0	0.0909	-0.00	1.00
$\phi[\ \phi(1020)\ ]$	-0.15	0.1134	-0.02	1.06

parameters would be very large. In addition to floating the isobar parameters, we float the yields for signal and continuum. We also float 21 continuum PDF parameters (mostly for the NN) and the means of the signal $m_{\rm ES}$ and ΔE shapes.

The fits are summarized in Table 5.10. There are no large biases on the *CP*-violating parameters. The isobar magnitude of the $NR(K^+K^0_S)$ term has a mean pull of ~ 0.5. However, this term was generated with a magnitude very close to zero, making it difficult to fit. We confirmed that generating toy with a larger magnitude for the $NR(K^+K^0_S)$ term eliminated the bias problem.

Table 5.10: Pure toy fit results for $B^+ \to K^0_S K^0_S K^+$. One set of *CP*-violating parameters for χ_{c0}, one set for all other isobars. 443/500 fits converge with good covariance matrix quality.

Parameter	Value	Mean error	Pull mean	Pull width
$b[\ \chi_{c0}\ ]$	0	0.1552	-0.08	0.86
$c[\ \chi_{c0}\ ]$	0.0298	0.006	-0.29	0.87
$\delta[\ \chi_{c0}\ ]$	0	0.6615	-0.05	0.98
$\phi[\ \chi_{c0}\ ]$	0.73	0.7957	-0.06	0.75
$c[\ f_X(1500)\ ]$	0.141	0.0216	-0.00	0.92
$\phi[\ f_X(1500)\ ]$	-0.37	0.1870	0.09	0.92
$c[\ f_0(980)\ ]$	0.542	0.0532	-0.06	0.93
$\phi[\ f_0(980)\ ]$	-0.2	0.1940	0.23	0.95
$c[\ \mathrm{NR}(K^+K^0_S)\ ]$	0.0227	0.0436	0.49	1.11
$\phi[\ \mathrm{NR}(K^+K^0_S)\ ]$	-2.36	2.0130	0.00	1.15
$b[\ \mathrm{NR}(K^0_S K^0_S)\ ]$	0	0.0237	-0.02	0.98

Embedded Toy Studies

In these embedded toy studies, we generate continuum and "BB 3" background events from the PDF's, but the signal events and other $B\overline{B}$ categories are taken from MC samples. The signal events are taken from SP-10338, and the embedded $B\overline{B}$ events are taken from the exclusive $B\overline{B}$ cocktails described in Sec. 5.4. We create 500 embedded toy datasets. We have sufficient signal MC events so that we do not need to re-use any of them among the different toy datasets. However, we do not have enough MC events for all of the different $B\overline{B}$ SP modes, so some of the $B\overline{B}$ SP events are re-used among the toy datasets. The datasets are generated without Poisson fluctuation.

The embedded toy fits are summarized in Table 5.11. There is a pull of ~ 0.2 on the b that is shared by all the charmless isobars. However, the error on this parameter is quite small, so the actual magnitude of the bias is not very large. We can tolerate this as a systematic. We also see some biases in the magnitude of the χ_{c0} and the phase of the $f_0(980)$. These biases were already present, to a lesser extent, in pure toy, and we consider them acceptable.

Table 5.11: Embedded toy fit results for $B^+ \to K^0_S K^0_S K^+$. One set of *CP* parameters for χ_{c0}, one set for all other isobars. 434/500 fits converge with good covariance matrix quality.

Parameter	Value	Mean error	Pull mean	Pull width
$b[\ \chi_{c0}\ ]$	0	0.1543	-0.00	0.86
$c[\ \chi_{c0}\ ]$	0.0298	0.005	-0.41	0.90
$\delta[\ \chi_{c0}\ ]$	0	0.6597	-0.03	0.97
$\phi[\ \chi_{c0}\ ]$	0.73	0.7728	-0.17	0.75
$c[\ f_X(1500)\ ]$	0.141	0.0210	-0.03	0.98
$\phi[\ f_X(1500)\ ]$	-0.37	0.1839	0.11	0.96
$c[\ f_0(980)\ ]$	0.542	0.0510	-0.05	0.95
$\phi[\ f_0(980)\ ]$	-0.2	0.1790	0.38	0.90
$c[\ \mathrm{NR}(K^+K^0_S)\ ]$	0.0227	0.0405	0.46	1.18
$\phi[\ \mathrm{NR}(K^+K^0_S)\ ]$	-2.36	1.8150	-0.03	1.20
$b[\ \mathrm{NR}(K^0_S K^0_S)\ ]$	0	0.0237	0.23	0.99

5.5.3 $B^0 \to K^+K^-K^0_S$

Pure Toy Studies

We generate 500 independent datasets with Poisson fluctuations. The signal DP model used is taken from BABAR's preliminary Run1-6 $B^0 \to K^+K^-K^0_S$ result [43]. It contains the $\phi(1020)$, $f_0(980)$, $f_X(1500)$, χ_{c0}, and an exponential NR model like that in Eq. 2.55. The signal events are generated with *CP*-violating parameters equal to the SM ($b = 0$, $\delta = 0$). We do not include peaking $B\overline{B}$ backgrounds from D^0 or J/ψ, since they were not included in [43].

We perform a fit to each toy dataset. We float three sets of *CP*-violating isobar parameters: for the $\phi(1020)$, the $f_0(980)$, and for everything else except the χ_{c0}. The *CP*-violation of the χ_{c0} is fixed to the SM ($b = \delta = 0$). We also float, separately for $K^0_S \to \pi^+\pi^-$ and $K^0_S \to \pi^0\pi^0$, yields for signal, continuum (split by tagging category), and $B\overline{B}$. We float 18 continuum NN parameters for both $K^0_S \to \pi^+\pi^-$ and $K^0_S \to \pi^0\pi^0$, and we float the means of the signal m_{ES} and ΔE shapes for $K^0_S \to \pi^+\pi^-$ only.

The results of these toy fits are summarized in Table 5.12. As can be seen from the table, none of the parameters have large biases.

Embedded Toy Studies

In these studies, we generate continuum and generic $B\overline{B}$ background events from the PDF, but the signal events are taken from MC samples (SP-7930 for $K^0_S \to \pi^+\pi^-$ and SP-7931 for $K^0_S \to \pi^0\pi^0$). We also take the peaking $B\overline{B}$ backgrounds $B^0 \to D^-(K^-K^0_S)K^+$ and $B^0 \to D^-_s(K^-K^0_S)K^+$ from exclusive MC samples (SP-6858 and SP-3089, respectively). We create 500 embedded toy datasets. No Poisson fluctuation is used when creating these datasets.

We perform a fit to each toy dataset. Just like in the pure toy case, we float three separate sets of *CP*-violating isobar parameters. These fits are summarized in Table 5.13. The *CP*-violating parameters all have negligibly small biases. Some of the *CP*-conserving isobar parameters have significant biases, but we will tolerate these, and treat them as systematic errors. We are regarding the D^- and D^-_s contributions as $B\overline{B}$ backgrounds rather than signal, so we will not worry about the large biases on their isobar parameters.

Table 5.12: Pure toy fit results for $B^0 \rightarrow K^+K^-K^0_S$. 490/500 fits converge with good covariance matrix quality.

Parameter	Value	Mean error	Pull mean	Pull width
$b[\ f_0(980)\ ]$	0	0.1081	0.00	1.02
$\delta[\ f_0(980)\ ]$	0	0.1072	-0.01	1.00
$b[$ Other $]$	0	0.0623	0.01	0.99
$\delta[$ Other $]$	0	0.0858	-0.04	1.02
$b[\ \phi(1020)\ ]$	0	0.0828	0.01	0.94
$\delta[\ \phi(1020)\ ]$	0	0.1065	-0.07	1.02
$c[\ \chi_{c0}\ ]$	0.0306	0.005	-0.26	0.97
$\phi[\ \chi_{c0}\ ]$	0.81	0.5753	-0.16	1.04
$c[\ f_X(1500)\ ]$	0.114	0.0169	0.10	0.97
$\phi[\ f_X(1500)\ ]$	-0.47	0.1785	0.08	0.97
$c[\ f_0(980)\ ]$	0.622	0.0421	-0.04	0.94
$\phi[\ f_0(980)\ ]$	-0.14	0.1298	0.05	0.88
$c[\ \mathrm{NR}(K^-K^0_S)\ ]$	0.31	0.0670	-0.03	0.93
$\phi[\ \mathrm{NR}(K^-K^0_S)\ ]$	-1.34	0.2951	-0.12	1.01
$c[\ \mathrm{NR}(K^+K^0_S)\ ]$	0.33	0.0561	-0.08	0.99
$\phi[\ \mathrm{NR}(K^+K^0_S)\ ]$	1.95	0.2396	0.01	0.94
$c[\ \phi(1020)\ ]$	0.0085	0.0009	-0.07	0.88
$\phi[\ \phi(1020)\ ]$	-0.02	0.2095	-0.08	0.99
$c[\ D^-\ ]$	1.96	0.2415	0.07	0.91
$c[\ D^-_s\ ]$	1.57	0.2092	0.07	0.94
$N(\text{signal}),\ K^0_S \rightarrow \pi^+\pi^-$	1415	43.9360	0.08	0.94
$N(\text{signal}),\ K^0_S \rightarrow \pi^0\pi^0$	147	17.2289	0.08	1.02

Table 5.13: Embedded toy fit results for $B^0 \to K^+K^-K^0_S$. 493/500 fits converge with good covariance matrix quality.

Parameter	Value	Mean error	Pull mean	Pull width
b[$f_0(980)$]	0	0.1105	-0.04	0.97
δ[$f_0(980)$]	0	0.1097	-0.08	1.02
b[Other]	0	0.0619	-0.00	1.00
δ[Other]	0	0.0854	-0.07	1.04
b[$\phi(1020)$]	0	0.0845	-0.01	0.96
δ[$\phi(1020)$]	0	0.1097	-0.02	0.93
c[χ_{c0}]	0.0306	0.005	-0.15	0.99
ϕ[χ_{c0}]	0.81	0.5693	-0.11	1.24
c[$f_X(1500)$]	0.114	0.0170	0.05	1.03
ϕ[$f_X(1500)$]	-0.47	0.1792	0.06	0.97
c[$f_0(980)$]	0.622	0.0423	-0.37	0.95
ϕ[$f_0(980)$]	-0.14	0.1306	0.01	0.91
c[NR($K^-K^0_S$)]	0.31	0.0670	0.25	1.00
ϕ[NR($K^-K^0_S$)]	-1.34	0.2820	-0.52	1.09
c[NR($K^+K^0_S$)]	0.33	0.0591	-0.36	1.01
ϕ[NR($K^+K^0_S$)]	1.95	0.2573	-0.30	1.00
c[$\phi(1020)$]	0.0085	0.0009	-0.21	0.97
ϕ[$\phi(1020)$]	-0.02	0.2160	-0.23	0.98
c[D^-]	1.96	0.2221	-1.58	0.90
c[D^-_s]	1.57	0.2028	-0.49	0.75
N(signal), $K^0_S \to \pi^+\pi^-$	1415	43.8441	-0.32	0.54
N(signal), $K^0_S \to \pi^0\pi^0$	147	16.9600	-0.43	0.74

Chapter 6

Determination of Dalitz Model

Before fitting the *CP*-violating parameters in data, we would like to settle on a nominal isobar model. So far, we have been using the isobar model from the previous *BABAR* analyses (or in the case of $B^+ \to K_S^0 K_S^0 K^+$, a reasonable guess at an isobar model). Now we want to test various isobar models on the data, and see if we can find an improvement over our current models. We do this in a "*CP*-blind" fashion, which means that for now we will fix the *CP*-violating parameters to zero (or in the case of $B^0 \to K^+ K^- K_S^0$, we fix $\delta = 0$, which means $\beta_{\text{eff}} = \beta_{SM}$). Only after we've settled on a nominal isobar model will we fit for the *CP*-violating observables.

Our main interest in these studies will be to understand the $f_X(1500)$ and the nonresonant decays better. In particular, we would like to know their spin, as this affects the time-dependent *CP*-asymmetry in $B^0 \to K^+ K^- K_S^0$. Our two main tools in this chapter will be the likelihood $\mathcal{L}$ and the *angular moments*. Since we are performing maximum-likelihood fits, it is clear that one way to judge how good a particular model is, will be to look at its $\mathcal{L}$. The angular moments, meanwhile, are a way of visualizing the goodness of fit of a DP model. Invariant-mass projections are an obvious way of seeing how well a particular DP model describes the data, but they turn out not to be that powerful, especially in determining the spin of resonances. Angular moments are a method of projecting out different features of the 2-dimensional DP distribution, thus providing a powerful tool for studying the partial-waves present.

In Sec. 6.1, we will go over the angular moments formalism. Then in the rest of this chapter we will present *CP*-blind fits to data using various isobar models, and on the basis of those studies we will decide what isobar model to use for our nominal fits.

6.1 Angular Moments

Consider the decay $B \to K_1K_2K_3$, where for the time being we will assume that the 3 K are distinguishable particles. Later, we will consider the effects that identical K have on the analysis.

Write the decay amplitude $\mathcal{A}(B \to K_1K_2K_3)$ as a function of m_{12} and $\cos\theta_3$, where $\cos\theta_3$ is the angle between K_3 and K_1, measured in the rest frame of K_1K_2 (as we defined in Sec. 2.5.4). Then, the $\cos\theta_3$ dependence of $\mathcal{A}(B \to K_1K_2K_3) = \mathcal{A}(m_{12}, \cos\theta_3)$ can be expanded in terms of Legendre polynomials, $P_l(\cos\theta_3)$:

$$\mathcal{A}(m_{12}, \cos\theta_3) = \sum_l \mathcal{A}_l(m_{12}) P_l(\cos\theta_3) \tag{6.1}$$

The amplitude $\mathcal{A}_l(m_{12})$ then represents the relative weight of the l-th partial-wave. For example, a spin-J (K_1K_2) resonance would contribute a non-zero $\mathcal{A}_J(m_{12})$, and would not contribute at all to the other F_l's. We can then calculate information about the $\mathcal{A}_J$ by calculating the *angular moments*, $\langle P_l(\cos\theta_3)\rangle$, defined as:

$$\langle P_l(\cos\theta_3)\rangle = \int_{-1}^{1} |\mathcal{A}(m_{12}, \cos\theta_3)|^2 P_l(\cos\theta_3) d\cos\theta_3 \tag{6.2}$$

Note that the angular moments are functions of m_{12}, but we will suppress this dependence in our notation.

In order to simplify the analysis, we will assume from now on that only $\mathcal{A}_0$, $\mathcal{A}_1$, and $\mathcal{A}_2$ are important, so that higher-order partial waves can be neglected. Under this assumption, we can write the expansion in Eq. 6.1 as:

$$\mathcal{A}(m_{12}, \cos\theta_3) \quad = \quad \mathcal{A}_S(m_{12}) P_0(\cos\theta_3) + \mathcal{A}_P(m_{12}) e^{i\phi_P(m_{12})} P_1(\cos\theta_3) +$$

$$\mathcal{A}_D(m_{12})e^{i\phi_D(m_{12})}P_2(\cos\theta_3)\,, \tag{6.3}$$

where the partial-wave complex amplitudes have been now explicitly decomposed into magnitudes and phases. $\mathcal{A}_S$, $\mathcal{A}_P$, and $\mathcal{A}_D$ are real-valued functions, and ϕ_P and ϕ_D are phases (the phase ϕ_S can freely be factored out without having any effect on $|\mathcal{A}|^2$).

Substituting Eq. 6.3 into Eq. 6.2, and making use of the orthonormality relation

$$\int_{-1}^{1} P_l(\cos\theta_3)P_k(\cos\theta_3)d\cos\theta_3 = \delta_{lk}\,, \tag{6.4}$$

we can calculate the angular moments:

$$\begin{aligned}
\langle P_0\rangle &= \frac{\mathcal{A}_S^2+\mathcal{A}_P^2+\mathcal{A}_D^2}{\sqrt{2}} \\
\langle P_1\rangle &= \sqrt{2}\mathcal{A}_S\mathcal{A}_P\cos\phi_P + \frac{2\sqrt{10}}{5}\mathcal{A}_P\mathcal{A}_D\cos\left(\phi_P-\phi_D\right) \\
\langle P_2\rangle &= \sqrt{\frac{2}{5}}\mathcal{A}_P^2 + \frac{\sqrt{10}}{7}\mathcal{A}_D^2 + \sqrt{2}\mathcal{A}_S\mathcal{A}_D\cos\phi_D \\
\langle P_3\rangle &= \frac{3}{5}\sqrt{\frac{30}{7}}\mathcal{A}_P\mathcal{A}_D\cos\left(\phi_P-\phi_D\right) \\
\langle P_4\rangle &= \frac{\sqrt{18}}{7}\mathcal{A}_D^2\,.
\end{aligned} \tag{6.5}$$

The moments that are higher-order than $\langle P_4\rangle$ are zero if there are no higher-order partial waves than D-wave. However, this is no longer valid if the effects of symmetrization in $B^+ \to K^+K^-K^+$ are taken into account, as explained in the next section.

Effect of Symmetrization on $B^+ \to K^+K^-K^+$ Angular Moments

Because the overall $B^+ \to K^+K^-K^+$ amplitude must be symmetrized under $\{1 \leftrightarrow 3\}$ exchange, this complicates the angular moments. For example, if the unsymmetrized amplitude has the form in Eq. 6.3, then a symmetric piece would have to be added with m_{12} replaced by m_{23}, and $\cos\theta_3$ replaced by $\cos\theta_1$. In principle, that symmetric piece could be re-written in terms of the DP variables m_{12} and $\cos\theta_3$, so that the symmetric piece could be brought into the form in Eq. 6.1, but these "reflected" amplitudes could contain higher-order terms than D-wave. Also, note that because of the definition $m_{12} < m_{23}$, this ends up causing further distortions, since this ends up translating into a restriction on the possible values of $\cos\theta_3$ for a given value of m_{12}, so that the integral of $\cos\theta_3$ does not necessarily extend from -1 to 1. All of this leads to the result that Eq. 6.5 does not directly apply. Still, angular moments can be calculated for data, and compared with predictions for a given DP model, and discrepancies can be noted.

As an illustration of what angular moments look like, we generate toy signal events for a single resonance with $m = 1.5\,\mathrm{GeV}/c^2$ and $\Gamma = 0.2\,\mathrm{GeV}$. Figs. 6.1, 6.2, and 6.3, show the angular moments for the case that this resonance has spin 0, 1, and 2, respectively. These figures can be understood by looking back at Eq. 6.5. There is a large peak in the 2nd-order moment for the spin-1 and spin-2 cases, and there is a large peak in the 4th-order moment only for the spin-2 case. The odd-moments are much smaller than the even moments, because the odd moments only arise due to interference between different partial waves. If there were no symmetrization effects, then the odd-moments would be identically zero, because there is only a single resonance. However, the odd-moments get non-zero values due to the two pieces of the symmetrized amplitude interfering with one another. Similarly the fifth-order and sixth-order moments are non-zero due to symmetrization.

Effect of Symmetrization on $B^+ \to K^0_S K^0_S K^+$ Angular Moments

Because of the identical K^0_S, the $B^+ \to K^0_S K^0_S K^+$ amplitude must be symmetric under $\{1 \leftrightarrow 2\}$ exchange. This in turn means the $B^+ \to K^0_S K^0_S K^+$ amplitude must be an even function of $\cos\theta_3$. This means no P-wave terms can be present, and that the odd angular moments ($\langle P_1 \rangle$, $\langle P_3 \rangle$, etc.) are automatically zero.

$B^0 \to K^+ K^- K^0_S$ Angular Moments

The $B^0 \to K^+ K^- K^0_S$ angular moments are complicated by the sign-flip for odd-L amplitudes, mentioned in Eq. 2.26. This causes the odd angular moments to flip sign

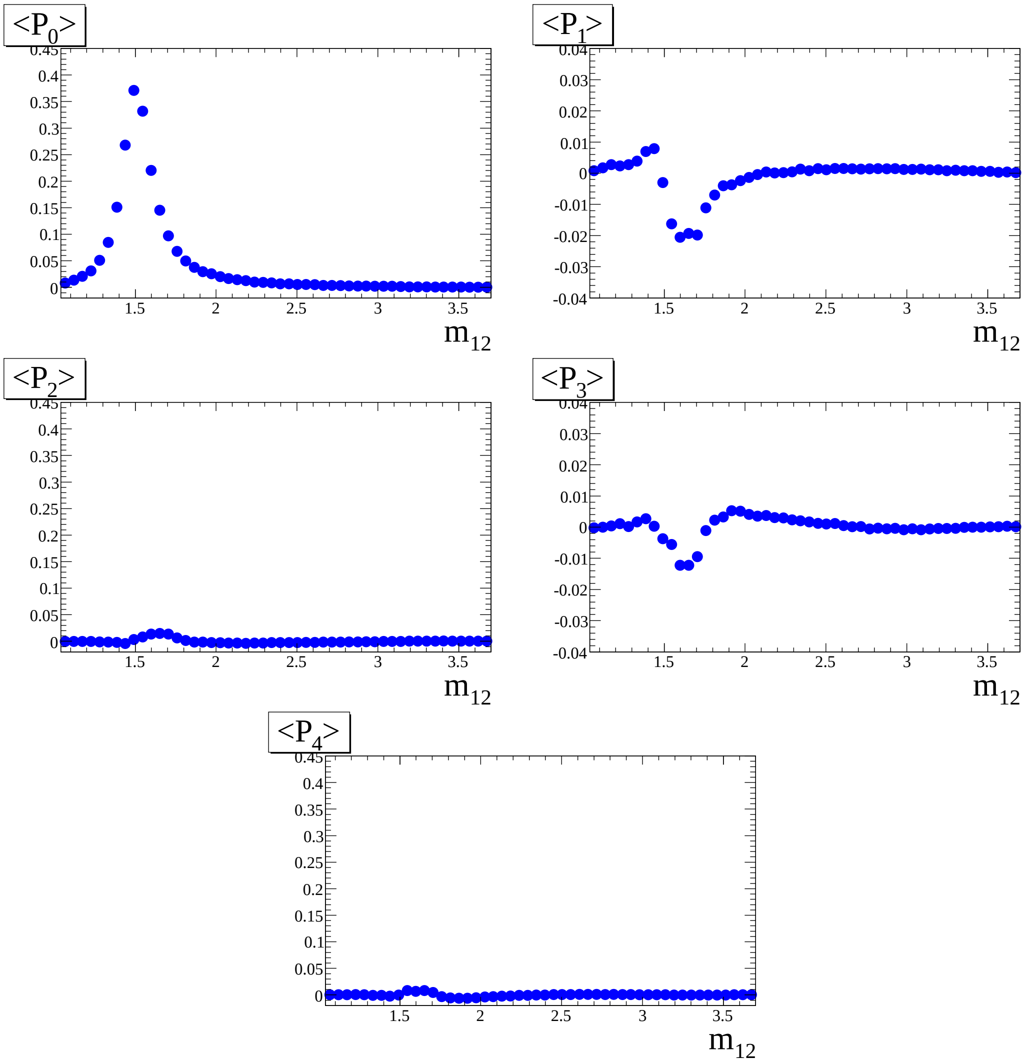

Figure 6.1: Angular moments plots for $B^+ \to K^+K^-K^+$ toy events generated for a single spin-0 resonance with $m = 1.5\,\mathrm{GeV}/c^2$ and $\Gamma = 0.2\,\mathrm{GeV}$.

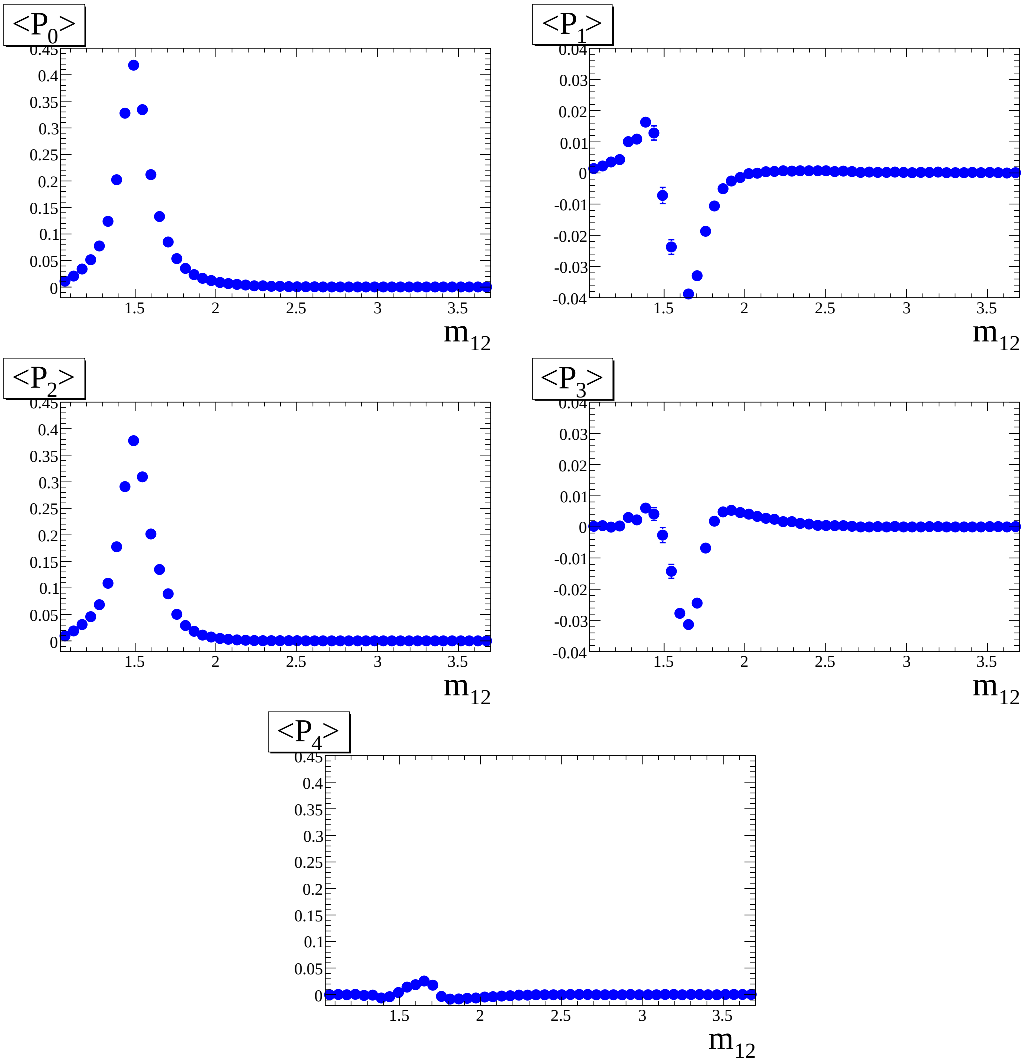

Figure 6.2: Angular moments plots for $B^+ \to K^+K^-K^+$ toy events generated for a single spin-1 resonance with $m = 1.5\,\mathrm{GeV}/c^2$ and $\Gamma = 0.2\,\mathrm{GeV}$.

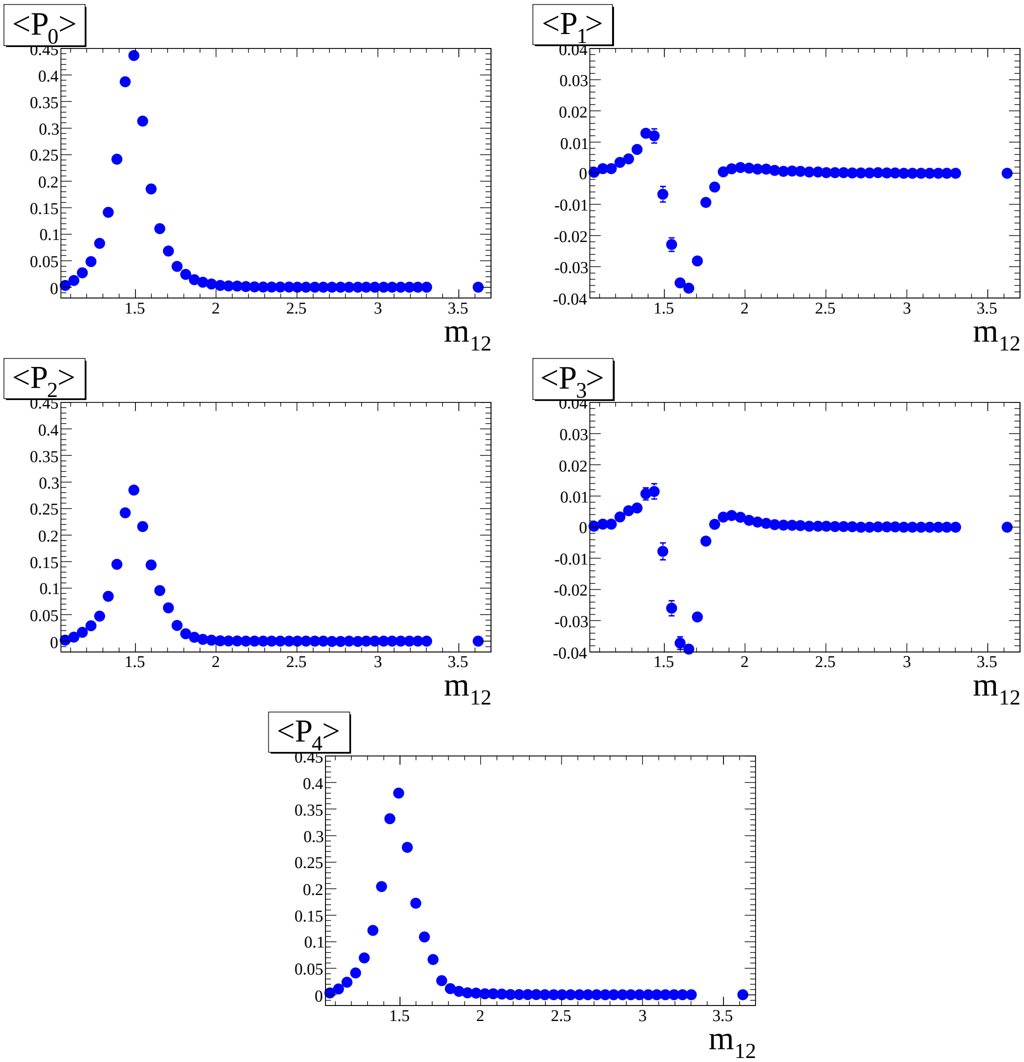

Figure 6.3: Angular moments plots for $B^+ \to K^+K^-K^+$ toy events generated for a single spin-2 resonance with $m = 1.5\,\mathrm{GeV}/c^2$ and $\Gamma = 0.2\,\mathrm{GeV}$.

depending on the tag flavor q_{tag}. By integrating Eq. 2.21 over Δt, it can be shown that the odd angular moments are proportional to $-q_{tag}(1-2w)/((\Delta m_d \tau)^2+1)$. The $(1-2w)$ factor is a dilution due to mistagging, and the $1/((\Delta m_d \tau)^2+1)$ factor is a dilution due to $B^0-\overline{B}^0$ mixing.

Because of the proportionality to q_{tag}, the odd angular moments would integrate to zero if we were to simply integrate over q_{tag} (at least, in the absence of direct *CP* violation). So, what we decide to do is multiply ($q_{tag}=+1$) events by -1 when calculating odd angular moments:

$$\langle P_l(\cos\theta_3)\rangle \equiv (-1)^l \langle P_l(\cos\theta_3)\rangle\,(q_{tag}=+1) + \langle P_l(\cos\theta_3)\rangle\,(q_{tag}=-1)\,. \tag{6.6}$$

With this convention in place, Eq. 6.5 applies to $B^0 \to K^+K^-K^0_S$, except that the odd moments get multiplied by $(1-2w)/((\Delta m_d \tau)^2+1)$.

6.2 $B^+ \to K^+K^-K^+$ Fits

6.2.1 Fit with Initial DP Model

We perform ML fits using the same isobar model used in BABAR's previous analysis [24]. The NR α parameter and the mass and width of the $f_X(1500)$ are floated in the fit. Maximizing the likelihood is equivalent to minimizing $-\log\mathcal{L}$ (NLL). In DP analyses, it is typical for the NLL function to have multiple local minima, due to the many interfering isobars. We will discuss these multiple solutions in detail when we report the final fit results (Chap. 7), but in this chapter, we will only refer to the best solution (global minimum). To make sure the true best solution is found, we perform 500 fits with the same model, randomizing the starting values for the isobar parameters in each fit. We will refer to this procedure as "performing randomized fits." The best solution found is shown in Table 6.1. This solution is consistent with BABAR's previous result. We will call this "Model A."

Table 6.1: Isobar magnitudes and phases from a CP-blind fit to $B^+ \to K^+K^-K^+$ data, using "Model A," floating the NR α and the mass and width of the $f_X(1500)$. The errors are statistical only.

Decay	Magnitude c_r	Phase ϕ_r (rad.)	Fraction $\mathcal{F}_r$ (%)
$\phi(1020)$	0.0100 ± 0.0006	-0.20 ± 0.12	12.9 ± 1.0
$f_0(980)$	0.4034 ± 0.0369	0.33 ± 0.09	15.8 ± 3.3
$f_X(1500)$	0.4930 ± 0.0386	1.41 ± 0.05	81 ± 7
$f_0(1710)$	0.0468 ± 0.0120	0.16 ± 0.27	1.1 ± 0.5
χ_{c0}	0.0321 ± 0.0029	-0.74 ± 0.21	2.48 ± 0.37
NR	1.0 (fixed)	0.0 (fixed)	123 ± 13
$f_X(1500)$ Mass	1543.1 ± 11.1		
$f_X(1500)$ Width	204.2 ± 15.5		
NR α	-0.149 ± 0.006		
N(BBcharm1)	169.2 ± 20.7		
N(BBcharm2)	22.1 ± 9.3		
N(BBcharm3)	131.8 ± 33.2		
N(BBcharm4)	238.9 ± 54.1		
N(BBcharm5)	230.5 ± 21.7		
N(BBcharm6)	44.4 ± 9.8		
N(cont)	6001.5 ± 91.0		
N(signal)	5316.9 ± 84.4		
NLL	-135990.2		

${}_s\mathcal{P}lot$s

We form ${}_s\mathcal{P}lot$s [44] for the signal and background categories. These plots use the fit result to weight each event by the probability that it belongs to a particular signal or background category. This allows us to see how well our PDF's match the observed distributions in data. The ${}_s\mathcal{P}lot$s for m_{ES}, ΔE, and NN are shown in Figs. 6.4, 6.5, and 6.6, respectively. [1]

---

[1] The basic idea behind an ${}_s\mathcal{P}lot$ is that the PDF variables that are *not* being plotted are used to discriminate between the various signal and background categories. However, this relies on the plotted variable being uncorrelated with the discriminating variables. So, when making the NN ${}_s\mathcal{P}lot$s, we do not use the DP variables as discriminating variables, because the continuum NN PDF is correlated with the DP. Without the DP, the signal and peaking backgrounds cannot be distinguished, so they are combined in these plots. Also, without the DP, it is more difficult to separate continuum and non-peaking $B\overline{B}$ categories, so we combined them together when making the NN ${}_s\mathcal{P}lot$s.

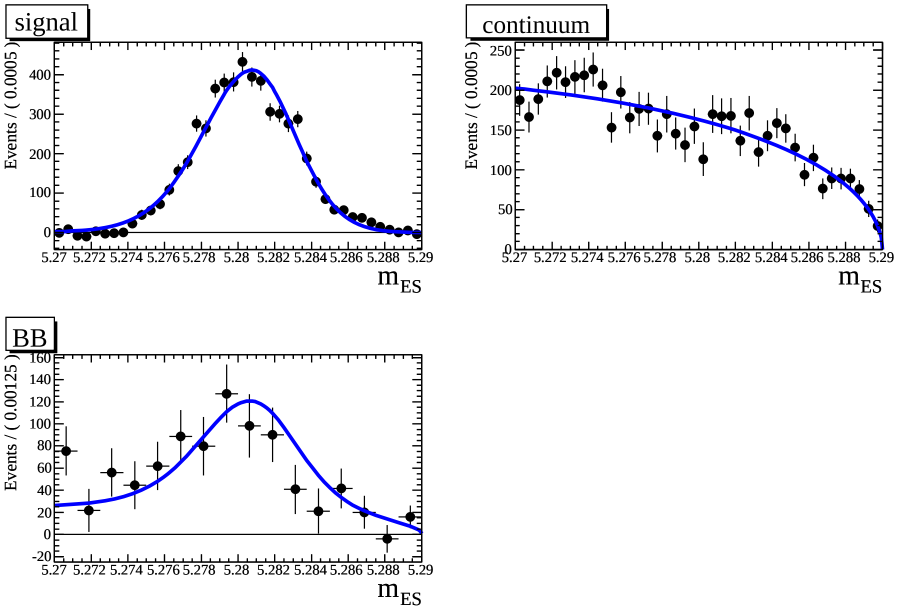

Figure 6.4: m_{ES} ${}_s\mathcal{P}lot$s for $B^+ \to K^+K^-K^+$, for signal, continuum, and $B\overline{B}$ backgrounds. Using the initial Dalitz model (Model A). The $B\overline{B}$ plot is a sum of all $B\overline{B}$ background categories.

In Fig. 6.7, we show the DP ${}_s\mathcal{P}lot$s for this fit. The agreement between the fit model and the data is fairly good, but not perfect. To examine the agreement between the signal model and the data more closely, we will look at angular moments, as shown in the next section.

Angular Moments

We look at plots of the angular moments, as described in Sec. 6.1. For data, we calculate the angular moments from the ${}_s\mathcal{W}eight$s. For comparison with the DP model, we generate a high-statistics toy sample based on the fit result, and calculate angular moments for the toy events. The angular moments are shown in Fig. 6.8. There are large discrepancies between the fit model and the data in the $f_X(1500)$ region, particularly for the 2nd-order moment, where in data a large peak can be seen that is not modeled by the DP model. There are also significant discrepancies

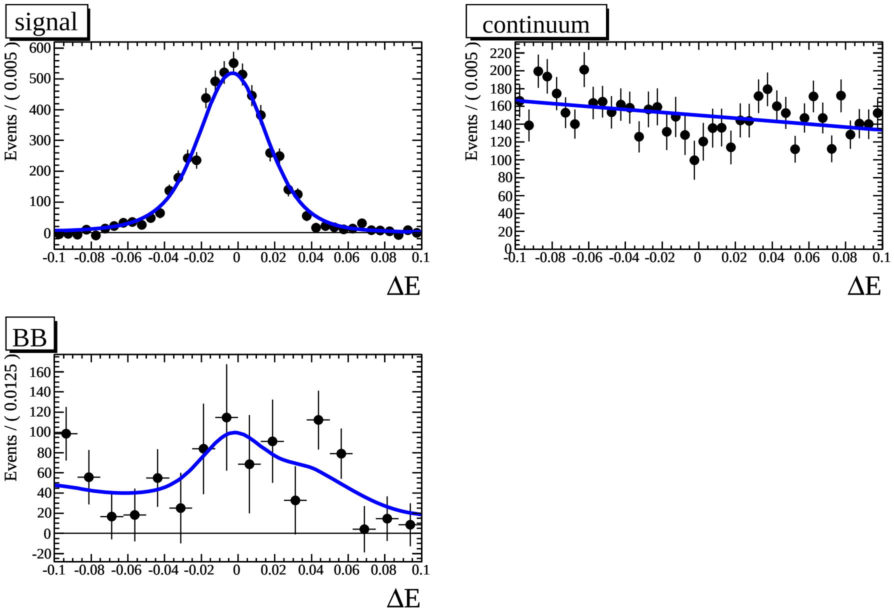

Figure 6.5: ΔE ${}_s\mathcal{P}lot$s for $B^+ \to K^+K^-K^+$, for signal, continuum, and $B\overline{B}$ backgrounds. Using the initial Dalitz model (Model A). The $B\overline{B}$ plot is a sum of all $B\overline{B}$ background categories.

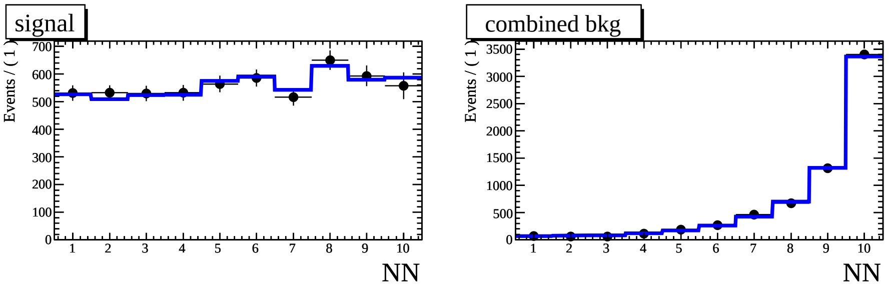

Figure 6.6: NN ${}_s\mathcal{P}lot$s for $B^+ \to K^+K^-K^+$, for signal and background. Using the initial Dalitz model (Model A). The signal plot contains both signal and the peaking $B\overline{B}$ backgrounds. The background plot contains all the other background categories combined (continuum and non-peaking $B\overline{B}$ backgrounds).

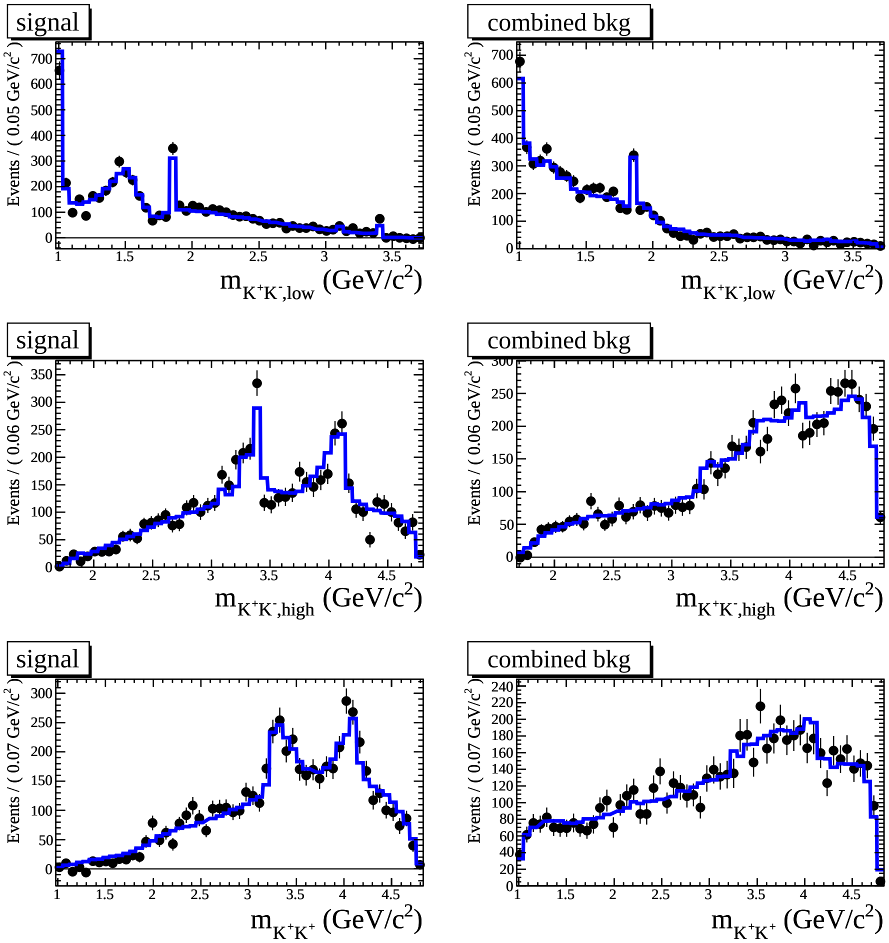

Figure 6.7: DP ${}_s\mathcal{P}lot$s for $B^+ \to K^+K^-K^+$, for signal and combined background. Using the initial Dalitz model (Model A). The signal plot contains both signal and the peaking $B\overline{B}$ backgrounds. The background plot contains all the other background categories combined (continuum and non-peaking $B\overline{B}$ backgrounds).

in the high-mass region, with $m_{12} > 2\,\mathrm{GeV}/c^2$.

6.2.2 Testing Alternative DP Models

Since the angular moments show that the DP model does not do a great job of describing the data, we test various different DP models.

The angular moments suggest some extra narrow structure around 1500 MeV/c^2 that is not included in our DP model. The presence of a peak in the 2nd-order angular moment suggests either a spin-1 or spin-2 structure (see Eq. 6.5). The PDG lists a spin-2 $K\overline{K}$ resonance called the $f_2'(1525)$. We add the $f_2'(1525)$ to the existing DP model, floating the NR α and the mass and width of the $f_X(1500)$. The best fit result is shown in Table 6.2. (The signal and background yields do not depend significantly on the DP model, so we do not list them again.) The inclusion of the $f_2'(1525)$ improves the NLL by 13.1 units. The fit fractions for some of the isobars change dramatically. Notably, the $f_X(1500)$ fraction is much smaller, the $f_0(1710)$ fraction is much larger, and the NR fraction is significantly smaller. Also, the mass and width of the $f_X(1500)$ have changed significantly. Interestingly, the mass and width are now similar to the mass and width listed in the PDG for the $f_0(1500)$, although the fitted mass is about 35 MeV/c^2 smaller than the PDG value. Because the mass and width are so similar, we decide to replace the $f_X(1500)$ with the PDG $f_0(1500)$.

The angular moments plots indicated problems with the DP model in the $m_{12} > 2\,\mathrm{GeV}/c^2$ region, which suggests problems with the NR parametrization. So, we test various NR models. We add an isobar proportional to $e^{\alpha_{13}\,\mathrm{m}_{13}^2}$, like the NR model given in Eq. 2.54. First, we fit with the parameter α_{13} constrained to be the same as the parameter α. The best fit gives $\alpha = -0.091 \pm 0.013$. The NLL improves by 38.5 units over the model without this extra NR term (and we were floating the $f_X(1500)$ mass and width in that model, instead of fixing the mass and width to the $f_0(1500)$ as we do now, so the NLL improvement is even more impressive).

We fit with a similar model, except this time allowing α_{13} and α to be different. The best fit is summarized in Table 6.3. The NLL improves by an additional 17.4

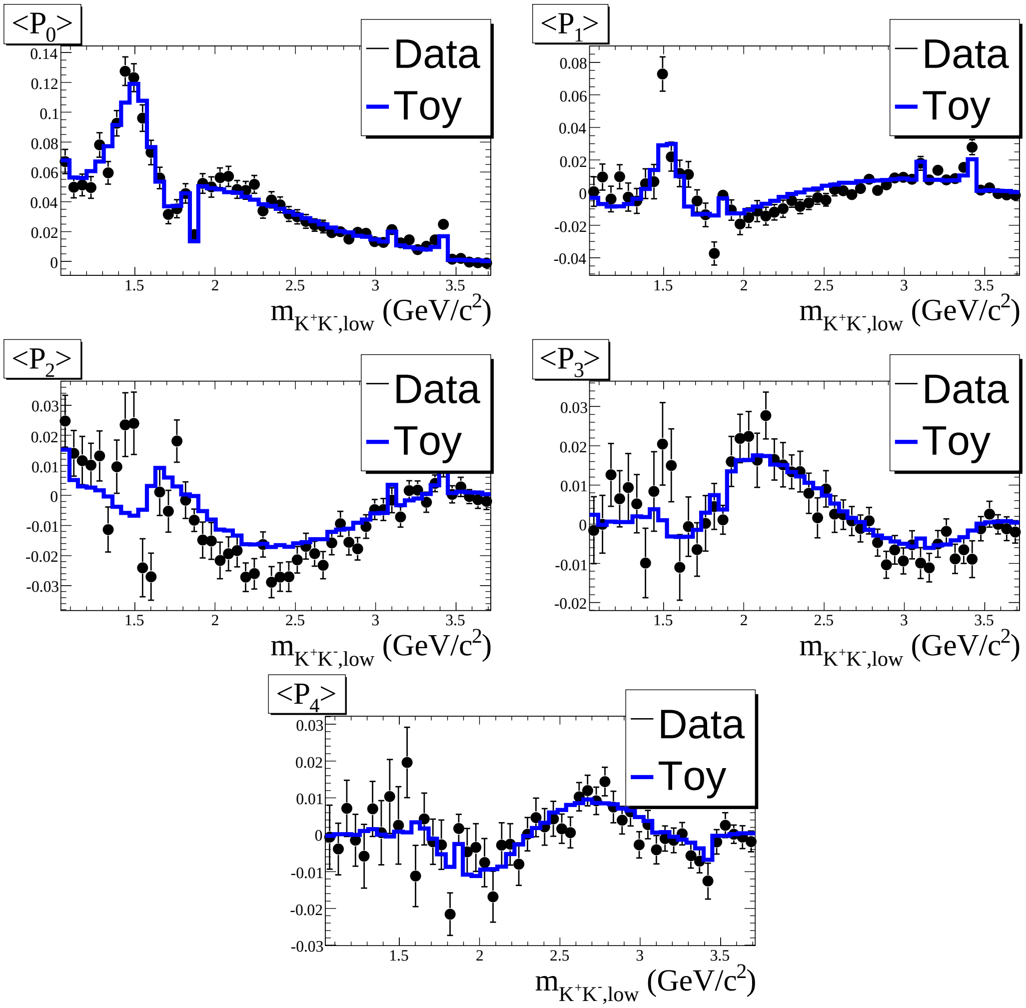

Figure 6.8: $B^+ \to K^+K^-K^+$ angular moments for data (points) and fit model (line). Fit model used is the initial Dalitz model (Model A). The $\phi(1020)$-region ($m_{12} <$ 1.04 GeV) is excluded, in order to make the interesting high-mass features more visible.

Table 6.2: Isobar magnitudes and phases from a CP-blind fit to $B^+ \to K^+K^-K^+$ data, with the $f_2'(1525)$ added to the original DP model, floating the NR α and the mass and width of the $f_X(1500)$. The errors are statistical only.

Decay	Magnitude c_r	Phase ϕ_r (rad.)	Fraction FF_r (%)
$\phi(1020)$	0.0184 ± 0.0016	-2.28 ± 0.26	13.5 ± 0.8
$f_0(980)$	0.6221 ± 0.1229	2.86 ± 0.32	11.7 ± 4.5
$f_X(1500)$	0.0889 ± 0.0243	-1.39 ± 0.25	1.8 ± 0.5
$f_2'(1525)$	0.0007 ± 0.0001	0.62 ± 0.16	1.6 ± 0.4
$f_0(1710)$	0.4458 ± 0.0394	1.37 ± 0.12	30 ± 10
χ_{c0}	0.0684 ± 0.0086	-0.04 ± 0.27	3.5 ± 0.6
NR	1.0 (fixed)	0.0 (fixed)	44.4 ± 2.8
$f_X(1500)$ Mass	1470.0 ± 10.3		
$f_X(1500)$ Width	96.0 ± 21.0		
NR α	-0.136 ± 0.010		
NLL	-136003.3		

units. Interestingly, the parameter α now becomes positive, and α_{13} is negative. The coefficient of the $e^{\alpha_{13}\,\mathrm{m}_{13}^2}$ term is very large.

Instead of using an exponential NR model, we try the 2D-polynomial NR model described in Eq. 2.59. The best fit is summarized in Table 6.4. The NLL improves by an additional 62.7 units. This model has 6 more floating DP parameters than the previous model mentioned, so we would expect some improvement in NLL just by virtue of having additional free parameters. To study this, we did some toy studies where we generated events with one NR model, and then fit the toy datasets both with the original NR model and with a more complex NR model having 6 more free parameters, and it was found that in 95% of toy trials, the NLL improvement due to the more complex NR model was less than 7.5 units. So, although some improvement in NLL is possible just due to having 6 more free parameters, the improvement of 62.7 units is clearly significant.

Finally, we try the S+P wave NR model given in Eq. 2.56. The best fit is summarized in Table 6.5. We will refer to this model as $B^+ \to K^+K^-K^+$ Model B. The angular moments for this model are shown in Fig. 6.9. The agreement between the model and data is quite good, but there are a few disagreements. There is some

Table 6.3: Isobar magnitudes and phases from a CP-blind fit to $B^+ \to K^+K^-K^+$ data, with a NR model like that described in Eq. 2.54. The NR parameters α_{13} and α are permitted to be different from one another. The errors are statistical only.

Decay	Magnitude c_r	Phase ϕ_r (rad.)	Fraction FF_r (%)
$\phi(1020)$	0.0154 ± 0.0020	-2.30 ± 0.21	13.4 ± 2.1
$f_0(980)$	0.65 ± 0.11	2.80 ± 0.19	18 ± 7
$f_0(1500)$	0.090 ± 0.016	-0.49 ± 0.16	2.3 ± 1.0
$f_2'(1525)$	0.0005 ± 0.0001	0.81 ± 0.14	1.5 ± 0.5
$f_0(1710)$	0.37 ± 0.05	1.55 ± 0.09	28 ± 5
χ_{c0}	0.055 ± 0.008	0.47 ± 0.18	3.2 ± 0.6
NR(K^+K^-)	1.0 (fixed)	0.0 (fixed)	53 ± 9
NR(K^+K^+)	4.35 ± 0.18	3.03 ± 0.01	
NR α	0.0492 ± 0.0022		
NR α_{13}	-0.0499 ± 0.0040		
NLL	-136059.2		

disagreement in the second-order moment in the 2-2.5 GeV/c^2 range, which could be due to an imperfect NR model, or missing broad tensor resonances. There is one bin in the first-order moment around 1.8 GeV/c^2 with a large discrepancy, but it doesn't appear to be a real resonance, since otherwise we would expect to see a peak in the zeroth-order moment as well. Model B gives an NLL 6.6 units worse than the 2D-polynomial NR model, with the same number of DP parameters. But the S+P wave NR model has an easier physical interpretation than the 2D-polynomial NR model. Also, we would like to use a similar NR model for the modes $B^+ \to K^+K^-K^+$, $B^0 \to K^+K^-K^0_S$, and $B^+ \to K^0_SK^0_SK^+$, and it is less clear how to generalize the 2D-polynomial NR model to the modes $B^0 \to K^+K^-K^0_S$ and $B^+ \to K^0_SK^0_SK^+$. So, we think the S+P wave NR model is the best choice, and we will test this choice in $B^+ \to K^0_SK^0_SK^+$ and $B^0 \to K^+K^-K^0_S$ later in this chapter.

Testing for Additional Components

We test for the presence of a number of additional resonances. These tests are summarized in Sec. 6.5. We do not see any conclusive evidence for any other resonances beyond what was included in Model B.

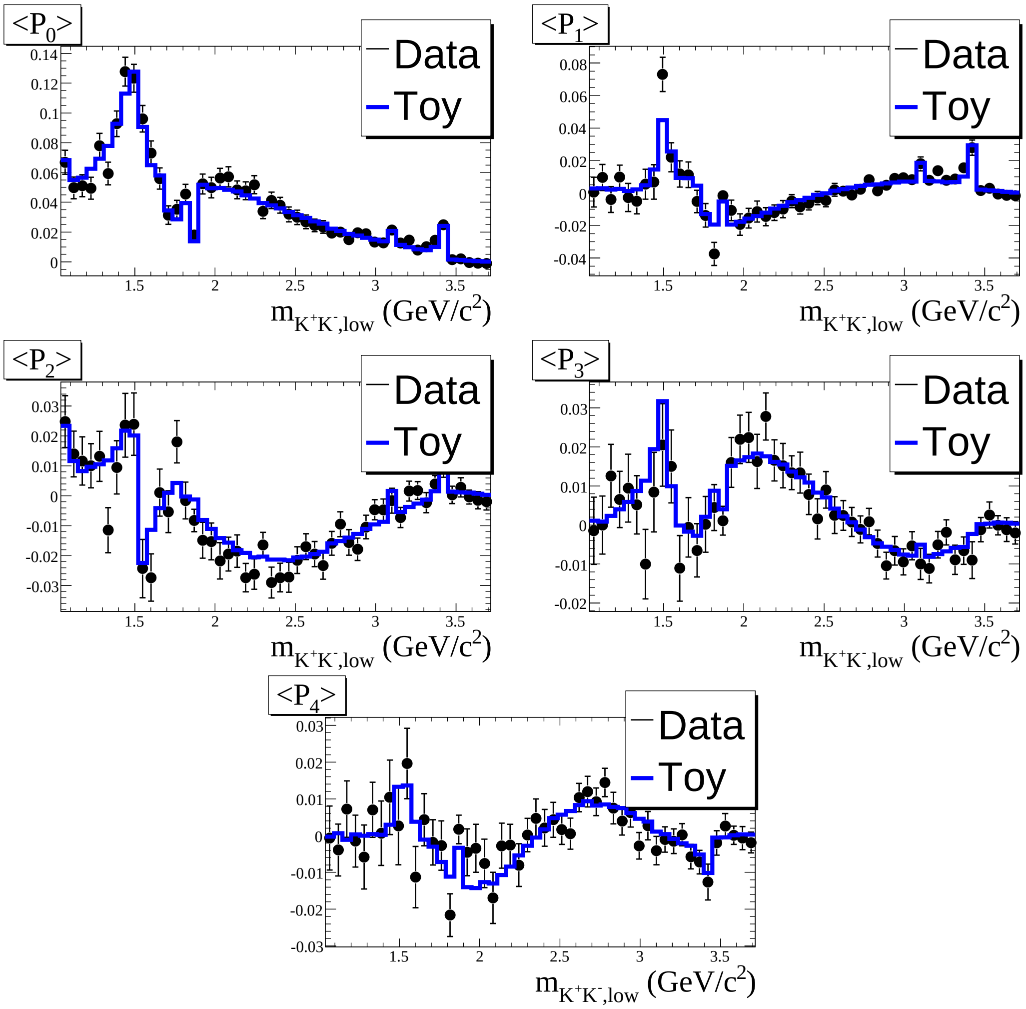

Figure 6.9: $B^+ \to K^+K^-K^+$ angular moments for data (points) and fit model (blue). Fit model used is Model B (see Table 6.5). The $\phi(1020)$-region ($m_{12} < 1.04\,\text{GeV}$) is excluded.

Table 6.4: Isobar magnitudes and phases from a CP-blind fit to $B^+ \to K^+K^-K^+$ data, with a 2D-polynomial NR model like that described in Eq. 2.59. The errors are statistical only.

Decay	Magnitude c_r	Phase ϕ_r (rad.)	Fraction $\mathcal{F}_r$ (%)
$\phi(1020)$	0.0159 ± 0.0007	-0.27 ± 0.20	12.52 ± 1.92
$f_0(980)$	0.8064 ± 0.0977	0.44 ± 0.21	24.32 ± 6.21
$f_0(1500)$	0.0989 ± 0.0106	-0.26 ± 0.16	2.43 ± 0.47
$f_2'(1525)$	0.0007 ± 0.0001	0.77 ± 0.20	1.98 ± 0.47
$f_0(1710)$	0.1247 ± 0.0139	1.06 ± 0.14	2.89 ± 0.76
χ_{c0}	0.0679 ± 0.0059	0.65 ± 0.19	4.28 ± 0.64
NR(a_{00})	1.0 (fixed)	0.0 (fixed)	
NR(a_{10})	0.5937 ± 0.0877	2.17 ± 0.12	
NR(a_{20})	0.1202 ± 0.0633	-1.09 ± 0.48	165.58 ± 13.35
NR(a_{11})	0.5210 ± 0.0651	-1.96 ± 0.09	
NR(a_{30})	0.1300 ± 0.0373	-2.17 ± 0.26	
NR(a_{21})	0.2591 ± 0.0808	-0.96 ± 0.23	
NLL	-136121.9		

We also try adding a polynomial D-wave term to the NR model, resulting in the NR model shown in Eq. 2.58. Including the D-wave NR term, the NLL improves by 17.6 units. Note that the D-wave NR term adds 6 additional degrees of freedom to the model. The best fit is summarized in Table 6.6. The fit fractions of the resonances have not changed significantly after adding the D-wave term. The fit fraction of the D-wave term is relatively small, and consistent with 0. We decide not to include a D-wave NR term in our isobar model.

6.2.3 Plotting the Nominal NR model

To look at the shape of the nonresonant contribution more closely, we take the best fit result for Model B, and set all of the resonant isobars to zero. Then, we generate toy with this model, so that there is only the NR contribution. The NR toy is shown in Fig. 6.10. To look at the magnitude and phase motion of the NR model, we "unsymmetrize" it, that is, we just look at

$$\mathcal{A}_{NR} = \left(a_{S0} + a_{S1}\, m_{K^+K^-} + a_{S2}\, m_{K^+K^-}^2\right) +$$

Table 6.5: Isobar magnitudes and phases from a CP-blind fit to $B^+ \to K^+K^-K^+$ data, using Model B, which uses an S+P wave NR model like that described in Eq. 2.56. The errors are statistical only.

Decay	Magnitude c_r	Phase ϕ_r (rad.)	Fraction FF_r (%)
$\phi(1020)$	0.031 ± 0.006	3.06 ± 0.23	12.9 ± 1.8
$f_0(980)$	1.65 ± 0.24	2.04 ± 0.21	27 ± 6
$f_0(1500)$	0.18 ± 0.03	-0.82 ± 0.22	2.2 ± 0.6
$f_2'(1525)$	0.0014 ± 0.0003	0.55 ± 0.21	2.1 ± 0.5
$f_0(1710)$	0.25 ± 0.05	0.74 ± 0.19	3.2 ± 0.8
χ_{c0}	0.11 ± 0.02	0.10 ± 0.22	3.2 ± 0.5
NR(a_{S0})	1.0 (fixed)	0.0 (fixed)	
NR(a_{S1})	2.0 ± 0.6	2.82 ± 0.23	141 ± 91
NR(a_{S2})	0.32 ± 0.11	2.78 ± 0.23	
NR(a_{P0})	1.57 ± 0.49	0.21 ± 0.53	
NR(a_{P1})	0.82 ± 0.08	-2.76 ± 0.16	66 ± 57
NR(a_{P2})	0.51 ± 0.21	-1.92 ± 0.28	
NLL	-136115.3		

$$\left(a_{P0} + a_{P1}\, m_{K^+K^-} + a_{P2}\, m^2_{K^+K^-}\right) P_1(\cos\theta_3) \qquad (6.7)$$

without distinguishing between m_{12} and m_{23}. Then, we plot the S-wave and P-wave magnitude and phase of Eq. 6.7 as a function of $m_{K^+K^-}$. This is shown in Fig. 6.11, without error bars. Caution should be used in interpreting the plots in this figure, because the S-wave and P-wave parameters are highly correlated with one another, and they could also be influenced by higher-wave terms not included in the model, or by the truncation of the polynomials to second-order in $m_{K^+K^-}$.

6.3 $B^+ \to K^0_S K^0_S K^+$ Fits

6.3.1 Fit with Initial DP Model

This is the first ever DP analysis of $B^+ \to K^0_S K^0_S K^+$, so we don't have a prior result to base our model on. For an initial DP model, we use the resonances from $B^+ \to K^+K^-K^+$ Model A (except for the forbidden $\phi(1020)$), namely: $f_0(980)$,

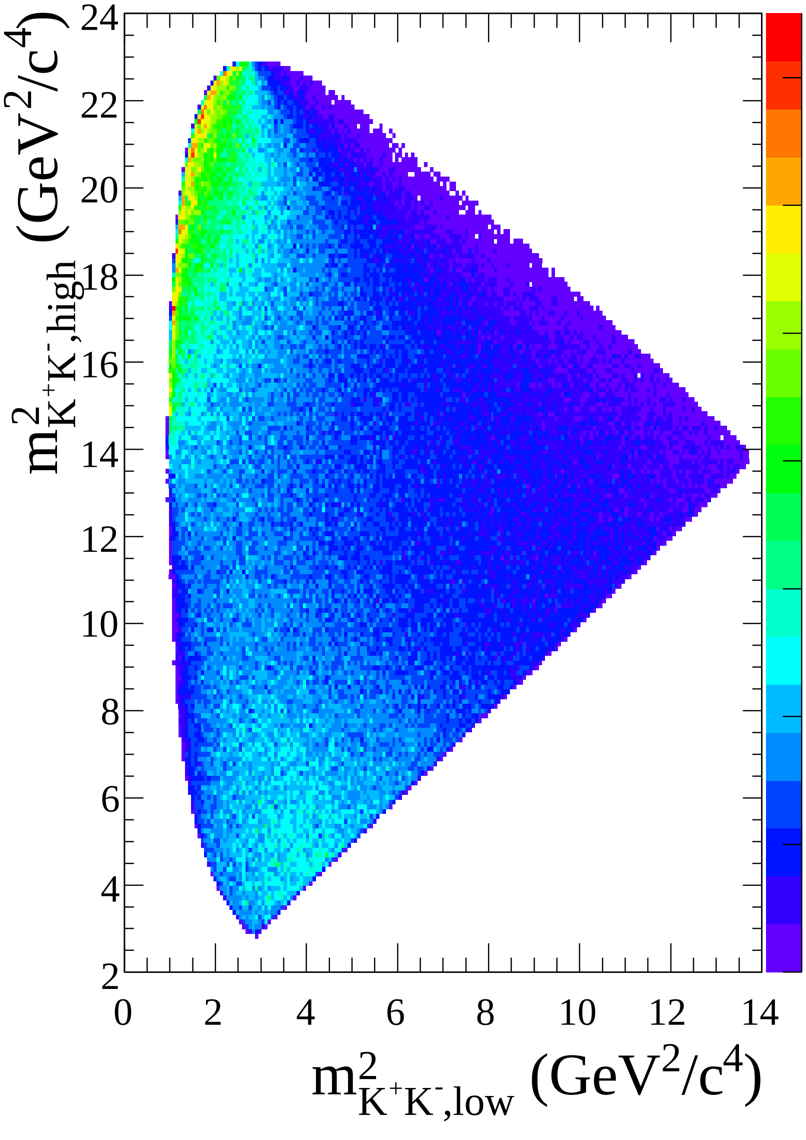

Figure 6.10: Dalitz plot distribution of toy NR events. The NR model is the polynomial S- and P-wave model used in Model B, using the fit result shown in Table 6.5.

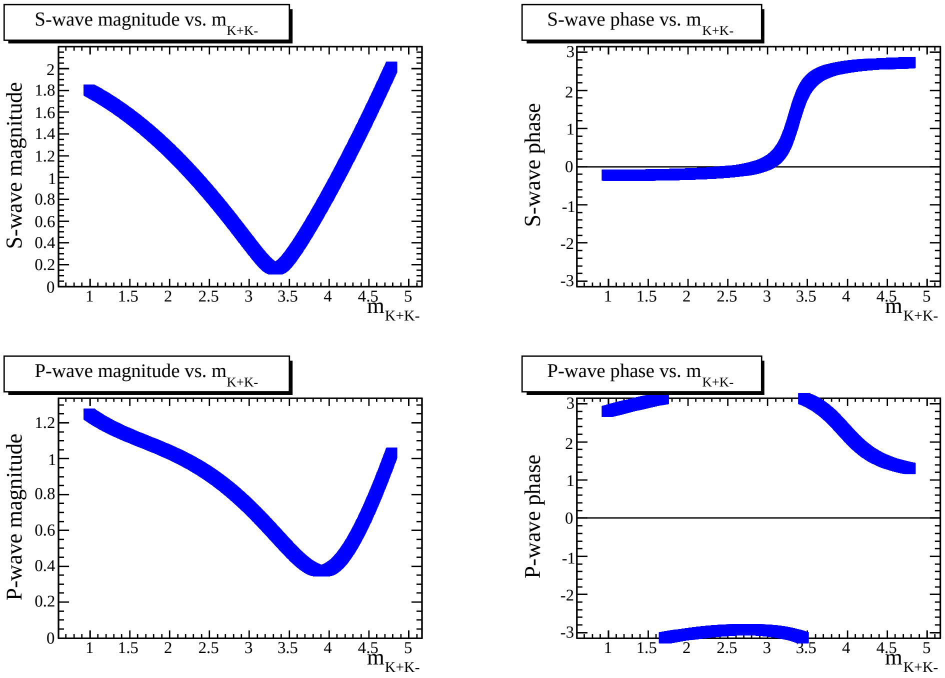

Figure 6.11: Magnitude and phase of the S-wave and P-wave portions of the NR model used in Model B, as shown in Eq. 6.7. The NR model uses the fit result shown in Table 6.5.

Table 6.6: Isobar magnitudes and phases from a CP-blind fit to $B^+ \to K^+K^-K^+$ data, with a NR model containing S-wave, P-wave, and D-wave terms, like described in Eq. 2.58.

Decay	Magnitude c_r	Phase ϕ_r (rad.)	Fraction FF_r (%)
$\phi(1020)$	0.0251 ± 0.0020	-3.08 ± 0.16	12.8 ± 0.7
$f_0(980)$	1.43 ± 0.13	2.29 ± 0.14	31 ± 5
$f_0(1500)$	0.147 ± 0.019	-0.52 ± 0.16	2.2 ± 0.5
$f_2'(1525)$	0.00103 ± 0.00014	0.58 ± 0.13	1.9 ± 0.5
$f_0(1710)$	0.209 ± 0.025	0.99 ± 0.12	3.3 ± 0.7
χ_{c0}	0.095 ± 0.010	0.20 ± 0.19	3.4 ± 0.5
a_{S0}	1.0 (fixed)	0.0 (fixed)	
a_{S1}	2.23 ± 0.09	3.01 ± 0.06	233 ± 36
a_{S2}	0.51 ± 0.07	2.74 ± 0.12	
a_{P0}	2.06 ± 0.11	0.15 ± 0.07	
a_{P1}	0.82 ± 0.05	-2.80 ± 0.13	145 ± 27
a_{P2}	0.55 ± 0.07	-2.35 ± 0.20	
a_{D0}	0.26 ± 0.19	-0.67 ± 0.67	
a_{D1}	0.20 ± 0.06	0.52 ± 0.42	1.9 ± 2.0
a_{D2}	0.135 ± 0.039	-3.06 ± 0.71	
NLL	-136132.2		

$f_X(1500)$, $f_0(1710)$, and χ_{c0}. For the NR, we use a polynomial model like that used in $B^+ \to K^+K^-K^+$ Model B, except we omit the forbidden P-wave terms. Using this model, we performed 500 randomized fits to data. The best solution found is shown in Table 6.7. We will call this $B^+ \to K^0_S K^0_S K^+$ Model A.

${}_s\mathcal{P}lot$s

We form ${}_s\mathcal{P}lot$s for the signal and background categories. The ${}_s\mathcal{P}lot$s for $m_{\rm ES}$, ΔE, and NN are shown in Figs. 6.12, 6.13, and 6.14, respectively. In Fig. 6.15, we show the DP ${}_s\mathcal{P}lot$s for this fit. The agreement between the fit model and the data is quite good. We will look at the angular moments next.

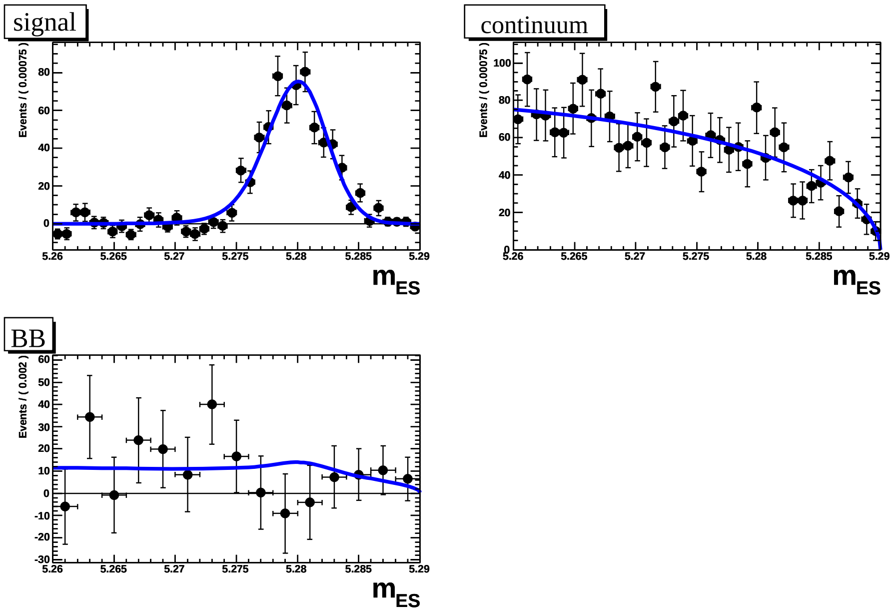

Figure 6.12: $m_{\rm ES}$ ${}_s\mathcal{P}lot$s for $B^+ \to K^0_S K^0_S K^+$, for signal, continuum, and $B\overline{B}$ backgrounds. Using the initial Dalitz model. The $B\overline{B}$ plot is a sum of all $B\overline{B}$ background categories.

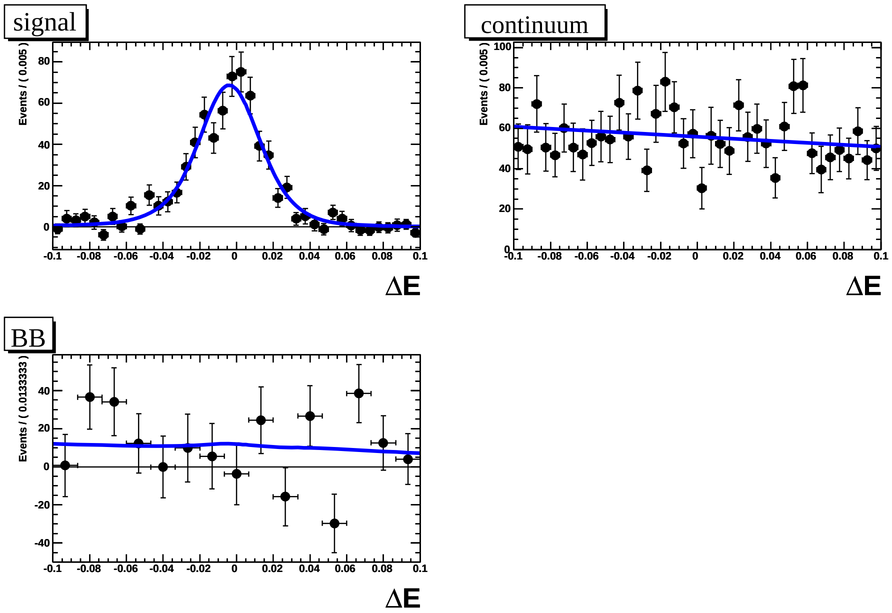

Figure 6.13: ΔE ${}_s\mathcal{P}lot$s for $B^+ \to K_S^0 K_S^0 K^+$, for signal, continuum, and $B\overline{B}$ backgrounds. Using the initial Dalitz model. The $B\overline{B}$ plot is a sum of all $B\overline{B}$ background categories.

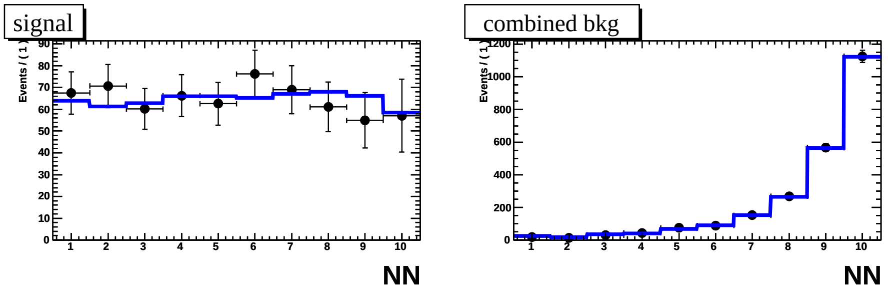

Figure 6.14: NN ${}_s\mathcal{P}lot$s for $B^+ \to K_S^0 K_S^0 K^+$, for signal and the combined background. Using the initial Dalitz model. The combined background category is a sum of all the background categories except for the peaking $B\overline{B}$ background. The signal category includes the peaking $B\overline{B}$ background.

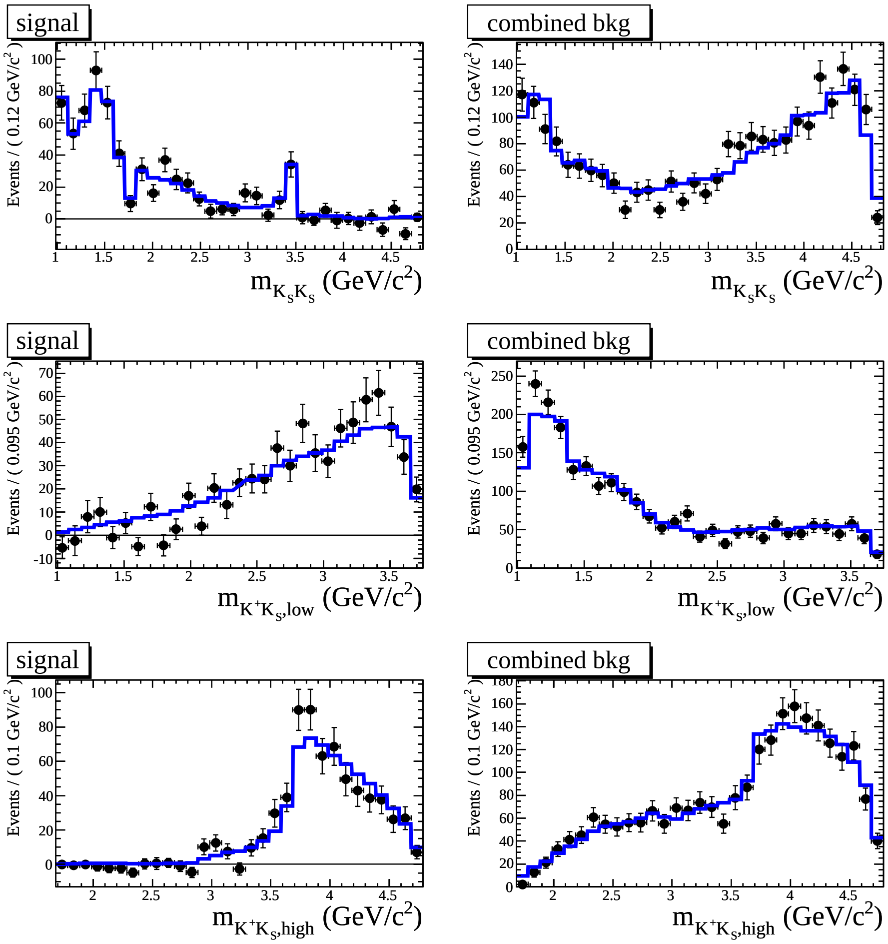

Figure 6.15: DP ${}_s\mathcal{P}lot$s for $B^+ \to K^0_S K^0_S K^+$, for signal and combined background. Using the initial Dalitz model. The combined background category is a sum of all the background categories except for the peaking $B\overline{B}$ background. The signal category includes the peaking $B\overline{B}$ background.

Table 6.7: Isobar magnitudes and phases from a CP-blind fit to $B^+ \to K^0_S K^0_S K^+$ data, with the initial DP model (Model A). The errors are statistical only.

Decay	Magnitude c_r	Phase ϕ_r (rad.)	Fraction $\mathcal{F}_r$ (%)
$f_0(980)$	5.217 ± 1.212	0.909 ± 0.119	92.082 ± 44.957
$f_X(1500)$	2.824 ± 0.579	1.550 ± 0.195	112.610 ± 27.346
$f_0(1710)$	0.612 ± 0.244	-0.256 ± 0.232	7.812 ± 6.200
χ_{c0}	0.211 ± 0.055	-1.810 ± 1.178	4.795 ± 2.470
a_{S0}	1.000 ± 0.000	0.000 ± 0.000	231.412 ± 101.773
a_{S1}	2.369 ± 0.523	-2.923 ± 0.154	231.412 ± 101.773
a_{S2}	1.368 ± 0.399	0.410 ± 0.223	231.412 ± 101.773
N_{sig}	637 ± 28		
N_{cont}	2232 ± 50		
NLL	-26858.0		

Angular Moments

We now calculate the angular moments, comparing data ${}_s\mathcal{P}lot$s versus toy, just like in Sec. 6.2.1. The angular moments are shown in Fig. 6.16. Most notably, the data exhibits a peak in the 2nd-order moment around 1500 MeV/c^2, which is not accounted for by the signal model. This is suggestive of a spin-2 $K^0_S K^0_S$ resonance around 1500 MeV/c^2.

6.3.2 Testing Alternative DP Models

Since the angular moments show that the initial DP model does not do a great job of describing the data, we test various different DP models. Motivated by the $B^+ \to K^+K^-K^+$ studies, we replace the $f_X(1500)$ with the $f_0(1500)$ and $f_2'(1525)$. This is also motivated by the peak in the 2nd-order angular moment, which suggests a tensor resonance around 1500 MeV/c^2, the most obvious candidate being the $f_2'(1525)$. The best fit result is shown in Table 6.8. We will call this the $B^+ \to K^0_S K^0_S K^+$ Model B. The NLL of Model B has an improvement of 18.6 units with respect Model A. We plot the angular moments for this fit result in Fig. 6.17. The peak in the 2nd-order moment is now well modeled. We will switch to using these resonances, both because of the fit improvement, and because it is the same model favored by $B^+ \to K^+K^-K^+$.

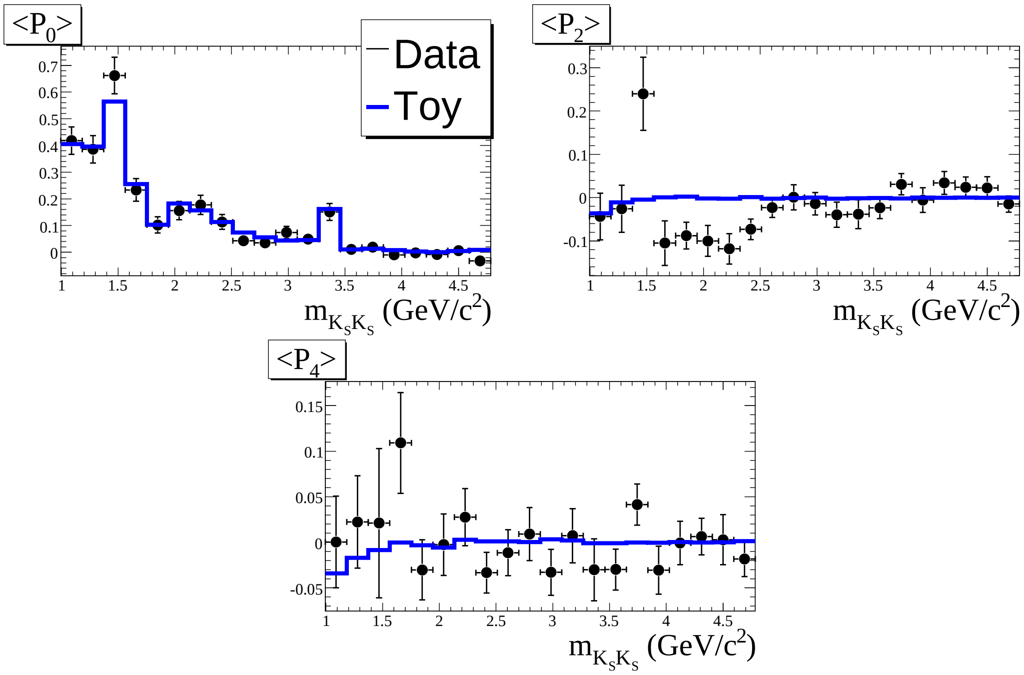

Figure 6.16: $B^+ \to K^0_S K^0_S K^+$ angular moments for data (points) and fit model (blue). Fit model used is the initial Dalitz model.

Table 6.8: Isobar magnitudes and phases from a CP-blind fit to $B^+ \to K^0_S K^0_S K^+$ data, using Model B (containing the standard resonances and an S-wave polynomial NR model). The errors are statistical only.

Decay	Magnitude c_r	Phase ϕ_r (rad.)	Fraction $\mathcal{F}_r$ (%)
$f_0(980)$	3.381 ± 0.218	0.535 ± 0.150	139.156 ± 25.414
$f_0(1500)$	0.199 ± 0.049	-1.446 ± 0.323	3.960 ± 1.791
$f_2'(1525)$	0.002 ± 0.000	-1.021 ± 0.209	5.730 ± 1.708
$f_0(1710)$	0.246 ± 0.068	-0.390 ± 0.184	4.546 ± 2.603
χ_{c0}	0.108 ± 0.024	0.404 ± 1.657	4.576 ± 1.966
a_{S0}	1.000 ± 0.000	0.000 ± 0.000	
a_{S1}	1.004 ± 0.080	2.249 ± 0.102	185.028 ± 34.703
a_{S2}	0.511 ± 0.086	-1.472 ± 0.143	
NLL	-26876.6		

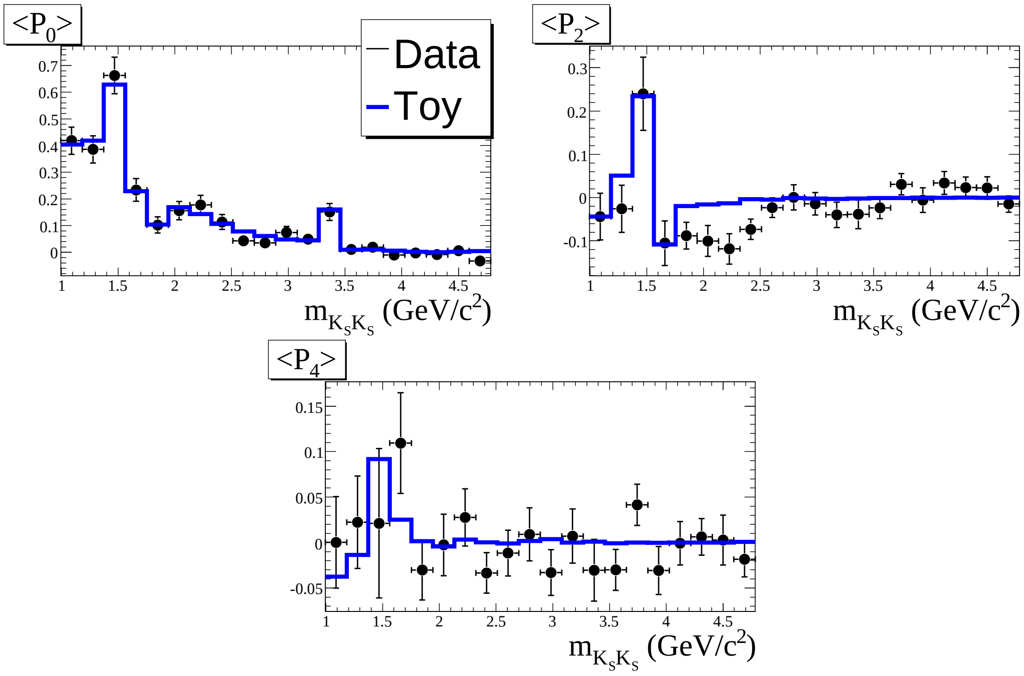

Figure 6.17: $B^+ \rightarrow K^0_S K^0_S K^+$ angular moments for data (points) and fit model (blue line). Fit model used is Model B (containing the standard resonances and an S-wave polynomial NR model; see Table 6.8).

As an alternative to the polynomial NR model, we try an exponential model like that previously used in $B^0 \to K^+K^-K^0_S$ (Eq. 2.55), except that the $e^{\alpha s_{13}}$ and $e^{\alpha s_{23}}$ coefficients are constrained to be equal to due Bose-symmetrization. The NLL of this model is 0.7 units worse than Model B. The fit result is shown in Table 6.9.

Table 6.9: Isobar magnitudes and phases from a CP-blind fit to $B^+ \to K^0_S K^0_S K^+$ data, with a model like Model B, except with an exponential NR model. The errors are statistical only.

Decay	Magnitude c_r	Phase ϕ_r (rad.)	Fraction $\mathcal{F}_r$ (%)
$f_0(980)$	1.014 ± 0.073	1.702 ± 0.164	77.848 ± 14.367
$f_0(1500)$	0.084 ± 0.018	-0.966 ± 0.326	4.454 ± 2.017
$f_2'(1525)$	0.001 ± 0.000	-0.281 ± 0.191	5.951 ± 1.925
$f_0(1710)$	0.079 ± 0.026	0.223 ± 0.255	2.895 ± 1.844
χ_{c0}	0.047 ± 0.007	0.321 ± 0.646	5.403 ± 1.099
NR($K^0_S K^0_S$)	1.000 ± 0.000	0.000 ± 0.000	69.914 ± 16.180
NR($K^+ K^0_S$)	0.108 ± 0.029	2.564 ± 0.475	69.914 ± 16.180
NLL	-26875.9		

Looking at Fig. 6.17, there still seems to be some discrepancy in the 2nd-order angular moment in the $1.6\,\mathrm{GeV}/c^2 < m_{12} < 2.5\,\mathrm{GeV}/c^2$ mass range. To see if we can model this, we add a NR D-wave component like the one in Eq. 2.58. The best fit result is summarized in Table 6.10. The inclusion of the D-wave component improves the NLL by 11.1 units (with 6 additional parameters). The angular moments for this fit result are shown in Fig. 6.18. It matches the 2nd-order angular moment quite well.

Instead of including a NR D-wave component, we try adding the $f_2(2300)$ resonance. The best fit result is summarized in Table 6.11. The NLL is improved by 9.0 units (with 2 additional parameters). The angular moments for this fit result are shown in Fig. 6.19. It also matches the 2nd-order angular moment fairly well.

As another alternative, we try adding the $f_2(2010)$ resonance. The best fit result is summarized in Table 6.12. The NLL is improved by only 5.2 units (with 2 additional parameters).

Since we did not find it appropriate to include a D-wave NR component in $B^+ \to K^+K^-K^+$, we decide not to include it here, either. In Sec. 6.5, we show the results of searches for the $f_2(2300)$ and $f_2(2010)$ in $B^+ \to K^+K^-K^+$ and $B^0 \to K^+K^-K^0_S$, and conclude that we should not include them in our nominal model. So, Model B is still our favored model for $B^+ \to K_S^0 K_S^0 K^+$.

Table 6.10: Isobar magnitudes and phases from a CP-blind fit to $B^+ \to K_S^0 K_S^0 K^+$ data, with a model like Model B, but with the addition of a D-wave polynomial NR contribution. The errors are statistical only.

Decay	Magnitude c_r	Phase ϕ_r (rad.)	Fraction $\mathcal{F}_r$ (%)
$f_0(980)$	4.684 ± 1.092	0.911 ± 0.119	75.198 ± 26.402
$f_0(1500)$	1.382 ± 0.277	1.775 ± 0.200	53.945 ± 13.543
$f_2'(1525)$	0.003 ± 0.001	0.525 ± 0.298	4.124 ± 2.311
$f_0(1710)$	0.658 ± 0.190	0.704 ± 0.205	9.148 ± 4.011
χ_{c0}	0.220 ± 0.047	-1.370 ± 0.694	5.323 ± 1.566
a_{S0}	1.000 ± 0.000	0.000 ± 0.000	
a_{S1}	2.254 ± 0.482	-2.770 ± 0.138	210.262 ± 32.671
a_{S2}	1.281 ± 0.369	0.585 ± 0.197	
a_{D0}	0.724 ± 0.281	2.214 ± 0.448	
a_{D1}	0.605 ± 0.334	-0.286 ± 0.424	4.598 ± 2.132
a_{D2}	0.417 ± 0.270	-2.360 ± 0.642	
NLL	-26887.7		

6.4 $B^0 \to K^+K^-K_S^0$ Fits

6.4.1 Fit with Initial DP Model

For our initial DP model, we used the same isobar model used in *BABAR*'s previous analysis [23] (also the same model used in *BABAR*'s preliminary Run1-6 result presented at ICHEP 2008). We performed 500 randomized fits. The best solution found is shown in Table 6.13. This solution is consistent with *BABAR*'s preliminary Run1-6 result. We will refer to it as $B^0 \to K^+K^-K_S^0$ Model A.

${}_s\mathcal{P}lot$s

We form ${}_s\mathcal{P}lot$s for the signal and background. The ${}_s\mathcal{P}lot$s for m_{ES}, ΔE, and NN are shown in Figs. 6.20, 6.21, and 6.22, respectively. The ${}_s\mathcal{P}lot$s are shown for the

Table 6.11: Isobar magnitudes and phases from a CP-blind fit to $B^+ \to K_S^0 K_S^0 K^+$ data, with a model like Model B, but with the addition of the $f_2(2300)$. The errors are statistical only.

Decay	Magnitude c_r	Phase ϕ_r (rad.)	Fraction $\mathcal{F}_r$ (%)
$f_0(980)$	3.378 ± 0.249	0.453 ± 0.131	137.406 ± 27.278
$f_0(1500)$	0.199 ± 0.050	-1.584 ± 0.347	3.918 ± 1.758
$f_2'(1525)$	0.002 ± 0.000	-1.241 ± 0.238	5.380 ± 1.731
$f_0(1710)$	0.242 ± 0.068	-0.481 ± 0.193	4.348 ± 2.322
$f_2(2300)$	0.002 ± 0.000	0.960 ± 0.316	2.121 ± 1.005
χ_{c0}	0.115 ± 0.023	0.769 ± 1.419	5.073 ± 1.933
a_{S0}	1.000 ± 0.000	0.000 ± 0.000	
a_{S1}	0.993 ± 0.084	2.169 ± 0.094	178.676 ± 32.303
a_{S2}	0.546 ± 0.081	-1.581 ± 0.133	
NLL	-26885.6		

Table 6.12: Isobar magnitudes and phases from a CP-blind fit to $B^+ \to K_S^0 K_S^0 K^+$ data, with a model like Model B, but with the addition of the $f_2(2010)$. The errors are statistical only.

Decay	Magnitude c_r	Phase ϕ_r (rad.)	Fraction $\mathcal{F}_r$ (%)
$f_0(980)$	3.350 ± 0.237	0.528 ± 0.155	133.960 ± 25.430
$f_0(1500)$	0.203 ± 0.050	-1.436 ± 0.322	4.067 ± 1.912
$f_2'(1525)$	0.002 ± 0.000	-1.013 ± 0.228	5.412 ± 1.718
$f_0(1710)$	0.244 ± 0.066	-0.508 ± 0.196	4.368 ± 2.408
$f_2(2010)$	0.001 ± 0.000	0.078 ± 0.382	1.463 ± 0.872
χ_{c0}	0.111 ± 0.031	0.429 ± 2.197	4.675 ± 2.466
a_{S0}	1.000 ± 0.000	0.000 ± 0.000	
a_{S1}	0.978 ± 0.085	2.233 ± 0.104	174.560 ± 33.552
a_{S2}	0.505 ± 0.089	-1.517 ± 0.144	
NLL	-26881.8		

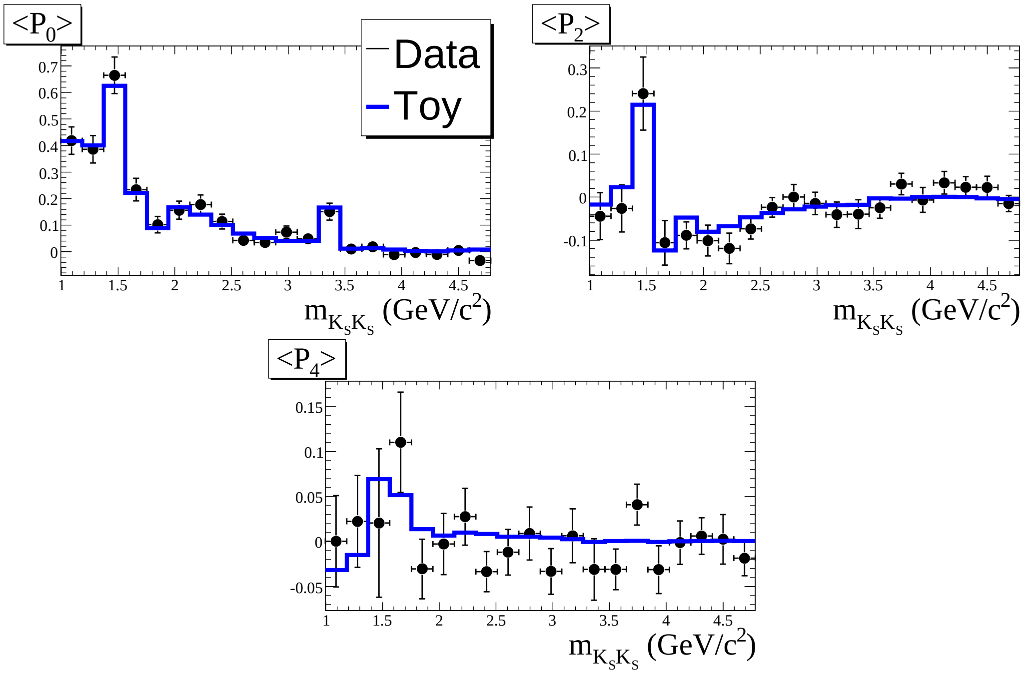

Figure 6.18: $B^+ \to K^0_S K^0_S K^+$ angular moments for data (points) and fit model (blue line). Fit model used is the one given in Table 6.10, which is like Model B, but with the addition of a D-wave polynomial NR contribution.

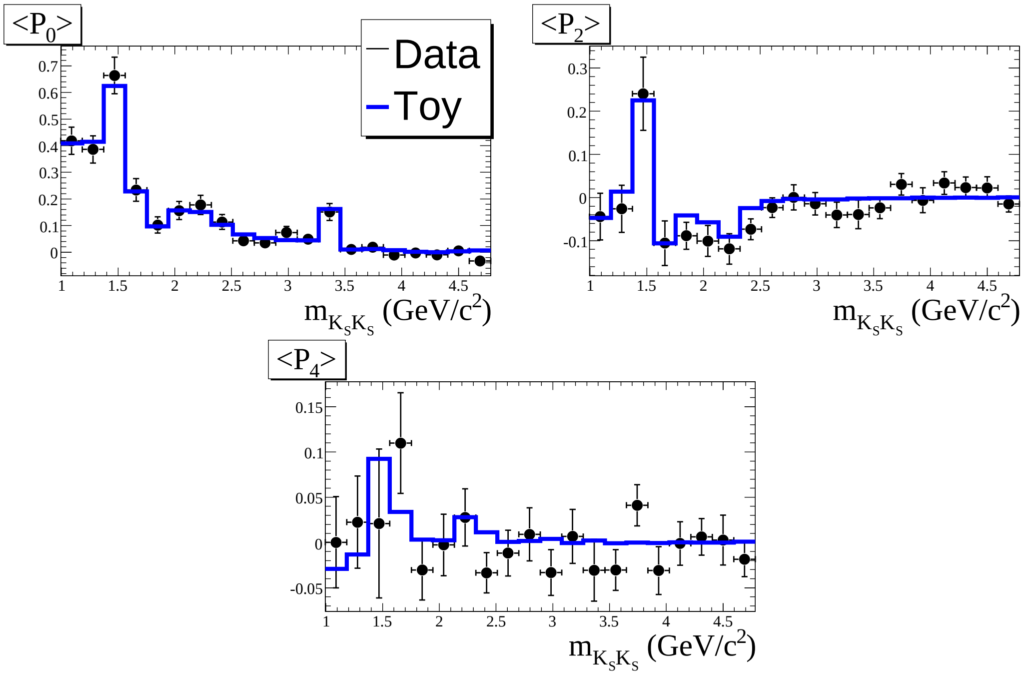

Figure 6.19: $B^+ \rightarrow K_S^0 K_S^0 K^+$ angular moments for data (points) and fit model (blue). Fit model used is the one given in Table 6.11, including the standard resonances, the $f_2(2300)$, and an S-wave polynomial NR model.

Table 6.13: Isobar magnitudes and phases from a CP-blind fit to $B^0 \to K^+K^-K^0_S$ data, with the initial Dalitz model (Model A). The errors are statistical only.

Decay	Magnitude c_r	Phase ϕ_r (rad.)	Fraction $\mathcal{F}_r$ (%)
$\phi(1020)$	0.00885 ± 0.00076	-0.384 ± 0.204	13.360 ± 1.099
$f_0(980)$	0.490 ± 0.040	-0.127 ± 0.128	24.336 ± 5.392
$f_X(1500)$	0.144 ± 0.015	-0.231 ± 0.128	6.484 ± 1.512
NR(K^+K^-)	1.0 (fixed)	0.0 (fixed)	106.630 ± 13.047
NR($K^+K^0_S$)	0.271 ± 0.053	1.556 ± 0.245	7.781 ± 2.844
NR($K^-K^0_S$)	0.339 ± 0.054	-1.680 ± 0.234	12.176 ± 3.801
χ_{c0}	0.033 ± 0.004	0.412 ± 0.502	3.277 ± 1.072
D^-	1.774 ± 0.205	-	3.516 ± 1.031
D^-_s	0.928 ± 0.187	-	1.130 ± 0.400
N(signal), $K^0_S \to \pi^+\pi^-$	1416 ± 44		
N(signal), $K^0_S \to \pi^0\pi^0$	156 ± 17		
$N(B\overline{B})$, $K^0_S \to \pi^+\pi^-$	48 ± 29		
$N(B\overline{B})$, $K^0_S \to \pi^0\pi^0$	54 ± 18		
NLL	-28304.5		

$K^0_S \to \pi^+\pi^-$ mode only. (The ${}_s\mathcal{P}lot$s for the $K^0_S \to \pi^0\pi^0$ mode look reasonable, but have large errors.)

In Fig. 6.23, we show the DP ${}_s\mathcal{P}lot$s for this fit. The background model does a good job overall of describing the DP distribution, with only small discrepancies. The signal PDF also agrees quite well with the data. To examine the agreement of the signal model more closely, we will look at angular moments, as shown in the next section.

Angular Moments

We now calculate the angular moments, comparing data ${}_s\mathcal{P}lot$s versus toy. The angular moments are shown in Fig. 6.24. The agreement between the fit model and data is good. There is a small hint of a discrepancy in the 2nd-order moment for $m_{K^+K^-}$ in the (1.5 - 2.3) GeV/c^2 region.

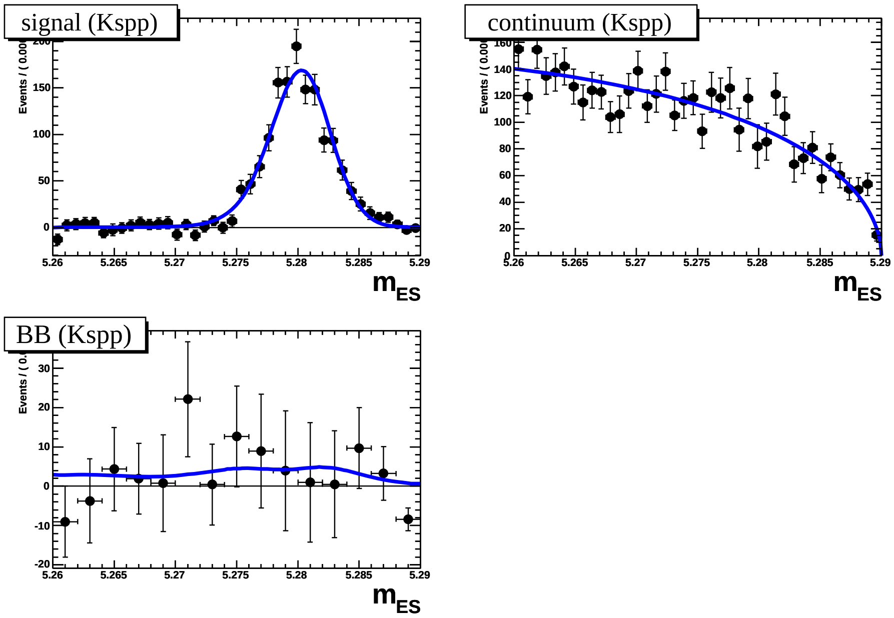

Figure 6.20: m_{ES} ${}_s\mathcal{P}lot$s for $B^0 \to K^+K^-K^0_S$, for signal and backgrounds. Using the initial Dalitz model (Model A). $K^0_S \to \pi^+\pi^-$ mode only.

6.4.2 Testing Alternative DP Models

We test other DP models in this section, motivated by the $B^+ \to K^+K^-K^+$ and $B^+ \to K^0_S K^0_S K^+$ studies.

First, we replace the $f_X(1500)$ with the $f_0(1500)$, $f_2'(1525)$, and $f_0(1710)$, so that we are using the same resonances as in $B^+ \to K^+K^-K^+$ and $B^+ \to K^0_S K^0_S K^+$. The NLL improves by 8.1 units, with 4 additional floating parameters.

Next, we replace the exponential NR model with a polynomial S+P-wave model, as shown in Eq. 2.56. The best fit result is shown in Table 6.14. The NLL improves by 7.3 units, with 6 additional floating parameters. We will refer to this as the $B^0 \to K^+K^-K^0_S$ Model B. It is similar to Model B in $B^+ \to K^+K^-K^+$ and $B^+ \to K^0_S K^0_S K^+$. The angular moments for this model are shown in Figs. 6.25 and 6.26.

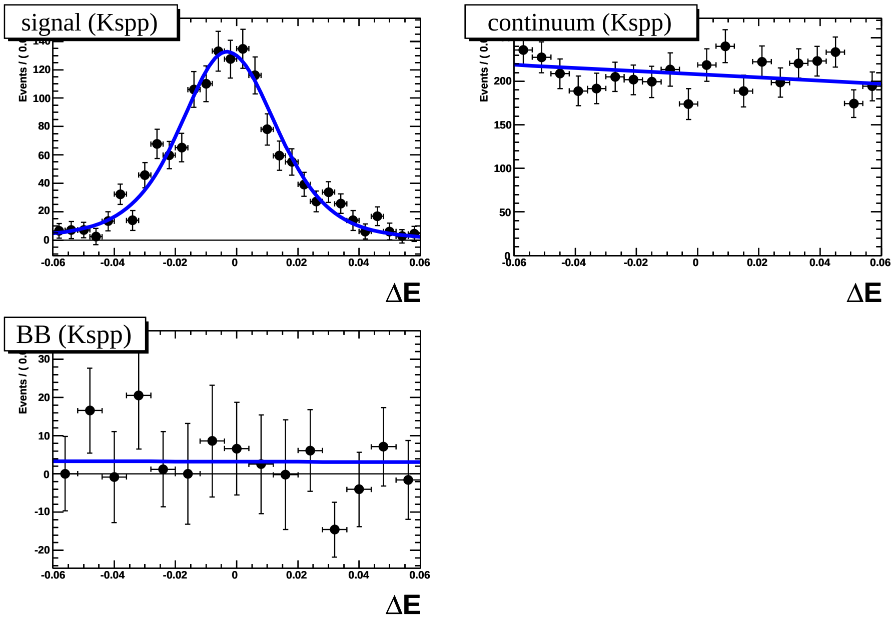

Figure 6.21: ΔE ${}_s\mathcal{P}lot$s for $B^0 \to K^+K^-K^0_S$, for signal and backgrounds. Using the initial Dalitz model (Model A). $K^0_S \to \pi^+\pi^-$ mode only.

6.5 Testing Additional Resonances

At this point, we would like to use the models that we have referred to as “Model B” for each of the three $B \to KKK$ modes. To see if there are any additional resonances that we should include in our models, we test for the following resonances:

- $f_0(1370)$, $a_0^0(1450)$, $f_2(1270)$, $f_2(2010)$, and $f_2(2300)$ in all three modes.
- $a_0^+(980)$ and $a_0^+(1450)$ in $B^+ \to K^0_S K^0_S K^+$, and $a_0^-(980)$ and $a_0^-(1450)$ in $B^0 \to K^+K^-K^0_S$.
- $\phi(1680)$ in $B^+ \to K^+K^-K^+$ and $B^0 \to K^+K^-K^0_S$.

We test for these resonances by adding them one-at-a-time to model B, performing *CP*-blind fits to data, and observing how much the NLL improves by including each resonance. The results of these fits are summarized in Table 6.15. This table also lists the fit fraction for each resonance. We can make a number of observations based on this table.

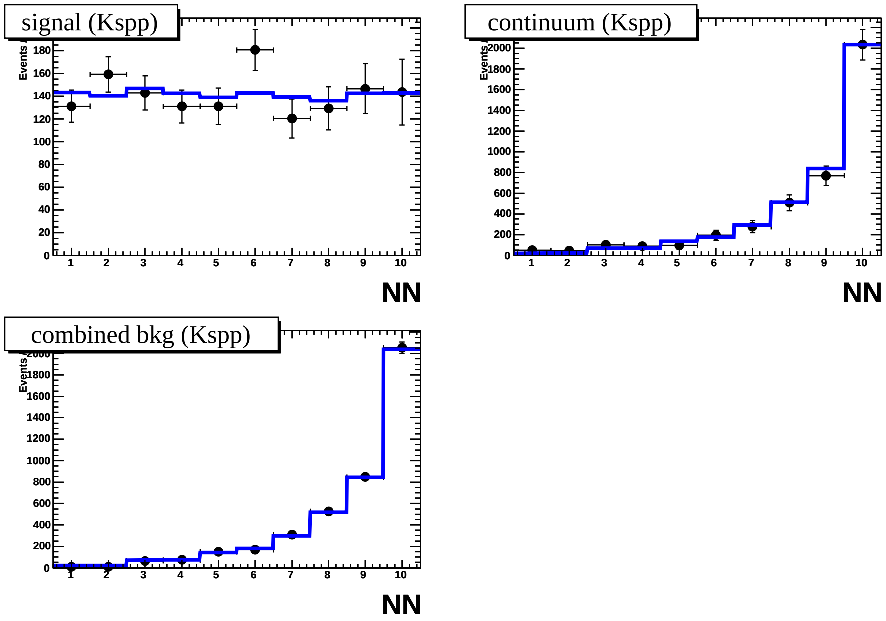

Figure 6.22: NN ${}_s\mathcal{P}lot$s for $B^0 \to K^+K^-K^0_S$, for signal, continuum, and the combined background (continuum plus $B\overline{B}$). Using the initial Dalitz model (Model A). $K^0_S \to \pi^+\pi^-$ mode only.

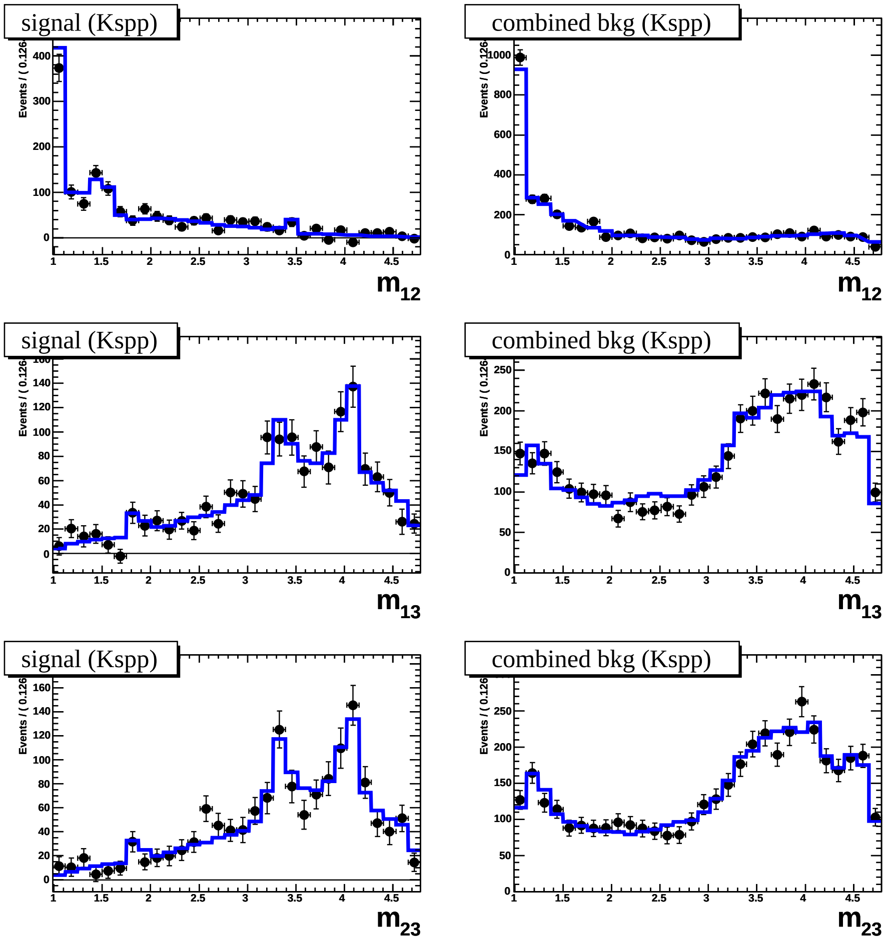

Figure 6.23: DP ${}_s\mathcal{P}lot$s for $B^0 \to K^+K^-K^0_S$, for signal and combined background (continuum plus non-peaking $B\overline{B}$). Using the initial Dalitz model (Model A). $K^0_S \to \pi^+\pi^-$ mode only.

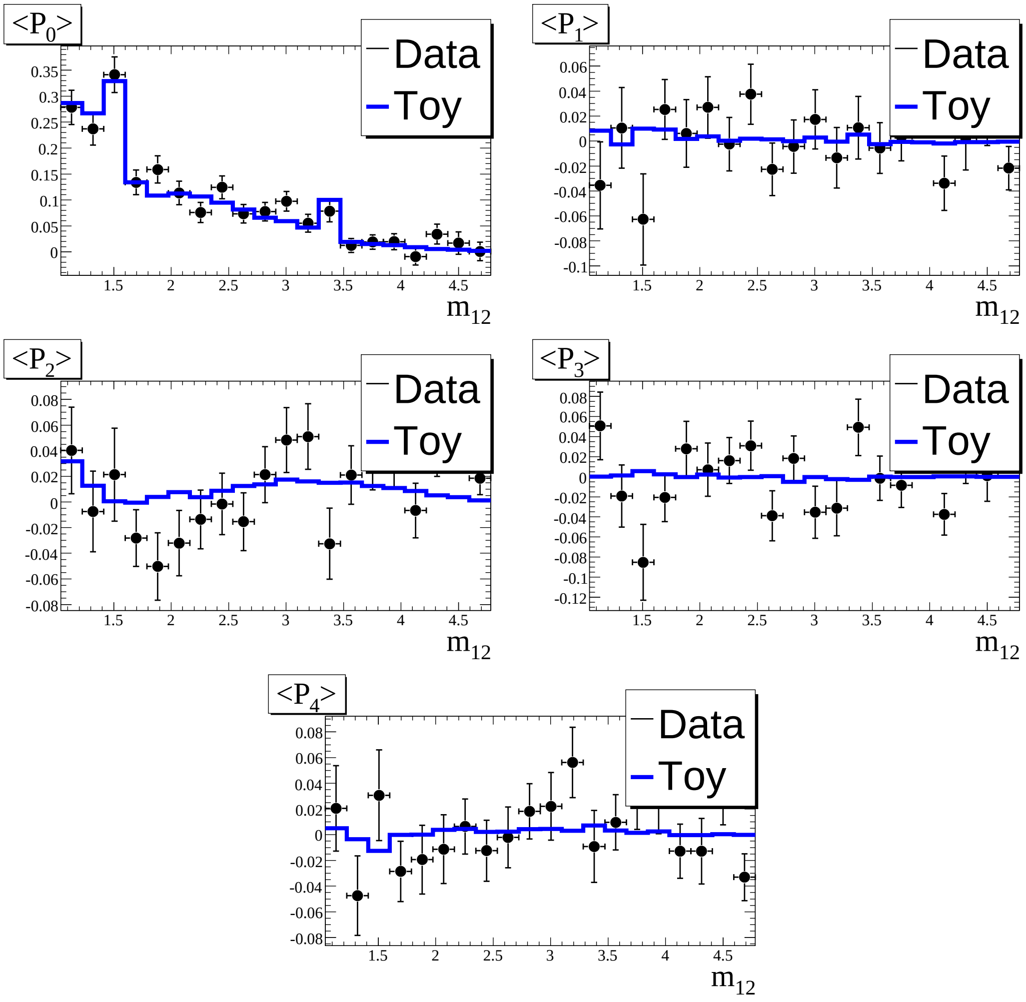

Figure 6.24: $B^0 \to K^+K^-K^0_S$ angular moments for data (points) and fit model (blue line). Using the initial Dalitz model (Model A). $K^0_S \to \pi^+\pi^-$ mode only. The $\phi(1020)$-region ($m_{K^+K^-} < 1.04\,\text{GeV}$) is excluded.

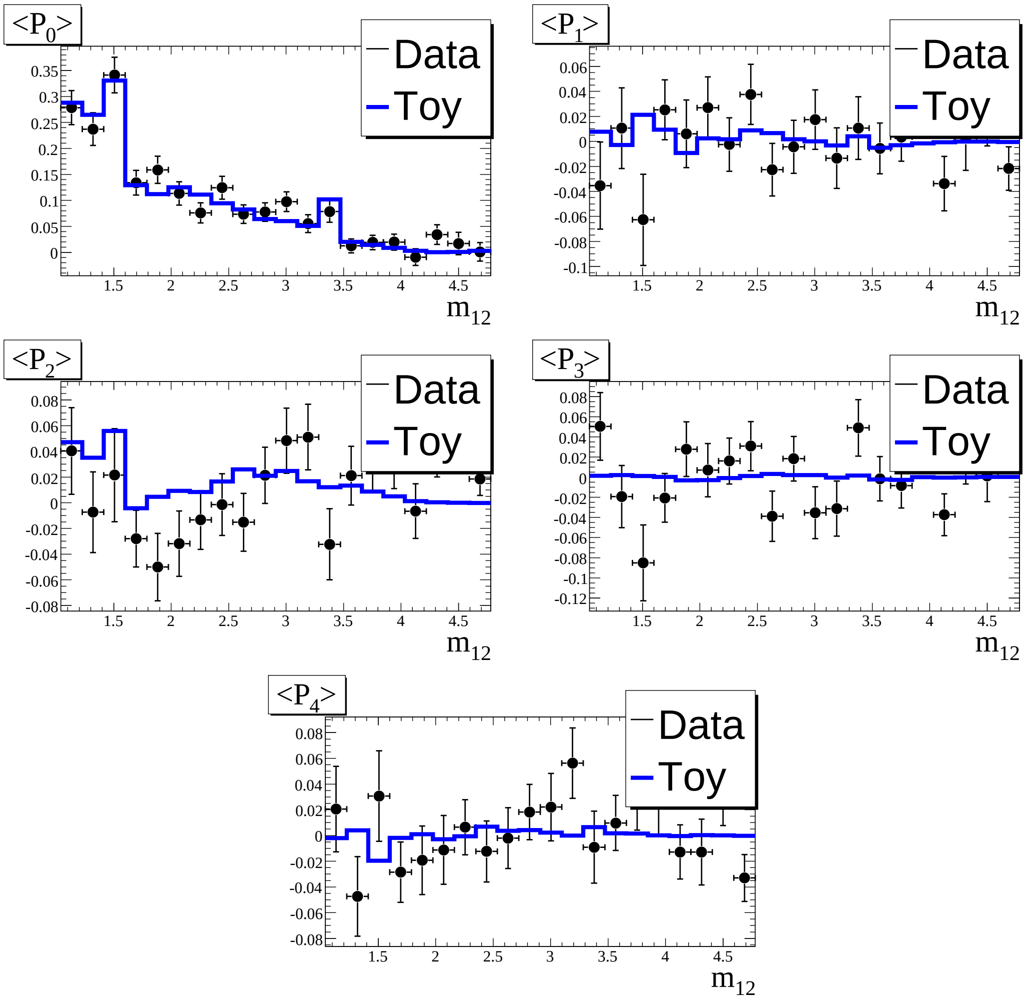

Figure 6.25: $B^0 \to K^+K^-K^0_S$ angular moments for data (points) and fit model (blue line). Fit model used is Model B (i.e., the $f_X(1500)$ replaced by the $f_0(1500)$, $f_2'(1525)$, and $f_0(1710)$, and using a polynomial S+P-wave NR model). $K^0_S \to \pi^+\pi^-$ mode only. The $\phi(1020)$-region ($m_{K^+K^-} < 1.04\,\text{GeV}$) is excluded.

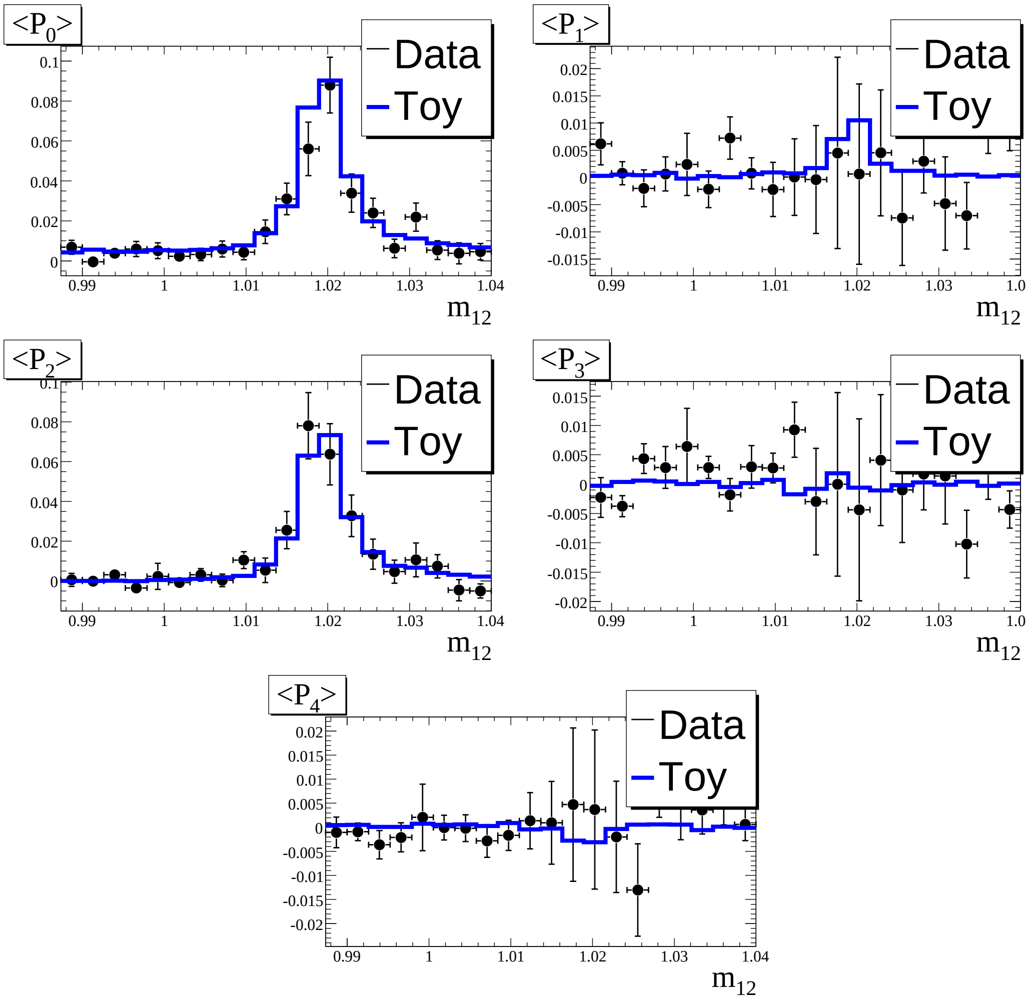

Figure 6.26: $B^0 \to K^+K^-K^0_S$ angular moments for data (points) and fit model (blue line), for the low-$m_{K^+K^-}$ region only. Fit model used is Model B (i.e., the $f_X(1500)$ replaced by the $f_0(1500)$, $f_2'(1525)$, and $f_0(1710)$, and using a polynomial S+P-wave NR model). $K^0_S \to \pi^+\pi^-$ mode only.

Table 6.14: Isobar magnitudes and phases from a CP-blind fit to $B^0 \to K^+K^-K^0_S$ data, using Model B (i.e., the $f_X(1500)$ replaced by the $f_0(1500)$, $f_2'(1525)$, and $f_0(1710)$, and using a polynomial S+P-wave NR model). The errors are statistical only.

Decay	Magnitude c_r	Phase ϕ_r (rad.)	Fraction $\mathcal{F}_r$ (%)
$\phi(1020)$	0.040 ± 0.004	0.379 ± 0.287	12.958 ± 1.299
$f_0(980)$	2.236 ± 0.424	0.761 ± 0.237	24.179 ± 7.516
$f_0(1500)$	0.224 ± 0.049	0.261 ± 0.271	1.892 ± 0.793
$f_2'(1525)$	0.00079 ± 0.00029	0.938 ± 0.423	0.419 ± 0.278
$f_0(1710)$	0.774 ± 0.099	2.026 ± 0.192	16.810 ± 5.974
a_{S0}	1.0 (fixed)	0.0 (fixed)	121.128 ± 17.612
a_{S1}	1.320 ± 0.219	-2.557 ± 0.144	121.128 ± 17.612
a_{S2}	0.654 ± 0.191	1.023 ± 0.235	121.128 ± 17.612
a_{P0}	1.297 ± 0.199	1.135 ± 0.218	121.128 ± 17.612
a_{P1}	0.295 ± 0.165	-1.328 ± 0.512	121.128 ± 17.612
a_{P2}	0.426 ± 0.143	-2.249 ± 0.441	121.128 ± 17.612
χ_{c0}	0.149 ± 0.022	-0.358 ± 0.494	3.204 ± 0.707
D^-	8.029 ± 1.056	-	3.429 ± 0.652
D_s^-	4.157 ± 0.883	-	1.081 ± 0.381
NLL	-28319.9		

We already mentioned the poor modeling of the second-order angular moment in $B^+ \to K^0_S K^0_S K^+$, and a possible explanation in terms of the $f_2(2300)$. However, the $B^+ \to K^+K^-K^+$ fit shows a negligibly small contribution for this resonance, putting a serious constraint on the $B^+ \to f_2(2300)K^+$ branching fraction.

BABAR's recent $B^0 \to K^0_S K^0_S K^0_S$ analysis found evidence for the $f_2(2010)$, but found a large fit fraction: $(9 \pm 3)\%$ for their first solution and $(10 \pm 2)\%$ for their second solution. We find much smaller fit fractions for this resonance, in strong disagreement with the $B^0 \to K^0_S K^0_S K^0_S$ result. There is some NLL improvement in both $B^+ \to K^+K^-K^+$ and $B^+ \to K^0_S K^0_S K^+$ when adding the $f_2(2010)$, but not enough to be conclusive.

Modest improvements in NLL are seen in $B^+ \to K^+K^-K^+$ for $f_0(1370)$, $a_0^0(1450)$, and $f_2(1270)$. However, there is no evidence for these resonances in $B^+ \to K^0_S K^0_S K^+$ or $B^0 \to K^+K^-K^0_S$. Furthermore, these are all broad resonances, which makes them more difficult to interpret. The $f_0(1370)$ and $a_0^0(1450)$, in particular, are broad scalars, which are very difficult to separate from the large fraction of nonresonant and f_0 decays. A mismodeling of the nonresonant decays could result in a fake signal for broad scalars.

In summary, we conclude that there is no strong evidence for any of these resonances.

Table 6.15: Summary of tests in which we added various resonances one-at-a-time to the isobar model. We show the improvement in $-\log\mathcal{L}$ (ΔNLL) due to the addition of each resonance, and the fit fraction FF_j for that resonance. The default isobar models in this table are the models called "Model B" in Sections 6.2-6.4.

Resonance	$B^+ \to K^+K^-K^+$		$B^+ \to K^0_S K^0_S K^+$		$B^0 \to K^+K^-K^0_S$	
	ΔNLL	FF_j (%)	ΔNLL	FF_j (%)	ΔNLL	FF_j (%)
$a_0^{\pm}(980)$	-	-	2.3	1.1 ± 0.8		
$f_0(1370)$	7.2	5.3 ± 2.0	1.3	7 ± 9	2.8	4.8 ± 3.7
$a_0^0(1450)$	7.2	8.5 ± 3.8	0.8	7 ± 18		
$a_0^{\pm}(1450)$	-	-	3.8	2.5 ± 1.4		
$\phi(1680)$	1.5	0.10 ± 0.13	-	-		
$f_2(1270)$	7.0	0.41 ± 0.18	0.6	0.3 ± 0.4	3.5	0.44 ± 0.30
$f_2(2010)$	5.4	0.35 ± 0.18	5.2	1.5 ± 0.9		
$f_2(2300)$	3.7	0.15 ± 0.10	9.0	2.1 ± 1.0		

6.6 Summary and Conclusions

Using previous analyses' DP models of $B^+ \to K^+K^-K^+$ and $B^0 \to K^+K^-K^0_S$ as a starting point, we have tested a number of different DP models. For each of the three $B \to KKK$ modes, we have found a model (which we have called Model B) which has a better NLL than the initial model.

The two primary reasons for testing different DP models in $B \to KKK$ are:

- Reducing systematic errors due to the use of an incorrect DP model. Knowing the NR model is particularly important for reducing the systematic on the β_{eff} measurement in $B^0 \to K^+K^-K^0_S$, as that measurement depends on knowing whether the K^+K^- is in an odd-L or even-L state.

- Understanding the nature of the $f_X(1500)$, seen previously in $B^+ \to K^+K^-K^+$ and $B^0 \to K^+K^-K^0_S$, but which doesn't fit easily into the known picture of K^+K^- resonances.

Our tests in $B^+ \to K^+K^-K^+$, as well as in $B^+ \to K^0_S K^0_S K^+$, indicate that the $f_X(1500)$ cannot be adequately described by a single scalar resonance, but that a combination of the $f_0(1500)$ and $f_2(1525)$, interfering with the $f_0(1710)$, does provide an adequate description. The angular moments show particularly strong evidence for a tensor resonance in this mass region. The evidence in $B^0 \to K^+K^-K^0_S$ is less strong, but even in that mode this $f_0(1500)$ / $f_2'(1525)$ / $f_0(1710)$ model produces a small improvement in NLL. Not only does this model match the $B \to KKK$ data better, it also allows us to eliminate the ad-hoc $f_X(1500)$ state.

The NR was and still is poorly understood. For all we know, it may be the sum of a large number of broad resonances. However, knowing its exact nature is less important right now than understanding its *CP* content in $B^0 \to K^+K^-K^0_S$. We found that in $B^+ \to K^+K^-K^+$, a polynomial NR model containing both S- and P-wave terms produced a greatly improved NLL with respect to the initial exponential NR model. The polynomial model also has a very simple *CP* structure in $B^0 \to K^+K^-K^0_S$, making it convenient. The large number of free parameters, including phase variation over the DP, makes the polynomial model very flexible and less "model-dependent." This reduces the risk that our measurements will depend on questionable assumptions about the NR model.

The models we have referred to as "Model B" include the $f_0(1500)$ / $f_2'(1525)$ / $f_0(1710)$ resonances, as well as the polynomial NR model. We have tested adding extra resonances to this model, and found no clear evidence for any of them. We also tested for a D-wave NR contribution in $B^+ \to K^+K^-K^+$ and $B^+ \to K^0_S K^0_S K^+$, and we decided that the modest fit improvement that it produces is not enough to merit including it, given that it greatly increases the (already large) number of parameters in the fit.

In conclusion, we believe that "Model B" is a good DP model, clearly superior to previous $B \to KKK$ models, and we will use it as our nominal model for all three $B \to KKK$ modes.

Chapter 7

Fit Results

7.1 $B^+ \to K^+K^-K^+$

We float 43 parameters in the nominal fit, including

- 11 isobar magnitudes (c) and 11 isobar phases (ϕ). Since we only measure *relative* magnitudes and phases, we fix the NR coefficient a_{S0} as a reference, with magnitude 1 and phase 0.

- 8 *CP*-violating isobar parameters: 4 b's and 4 δ's. We have one (b, δ) pair for the $\phi(1020)$, one pair for the $f_0(980)$, and one pair for the χ_{c0}. To keep the number of parameters small (which helps fit stability), we have another pair that is shared by all of the NR isobars. Finally, we have a pair that is shared by the $f_0(1500)$, $f_2'(1525)$, and $f_0(1710)$. Since only relative values of δ can be measured in B^+ decays, we fix the NR δ to zero as a reference. We also fix the χ_{c0} b to zero, since direct A_{CP} is known to be very small in $B^+ \to (c\bar{c})K^+$ decays.

- 8 yields: signal, continuum, and 6 $B\overline{B}$ categories (all of them except for "BBchmls").

- The means of the signal m_{ES} and ΔE PDF's (i.e., the x_0 in Eq. 5.7).

- The slope of the continuum ΔE PDF, and the shape parameter c of the continuum m_{ES} PDF (Eq. 5.13).

- The overall asymmetry A_{CP} of the continuum backgrounds.

We perform hundreds of randomized fits to data, using the nominal isobar model. The two best solutions that we find are separated by 2.8 units of NLL. The best solution is shown in Tables 7.1-7.3. The second solution is shown in Tables 7.4-7.6. The total branching fraction is calculated as

$$\mathcal{B}(B \to KKK) = \frac{N_{sig}}{\bar{\varepsilon} N_{B\bar{B}}}\,, \tag{7.1}$$

where $\bar{\varepsilon}$ is the efficiency averaged over the DP, which we compute by weighting the efficiency map (Sec. 5.2.4) by the measured DP distribution.

The second solution differs from the best solution in several respects. The second solution has a smaller $f_0(980)$ fraction, a different NR structure, and rather different *CP*-violating parameters. Most strikingly, the $f_0(980)$ A_{CP} is very large for the second solution, nearly 60%. One might be surprised that it is possible for a solution to have such a large A_{CP}, given how many signal events there are. However a couple of points should be noted. First, the $f_0(980)$ is very broad, making it difficult to distinguish from the NR. Second, in addition to the *CP*-asymmetries in isobars (quantified by A_{CP}), there can be *CP*-asymmetries in the interference between isobars (which depend on the A_{CP} and $\Delta\phi$ of each of the interfering isobars). The result is that the A_{CP} of the $f_0(980)$ can be large by trading off with the NR A_{CP} and the *CP*-asymmetry in $f_0(980)$-NR interference.

Interestingly, a fairly significant A_{CP} is seen for the $\phi(1020)$ in the best solution. As we mentioned in Sec. 2.5, this A_{CP} is expected to be quite small in the SM, $(0.0 - 4.7)\%$. To calculate the significance of this result, we perform a likelihood scan in $A_{CP}(\phi(1020))$, shown in Fig. 7.1. At each scan point, we perform randomized fits, taking the result with the best likelihood at each point. In this fashion, the likelihood scan explores the multiple solutions. We include systematic errors in the likelihood scan by convolving the statistical likelihood scan with a Gaussian function representing the systematic uncertainty. The systematic uncertainty is calculated only for the best solution, and then assumed to be constant over the entire likelihood scan range. From the likelihood scan, we find that $A_{CP}(\phi(1020))$ differs from zero at

2.8σ significance (or 2.9σ if only statistical errors are included). The significance is calculated as $\sqrt{2\Delta\log\mathcal{L}}$.

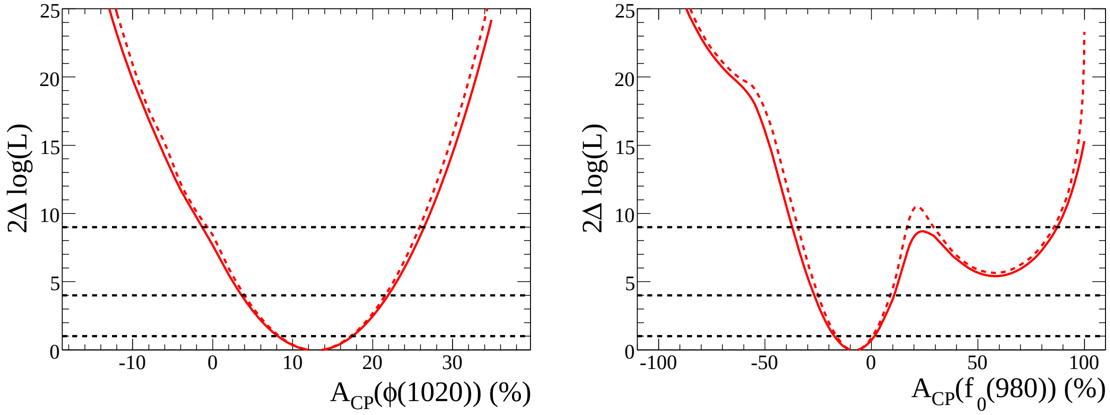

Figure 7.1: Statistical (dashed line) and total (solid line) scans of $-2\Delta\log\mathcal{L}$ as a function of $A_{CP}(\phi K^+)$ (left) and $A_{CP}(f_0(980)K^+)$ (right) for $B^+ \to K^+K^-K^+$.

Similarly, we perform a likelihood scan in $A_{CP}(f_0(980))$, shown in Fig. 7.1. The second solution is clearly visible. This is a different situation from the $A_{CP}(\phi(1020))$ scan, where the second solution is only barely visible because it has only a slightly different value of $A_{CP}(\phi(1020))$ than the best solution.

Figures 7.2 and 7.3 show the signal m_{12} distribution (using ${}_s\mathcal{P}lots$) for B^+ and B^- events separately. In addition to the hint of *CP*-violation for the $\phi(1020)$, there is a clear indication of *CP*-violation in the D^0 peak. This *CP*-violation has already been measured by *BABAR* in a separate analysis [45], so we do not measure it in this analysis, but rather fix it to the world-average value of $A_{CP} = 0.24 \pm 0.08$. As a cross-check, we float it, and find $A_{CP} = 0.35 \pm 0.09$, consistent with the world-average.

Systematics are done for the best solution only, and are described in detail in Sec. 7.4.

7.2 $B^+ \to K^0_S K^0_S K^+$

We float 41 parameters in the nominal fit, including

Table 7.1: Isobar parameters from the unblinded fit to $B^+ \to K^+K^-K^+$ data, using the nominal signal model. Errors are statistical only.

Component	c_r	ϕ_r (rad.)	b_r	δ_r (rad.)
$\phi(1020)K^+$	0.0311 ± 0.0043	3.10 ± 0.23	-0.064 ± 0.022	0.20 ± 0.12
$f_0(980)K^+$	1.64 ± 0.23	2.07 ± 0.20	0.040 ± 0.041	0.08 ± 0.06
$f_0(1500)K^+$	0.179 ± 0.031	-0.78 ± 0.19		
$f_2'(1525)K^+$	0.00130 ± 0.00022	0.59 ± 0.18	-0.07 ± 0.05	-0.01 ± 0.05
$f_0(1710)K^+$	0.254 ± 0.044	0.77 ± 0.16		
$\chi_{c0}K^+$	0.114 ± 0.017	0.16 ± 0.20	0 (fixed)	-0.04 ± 0.11
a_{S0}	1.0 (fixed)	0.0 (fixed)	-0.030 ± 0.022	0 (fixed)
a_{S1}	2.09 ± 0.38	2.79 ± 0.24		
a_{S2}	0.33 ± 0.08	2.74 ± 0.22		
a_{P0}	1.6 ± 0.5	0.12 ± 0.34		
a_{P1}	0.80 ± 0.07	-2.78 ± 0.11		
a_{P2}	0.49 ± 0.15	-1.93 ± 0.30		
N(BBcharm1)	169.8 ± 20.6			
N(BBcharm2)	22.9 ± 9.4			
N(BBcharm3)	132.9 ± 33.8			
N(BBcharm4)	260.8 ± 55.6			
N(BBcharm5)	238.2 ± 21.6			
N(BBcharm6)	45.5 ± 9.7			
N(cont)	6015.9 ± 91.2			
N(signal)	5269.0 ± 84.2			

Table 7.2: Fit fractions and branching fractions from the unblinded fit to $B^+ \to K^+K^-K^+$ data, using the nominal signal model. We quote numbers both for the total NR contribution, and for the S-wave and P-wave NR pieces individually. Both statistical and systematic errors are given.

Component	Fraction $\mathcal{F}_r$ (%)	$\mathcal{B}(B^+ \to K^+K^-K^+) \times \mathcal{F}_r (\times 10^{-6})$
$\phi(1020)K^+$	$12.9^{+0.5+1.0}_{-0.7-0.7}$	$4.48 \pm 0.22^{+0.33}_{-0.24}$
$f_0(980)K^+$	$27 \pm 5 \pm 8$	$9.4 \pm 1.6 \pm 2.8$
$f_0(1500)K^+$	$2.1 \pm 0.5 \pm 1.6$	$0.74 \pm 0.18 \pm 0.52$
$f_2'(1525)K^+$	$2.0 \pm 0.4 \pm 0.4$	$0.69 \pm 0.16 \pm 0.13$
$f_0(1710)K^+$	$3.2^{+0.8}_{-0.6} \pm 1.4$	$1.12 \pm 0.25 \pm 0.50$
$\chi_{c0}K^+$	$3.2 \pm 0.4 \pm 0.1$	$1.12 \pm 0.15 \pm 0.06$
NR	$66 \pm 8 \pm 22$	$22.8 \pm 2.7 \pm 7.6$
NR (S-wave)	$151^{+66}_{-44} \pm 77$	$52^{+23}_{-14} \pm 27$
NR (P-wave)	$69^{+62}_{-33} \pm 77$	$24^{+22}_{-12} \pm 27$
$\mathcal{B}$ (Total) ($\times 10^{-6}$)	$34.6 \pm 0.6 \pm 0.9$	
$\mathcal{B}$ (Charmless) ($\times 10^{-6}$)	$33.4 \pm 0.5 \pm 0.9$	

Table 7.3: *CP*-violating parameters from the unblinded fit to $B^+ \to K^+K^-K^+$ data, using the nominal signal model. Note that the *CP*-violating parameters for the $f_2'(1525)$ are also shared by the $f_0(1500)$ and $f_0(1710)$. A_{CP} (Charmless) gives the total integrated A_{CP}, excluding the χ_{c0}. Both statistical and systematic errors are given.

Component	A_{CP} (%)	$\Delta\phi$ (rad.)
$\phi(1020)$	$12.8 \pm 4.4 \pm 1.3$	$0.39 \pm 0.24^{+0.06}_{-0.08}$
$f_0(980)$	$-8 \pm 8 \pm 4$	$0.16 \pm 0.12 \pm 0.11$
$f_2'(1525)$	$14 \pm 10 \pm 4$	$-0.03 \pm 0.10 \pm 0.06$
χ_{c0}	0.0 (fixed)	$-0.08 \pm 0.22 \pm 0.03$
NR	$6.0 \pm 4.4 \pm 1.9$	0.0 (fixed)
A_{CP} (Charmless) (%)	$-1.7^{+1.9}_{-1.4} \pm 1.4$	

Table 7.4: Isobar parameters for the second solution from the unblinded fit to $B^+ \to K^+K^-K^+$ data, using the nominal signal model. Errors are statistical only.

Component	c_r	ϕ_r (rad.)	b_r	δ_r (rad.)
$\phi(1020)K^+$	0.043 ± 0.009	-0.93 ± 0.22	-0.037 ± 0.022	-0.17 ± 0.11
$f_0(980)K^+$	1.5 ± 0.5	-0.60 ± 0.20	-0.32 ± 0.11	-0.21 ± 0.12
$f_0(1500)K^+$	0.28 ± 0.07	-0.72 ± 0.26		
$f_2'(1525)K^+$	0.00160 ± 0.00038	0.75 ± 0.27	-0.09 ± 0.05	0.01 ± 0.05
$f_0(1710)K^+$	0.32 ± 0.08	0.79 ± 0.29		
$\chi_{c0}K^+$	0.170 ± 0.038	0.53 ± 0.27	0 (fixed)	-0.04 ± 0.10
a_{S0}	1.0 (fixed)	0.0 (fixed)	-0.062 ± 0.024	0 (fixed)
a_{S1}	0.4 ± 1.2	0.0 ± 2.8		
a_{S2}	0.45 ± 0.35	-1.14 ± 0.33		
a_{P0}	2.3 ± 1.9	2.27 ± 0.44		
a_{P1}	0.85 ± 0.30	-1.99 ± 0.21		
a_{P2}	0.77 ± 0.38	-1.04 ± 0.32		
N(BBcharm1)	170.0 ± 20.6			
N(BBcharm2)	23.1 ± 9.4			
N(BBcharm3)	133.4 ± 33.8			
N(BBcharm4)	255.6 ± 55.4			
N(BBcharm5)	239.2 ± 21.7			
N(BBcharm6)	45.5 ± 9.7			
N(cont)	6012.7 ± 91.2			
N(signal)	5275.4 ± 84.2			

Table 7.5: Fit fractions for the second solution from the unblinded fit to $B^+ \to K^+K^-K^+$ data, using the nominal signal model. The errors are statistical only.

Component	Fraction $\mathcal{F}_r$ (%)
$\phi(1020)K^+$	12.3 ± 0.6
$f_0(980)K^+$	12.5 ± 4.5
$f_0(1500)K^+$	2.6 ± 0.5
$f_2'(1525)K^+$	1.50 ± 0.36
$f_0(1710)K^+$	2.5 ± 0.6
$\chi_{c0}K^+$	3.6 ± 0.5
NR	122 ± 16
NR (S-wave)	91 ± 23
NR (P-wave)	48 ± 64

Table 7.6: CP-violating parameters for the second solution from the unblinded fit to $B^+ \to K^+K^-K^+$ data, using the nominal signal model. The errors are statistical only.

Component	A_{CP} (%)	$\Delta\phi$ (rad.)
$\phi(1020)$	7.4 ± 4.5	-0.34 ± 0.22
$f_0(980)$	58 ± 16	-0.42 ± 0.24
$f_2'(1525)$	17 ± 9	0.02 ± 0.09
χ_{c0}	0.0 (fixed)	-0.07 ± 0.20
NR	12 ± 5	0.0 (fixed)
A_{CP} (Total) (%)	-1.6 ± 1.6	

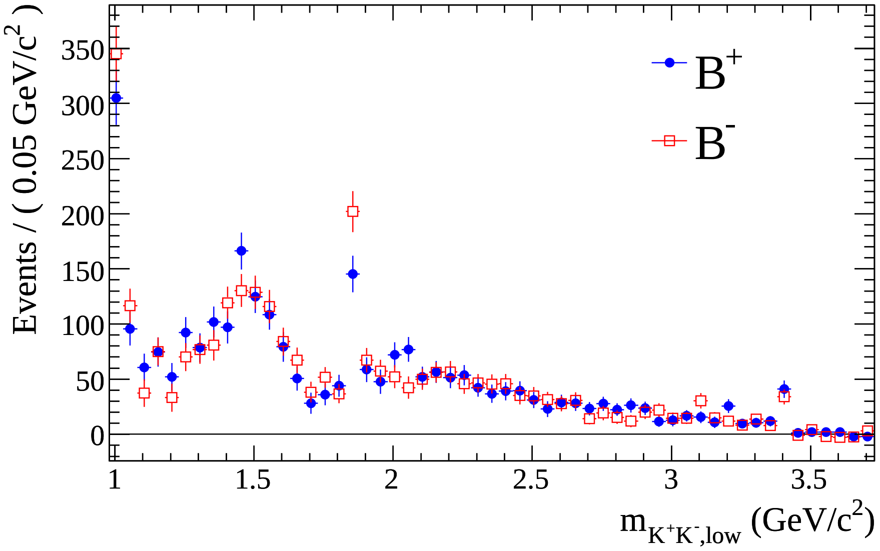

Figure 7.2: $B^+ \to K^+K^-K^+$ signal ${}_s\mathcal{P}lot$s, showing the m_{12} distribution separately for B^+ (blue filled circles) and B^- (red open squares) events. The signal category includes peaking backgrounds “BB charm5” and “BB charm 6.”

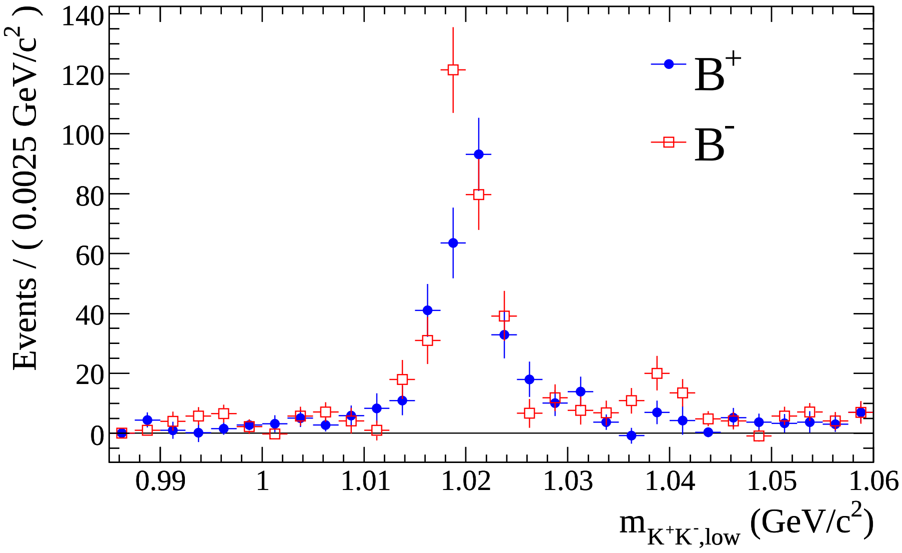

Figure 7.3: $B^+ \rightarrow K^+K^-K^+$ signal ${}_s\mathcal{P}lot$s, showing the m_{12} distribution separately for B^+ (blue filled circles) and B^- (red open squares) events, in the low-mass region. The signal category includes peaking backgrounds “BB charm5” and “BB charm 6.”

- 7 isobar magnitudes (c) and 7 isobar phases (ϕ). We fix the NR coefficient a_{S0} as a reference, with magnitude 1 and phase 0.
- 2 *CP*-violating isobar parameters: one b and one δ. Because of the small number of signal events in $B^+ \rightarrow K^0_S K^0_S K^+$, we decide to have one (b, δ) pair that is shared by all of the charmless isobars. We use a separate (b, δ) pair for the χ_{c0}, since the χ_{c0} comes from a $b \rightarrow c$ tree amplitude, rather than a $b \rightarrow s$ penguin. We fix the charmless δ to zero as a reference, and fix the χ_{c0} b to zero as we did in $B^+ \rightarrow K^+K^-K^+$.
- 2 yields: signal and continuum.
- The means of the signal m_{ES} and ΔE PDF's (i.e., the x_0 in Eq. 5.7).
- The slope of the continuum ΔE PDF, and the shape parameter c of the continuum m_{ES} PDF (Eq. 5.13).
- 18 parameters for the continuum NN PDF: 9 a_i's and 9 b_i's (see Eq. 5.14).
- The overall asymmetry A_{CP} of the continuum backgrounds.

We fit to data with the nominal isobar model. Fourteen secondary solutions are found within 4.5 NLL (i.e., 3σ) of the best solution. Of these fourteen additional solutions, two are within 1σ of the best solution. The large number of solutions indicates that there is an insufficient number of events in this mode to fully constrain all the parameters in our model. Clearly, with so many solutions, care needs to be taken in understanding our results.

The best solution is shown in Tables 7.7 and 7.8. The fourteen additional solutions are given in Appendix C. Rather than look at the additional solutions in detail, we will merely summarize their features. All solutions have similar values for the A_{CP}, varying from 2% to 4%. They also all have almost exactly the same signal yield. Where the solutions differ greatly is is in many of their fit fractions. All the solutions have consistent values for the $f_2'(1525)$ and χ_{c0} fit fractions. On the other hand, the $f_0(980)$ fit fraction varies between 69% and 152%, the $f_0(1500)$ varies between 3% and 73%, the $f_0(1710)$ varies between 4% and 38%, and the NR varies between 97 and 290. So, the branching fractions of those components cannot be measured well in $B^+ \to K^0_S K^0_S K^+$ given the present statistics.

Table 7.7: Isobar parameters from the unblinded fit to $B^+ \to K^0_S K^0_S K^+$ data, with the nominal fit model. The parameters are only given for the global best solution. See the text for discussion of the multiple solutions. The errors are statistical only.

Decay	c_r	ϕ_r (rad.)
$f_0(980)K^+$	3.35 ± 0.22	0.53 ± 0.15
$f_0(1500)K^+$	0.20 ± 0.05	-1.44 ± 0.32
$f_2'(1525)K^+$	0.00179 ± 0.00032	-1.02 ± 0.21
$f_0(1710)K^+$	0.24 ± 0.07	-0.39 ± 0.18
$\chi_{c0}K^+$	0.113 ± 0.017	0.8 ± 1.0
a_{S0}	1.0 (fixed)	0.0 (fixed)
a_{S1}	1.00 ± 0.08	2.25 ± 0.10
a_{S2}	0.51 ± 0.08	-1.48 ± 0.15
b	-0.018 ± 0.023	
δ (rad.)	-0.2 ± 0.6	
N(signal)	636 ± 28	

Because of the multiple solutions, the errors on the best solution don't give a complete picture of the errors. A better way of estimating the errors in the presence of multiple solutions is to perform a likelihood scan. We only perform a likelihood scan for A_{CP}, since this is the most important parameter for $B^+ \to K^0_S K^0_S K^+$. The scan is shown in Fig. 7.4. The systematics are calculated for the best solution only. Calculating the statistical errors by seeing where the likelihood curve crosses the line $\Delta \log \mathcal{L} = 0.5$, we get $A_{CP} = (4^{+4}_{-5} \pm 2)\%$. [1] We regard this as our final result for A_{CP}.

Figure 7.5 shows the signal $m_{K^0_S K^0_S}$ distribution (using ${}_s\mathcal{P}lot$s) for B^+ and B^- events separately. No obvious asymmetries are seen.

---

[1] One might be surprised that the errors from the likelihood scan appear to be smaller than the errors from the best solution, $A_{CP} = (4 \pm 5)\%$. After all, the likelihood scan incorporates the multiple solutions, which should make the errors bigger, not smaller. However, the errors on the best solution were determined using a method that assumes symmetric errors, and we are also rounding the errors.

Table 7.8: Fit fractions and branching fractions from the unblinded fit to $B^+ \to K^0_S K^0_S K^+$ data, using the nominal signal model. The parameters are only given for the global best solution. See the text for discussion of the multiple solutions.

Decay	Fraction $\mathcal{F}_r$ (%)	$\mathcal{B}(B^+ \to K^0_S K^0_S K^+) \times \mathcal{F}_r$
$f_0(980)K^+$	$139 \pm 25 \pm 17$	$14.7 \pm 2.8 \pm 1.8$
$f_0(1500)K^+$	$4.0 \pm 2.0 \pm 5.5$	$0.42 \pm 0.22 \pm 0.58$
$f_2'(1525)K^+$	$5.7 \pm 1.9^{+1.1}_{-0.8}$	$0.61 \pm 0.21^{+0.12}_{-0.09}$
$f_0(1710)K^+$	$4.5^{+3.7}_{-2.2} \pm 1.0$	$0.48^{+0.40}_{-0.24} \pm 0.11$
$\chi_{c0}K^+$	$5.0 \pm 0.9 \pm 0.3$	$0.53 \pm 0.10 \pm 0.04$
NR (S-wave)	$187 \pm 35 \pm 21$	$19.8 \pm 3.7 \pm 2.5$
$\Delta\phi$ (rad.)	$-0.4 \pm 1.1 \pm 0.2$	
A_{CP}(%)	$4 \pm 5 \pm 2$	
$\mathcal{B}$(Total) ($\times 10^{-6}$)	$10.6 \pm 0.5 \pm 0.3$	
$\mathcal{B}$(Charmless)($\times 10^{-6}$)	$10.1 \pm 0.5 \pm 0.3$	

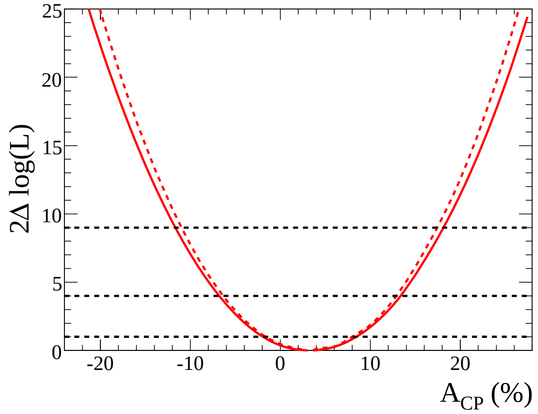

Figure 7.4: Statistical (dashed line) and total (solid line) scans of $-2\Delta \log \mathcal{L}$ as a function of A_{CP} for $B^+ \to K^0_S K^0_S K^+$.

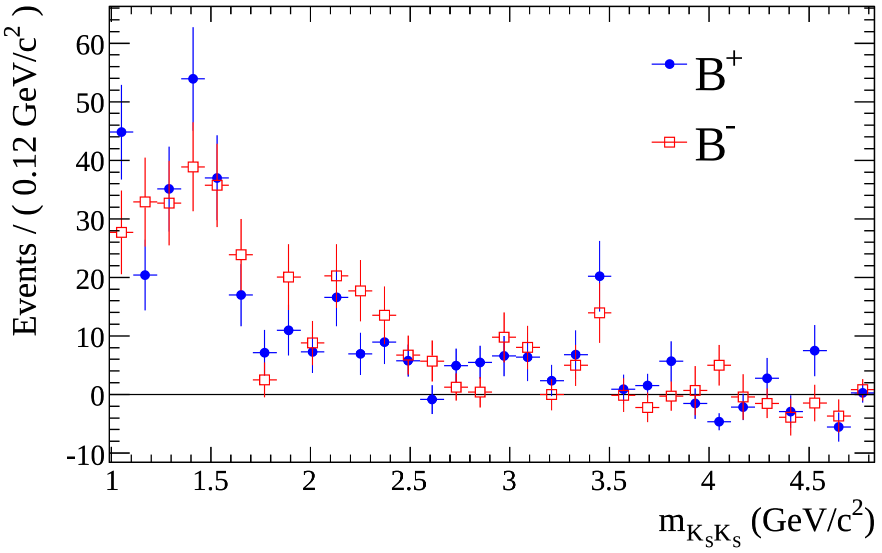

Figure 7.5: $B^+ \to K_S^0 K_S^0 K^+$ signal ${}_s\mathcal{P}lot$s, showing the $m_{K_S^0 K_S^0}$ distribution separately for B^+ (blue) and B^- (red) events. Points are signal-weighted data, and the lines are the fit model. The signal category includes the "BB 4" category.

7.3 $B^0 \to K^+K^-K^0_S$

We float 90 parameters in the nominal fit, including

- 11 isobar magnitudes (c) and 11 isobar phases (ϕ). We fix the NR coefficient a_{S0} as a reference, with magnitude 1 and phase 0.
- An additional 4 isobar magnitudes, representing the contributions from peaking backgrounds. Since these are treated as non-interfering backgrounds, the isobars only have magnitudes, not phases.
- 6 *CP*-violating isobar parameters: three b's and three δ's. We have one (b, δ) pair for $\phi(1020)$ and one for $f_0(980)$. To keep the number of parameters reasonably small, we have one (b, δ) pair that is shared by all the remaining charmless isobars (which we will refer to as the "Other" category). We fix the b and δ of the χ_{c0} to zero. This is equivalent to $A_{CP} = 0$ and $\beta_{\text{eff}} = \beta_{SM}$.
- 18 yields: 9 yields each for the $K^0_S \to \pi^+\pi^-$ and $K^0_S \to \pi^0\pi^0$ channels. The 9 yields include one for signal, one for the non-peaking $B\overline{B}$ backgrounds, and 7 for continuum (separate yields for each of the 7 tagging categories).
- The means of the signal m_{ES} and ΔE PDF's, for the $K^0_S \to \pi^+\pi^-$ channel only. (For $K^0_S \to \pi^0\pi^0$, these means are fixed to their MC values.) For $K^0_S \to \pi^+\pi^-$, we see some disagreement in m_{ES} between our fit model and the data, so we float the widths (σ_+ and σ_- in Eq. 5.7) of the signal m_{ES} PDF in a *CP*-blind fit to data, and fix them to those values in the nominal fit.
- The slope of the continuum ΔE PDF, separately for $K^0_S \to \pi^+\pi^-$ and $K^0_S \to \pi^0\pi^0$.
- 36 parameters for the continuum NN PDF: 18 each for $K^0_S \to \pi^+\pi^-$ and $K^0_S \to \pi^0\pi^0$. The 18 parameters are the 9 a_i's and 9 b_i's (see Eq. 5.14).

We perform randomized fits to data, with the *CP*-parameters of the $\phi(1020)$, $f_0(980)$, and remaining charmless isobars floating. We find four secondary solutions within 4.5 NLL of the best solution. The best solution is shown in Tables 7.9-7.11. The isobar magnitudes and phases are consistent with the *CP*-blind best solution. The *CP*-violating parameters are all consistent with the SM expectation of $A_{CP} = 0$, $\beta_{\text{eff}} = 0.368$ rad. The branching fractions are only computed based on the yield in the $K_S^0 \to \pi^+\pi^-$ channel, since the $K_S^0 \to \pi^0\pi^0$ channel has not only much worse statistical errors, but also worse systematic errors, due to uncertainty in the π^0 efficiency.

The *CP*-violating parameters for the four additional solutions are summarized in Tables 7.12-7.15. More detailed tables of these solutions are given in Appendix C. The second-best solution is about 2σ away (in terms of $\Delta \log \mathcal{L}$) from the best solution, so at least at the one-sigma level, the multiple solutions do not affect our confidence intervals. At the three-sigma level, however, some of the partial branching fractions are poorly constrained due to the multiple solutions. In particular, the $f_0(1500)$ fit fraction varies between 2% and 51% for the different solutions, the $f_0(1710)$ fit fraction varies between 2% and 27%, and the NR S-wave fit fraction varies between 34% and 120%. However, the $\phi(1020)$, $f_2'(1525)$, χ_{c0}, and NR P-wave fit fractions are very consistent among the different solutions. The $f_0(980)$ fit fraction is also fairly consistent among the different solutions, only varying between 19% and 41%.

We show the Δt distributions in the $\phi(1020)$ and $\phi(1020)$-excluded regions, for both B^0- and $\overline{B}^0$-tagged events, in Fig. 7.6. The distribution is only shown for $K_S^0 \to \pi^+\pi^-$ signal events, calculated using the ${}_s\mathcal{P}lot$s method. This figure also shows the signal asymmetry as a function of Δt. The time-dependent asymmetry has the opposite sign in the $\phi(1020)$ and $\phi(1020)$-excluded regions, because the $\phi(1020)$ is *CP*-odd, while the rest of the DP is mostly CP-even.

Since the most important measurements in the $B^0 \to K^+K^-K_S^0$ analysis are the *CP*-violating parameters, we perform likelihood scans in each of the three A_{CP}'s and β_{eff}'s. As usual, we perform many randomized fits for each scan point. The scans are shown in Figs. 7.7-7.9. We can see that the errors are basically Gaussian to about three-sigma. It is important to note the secondary minima visible in the $\beta_{\text{eff}}(\phi(1020))$ and $\beta_{\text{eff}}(\text{Other})$ plots around $60 - 80$ degrees. These minima are caused by the "trigonometric ambiguity" between β and $\pi/2 - \beta$ which was mentioned back in Sec. 2.5.3. As we explained then, we can discriminate between β and $\pi/2 - \beta$ due

Table 7.9: Isobar parameters for the best solution from the unblinded fit to $B^0 \to K^+K^-K^0_S$ data, using the nominal fit model. Signal and $B\overline{B}$ yields are also given.

Decay	Magnitude c_r	Phase ϕ_r (rad.)
$\phi(1020)K^0_S$	0.039 ± 0.005	0.35 ± 0.32
$f_0(980)K^0_S$	2.2 ± 0.5	0.70 ± 0.29
$f_0(1500)K^0_S$	0.22 ± 0.05	0.30 ± 0.27
$f_2'(1525)K^0_S$	0.00080 ± 0.00028	0.93 ± 0.40
$f_0(1710)K^0_S$	0.72 ± 0.11	1.92 ± 0.20
$\chi_{c0}K^0_S$	0.144 ± 0.023	-0.3 ± 0.5
a_{S0}	1.0 (fixed)	0.0 (fixed)
a_{S1}	1.25 ± 0.25	-2.60 ± 0.16
a_{S2}	0.58 ± 0.22	0.98 ± 0.27
a_{P0}	1.22 ± 0.22	1.14 ± 0.23
a_{P1}	0.28 ± 0.18	-1.2 ± 0.5
a_{P2}	0.42 ± 0.16	-2.29 ± 0.44
D^-	7.8 ± 1.2	-
D^-_s	4.0 ± 0.9	-
D^0	4.7 ± 0.9	-
J/ψ	3.0 ± 1.1	-
$\delta(\phi(1020))$	-0.01 ± 0.11	
$b(\phi(1020))$	0.03 ± 0.09	
$\delta(f_0(980))$	-0.06 ± 0.11	
$b(f_0(980))$	$0.14 \pm 0.13 \pm 0.05$	
δ(Other)	-0.01 ± 0.08	
b(Other)	0.01 ± 0.05	
N(signal), $K^0_S \to \pi^+\pi^-$	1419 ± 43	
N(signal), $K^0_S \to \pi^0\pi^0$	160 ± 17	
$N(B\overline{B})$, $K^0_S \to \pi^+\pi^-$	29 ± 28	
$N(B\overline{B})$, $K^0_S \to \pi^0\pi^0$	48 ± 18	
NLL	-28346.1	

Table 7.10: Fit fractions and partial branching fractions for the best solution from the unblinded fit to $B^0 \to K^+K^-K^0_S$ data, using the nominal fit model.

Decay	Fraction $\mathcal{F}_r$ (%)	$\mathcal{B}(B^+ \to K^+K^-K^+) \times \mathcal{F}_r (\times 10^{-6})$
$\phi(1020)K^0$	$13.1 \pm 1.0^{+0.8}_{-0.4}$	$3.48 \pm 0.28^{+0.21}_{-0.14}$
$f_0(980)K^0$	$26^{+9}_{-7} \pm 9$	$7.0^{+2.6}_{-1.8} \pm 2.4$
$f_0(1500)K^0$	$2.1 \pm 0.8 \pm 0.5$	$0.57^{+0.25}_{-0.19} \pm 0.12$
$f_2'(1525)K^0$	$0.5^{+0.5}_{-0.3} \pm 0.6$	$0.13^{+0.12}_{-0.08} \pm 0.16$
$f_0(1710)K^0$	$16.7 \pm 2.5 \pm 2.0$	$4.4 \pm 0.7 \pm 0.5$
$\chi_{c0}K^0$	$3.4 \pm 0.7 \pm 0.2$	$0.90 \pm 0.18 \pm 0.06$
NR (S-wave)	$115 \pm 17 \pm 31$	$30 \pm 5 \pm 8$
NR (P-wave)	$11.7 \pm 2.5 \pm 1.4$	$3.1 \pm 0.7 \pm 0.4$

Table 7.11: *CP*-violating parameters for the best solution from the unblinded fit to $B^0 \to K^+K^-K^0_S$ data, using the nominal fit model.

Component	β_{eff} (rad.)	A_{CP} (%)
$\phi(1020)$	$0.36 \pm 0.11 \pm 0.04$	$-5 \pm 18 \pm 5$
$f_0(980)$	$0.31 \pm 0.11 \pm 0.07$	$-28 \pm 24 \pm 9$
Other	$0.35 \pm 0.08 \pm 0.02$	$-2 \pm 9 \pm 3$

Table 7.12: Parameters for Solution 2 from the unblinded fit to $B^0 \to K^+K^-K^0_S$ data, using the nominal fit model. The errors are statistical only.

Component	β_{eff} (rad.)	A_{CP} (%)
$\phi(1020)$	0.33 ± 0.10	0.3 ± 17.1
$f_0(980)$	0.30 ± 0.09	-24.1 ± 19.9
Other	0.37 ± 0.07	-3.0 ± 8.1
N(signal), $K^0_S \to \pi^0\pi^0$	159 ± 17	
N(signal), $K^0_S \to \pi^+\pi^-$	1420 ± 43	
Δ(NLL)	2.0	

Table 7.13: Parameters for Solution 3 from the unblinded fit to $B^0 \to K^+K^-K^0_S$ data, using the nominal fit model. The errors are statistical only.

Component	β_{eff} (rad.)	A_{CP} (%)
$\phi(1020)$	0.32 ± 0.11	-9.3 ± 17.2
$f_0(980)$	0.32 ± 0.12	-12.6 ± 26.3
Other	0.39 ± 0.08	-1.3 ± 10.4
N(signal), $K^0_S \to \pi^0\pi^0$	160 ± 17	
N(signal), $K^0_S \to \pi^+\pi^-$	1418 ± 43	
Δ(NLL)	2.0	

Table 7.14: Parameters for Solution 4 from the unblinded fit to $B^0 \to K^+K^-K^0_S$ data, using the nominal fit model. The errors are statistical only.

Component	β_{eff} (rad.)	A_{CP} (%)
$\phi(1020)$	0.28 ± 0.15	-10.0 ± 17.1
$f_0(980)$	0.26 ± 0.20	10.7 ± 55.9
Other	0.43 ± 0.12	12.6 ± 24.9
N(signal), $K^0_S \to \pi^0\pi^0$	162 ± 17	
N(signal), $K^0_S \to \pi^+\pi^-$	1419 ± 43	
Δ(NLL)	3.7	

Table 7.15: Parameters for Solution 5 from the unblinded fit to $B^0 \to K^+K^-K^0_S$ data, using the nominal fit model. The errors are statistical only.

Component	β_{eff} (rad.)	A_{CP} (%)
$\phi(1020)$	0.25 ± 0.11	-3.5 ± 16.3
$f_0(980)$	0.39 ± 0.09	-21.0 ± 14.0
Other	0.51 ± 0.08	-2.7 ± 12.7
N(signal), $K^0_S \to \pi^0\pi^0$	161 ± 17	
N(signal), $K^0_S \to \pi^+\pi^-$	1418 ± 43	
Δ(NLL)	4.2	

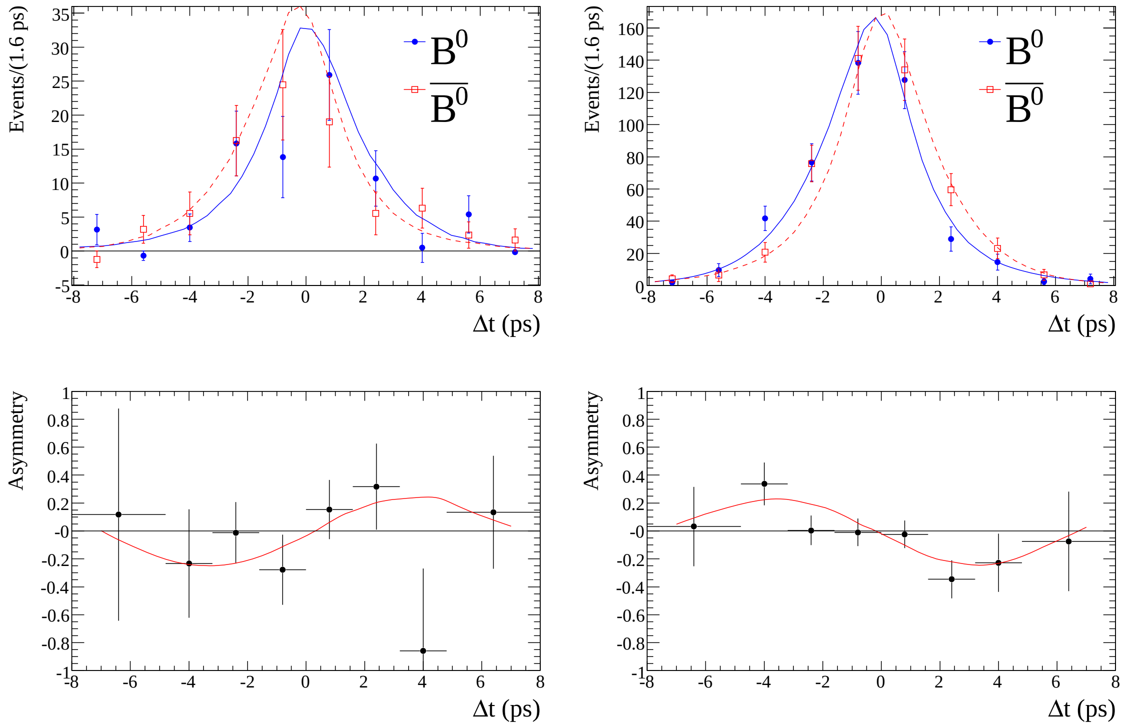

Figure 7.6: Top: The Δt distributions for $B^0 \rightarrow K^+K^-K^0_S$ ($K^0_S \rightarrow \pi^+\pi^-$) signal events, in the $\phi(1020)$ region $1.01\,\mathrm{GeV}/c^2 < m_{K^+K^-} < 1.03\,\mathrm{GeV}/c^2$ (left) and $\phi(1020)$-excluded region (right). B^0 ($\overline{B}^0$) tagged events are shown as closed circles (open squares). The fit model for B^0 ($\overline{B}^0$) tagged events is shown by a solid (dashed) line. The data points are signal-weighted using the ${}_s\mathcal{P}lot$s method. Bottom: The asymmetry $(N_{B^0} - N_{\overline{B}^0})/(N_{B^0} + N_{\overline{B}^0})$ as a function of Δt, in the $\phi(1020)$ region (left) and $\phi(1020)$-excluded region (right). The points represent signal-weighted data, and the line is the fit model.

to S-wave/P-wave interference (see Eq. 2.33). This is in contrast to the $B^0 \to J/\psi K_S^0$ analysis, which can only measure sin2β, and therefore cannot discriminate between β and $\pi/2-\beta$. From the likelihood scans, we exclude this secondary solution at 4.8σ for β_{eff}(Other), and at 4.1σ for $\beta_{\text{eff}}(\phi(1020))$.

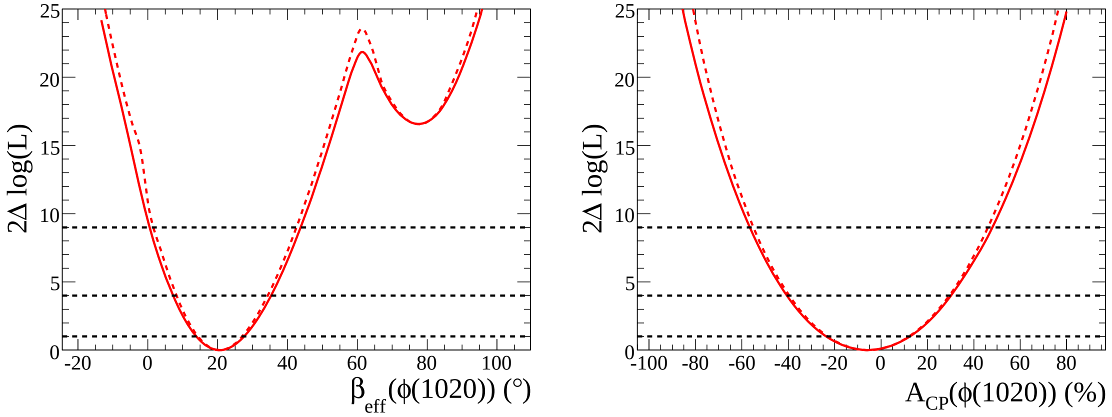

Figure 7.7: Statistical (dashed line) and total (solid line) scans of $-2\Delta\log\mathcal{L}$ as a function of β_{eff} (left) and A_{CP} (right) for $B^0 \to \phi(1020)K_S^0$.

7.4 Systematics

In this section, we describe the studies of systematic uncertainties on the final result. Detailed tables of all the systematics can be found in Appendix D.

7.4.1 Fit Bias

To assess the bias in our fit, we run hundreds of embedded toy experiments (see Sec. 5.5 for a description of the method). The signal events are generated using MC based on the nominal fit result. For $B^+ \to K^+K^-K^+$, all $B\overline{B}$ backgrounds are embedded from exclusive MC, except for the "BB charm 4" category, which is generated with toy. For $B^+ \to K_S^0K_S^0K^+$, all $B\overline{B}$ backgrounds are generated with toy. For $B^0 \to K^+K^-K_S^0$, peaking $B\overline{B}$ backgrounds from D^+, D_s^+, and D^0 are embedded

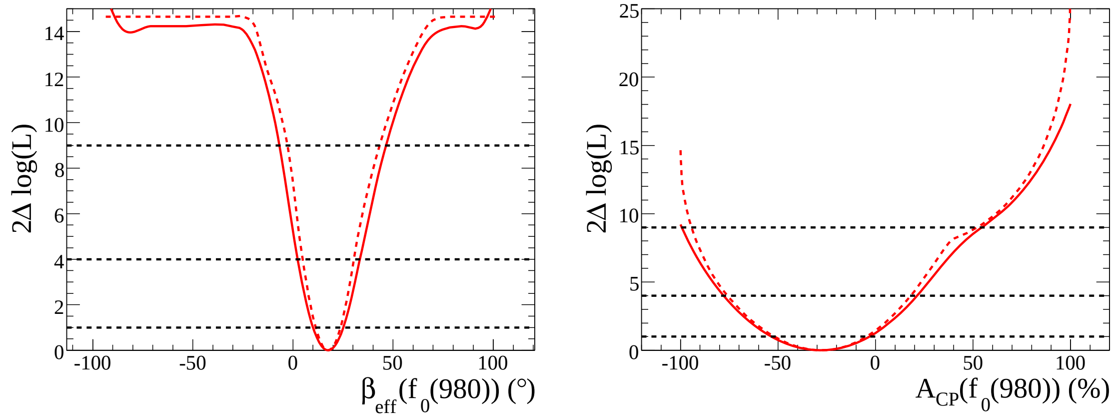

Figure 7.8: Statistical (dashed line) and total (solid line) scans of $-2\Delta\log\mathcal{L}$ as a function of β_{eff} (left) and A_{CP} (right) for $B^0 \to f_0(980)K^0_S$. The reason that the β_{eff} scan reaches a flat plateau is that in that region the fit happens to prefer $A_{CP}(f_0(980)) = -100\%$, but when $A_{CP} = \pm 100\%$, the β_{eff} parameter has no effect.

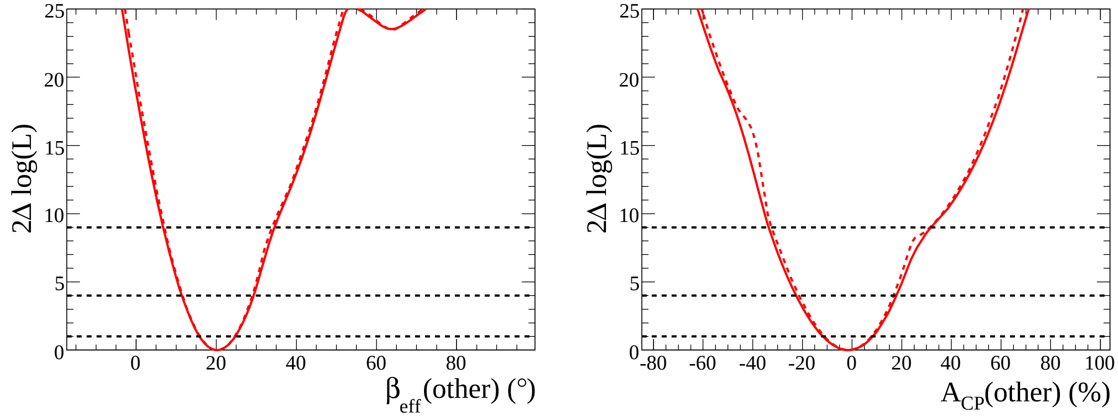

Figure 7.9: Statistical (dashed line) and total (solid line) scans of $-2\Delta\log\mathcal{L}$ as a function of β_{eff} (left) and A_{CP} (right) for $B^0 \to K^+K^-K^0_S$, excluding the $\phi(1020)$, $f_0(980)$, and χ_{c0}.

from exclusive MC, while J/ψ backgrounds and non-peaking $B\overline{B}$ backgrounds are generated with toy.

The mean of the pull distribution, μ, for each parameter is computed using a Gaussian fit. The error on the mean, σ_μ, is also computed from the Gaussian fit. We then add μ and σ_μ in quadrature to get a conservative estimate of the possible pull, and multiply this result by the statistical error on the parameter from the nominal data fit. We take this as the systematic error due to fit bias. We do not correct for the fit biases.

7.4.2 Efficiency and $B\overline{B}$ counting

The computed branching fractions depend on the signal efficiency and the number of $B\overline{B}$ pairs. The systematic on the efficiency comes from a number of different sources: tracking, K_S^0 efficiency, PID, and limited statistics in the efficiency map.

Tracking Efficiency

BABAR has an official prescription for estimating the systematic on tracking efficiency, which is based on studies of $\tau^+\tau^-$ events. We compute systematics both for the $K^\pm$ tracks and the $\pi^\pm$ tracks coming from K_S^0 decays. Based on the prescription, we find a total tracking systematic of 1.1% in $B^+ \to K^+K^-K^+$, 0.752% in $B^+ \to K_S^0K_S^0K^+$, and 0.736% in $B^0 \to K^+K^-K_S^0$.

K_S^0 Efficiency

In addition to the tracking systematic, there is an additional systematic on the K_S^0 efficiency due to uncertainty in how the efficiency varies as a function of flight distance. *BABAR* has official tables of data-MC corrections to the K_S^0 efficiency, which are calculated as a function of the transverse vertex displacement, polar angle, and transverse momentum of the K_S^0. Using these tables, we find a total efficiency correction of 0.99 ± 0.014 in $B^+ \to K_S^0K_S^0K^+$, and 0.992 ± 0.009 in $B^0 \to K^+K^-K_S^0$. We apply the correction to the nominal fit result, and take the error on the correction as a systematic.

PID Efficiency

To account for data-MC difference in PID efficiency, we correct the efficiency map using PID weights (see Sec. 5.2.4). To estimate the systematic on the PID efficiency, we refit to data with the PID corrections turned off. We take half the difference as the systematic. The overall PID systematic is about 1.8%, 0.5%, and 2.5% in $B^+ \to K^+K^-K^+$, $B^+ \to K^0_S K^0_S K^+$, and $B^0 \to K^+K^-K^0_S$, respectively.

Efficiency Map Statistics

There is also a systematic due to the finite MC statistics used to produce the efficiency map. To account for this, we fluctuate each bin of the efficiency map by its statistical error, and in this manner create 100 different efficiency maps. We then perform a fit to data using each of these different efficiency maps. For a given parameter, we look at its distribution for the ensemble of 100 fits. We take the RMS of this distribution as the systematic error on that parameter.

$B\overline{B}$ Counting

We use *BABAR*'s official values for the number of $B\overline{B}$ pairs and the uncertainty on this number. As previously mentioned, the $B^+ \to K^+K^-K^+$ analysis is based on a different processing cycle than $B^+ \to K^0_S K^0_S K^+$ and $B^0 \to K^+K^-K^0_S$, so it has a different number of $B\overline{B}$ pairs and different associated systematic. For $B^+ \to K^+K^-K^+$, the systematic is 1.1%, while for the other modes, the systematic is 0.6%.

7.4.3 Resonance Lineshapes

To account for uncertainties in the lineshapes of the various resonances in the isobar model, we vary the mass, width, and Blatt-Weisskopf radius of each resonance one-by-one by $+\sigma$ and $-\sigma$, and refit the data. We look at the shifts in each parameter, Δ_+ and Δ_-. If one of the $\Delta_\pm$ is positive, and one negative, then we keep track of the positive and negative shift separately. However, if both $\Delta_\pm$ are positive (negative), then the positive (negative) systematic error is taken to be the average of $|\Delta_+|$ and $|\Delta_-|$, and the negative (positive) systematic error is taken to be zero.

The errors on the masses and widths of the resonances are taken from the PDG [9], except for the $f_0(980)$ and the peaking $B\overline{B}$ backgrounds in $B^0 \to K^+K^-K^0_S$ (D^+, D^+_s, D^0, J/ψ). The $f_0(980)$ errors are taken from the BESII measurement [19]. The $f_0(980)$ g_π and g_K constants are varied separately. For the peaking $B\overline{B}$ backgrounds in $B^0 \to K^+K^-K^0_S$, the errors on the resonance masses are taken from the PDG, while their effective widths (which are due to detector resolution) are varied by ±10%.

As mentioned in Sec. 2.5.4, we vary the Blatt-Weisskopf radii by $\pm 2.5\ (\mathrm{GeV}/c)^{-1}$ as a systematic. Also, we set the Blatt-Weisskopf radius of the B meson to zero in the nominal fit, but change it to $1.5\ (\mathrm{GeV}/c)^{-1}$ as a systematic.

7.4.4 $B\overline{B}$ Background Yields and A_{CP}

The yields for some of the $B\overline{B}$ background categories are fixed in the nominal fit: all of the $B\overline{B}$ categories in $B^+ \to K^0_S K^0_S K^+$ and "BB chmls" in $B^+ \to K^+K^-K^+$. There is some uncertainty on these yields due to the uncertainties on the BF's of the various decay modes that contribute to them. Most of these $B\overline{B}$ categories consist of multiple decay modes, and so the uncertainties on the BF's also create an uncertainty in the PDF shapes (m_{ES},ΔE,NN) for these $B\overline{B}$ backgrounds. Since the systematics due to the $B\overline{B}$ backgrounds turn out to be small, we do not bother to explicitly account for this uncertainty in the PDF shapes. Instead, we vary each of the $B\overline{B}$ yields by a large amount (50%), and assume that this covers the systematic uncertainty. The other $B\overline{B}$ category yields are floated in the nominal fit. In principle, there should be a systematic on their PDF shapes due to the BF uncertainties, but we believe this systematic to be safely negligible.

In $B^+ \to K^+K^-K^+$ and $B^+ \to K^0_S K^0_S K^+$, we estimate systematics due to the A_{CP} of the $B\overline{B}$ backgrounds. The "BB charm 5" category in $B^+ \to K^+K^-K^+$ and the "BB 4" category in $B^+ \to K^0_S K^0_S K^+$ both refer to $B^+ \to \bar{D}^0 K^+$ decays. We fix their A_{CP} to the PDG measurement and vary the A_{CP} by the PDG errors as a systematic, $A_{CP} = 0.24 \pm 0.08$. The A_{CP}'s of the other $B\overline{B}$ categories are fixed to their values in MC (≈ 0). As a systematic, we vary the A_{CP} of the other $B\overline{B}$ categories, either based on the world-average A_{CP} measurements of the sub-decays contributing to the particular categories, or based on a conservative guess. In most cases, the variation is between ±0.05 and ±0.1.

In $B^0 \to K^+K^-K^0_S$, we fix the A_{CP} of the peaking backgrounds to zero in the nominal fit, and vary them by ±20% as a systematic (except for the $J/\psi K^0_S$ background, which we do not vary at all). The generic $B\overline{B}$ category has a long-lived component, with *CP*-violating parameters C and S fixed to zero in the nominal fit (Eq. 5.19). As a systematic, we vary C by ±0.2, and S by ±0.75.

7.4.5 Fixed PDF Parameters

There are many PDF parameters that are fixed in the nominal fit. Systematics for fixed PDF parameters are calculated in one of two ways, depending on the PDF parameter in question. The first group of parameters are varied by their individual errors, and a systematic is calculated using the same method that was used for the resonance lineshapes (varying the parameter up and down by some amount). This first group is only used for $B^0 \to K^+K^-K^0_S$. The parameters in this group include the following parameters:

- Signal tagging efficiencies, mistag rates, and mistag rate asymmetries. The errors are taken from BABAR's B Tagging group [41].
- Signal Δt resolution parameters. The errors are taken from [41].
- The B^0 lifetime and mixing frequency, and the CKM angle β. Errors are from the PDG.
- Parameters describing the $B\overline{B}$ background Δt and DP distributions. Errors are either taken from fits to $B\overline{B}$ MC, or are guesses.

For the second group of PDF parameters, the systematics are calculated in a different fashion. We split these parameters into different subgroups. For each subgroup, we vary all the fixed PDF parameters by their errors. Since the PDF parameters are correlated with one another, we do not vary the parameters one-by-one. Instead, we take the full covariance matrix for the parameters of a given PDF, and generate

10 sets of randomized parameters distributed in a Gaussian fashion according to the covariance matrix, including the correlations.

We do this for each of the PDF's in the subgroup. Then for each subgroup, we perform 10 fits to data, each fit using a different set of the randomized PDF parameters. The systematic for that subgroup is then calculated as the RMS of these 10 fits.

The parameters in this second group include:

- $B^+ \rightarrow K^+K^-K^+$: $m_{\rm ES}$, ΔE, and NN PDF parameters for signal and for the various $B\overline{B}$ background categories. NN PDF parameters for continuum.
- $B^+ \rightarrow K^0_S K^0_S K^+$: $m_{\rm ES}$ and ΔE PDF parameters for signal. $m_{\rm ES}$, ΔE, and NN PDF parameters for the various $B\overline{B}$ background categories.
- $B^0 \rightarrow K^+K^-K^0_S$: $m_{\rm ES}$ parameters for signal, $B\overline{B}$, and continuum; ΔE parameters for signal and $B\overline{B}$; Δt parameters for $B\overline{B}$ and continuum; and NN parameters for $B\overline{B}$.

For the $B\overline{B}$ PDF's, the covariance matrices used to generate the randomized parameters come from the fits to MC. For the continuum PDF's, the covariance matrices come from sideband data fits. Since the signal PDF's agree well with the data (see the ${}_s\mathcal{P}lot$s), then we assume that the signal PDF's are valid to within the statistics of our data sample. So, we fit the signal PDF's to a data-sized sample of toy signal events, and we use the covariance matrix from this fit to generate the randomized parameters. There are a few exceptions to this: the signal and continuum NN parameters in $B^+ \rightarrow K^+K^-K^+$, as well as the width of the signal $m_{\rm ES}$ distribution in $B^0 \rightarrow K^+K^-K^0_S$ ($K^0_S \rightarrow \pi^+\pi^-$), are obtained from *CP*-blind fits to data, and then varied by the errors obtained from those fits.

7.4.6 Signal NN Shape

In $B^+ \rightarrow K^+K^-K^+$, we saw a discrepancy in the signal NN shape between data and MC, and decided to take the NN parameters from a *CP*-blind fit to data. Since this same data-MC discrepancy may exist in $B^+ \rightarrow K^0_S K^0_S K^+$ and $B^0 \rightarrow K^+K^-K^0_S$ (but we don't have sufficient statistics to see it), we account for it as a systematic. To quantify this discrepancy, we fit a straight line to the NN shape for data and MC in $B^+ \to K^+K^-K^+$, and take the ratio of these two lines. We then adjust the NN PDF's in $B^+ \to K^0_S K^0_S K^+$ and $B^0 \to K^+K^-K^0_S$ by this ratio, and refit the data, and take the difference as a systematic. (The NN used in $B^0 \to K^+K^-K^0_S$ is slightly different from the NN used in $B^+ \to K^+K^-K^+$ and $B^+ \to K^0_S K^0_S K^+$, but we assume the data/MC discrepancy has a similar magnitude in all three analyses.)

7.4.7 DP PDF Statistics

Our background DP PDF's are based on finite statistics (limited MC statistics in the case of the $B\overline{B}$ PDF's, or limited sideband data statistics in the case of the continuum PDF). To estimate the effect this has on our fit parameters, we generate N random toy datasets from each of the DP PDF's, with each toy dataset containing the number of events that were used to originally create that PDF. Here, N is some number; 10 is sufficient, although we chose 50 in $B^+ \to K^0_S K^0_S K^+$. For example, if a particular $B\overline{B}$ DP PDF were created from 10000 MC events, then we generate 10000 events from that PDF in each of N datasets. Then, for each of those toy datasets, we create a new DP PDF, using the adaptive binning procedure. This results in us having N statistically independent sets of DP PDF's.

We generate N full pure toy datasets, using the nominal background PDF's. We then perform fits to each of these pure toy datasets, using the nominal backgrounds PDF's. We will call these "reference fits." We then perform fits to each of the pure toy datasets, but with the background PDF's replaced by the DP PDF's that were described in the previous paragraph. Since there are N sets of those PDF's, this means we perform N^2 fits. We then compare these fits to the reference fits, and do a Gaussian fit to the difference. The Gaussian has a mean μ and width σ. The systematic is calculated as $\sqrt{\mu^2 + \sigma^2}$.

7.4.8 Dalitz Model

One of the largest systematic uncertainties comes from our lack of knowledge of the true DP model. We estimate this uncertainty by adding the following resonances to our DP model: $f_0(1370)$, $a_0^0(1450)$, $a_0^{\pm}(980)$, $a_0^{\pm}(1450)$, $\phi(1680)$, $f_2(1270)$, $f_2(2010)$, and $f_2(2300)$. These are the same resonances that we tested in Sec. 6.5.

In $B^+ \to K_S^0 K_S^0 K^+$, we add all of the resonances to the DP model at once. In $B^0 \to K^+K^-K_S^0$, fitting with all of the additional resonances at once is computationally intensive, so we add each resonance separately to the DP model (except we add the $f_0(1370)$ and $a_0^0(1450)$ together, and the $f_2(2010)$ and $f_2(2300)$ together, since they are similar and we would therefore like to account for correlations between them). In $B^+ \to K^+K^-K^+$, we add each resonance separately, except we add the $f_2(2010)$ and $f_2(2300)$ together.

When we add the $f_0(1370)$ to $B^+ \to K^+K^-K^+$, we find that the likelihood function changes considerably: the region of parameter space that had corresponded to the best solution is no longer a minimum (not even a local minimum), while the region of parameter that had corresponded to the second solution is now the global minimum. Therefore, we cannot sensibly treat the effect of the $f_0(1370)$ as a Gaussian systematic, so we do not include the $f_0(1370)$ as a systematic for $B^+ \to K^+K^-K^+$.

After adding the resonance(s) to the model, we refit data. We then generate many toy datasets using this new fit result. We then fit to each of the toy datasets twice: once with the additional resonance(s), and once without. We compute the difference between the two fits (without - with) for each dataset, and fit a Gaussian to this distribution. The Gaussian has a mean μ and error on the mean σ_μ. We add μ and σ_μ in quadrature as a systematic.

7.4.9 Detection Charge Asymmetry

A bias on the A_{CP} measurements in $B^+ \to K^+K^-K^+$ and $B^+ \to K_S^0 K_S^0 K^+$ can be caused by different detection efficiencies for K^+ and K^-. A small asymmetry is expected due to the fact that K^+ and K^- have different cross-sections for interacting with the material in the detector. In $B^+ \to K^+K^-K^+$ signal MC (SP-9688), generated with zero A_{CP}, we find an overall A_{CP} of $(-0.8 \pm 0.08)\%$. Since this detector-related A_{CP} is present in the MC, the systematic effect due to our ignoring it will be accounted for in the embedded toy (fit bias) systematic, so we do not need to account for it separately.

However, the MC may not perfectly model this asymmetry, resulting in another systematic uncertainty. There was an extensive study of $K^{\pm}$ material interactions in *BABAR*'s analysis of $B^0 \to K^+\pi^-$ [46, 5], which compared MC, data, and independent calculations. That analysis shifted the A_{CP} by -0.5%, and assigned a systematic of $(+0.25 - 0.60)\%$. As an independent cross-check, we look at onpeak sideband data, and find $A_{CP} = (-1.45 \pm 0.32)\%$ in the region $|\Delta E| < 0.3\,\text{GeV}$ and $A_{CP} = (-2.16 \pm 0.56)\%$ in the region $|\Delta E| < 0.1\,\text{GeV}$. In *uds* MC, we find $A_{CP} = (-1.96 \pm 0.39)\%$ in the wide ΔE region, and $A_{CP} = (-2.6 \pm 0.7)\%$ in the narrow ΔE region. Although this study does not include $c\bar{c}$ or $B\overline{B}$ MC, it does give us some added confidence that the MC simulation does a reasonable job of modeling the detector asymmetry. We decide to add a 1% A_{CP} systematic, which we believe is sufficiently conservative.

7.4.10 Other

In $B^0 \to K^+K^-K^0_S$, there are a few additional systematic uncertainties on the *CP*-violating parameters. Interference between Cabibbo-favored and Doubly Cabibbo-suppressed (DCS) decays in the tag-side B decays can affect the extracted *CP*-violating parameters in tagged analyses [47]. There are also systematics due to uncertainty on the beam spot position and SVT alignment. We take all of these systematic errors from *BABAR*'s $c\bar{c}K^0$ analysis [15].

7.5 Interpretation

The *CP*-violation measurements for ϕK are quite interesting. We measure $A_{CP}(\phi K^+)$ to be rather different than the SM expectation, while $\beta_{\text{eff}}(\phi K^0_S)$ is measured to be very consistent with the SM. We can ask ourselves what kind of constraints these measurements make on contributions from NP amplitudes, or on CKM-suppressed

SM amplitudes.

To proceed, we will assume isospin conservation, so $\mathcal{A}(B^+ \to \phi K^+) = \mathcal{A}(B^0 \to \phi K^0)$. We will also assume that this amplitude can be written as $\mathcal{A} = \mathcal{A}_1 + \mathcal{A}_2$, where $\mathcal{A}_1$ is the dominant "c-penguin" amplitude (see Sec. 2.4 and Eq. 2.18). $\mathcal{A}_2$ is allowed to have a different weak and strong phase than $\mathcal{A}_1$. If there is no NP contribution, then $\mathcal{A}_2$ would represent the tree and u-penguin amplitudes (SM pollution) in Eq. 2.18 (recall that tree amplitudes can contribute to $\mathcal{A}(\phi K)$ through rescattering). In contrast, if we ignore tree and u-penguin amplitudes, $\mathcal{A}_2$ would represent NP. Obviously, since our $A_{CP}(\phi K^+)$ measurement differs from the SM expectation, then if the SM calculations were perfect, there would have to be a NP component to $\mathcal{A}_2$. However, there is enough uncertainty in the SM prediction that we do not attempt to subtract off the SM pollution.

We can then write the amplitudes as:

$$\begin{aligned} \mathcal{A} &= \mathcal{A}_1(1 + re^{i(\eta+\zeta)}) \\ \overline{\mathcal{A}} &= \mathcal{A}_1(1 + re^{i(\eta-\zeta)})\,. \end{aligned} \tag{7.2}$$

In this equation, r is the amplitude ratio $\mathcal{A}_2/\mathcal{A}_1$, η is the strong phase of $\mathcal{A}_2$ relative to $\mathcal{A}_1$, and ζ is the relative weak phase between $\mathcal{A}_2$ and $\mathcal{A}_1$. We can then calculate the asymmetries:

$$A_{CP}(\phi K^+) = \frac{2r\sin\zeta\sin\eta}{1 + 2r\cos\zeta\cos\eta + r^2}\,, \tag{7.3}$$

$$\beta_{\text{eff}}(\phi K^0_S) = \beta + \frac{1}{2}\arctan\left(\frac{2r\sin\zeta\cos\eta + r^2\sin(2\zeta)}{1 + 2r\cos\zeta\cos\eta + r^2\cos(2\zeta)}\right)\,. \tag{7.4}$$

Using our measured values of $A_{CP}(\phi K^+)$ and $\beta_{\text{eff}}(\phi K^0_S)$, we can place constraints on r, η, and ζ. We should note that under our isospin-conservation assumption, $A_{CP}(\phi K^0_S) = A_{CP}(\phi K^+)$. However, our measurement of $A_{CP}(\phi K^0_S)$ has much larger errors than $A_{CP}(\phi K^+)$, so we decided not to include that measurement when making the constraints. [2] For each set of values of r, η, and ζ, we calculate the predicted asymmetries, and compute a χ^2 for that set of asymmetries by using the likelihood

---

[2] Since the $A_{CP}(\phi K^0_S)$ measurement has a negative central value, its inclusion may slightly decrease the significance of $A_{CP}(\phi K)$, but this is not why we left it out. Rather, because $A_{CP}(\phi K^0_S)$

scans for $A_{CP}(\phi K^+)$ and $\beta_{\text{eff}}(\phi K^0_S)$, interpreting $2\Delta \log \mathcal{L}$ as a χ^2.

We show our resulting constraints in the $r-\zeta$, $r-\eta$, and $\eta-\zeta$ planes in Fig. 7.10. Most of the constraints come from the $A_{CP}(\phi K^+)$ measurement, so we can understand the constraints by looking at Eq. 7.3. The fact that we measure a non-zero value for $A_{CP}(\phi K^+)$ means that r must be non-zero, and ζ and η cannot be 0 or $\pm 180°$. This is reflected in Fig. 7.10. For most values of ζ and η, r is favored to be roughly 0.1. However, if ζ or η are close to 0 or $\pm 180°$, then the favored value of r becomes larger. The fact that we measure $A_{CP}(\phi K^+)$ to be *positive* explains why the first and third quadrants of the $\eta - \zeta$ plane are favored, since A_{CP} is proportional to $\sin\zeta \sin\eta$. Finally, note that although the SM expectation for η is difficult to calculate, the SM expectation for ζ is quite simple. By looking at Eq. 2.18, we can observe that in the SM, ζ must be approximately equal to $-\gamma$.

---

is correlated with $\beta_{\text{eff}}(\phi K^0_S)$, it would require extra work to properly include the $A_{CP}(\phi K^0_S)$ measurement.

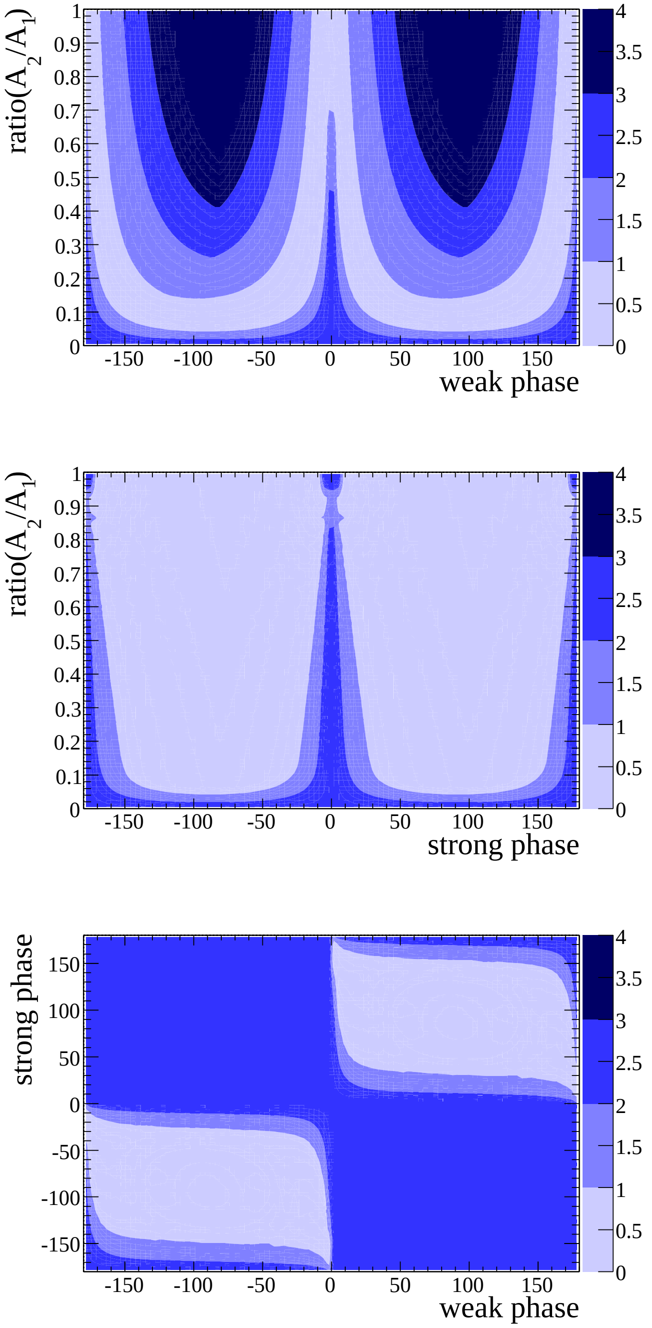

Figure 7.10: Constraints on the contribution of an extra amplitude $\mathcal{A}_2$ to $B \rightarrow \phi K$ decays. See Sec. 7.5 for the meaning of the parameters. The shaded regions (from light to dark) show the 1σ, 2σ, 3σ, and 4σ allowed regions. The contours are computed from a χ^2 using one degree of freedom.

Chapter 8

Conclusions

By means of a Dalitz plot amplitude analysis, we make measurements of *CP*-violation and study the resonant and nonresonant decay structure in $B^+ \rightarrow K^+K^-K^+$, $B^+ \rightarrow K^0_S K^0_S K^+$, and $B^0 \rightarrow K^+K^-K^0_S$.

In $B^+ \rightarrow K^+K^-K^+$, we measure a direct *CP* asymmetry in the $\phi(1020)K^+$ channel of $A_{CP} = (12.8 \pm 4.4 \pm 1.3)\%$, which is non-zero at the 2.8 sigma level. We also measure A_{CP} for the $f_0(980)$, the nonresonant, and the combined $f_0(1500)$-$f_2'(1525)$-$f_0(1710)$ channels, and find no evidence of *CP* violation. We find an inclusive charmless A_{CP} of $(-1.7^{+1.9}_{-1.4} \pm 1.4)\%$.

The $A_{CP}(\phi K^+)$ measurement is in tension with the SM predictions, which say this value should be in the range $(0.0 - 4.7)\%$. This is intriguing, as $B \rightarrow KKK$ decays are sensitive to new physics. We hope that this measurement encourages further theoretical work on this channel. Previous measurements of $A_{CP}(\phi K^+)$ are given in Table 8.1. Those measurements are consistent with ours, but with much larger errors. However, the previous measurements are quite old; Belle now has about 10 times as much data, and CDF has about 50 times as much data. So, our $A_{CP}(\phi K^+)$ measurement could be tested quite soon by other experiments.

In $B^+ \rightarrow K^0_S K^0_S K^+$, the number of signal events is too small to measure the A_{CP} of individual resonances, so we measure only an inclusive A_{CP} (excluding the χ_{c0}). We measure $A_{CP} = (4^{+4}_{-5} \pm 2)\%$, consistent with no *CP* violation. This improves greatly over *BABAR*'s previous measurement of $A_{CP} = (-4 \pm 11 \pm 2)\%$ [35].

Table 8.1: Previous measurements of $A_{CP}(\phi K^+)$. The *BABAR* measurement listed is superseded by the present analysis.

Measurement	Experiment	Integrated Luminosity
$(0 \pm 8 \pm 2)\%$	*BABAR* [24]	205 fb^{-1}
$(-7 \pm 17^{+3}_{-2})\%$	CDF [48]	180 pb^{-1}
$(1 \pm 12 \pm 5)\%$	Belle [49]	78 fb^{-1}

In $B^0 \to K^+K^-K^0_S$, we measure time-dependent *CP* violation as a function of location on the Dalitz plot. We determine *CP*-violating parameters β_{eff} and A_{CP} ($= -C$) for $B^0 \to \phi K^0_S$, $B^0 \to f_0(980)K^0_S$, and for the remaining charmless $K^+K^-K^0_S$ decays (mostly nonresonant). The measurement of $\beta_{\text{eff}}(\phi K^0_S)$ is especially important, as this is a theoretically clean probe of new physics. We find $\beta_{\text{eff}}(\phi K^0_S) = 0.36 \pm 0.11 \pm 0.04$ rad, in excellent agreement with the SM expectation of $\beta_{\text{eff}} \approx \beta \approx 0.37$. This is the world's most precise measurement of this quantity, and can be compared with Belle's most recent result [28] of $\beta_{\text{eff}}(\phi K^0_S) = 0.56 \pm 0.16 \pm 0.05 \pm 0.02$, obtained with about 40% more data. For ϕK^0_S, we exclude the trigonometric solution $\beta_{\text{eff}} \approx \pi/2 - \beta$ at 4.1σ.

The total signal yield in $B^0 \to K^+K^-K^0_S$ is quite large, but most of the events are not in the low-$m_{K^+K^-}$ region. Our measurement of β_{eff} for the non-ϕK^0_S, non-$f_0(980)K^0_S$ decays, β_{eff} (Other), takes advantage of the large number of nonresonant events in $B^0 \to K^+K^-K^0_S$. We measure $\beta_{\text{eff}}(\text{Other}) = 0.35 \pm 0.08 \pm 0.02$, and exclude $\beta_{\text{eff}} \approx \pi/2 - \beta$ at 4.8σ. This is one of the most precise measurements of β_{eff} in any $b \to s$ penguin mode, although the SM prediction for this is not as clean as for ϕK^0_S.

By combining the $A_{CP}(\phi K^+)$ and $\beta_{\text{eff}}(\phi K^0_S)$ measurements, we put constraints on the amplitudes contributing to these decays. We find that in order to produce the observed 13% A_{CP} in ϕK^+, there would need to be, in addition to the dominant c-penguin amplitude, another amplitude with differing weak phase, and this amplitude would have to be about one-tenth the size of the c-penguin amplitude or larger.

We also performed extensive studies of the resonances and nonresonant structure in $B \to KKK$ decays, which were shown in Chapter 6. One of our aims was to clarify the nature of the mysterious $f_X(1500)$, previously modeled as a single scalar resonance. We were able to convincingly show that the peak previously ascribed to the $f_X(1500)$ is in fact not a single resonance. On the other hand, we found that the $f_X(1500)$ region could be effectively modeled with a combination of the well-established resonances $f_0(1500)$, $f_2'(1525)$, and $f_0(1710)$. This model not only fits the data better, it also is able to explain this peak without resort to a new ad-hoc resonance.

Our studies of the nonresonant $B \to KKK$ decays were less conclusive than our $f_X(1500)$ studies. We were able to refute the simple exponential nonresonant model, at least in $B^+ \to K^+K^-K^+$. Our final nonresonant model is decidedly more complicated, including both S-wave and P-wave terms, as well as phase motion across the Dalitz plot.

There are two ways of looking at the nonresonant decays. From one perspective, they are an object of interest, whose nature we would like to understand. From this perspective, we measure a lot of parameters (complex coefficients) describing these decays, but do not have any real physical interpretation of these parameters. We are still a long way from understanding the nature of the nonresonant decays, but we hope that our detailed measurements will spur more theoretical work on them.

From another perspective, nonresonant decays are just a nuisance interfering with other measurements we would like to make: *CP*-violating observables and resonant branching fractions. From this perspective, we have made great progress. Previous analyses have used relatively rigid models for nonresonant decays, with few adjustable parameters. This can make one question how dependent their results are on the choice of nonresonant model. However, the new nonresonant model we have chosen has an incredible amount of freedom, thus making our measurements less dependent on a particular model. It is particularly heartening that we are able to measure $\beta_{\text{eff}}(\text{Other})$ precisely, despite the large number of free parameters in the nonresonant model.

Understanding the decay structure of $B \to KKK$ will be an interesting challenge for future experiments like Belle II and SuperB, which are expected to have about 100 times more data than BABAR. Although we relied extensively on $B^+ \to K^+K^-K^+$ for determining the Dalitz model (due to the large number of events), with the enormous datasets possible in the future, it is likely that $B^+ \to K^+K^-K^+$ will have less of an advantage over other $B \to KKK$ modes. In particular, $B^+ \to K_S^0K_S^0K^+$ should be an ideal mode to study the D-wave nonresonant content, since there is no P-wave contamination in this mode. And to study the P-wave content, the ideal mode would be $B^+ \rightarrow K^0_S K^0_L K^+$, since this has no S- or D-wave contribution, although experimentally this mode will be challenging.

Appendix A

$B\overline{B}$ Background PDF's and Distributions

The plots in this section show the PDF's for the various $B\overline{B}$ backgrounds for $B^+ \to K^+K^-K^+$ and $B^+ \to K^0_S K^0_S K^+$, described in Sections 5.4.1 and 5.4.2.

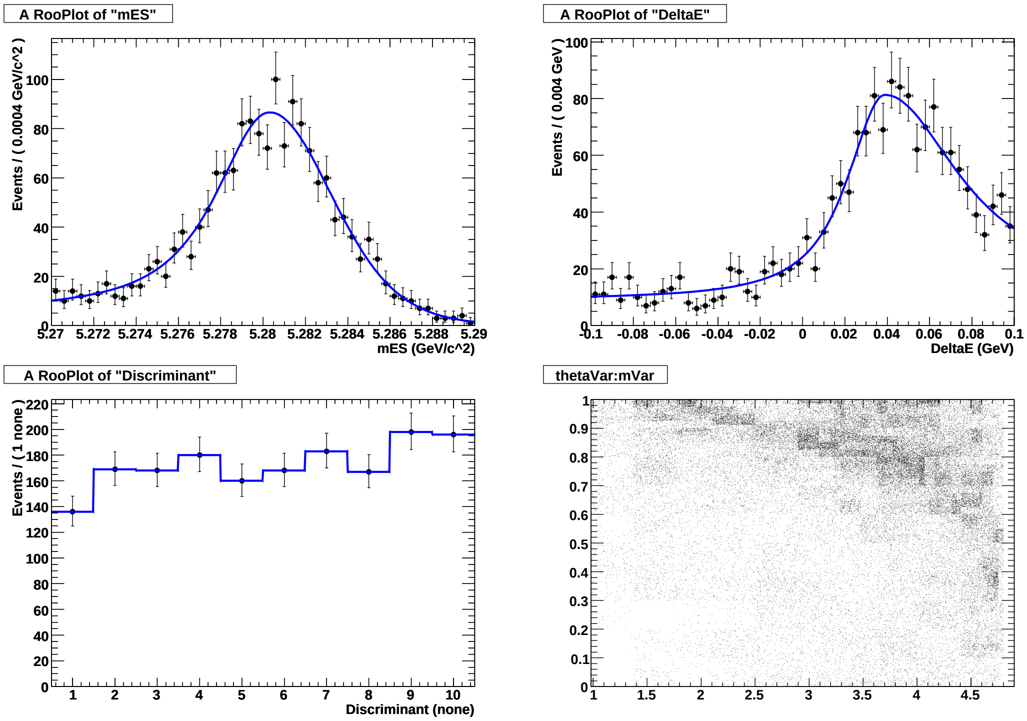

Figure A.1: $B^+ \to K^+K^-K^+$ PDF's used for the $B\overline{B}$ background category referred to as "BB chmls" in Table 5.4. Top left: m_{ES}, top right: ΔE, bottom left: binned NN, bottom right: square DP.

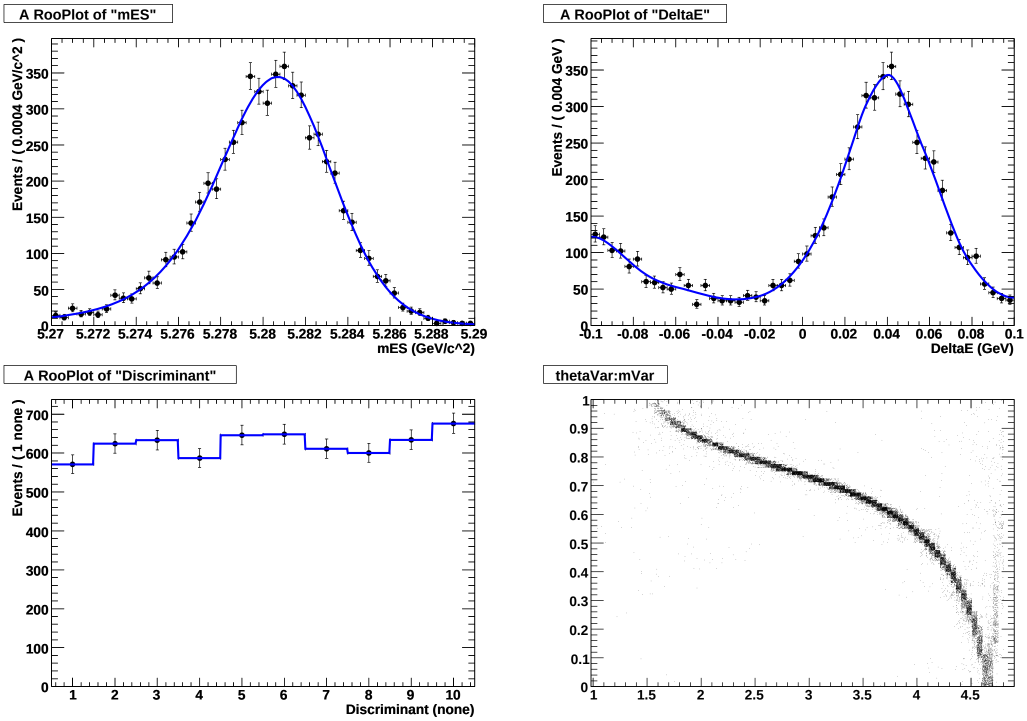

Figure A.2: $B^+ \to K^+K^-K^+$ PDF's used for the $B\overline{B}$ background category referred to as "BB charm 1" in Table 5.4. Top left: $m_{\rm ES}$, top right: ΔE, bottom left: binned NN, bottom right: square DP.

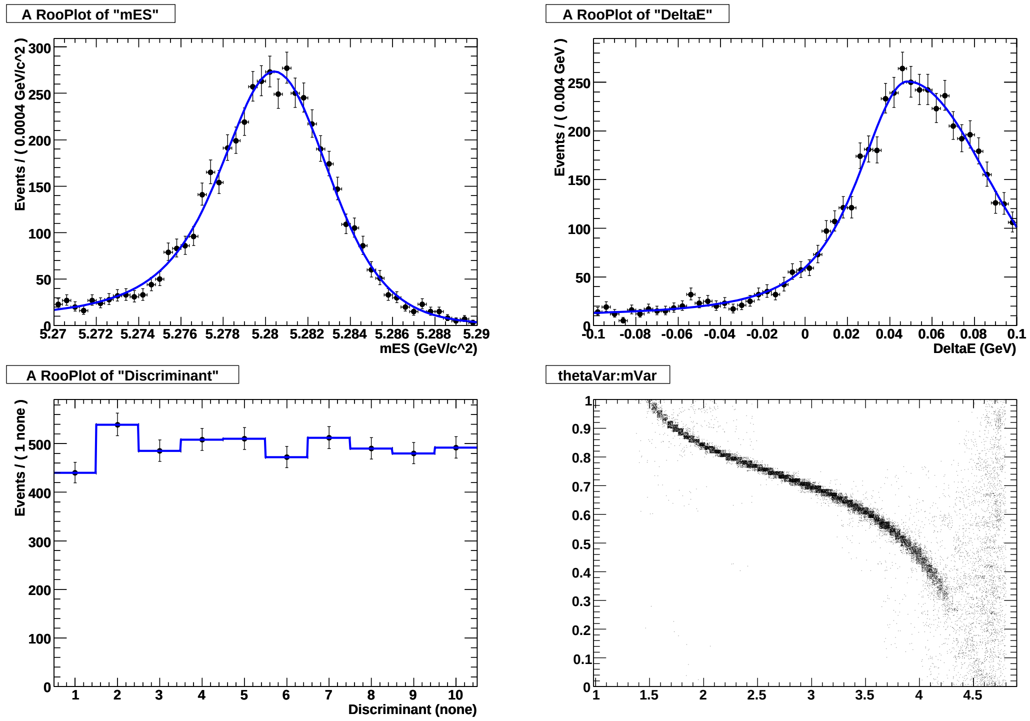

Figure A.3: $B^+ \to K^+K^-K^+$ PDF's used for the $B\overline{B}$ background category referred to as "BB charm 2" in Table 5.4. Top left: m_{ES}, top right: ΔE, bottom left: binned NN, bottom right: square DP.

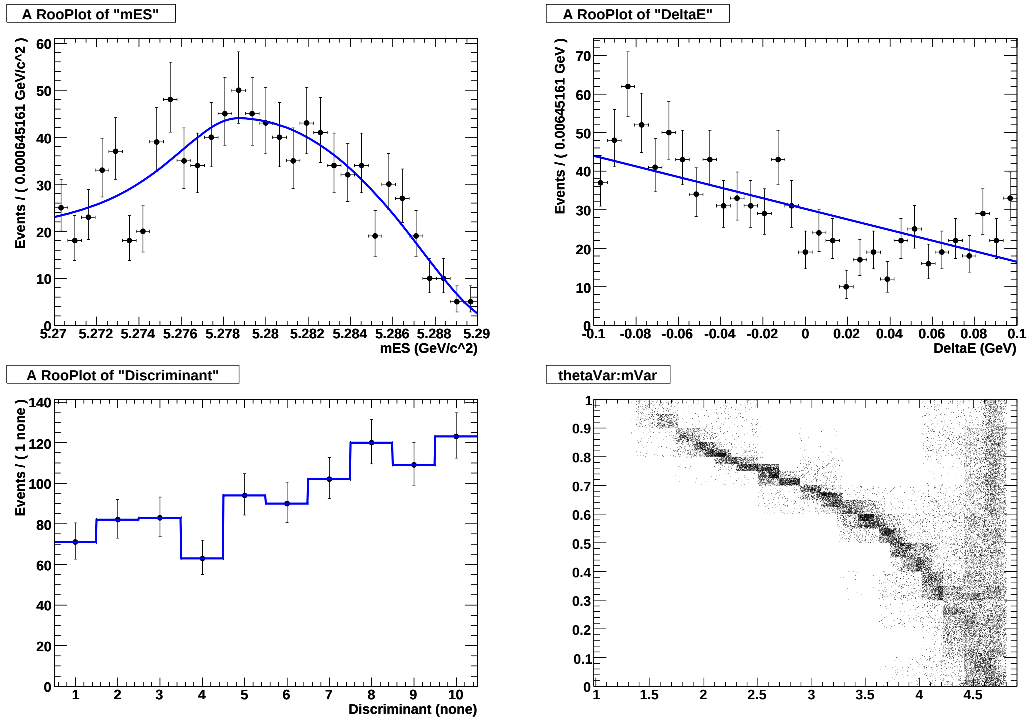

Figure A.4: $B^+ \to K^+K^-K^+$ PDF's used for the $B\overline{B}$ background category referred to as "BB charm 3" in Table 5.4. Top left: m_{ES}, top right: ΔE, bottom left: binned NN, bottom right: square DP.

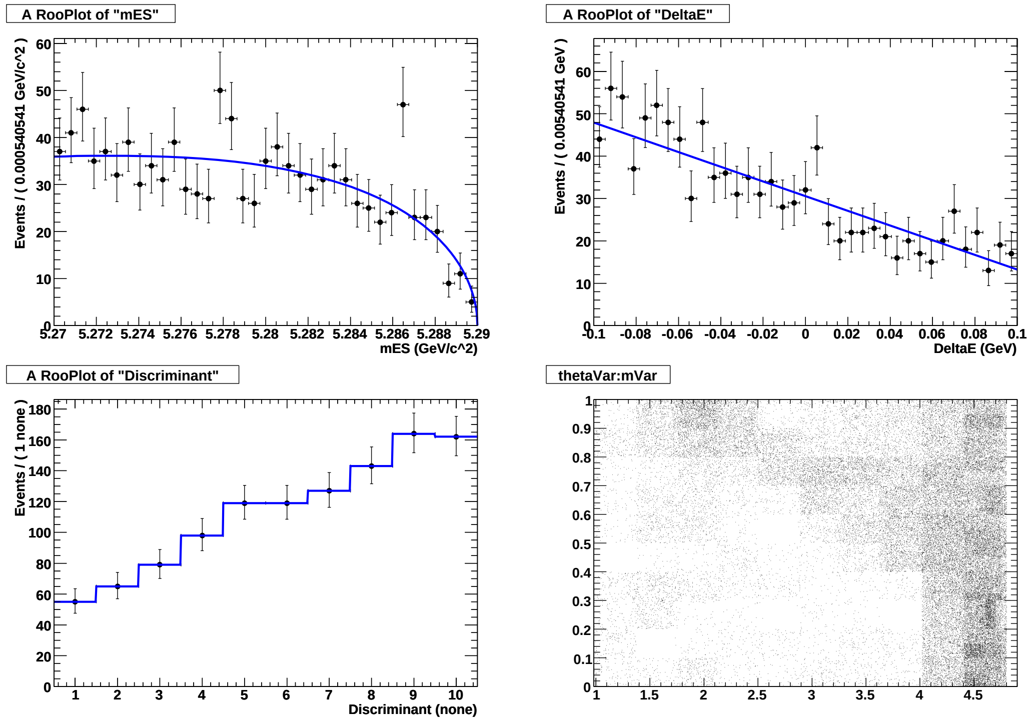

Figure A.5: $B^+ \to K^+K^-K^+$ PDF's used for the $B\overline{B}$ background category referred to as "BB charm 4" in Table 5.4. Top left: $m_{\rm ES}$, top right: ΔE, bottom left: binned NN, bottom right: square DP.

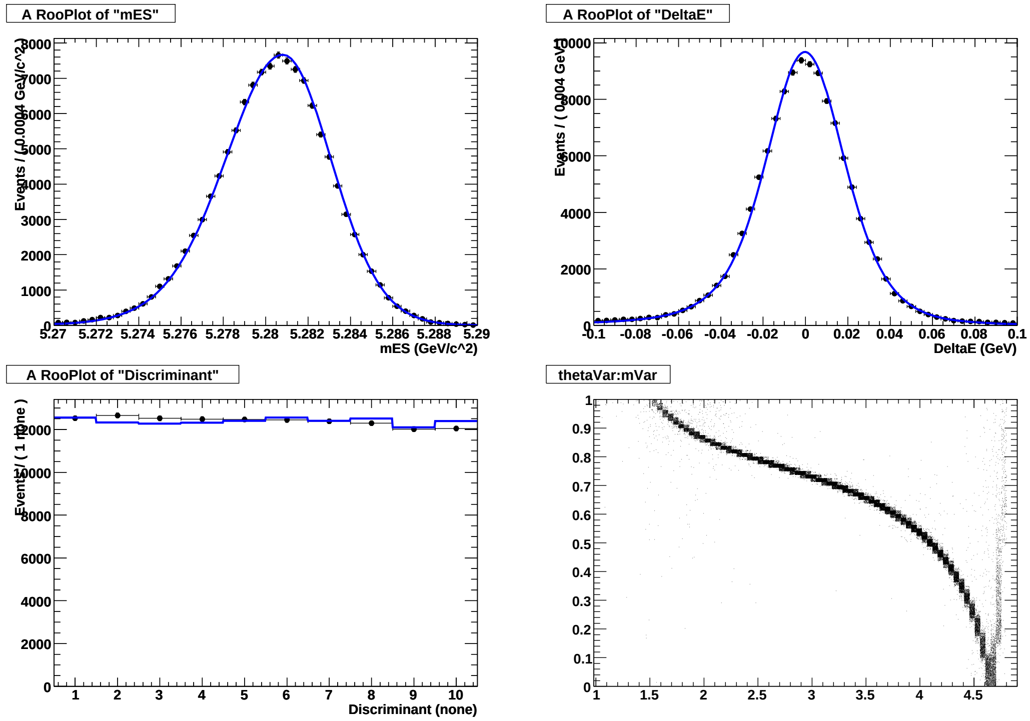

Figure A.6: $B^+ \rightarrow K^+K^-K^+$ PDF's used for the $B\overline{B}$ background category referred to as "BB charm 5" in Table 5.4. Top left: m_{ES}, top right: ΔE, bottom left: binned NN, bottom right: square DP. Note that this $B\overline{B}$ background category uses the same non-DP PDF's as signal.

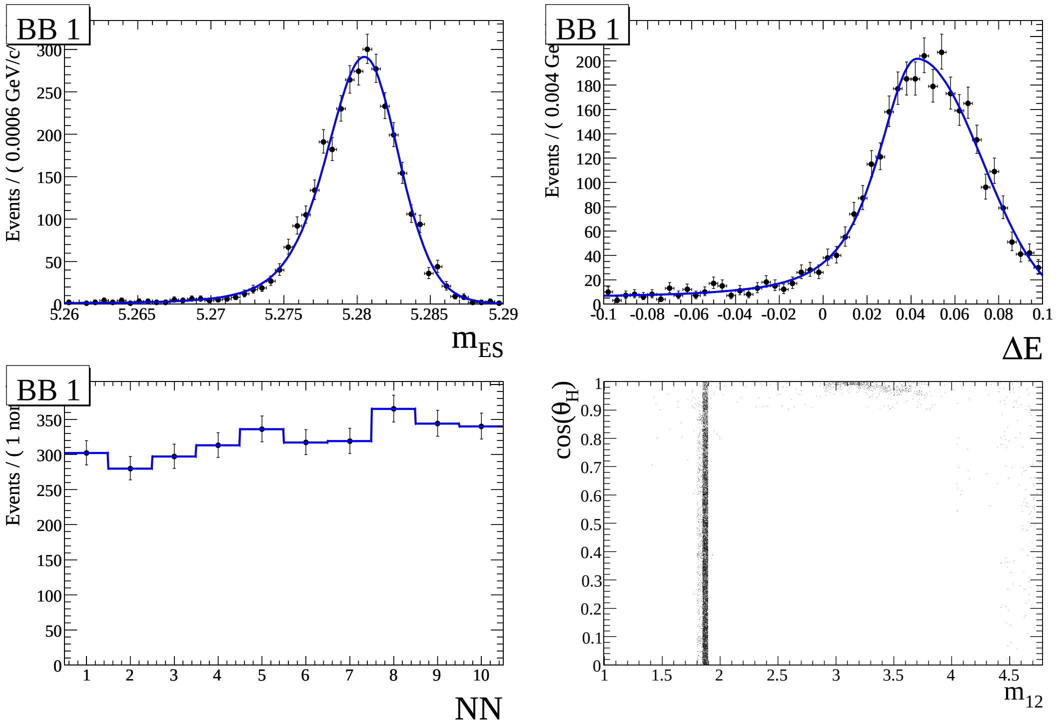

Figure A.7: $B^+ \to K^0_S K^0_S K^+$ PDF's used for the $B\overline{B}$ background category referred to as "BB 1" in Table 5.6. Top left: m_{ES}, top right: ΔE, bottom left: binned NN, bottom right: square DP.

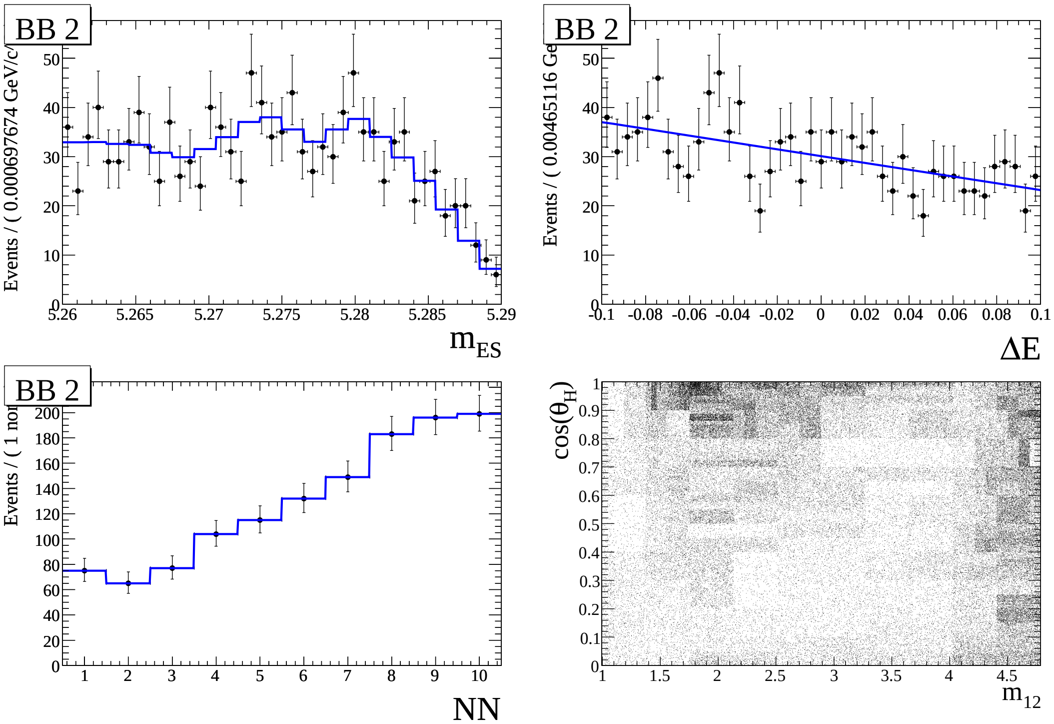

Figure A.8: $B^+ \to K^0_S K^0_S K^+$ PDF's used for the $B\overline{B}$ background category referred to as “BB 2” in Table 5.6. Top left: $m_{\rm ES}$, top right: ΔE, bottom left: binned NN, bottom right: square DP.

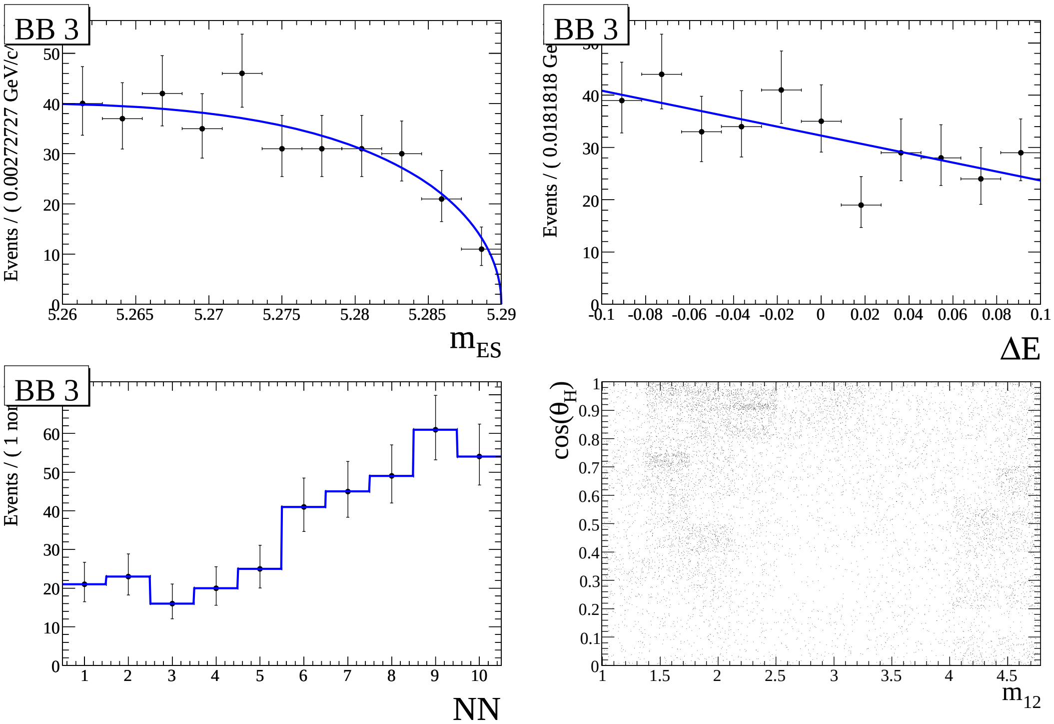

Figure A.9: $B^+ \to K^0_S K^0_S K^+$ PDF's used for the $B\overline{B}$ background category referred to as "BB 3" in Table 5.6. Top left: $m_{\rm ES}$, top right: ΔE, bottom left: binned NN, bottom right: square DP.

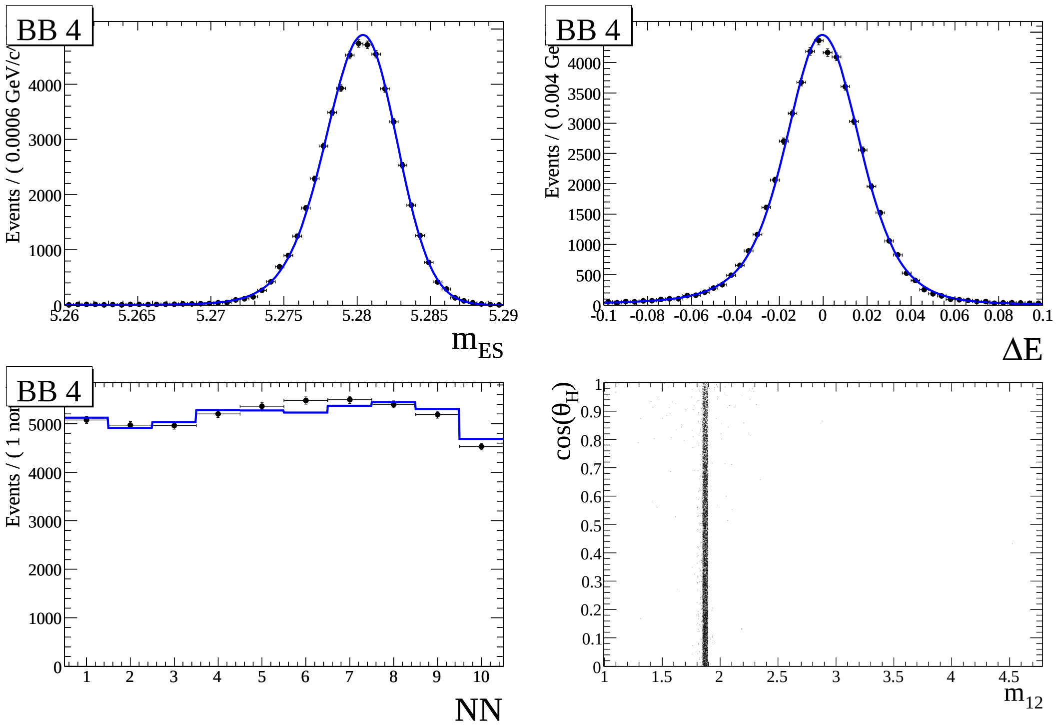

Figure A.10: $B^+ \to K^0_S K^0_S K^+$ PDF's used for the $B\overline{B}$ background category referred to as "BB 4" in Table 5.6. Top left: $m_{\rm ES}$, top right: ΔE, bottom left: binned NN, bottom right: square DP. Note that this $B\overline{B}$ background category uses the same non-DP PDF's as signal.

Appendix B

Background DP PDF's with Adaptive Binning

Here we briefly describe the manner in which the DP PDF's for the various background categories are created. For illustration purposes, we will use the continuum PDF as an example, but the other backgrounds categories are done similarly.

Fig. B.1 shows the DP distribution of $B^+ \to K^+K^-K^+$ onpeak sideband events, both using the square DP coordinates, and using m_{23} versus m_{12}. The basic idea is to create a histogram PDF that describes the onpeak sideband events well, without having lots of bins with very few events in them, which would result in the PDF capturing lots of statistical fluctuations. We calculate appropriate bin sizes for the histogram using an adaptive binning algorithm.

The adaptive binning algorithm scans through every bin, and decides to split a bin in half as long as the two resulting bins each have a sufficient number of events in them (the exact number is a parameter that may be adjusted by hand). The algorithm splits the bin either horizontally or vertically, depending on whether the event density is changing more rapidly in the vertical or horizontal direction. If the event density is changing extremely rapidly, the algorithm may decide to split a bin, even if splitting the bin results in one half of the bin containing fewer than the usual minimum number of events. This is necessary for handling sharp peaks. Additionally, the initial binning used to get the algorithm started may be adjusted by hand.

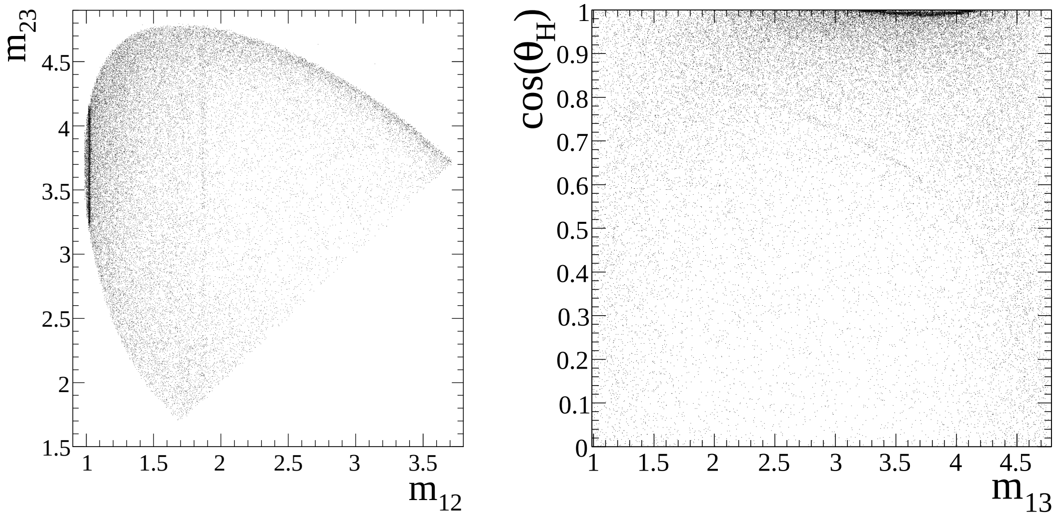

Figure B.1: The $B^+ \to K^+K^-K^+$ onpeak sideband DP distributions. m_{23} versus m_{12} (left). Square DP (right).

For $B^+ \to K^+K^-K^+$ (but not for the other modes), there is an additional complication. Narrow resonances tend to appear as vertical or horizontal bands in the m_{23} versus m_{12} plot, but have more unusual shapes in the square DP. As a consequence, it takes fewer rectangular bins to describe these resonances in the m_{23} versus m_{12} plot than in the square DP. So, to begin, we apply our adaptive binning algorithm to the m_{23} versus m_{12} plot. The resulting binning, along with the PDF value per bin, is shown in Fig. B.2.

We now have a PDF, without $B\overline{B}$ subtraction, in the m_{23} versus m_{12} coordinates. Next, we apply $B\overline{B}$ subtraction to this PDF (using generic $B\overline{B}$ MC), and generate a large number of toy events (600,000 in this case) with the resulting PDF. Then, we apply the adaptive binning algorithm to these toy events, using the square DP coordinates. The large number of toy events is necessary, because a greater number of bins are necessary when using the square DP coordinates. The result of the adaptive binning is shown in Fig. B.3.

For the case of the $B^+ \to K^+K^-K^+$ continuum PDF, in order to better match the D^0-peak seen in the onpeak sideband, we add an extra small peaking component

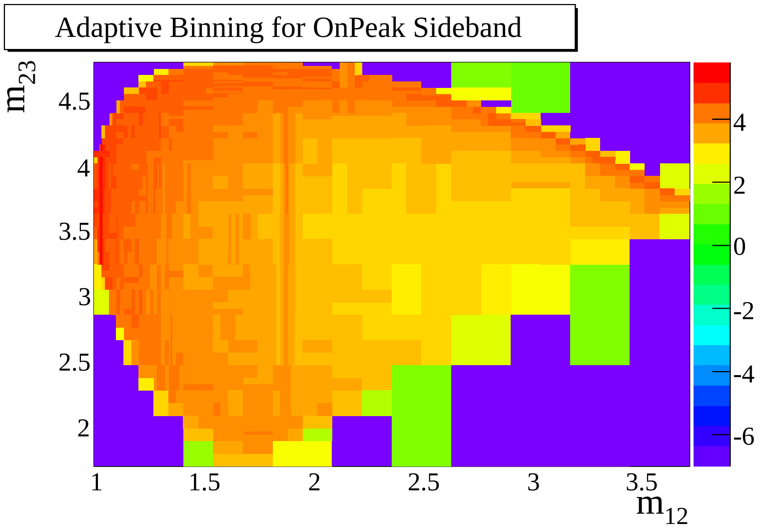

Figure B.2: Adaptive binning applied to the $B^+ \rightarrow K^+K^-K^+$ onpeak sideband, using the m_{23} and m_{12} coordinates. Color indicates the density of events in a given bin, done in log scale.

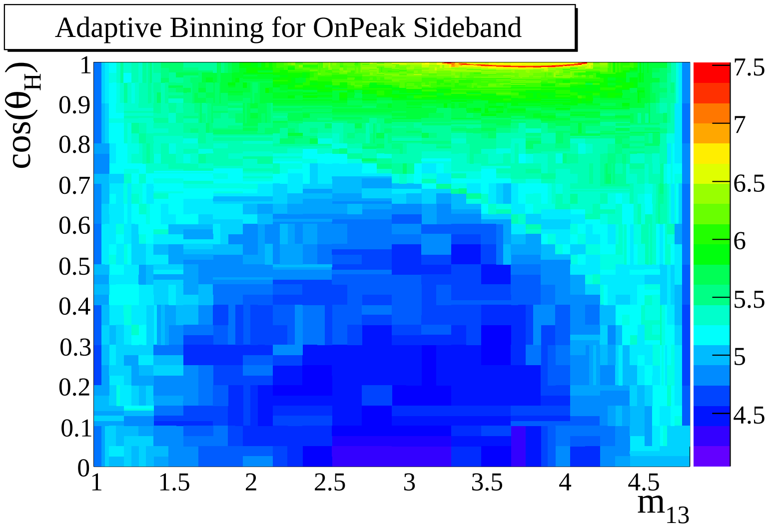

Figure B.3: Adaptive binning applied to $B^+ \rightarrow K^+K^-K^+$ continuum toy events described in the text, using the square DP coordinates. Color indicates the density of events in a given bin, done in log scale.

to the PDF by hand. This gives our final PDF.

In the case of $B^+ \to K^0_S K^0_S K^+$ and $B^0 \to K^+ K^- K^0_S$, there are fewer steps in creating the DP PDF's, because there is no need to go through the steps with the m_{23} versus m_{12} plot. For these decay modes, we simply apply the adaptive binning algorithm to the square DP, right from the start.

Appendix C

Multiple Solutions

In this appendix, we give tables of all the solutions (i.e., local minima in the likelihood function) for $B^+ \to K^0_S K^0_S K^+$ and $B^0 \to K^+ K^- K^0_S$, except the global best solution. The Δ(NLL) row indicates the difference in $\log \mathcal{L}$ between that solution and the global best solution.

C.1 $B^+ \to K^0_S K^0_S K^+$

Table C.1: $B^+ \to K^0_S K^0_S K^+$ Solution 2.

Decay	Magnitude c_r	Phase ϕ_r (rad.)	Fraction FF_r (%)
$f_0(980)$	12 ± 6	2.00 ± 0.37	128 ± 54
$f_0(1500)$	0.69 ± 0.30	-0.29 ± 0.39	3.6 ± 1.8
$f_2'(1525)$	0.0062 ± 0.0031	0.13 ± 0.31	5.2 ± 2.3
$f_0(1710)$	0.8 ± 0.5	0.70 ± 0.40	3.9 ± 2.3
χ_{c0}	0.40 ± 0.21	-1.2 ± 0.8	4.8 ± 2.0
a_{S0}	1.0 (fixed)	0.0 (fixed)	
a_{S1}	3.1 ± 1.7	-2.66 ± 0.29	97 ± 55
a_{S2}	1.8 ± 1.2	0.77 ± 0.35	
$A_{CP}(\%)$	3 ± 5		
$\Delta\phi$ (rad.)	-0.9 ± 1.1		
N(signal)	637 ± 28		
Δ(NLL)	0.05		

Table C.2: $B^+ \to K^0_S K^0_S K^+$ Solution 3.

Decay	Magnitude c_r	Phase ϕ_r (rad.)	Fraction FF_r (%)
$f_0(980)$	2.80 ± 0.29	-0.38 ± 0.12	75 ± 19
$f_0(1500)$	0.23 ± 0.05	-0.45 ± 0.26	4.2 ± 1.9
$f_2'(1525)$	0.00181 ± 0.00033	0.01 ± 0.23	4.5 ± 1.4
$f_0(1710)$	0.28 ± 0.07	0.32 ± 0.20	4.7 ± 2.6
χ_{c0}	0.128 ± 0.019	1.4 ± 0.8	5.0 ± 1.4
a_{S0}	1.0 (fixed)	0.0 (fixed)	
a_{S1}	1.44 ± 0.12	2.41 ± 0.09	262 ± 39
a_{S2}	0.79 ± 0.11	-1.12 ± 0.12	
$A_{CP}(\%)$	4 ± 5		
$\Delta\phi$ (rad.)	-0.4 ± 1.0		
N(signal)	639 ± 28		
Δ(NLL)	0.4		

Table C.3: $B^+ \to K^0_S K^0_S K^+$ Solution 4.

Decay	Magnitude c_r	Phase ϕ_r (rad.)	Fraction FF_r (%)
$f_0(980)$	3.6 ± 0.7	0.99 ± 0.12	69 ± 32
$f_0(1500)$	0.29 ± 0.07	0.66 ± 0.25	3.8 ± 1.8
$f_2'(1525)$	0.0023 ± 0.0005	1.08 ± 0.22	4.0 ± 1.7
$f_0(1710)$	0.36 ± 0.11	1.35 ± 0.24	4.3 ± 2.8
χ_{c0}	0.168 ± 0.028	-1.2 ± 0.6	4.8 ± 1.8
a_{S0}	1.0 (fixed)	0.0 (fixed)	
a_{S1}	1.88 ± 0.29	-2.58 ± 0.11	237 ± 33
a_{S2}	1.06 ± 0.23	0.85 ± 0.16	
$A_{CP}(\%)$	2 ± 5		
$\Delta\phi$ (rad.)	-0.8 ± 1.0		
N(signal)	639 ± 28		
Δ(NLL)	1.3		

Table C.4: $B^+ \to K_S^0 K_S^0 K^+$ Solution 5.

Decay	Magnitude c_r	Phase ϕ_r (rad.)	Fraction FF_r (%)
$f_0(980)$	29.7 ± 1.9	2.1 ± 0.5	140 ± 21
$f_0(1500)$	1.43 ± 0.37	-0.1 ± 0.5	2.7 ± 1.6
$f_2'(1525)$	0.0148 ± 0.0028	0.2 ± 0.5	5.0 ± 1.6
$f_0(1710)$	2.1 ± 0.6	1.0 ± 0.5	4.3 ± 2.5
χ_{c0}	0.99 ± 0.15	-1.3 ± 0.8	5.0 ± 1.2
a_{S0}	1.0 (fixed)	0.0 (fixed)	
a_{S1}	8.0 ± 2.9	-2.5 ± 0.5	108 ± 22
a_{S2}	5.53 ± 0.45	0.8 ± 0.5	
A_{CP}(%)	3 ± 5		
$\Delta\phi$ (rad.)	-0.8 ± 1.0		
N(signal)	639 ± 28		
Δ(NLL)	1.4		

Table C.5: $B^+ \to K_S^0 K_S^0 K^+$ Solution 6.

Decay	Magnitude c_r	Phase ϕ_r (rad.)	Fraction FF_r (%)
$f_0(980)$	3.20 ± 0.20	0.67 ± 0.14	152 ± 24
$f_0(1500)$	0.75 ± 0.06	-0.14 ± 0.10	68 ± 7
$f_2'(1525)$	0.00162 ± 0.00028	-1.20 ± 0.20	5.6 ± 1.6
$f_0(1710)$	0.29 ± 0.07	-0.89 ± 0.15	7.4 ± 3.6
χ_{c0}	0.103 ± 0.015	0.8 ± 0.9	5.0 ± 1.4
a_{S0}	1.0 (fixed)	0.0 (fixed)	
a_{S1}	0.95 ± 0.07	2.24 ± 0.08	209 ± 32
a_{S2}	0.48 ± 0.07	-1.52 ± 0.13	
A_{CP}(%)	4 ± 5		
$\Delta\phi$ (rad.)	-0.4 ± 1.1		
N(signal)	637 ± 28		
Δ(NLL)	1.5		

Table C.6: $B^+ \to K^0_S K^0_S K^+$ Solution 7.

Decay	Magnitude c_r	Phase ϕ_r (rad.)	Fraction FF_r (%)
$f_0(980)$	2.61 ± 0.25	-0.28 ± 0.10	85 ± 20
$f_0(1500)$	0.73 ± 0.06	0.73 ± 0.13	54 ± 6
$f'_2(1525)$	0.00186 ± 0.00032	-0.42 ± 0.20	6.1 ± 1.8
$f_0(1710)$	0.32 ± 0.07	-0.27 ± 0.15	7.7 ± 3.7
χ_{c0}	0.113 ± 0.015	1.3 ± 0.8	5.0 ± 1.3
a_{S0}	1.0 (fixed)	0.0 (fixed)	
a_{S1}	1.31 ± 0.10	2.36 ± 0.08	290 ± 36
a_{S2}	0.71 ± 0.09	-1.20 ± 0.11	
A_{CP}(%)	3 ± 5		
$\Delta\phi$ (rad.)	-0.4 ± 1.0		
N(signal)	638 ± 28		
Δ(NLL)	1.6		

Table C.7: $B^+ \to K^0_S K^0_S K^+$ Solution 8.

Decay	Magnitude c_r	Phase ϕ_r (rad.)	Fraction FF_r (%)
$f_0(980)$	3.6 ± 0.6	1.00 ± 0.11	70 ± 27
$f_0(1500)$	0.29 ± 0.06	0.66 ± 0.24	3.8 ± 1.7
$f'_2(1525)$	0.00226 ± 0.00045	1.08 ± 0.22	4.0 ± 1.6
$f_0(1710)$	0.36 ± 0.11	1.35 ± 0.24	4.3 ± 2.5
χ_{c0}	0.168 ± 0.027	-1.2 ± 0.6	4.8 ± 1.6
a_{S0}	1.0 (fixed)	0.0 (fixed)	
a_{S1}	1.88 ± 0.26	-2.58 ± 0.11	237 ± 29
a_{S2}	1.06 ± 0.20	0.85 ± 0.16	
A_{CP}(%)	2 ± 5		
$\Delta\phi$ (rad.)	-0.8 ± 1.0		
N(signal)	640 ± 28		
Δ(NLL)	1.6		

Table C.8: $B^+ \rightarrow K^0_S K^0_S K^+$ Solution 9.

Decay	Magnitude c_r	Phase ϕ_r (rad.)	Fraction FF_r (%)
$f_0(980)$	15 ± 5	1.81 ± 0.34	143 ± 47
$f_0(1500)$	3.5 ± 1.2	0.75 ± 0.27	63 ± 20
$f_2'(1525)$	0.0080 ± 0.0029	-0.37 ± 0.31	5.7 ± 3.5
$f_0(1710)$	1.3 ± 0.5	-0.12 ± 0.27	6.4 ± 3.1
χ_{c0}	0.49 ± 0.18	-1.7 ± 0.8	4.8 ± 1.7
a_{S0}	1.0 (fixed)	0.0 (fixed)	
a_{S1}	3.8 ± 1.4	-2.96 ± 0.28	100 ± 52
a_{S2}	2.3 ± 1.0	0.40 ± 0.35	
$A_{CP}(\%)$	3 ± 5		
$\Delta\phi$ (rad.)	-0.9 ± 1.1		
N(signal)	637 ± 28		
Δ(NLL)	1.7		

Table C.9: $B^+ \rightarrow K^0_S K^0_S K^+$ Solution 10.

Decay	Magnitude c_r	Phase ϕ_r (rad.)	Fraction FF_r (%)
$f_0(980)$	4.5 ± 1.1	0.99 ± 0.11	80 ± 20
$f_0(1500)$	1.23 ± 0.25	1.76 ± 0.17	50 ± 7
$f_2'(1525)$	0.0034 ± 0.0007	0.55 ± 0.22	6.4 ± 2.0
$f_0(1710)$	0.52 ± 0.17	0.65 ± 0.19	6.8 ± 3.5
χ_{c0}	0.196 ± 0.042	-1.4 ± 0.6	4.9 ± 1.1
a_{S0}	1.0 (fixed)	0.0 (fixed)	
a_{S1}	2.2 ± 0.5	-2.73 ± 0.12	232 ± 30
a_{S2}	1.26 ± 0.37	0.65 ± 0.18	
$A_{CP}(\%)$	3 ± 5		
$\Delta\phi$ (rad.)	-0.8 ± 1.0		
N(signal)	638 ± 28		
Δ(NLL)	2.2		

Table C.10: $B^+ \to K_S^0 K_S^0 K^+$ Solution 11.

Decay	Magnitude c_r	Phase ϕ_r (rad.)	Fraction FF_r (%)
$f_0(980)$	15 ± 7	1.82 ± 0.41	142 ± 35
$f_0(1500)$	3.5 ± 1.6	0.75 ± 0.33	63 ± 10
$f_2'(1525)$	0.0079 ± 0.0038	-0.37 ± 0.36	5.7 ± 2.2
$f_0(1710)$	1.3 ± 0.6	-0.11 ± 0.32	6.4 ± 4.2
χ_{c0}	0.49 ± 0.23	-1.7 ± 0.8	4.8 ± 1.6
a_{S0}	1.0 (fixed)	0.0 (fixed)	
a_{S1}	3.8 ± 1.8	-2.96 ± 0.32	100 ± 28
a_{S2}	2.3 ± 1.3	0.41 ± 0.41	
$A_{CP}(\%)$	3 ± 5		
$\Delta\phi$ (rad.)	-0.9 ± 1.1		
N(signal)	637 ± 28		
Δ(NLL)	2.3		

Table C.11: $B^+ \to K_S^0 K_S^0 K^+$ Solution 12.

Decay	Magnitude c_r	Phase ϕ_r (rad.)	Fraction FF_r (%)
$f_0(980)$	13 ± 5	1.84 ± 0.32	134 ± 51
$f_0(1500)$	0.79 ± 0.29	-0.18 ± 0.34	3.8 ± 1.9
$f_2'(1525)$	0.0068 ± 0.0026	0.20 ± 0.30	4.9 ± 2.2
$f_0(1710)$	2.5 ± 0.9	0.83 ± 0.28	28 ± 10
χ_{c0}	0.45 ± 0.16	-1.6 ± 0.7	4.8 ± 1.8
a_{S0}	1.0 (fixed)	0.0 (fixed)	
a_{S1}	3.5 ± 1.3	-2.87 ± 0.25	98 ± 52
a_{S2}	2.1 ± 0.9	0.51 ± 0.33	
$A_{CP}(\%)$	2 ± 5		
$\Delta\phi$ (rad.)	-0.9 ± 1.1		
N(signal)	637 ± 28		
Δ(NLL)	3.2		

Table C.12: $B^+ \to K^0_S K^0_S K^+$ Solution 13.

Decay	Magnitude c_r	Phase ϕ_r (rad.)	Fraction FF_r (%)
$f_0(980)$	30.8 ± 2.2	1.9 ± 0.5	137 ± 30
$f_0(1500)$	1.57 ± 0.43	-0.1 ± 0.5	2.9 ± 1.5
$f_2'(1525)$	0.0151 ± 0.0032	0.2 ± 0.5	4.8 ± 1.7
$f_0(1710)$	5.7 ± 0.7	0.9 ± 0.5	28 ± 6
χ_{c0}	1.02 ± 0.16	-1.7 ± 0.8	4.8 ± 1.4
a_{S0}	1.0 (fixed)	0.0 (fixed)	
a_{S1}	8 ± 11	-2.8 ± 0.5	100 ± 35
a_{S2}	5.48 ± 0.45	0.5 ± 0.5	
A_{CP}(%)	2 ± 5		
$\Delta\phi$ (rad.)	-0.9 ± 1.0		
N(signal)	640 ± 28		
Δ(NLL)	4.0		

Table C.13: $B^+ \to K^0_S K^0_S K^+$ Solution 14.

Decay	Magnitude c_r	Phase ϕ_r (rad.)	Fraction FF_r (%)
$f_0(980)$	15 ± 6	1.62 ± 0.38	146 ± 28
$f_0(1500)$	3.8 ± 1.4	0.75 ± 0.31	73 ± 8
$f_2'(1525)$	0.0074 ± 0.0028	-0.32 ± 0.35	4.9 ± 1.9
$f_0(1710)$	3.1 ± 1.2	-0.01 ± 0.30	38 ± 6
χ_{c0}	0.49 ± 0.19	-2.0 ± 0.8	4.8 ± 1.3
a_{S0}	1.0 (fixed)	0.0 (fixed)	
a_{S1}	3.8 ± 1.5	3.07 ± 0.31	99 ± 25
a_{S2}	2.3 ± 1.1	0.12 ± 0.38	
A_{CP}(%)	3 ± 5		
$\Delta\phi$ (rad.)	-0.9 ± 1.1		
N(signal)	637 ± 28		
Δ(NLL)	4.0		

Table C.14: $B^+ \to K_S^0 K_S^0 K^+$ Solution 15.

Decay	Magnitude c_r	Phase ϕ_r (rad.)	Fraction FF_r (%)
$f_0(980)$	4.1 ± 0.9	0.97 ± 0.11	74 ± 19
$f_0(1500)$	0.34 ± 0.08	0.84 ± 0.24	4.1 ± 1.8
$f_2'(1525)$	0.0024 ± 0.0006	1.25 ± 0.24	3.7 ± 1.4
$f_0(1710)$	0.94 ± 0.18	1.59 ± 0.20	24.2 ± 4.1
χ_{c0}	0.185 ± 0.035	-1.3 ± 0.6	4.8 ± 1.0
a_{S0}	1.0 (fixed)	0.0 (fixed)	
a_{S1}	2.06 ± 0.39	-2.67 ± 0.11	232 ± 30
a_{S2}	1.18 ± 0.30	0.72 ± 0.17	
$A_{CP}(\%)$	2 ± 5		
$\Delta\phi$ (rad.)	-0.9 ± 1.0		
N(signal)	640 ± 28		
Δ(NLL)	4.1		

C.2 $B^0 \to K^+K^-K^0_S$

Table C.15: $B^0 \to K^+K^-K^0_S$ Solution 2.

Decay	Magnitude c_r	Phase ϕ_r (rad.)	Fraction FF_r (%)
$\phi(1020)$	0.046 ± 0.007	0.47 ± 0.30	13.3 ± 1.1
$f_0(980)$	2.6 ± 0.6	0.79 ± 0.26	27 ± 8
$f_0(1500)$	1.30 ± 0.20	2.42 ± 0.21	50.8 ± 3.1
$f_2'(1525)$	0.00085 ± 0.00037	2.1 ± 0.5	0.39 ± 0.31
$f_0(1710)$	1.09 ± 0.18	1.18 ± 0.19	26.6 ± 3.2
χ_{c0}	0.170 ± 0.031	-0.5 ± 0.5	3.4 ± 0.7
a_{S0}	1.0 (fixed)	0.0 (fixed)	
a_{S1}	1.44 ± 0.31	-2.68 ± 0.17	101 ± 16
a_{S2}	0.69 ± 0.27	0.84 ± 0.28	
a_{P0}	1.48 ± 0.28	0.87 ± 0.22	
a_{P1}	0.21 ± 0.19	-1.3 ± 0.7	10.7 ± 2.2
a_{P2}	0.62 ± 0.19	-2.45 ± 0.35	

N(signal), $K^0_S \to \pi^+\pi^-$	1420 ± 43
N(signal), $K^0_S \to \pi^0\pi^0$	159 ± 17
Δ(NLL)	2.0

Table C.16: $B^0 \to K^+K^-K_S^0$ Solution 3.

Decay	Magnitude c_r	Phase ϕ_r (rad.)	Fraction FF_r (%)
$\phi(1020)$	0.0358 ± 0.0041	0.33 ± 0.40	13.2 ± 1.2
$f_0(980)$	2.0 ± 0.5	0.66 ± 0.42	25 ± 9
$f_0(1500)$	0.196 ± 0.039	0.03 ± 0.32	1.9 ± 0.9
$f_2'(1525)$	0.00079 ± 0.00025	0.65 ± 0.37	0.56 ± 0.39
$f_0(1710)$	0.23 ± 0.08	1.54 ± 0.29	2.0 ± 1.1
χ_{c0}	0.133 ± 0.021	-0.2 ± 0.6	3.4 ± 0.7
a_{S0}	1.0 (fixed)	0.0 (fixed)	
a_{S1}	1.17 ± 0.29	-2.55 ± 0.20	120 ± 21
a_{S2}	0.55 ± 0.27	1.07 ± 0.28	
a_{P0}	1.12 ± 0.19	1.33 ± 0.26	
a_{P1}	0.28 ± 0.18	-1.1 ± 0.5	11.9 ± 2.7
a_{P2}	0.35 ± 0.15	-2.1 ± 0.5	

N(signal), $K_S^0 \to \pi^+\pi^-$	1418 ± 43
N(signal), $K_S^0 \to \pi^0\pi^0$	160 ± 17
Δ(NLL)	2.0

Table C.17: $B^0 \to K^+K^-K_S^0$ Solution 4.

Decay	Magnitude c_r	Phase ϕ_r (rad.)	Fraction FF_r (%)
$\phi(1020)$	0.036 ± 0.006	-0.8 ± 0.8	13.2 ± 2.3
$f_0(980)$	1.8 ± 0.5	-0.6 ± 0.8	19 ± 10
$f_0(1500)$	0.208 ± 0.045	-0.8 ± 0.9	2.1 ± 1.1
$f_2'(1525)$	0.00082 ± 0.00027	-0.0 ± 0.9	0.60 ± 0.37
$f_0(1710)$	0.22 ± 0.09	0.9 ± 0.7	1.8 ± 1.3
χ_{c0}	0.136 ± 0.027	1.0 ± 1.0	3.5 ± 1.0
a_{S0}	1.0 (fixed)	0.0 (fixed)	
a_{S1}	0.96 ± 0.35	2.8 ± 0.9	94 ± 21
a_{S2}	0.36 ± 0.44	-0.8 ± 1.5	
a_{P0}	1.12 ± 0.22	1.72 ± 0.27	
a_{P1}	0.31 ± 0.32	-2.3 ± 0.8	11.9 ± 4.0
a_{P2}	0.34 ± 0.22	-1.2 ± 0.7	

N(signal), $K_S^0 \to \pi^+\pi^-$	1419 ± 43
N(signal), $K_S^0 \to \pi^0\pi^0$	162 ± 17
Δ(NLL)	3.7

Table C.18: $B^0 \to K^+K^-K^0_S$ Solution 5.

Decay	Magnitude c_r	Phase ϕ_r (rad.)	Fraction FF_r (%)
$\phi(1020)$	0.051 ± 0.021	2.9 ± 0.9	13.7 ± 2.2
$f_0(980)$	3.6 ± 1.5	2.0 ± 1.0	41 ± 14
$f_0(1500)$	0.32 ± 0.18	-1.5 ± 0.9	2.6 ± 1.3
$f_2'(1525)$	0.0012 ± 0.0006	-0.5 ± 0.8	0.61 ± 0.43
$f_0(1710)$	1.00 ± 0.36	0.8 ± 0.6	18.9 ± 4.0
χ_{c0}	0.19 ± 0.08	0.1 ± 0.5	3.4 ± 0.9
a_{S0}	1.0 (fixed)	0.0 (fixed)	
a_{S1}	0.80 ± 0.21	3.0 ± 0.8	34 ± 31
a_{S2}	0.09 ± 0.20	-1 ± 5	
a_{P0}	1.6 ± 0.6	1.07 ± 0.25	
a_{P1}	0.37 ± 0.20	-2.8 ± 0.9	11.7 ± 3.2
a_{P2}	0.47 ± 0.18	-1.82 ± 0.45	

N(signal), $K^0_S \to \pi^+\pi^-$	1418 ± 43
N(signal), $K^0_S \to \pi^0\pi^0$	161 ± 17
Δ(NLL)	4.2

Appendix D

Systematics Tables

Here we include tables of the systematic uncertainties. The biggest systematics for each parameter are highlighted in **bold** in the tables. Fit fractions are given in percent, branching fractions are given in units of 10^{-6}, and all phases are given in radians.

Table D.1: $B^+ \to K^+K^-K^+$ systematics.

$\phi(1020)$				
	FF $(+\sigma)$	FF $(-\sigma)$	$\mathcal{B}$ $(+\sigma)$	$\mathcal{B}$ $(-\sigma)$
$\phi(1020)$ Mass/Width	+0.022	-0.032	+0.008	-0.011
$f_0(1500)$ Mass/Width	+0.023	-0.031	+0.008	-0.011
$f_2'(1525)$ Mass/Width	+0.018	-0.019	+0.006	-0.007
$f_0(1710)$ Mass/Width	+0.008	-0.009	+0.002	-0.002
χ_{c0} Mass/Width	+0.004	-0.002	+0.001	-0.000
$\phi(1020)$ BW radius	**+0.769**	**-0.360**	**+0.267**	**-0.124**
$f_2'(1525)$ BW radius	+0.029	-0.054	+0.010	-0.019
$f_0(980)$ Mass	+0.048	-0.053	+0.017	-0.018
$f_0(980)$ g_π	+0.024	-0.030	+0.008	-0.011
$f_0(980)$ g_K	+0.039	-0.036	+0.013	-0.012
B-meson BW radius	+0.024	-0.024	+0.008	-0.008
Eff. map statistics	+0.068	-0.068	+0.027	-0.027
Tracking	+0.000	-0.000	+0.049	**-0.049**
$N_{B\bar{B}}$	+0.000	-0.000	+0.049	**-0.049**
PID	+0.011	-0.011	**+0.083**	**-0.083**
Fixed $B\overline{B}$ A_{CP} and yield	+0.023	-0.023	+0.001	-0.001
Fixed PDF Params	+0.022	-0.022	+0.020	-0.020
Add $f_2(1270)$	+0.124	-0.124	+0.046	-0.046
Add $a_0^0(1450)$	**+0.387**	**-0.387**	**+0.131**	**-0.131**
Add $\phi(1680)$	+0.037	-0.037	+0.015	-0.015
Add $f_2(2010)$, $f_2(2300)$	+0.005	-0.005	+0.006	-0.006
DP PDF Stat.	+0.094	-0.094	+0.035	-0.035
Fit Bias	**+0.362**	**-0.362**	**+0.081**	**-0.081**
Detector Asym.	+0.000	-0.000	+0.000	-0.000
Total	+0.954	-0.673	+0.335	-0.238

Table D.2: $B^+ \to K^+K^-K^+$ systematics.

$f_0(980)$				
	FF ($+\sigma$)	FF ($-\sigma$)	$\mathcal{B}$ ($+\sigma$)	$\mathcal{B}$ ($-\sigma$)
$\phi(1020)$ Mass/Width	+0.085	-0.028	+0.041	-0.010
$f_0(1500)$ Mass/Width	+0.537	-0.555	+0.186	-0.192
$f_2'(1525)$ Mass/Width	+0.206	-0.141	+0.070	-0.049
$f_0(1710)$ Mass/Width	+0.441	-0.442	+0.151	-0.151
χ_{c0} Mass/Width	+0.075	-0.041	+0.026	-0.014
$\phi(1020)$ BW radius	+0.000	-0.163	+0.000	-0.056
$f_2'(1525)$ BW radius	+0.109	-0.000	+0.038	-0.000
$f_0(980)$ Mass	+0.478	-0.074	+0.166	-0.025
$f_0(980)$ g_π	**+3.248**	**-3.242**	**+1.123**	**-1.122**
$f_0(980)$ g_K	+0.248	-0.228	+0.086	-0.079
B-meson BW radius	+0.064	-0.064	+0.022	-0.022
Eff. map statistics	+0.233	-0.233	+0.082	-0.082
Tracking	+0.000	-0.000	+0.102	-0.102
$N_{B\bar{B}}$	+0.000	-0.000	+0.102	-0.102
PID	+0.132	-0.132	+0.212	-0.212
Fixed $B\overline{B}$ A_{CP} and yield	+0.018	-0.011	+0.014	-0.012
Fixed PDF Params	+0.094	-0.094	+0.048	-0.048
Add $f_2(1270)$	+0.335	-0.335	+0.119	-0.119
Add $a_0^0(1450)$	**+7.191**	**-7.191**	**+2.498**	**-2.498**
Add $\phi(1680)$	+0.476	-0.476	+0.167	-0.167
Add $f_2(2010)$, $f_2(2300)$	+0.109	-0.109	+0.031	-0.031
DP PDF Stat.	+0.334	-0.334	+0.114	-0.114
Fit Bias	+0.769	-0.769	+0.357	-0.357
Detector Asym.	+0.000	-0.000	+0.000	-0.000
Total	+8.014	-7.998	+2.804	-2.798

Table D.3: $B^+ \to K^+K^-K^+$ systematics.

$f_0(1500)$				
	FF $(+\sigma)$	FF $(-\sigma)$	$\mathcal{B}$ $(+\sigma)$	$\mathcal{B}$ $(-\sigma)$
$\phi(1020)$ Mass/Width	+0.010	-0.000	+0.003	-0.000
$f_0(1500)$ Mass/Width	+0.142	-0.138	+0.049	-0.048
$f_2'(1525)$ Mass/Width	+0.025	-0.024	+0.009	-0.008
$f_0(1710)$ Mass/Width	+0.091	-0.082	+0.031	-0.028
χ_{c0} Mass/Width	+0.003	-0.000	+0.001	-0.000
$\phi(1020)$ BW radius	+0.009	-0.000	+0.003	-0.000
$f_2'(1525)$ BW radius	+0.017	-0.000	+0.006	-0.000
$f_0(980)$ Mass	+0.019	-0.014	+0.007	-0.005
$f_0(980)$ g_π	+0.008	-0.004	+0.003	-0.001
$f_0(980)$ g_K	+0.004	-0.001	+0.001	-0.000
B-meson BW radius	+0.008	-0.008	+0.003	-0.003
Eff. map statistics	+0.020	-0.020	+0.007	-0.007
Tracking	+0.000	-0.000	+0.008	-0.008
$N_{B\overline{B}}$	+0.000	-0.000	+0.008	-0.008
PID	+0.012	-0.012	+0.009	-0.009
Fixed $B\overline{B}$ A_{CP} and yield	+0.008	-0.006	+0.003	-0.003
Fixed PDF Params	+0.014	-0.014	+0.004	-0.004
Add $f_2(1270)$	+0.112	-0.112	+0.038	-0.038
Add $a_0^0(1450)$	**+1.557**	**-1.557**	**+0.516**	**-0.516**
Add $\phi(1680)$	+0.014	-0.014	+0.005	-0.005
Add $f_2(2010)$, $f_2(2300)$	+0.084	-0.084	+0.030	-0.030
DP PDF Stat.	+0.057	-0.057	+0.020	-0.020
Fit Bias	+0.055	-0.055	+0.024	-0.024
Detector Asym.	+0.000	-0.000	+0.000	-0.000
Total	+1.575	-1.574	+0.523	-0.523

Table D.4: $B^+ \to K^+K^-K^+$ systematics.

$f_2'(1525)$				
	FF ($+\sigma$)	FF ($-\sigma$)	$\mathcal{B}$ ($+\sigma$)	$\mathcal{B}$ ($-\sigma$)
$\phi(1020)$ Mass/Width	+0.002	-0.000	+0.001	-0.000
$f_0(1500)$ Mass/Width	+0.036	-0.035	+0.013	-0.012
$f_2'(1525)$ Mass/Width	**+0.103**	**-0.107**	**+0.036**	**-0.037**
$f_0(1710)$ Mass/Width	+0.012	-0.009	+0.004	-0.003
χ_{c0} Mass/Width	+0.004	-0.003	+0.001	-0.001
$\phi(1020)$ BW radius	+0.009	-0.027	+0.003	-0.009
$f_2'(1525)$ BW radius	**+0.129**	-0.017	**+0.045**	-0.006
$f_0(980)$ Mass	+0.008	-0.001	+0.003	-0.000
$f_0(980)$ g_π	+0.029	-0.027	+0.010	-0.009
$f_0(980)$ g_K	+0.006	-0.005	+0.002	-0.002
B-meson BW radius	+0.028	-0.028	+0.010	-0.010
Eff. map statistics	+0.020	-0.020	+0.007	-0.007
Tracking	+0.000	-0.000	+0.008	-0.008
$N_{B\overline{B}}$	+0.000	-0.000	+0.008	-0.008
PID	+0.008	-0.008	+0.010	-0.010
Fixed $B\overline{B}$ A_{CP} and yield	+0.010	-0.008	+0.004	-0.003
Fixed PDF Params	+0.019	-0.019	+0.005	-0.005
Add $f_2(1270)$	+0.017	-0.017	+0.006	-0.006
Add $a_0^0(1450)$	+0.060	-0.060	+0.022	-0.022
Add $\phi(1680)$	+0.021	-0.021	+0.007	-0.007
Add $f_2(2010)$, $f_2(2300)$	**+0.179**	**-0.179**	**+0.061**	**-0.061**
DP PDF Stat.	+0.032	-0.032	+0.011	-0.011
Fit Bias	**+0.274**	**-0.274**	**+0.103**	**-0.103**
Detector Asym.	+0.000	-0.000	+0.000	-0.000
Total	+0.379	-0.358	+0.138	-0.131

Table D.5: $B^+ \to K^+K^-K^+$ systematics.

$f_0(1710)$				
	FF $(+\sigma)$	FF $(-\sigma)$	$\mathcal{B}$ $(+\sigma)$	$\mathcal{B}$ $(-\sigma)$
$\phi(1020)$ Mass/Width	+0.001	-0.004	+0.000	-0.001
$f_0(1500)$ Mass/Width	+0.141	-0.126	+0.049	-0.044
$f_2'(1525)$ Mass/Width	+0.054	-0.058	+0.019	-0.020
$f_0(1710)$ Mass/Width	+0.148	-0.151	+0.051	-0.052
χ_{c0} Mass/Width	+0.007	-0.004	+0.003	-0.001
$\phi(1020)$ BW radius	+0.000	-0.030	+0.000	-0.010
$f_2'(1525)$ BW radius	+0.058	-0.022	+0.020	-0.007
$f_0(980)$ Mass	+0.013	-0.005	+0.005	-0.002
$f_0(980)$ g_π	+0.070	-0.071	+0.024	-0.024
$f_0(980)$ g_K	+0.002	-0.000	+0.001	-0.000
B-meson BW radius	+0.003	-0.003	+0.001	-0.001
Eff. map statistics	+0.021	-0.021	+0.007	-0.007
Tracking	+0.000	-0.000	+0.012	-0.012
$N_{B\overline{B}}$	+0.000	-0.000	+0.012	-0.012
PID	+0.007	-0.007	+0.018	-0.018
Fixed $B\overline{B}$ A_{CP} and yield	+0.012	-0.011	+0.003	-0.002
Fixed PDF Params	+0.022	-0.022	+0.007	-0.007
Add $f_2(1270)$	+0.088	-0.088	+0.031	-0.031
Add $a_0^0(1450)$	**+1.348**	**-1.348**	**+0.470**	**-0.470**
Add $\phi(1680)$	+0.014	-0.014	+0.005	-0.005
Add $f_2(2010)$, $f_2(2300)$	**+0.392**	**-0.392**	**+0.136**	**-0.136**
DP PDF Stat.	+0.102	-0.102	+0.036	-0.036
Fit Bias	+0.165	-0.165	+0.047	-0.047
Detector Asym.	+0.000	-0.000	+0.000	-0.000
Total	+1.439	-1.438	+0.501	-0.501

Table D.6: $B^+ \to K^+K^-K^+$ systematics.

χ_{c0}				
	FF ($+\sigma$)	FF ($-\sigma$)	$\mathcal{B}$ ($+\sigma$)	$\mathcal{B}$ ($-\sigma$)
$\phi(1020)$ Mass/Width	+0.000	-0.002	+0.000	-0.001
$f_0(1500)$ Mass/Width	+0.001	-0.000	+0.000	-0.000
$f_2'(1525)$ Mass/Width	+0.013	-0.011	+0.005	-0.004
$f_0(1710)$ Mass/Width	+0.001	-0.000	+0.000	-0.000
χ_{c0} Mass/Width	+0.012	-0.015	+0.004	-0.005
$\phi(1020)$ BW radius	+0.000	-0.007	+0.000	-0.002
$f_2'(1525)$ BW radius	**+0.026**	-0.013	+0.009	-0.005
$f_0(980)$ Mass	+0.007	-0.004	+0.002	-0.002
$f_0(980)$ g_π	+0.001	-0.002	+0.000	-0.000
$f_0(980)$ g_K	+0.006	-0.006	+0.002	-0.002
B-meson BW radius	+0.005	-0.005	+0.002	-0.002
Eff. map statistics	+0.012	-0.012	+0.004	-0.004
Tracking	+0.000	-0.000	**+0.012**	**-0.012**
$N_{B\bar{B}}$	+0.000	-0.000	**+0.012**	**-0.012**
PID	+0.013	-0.013	**+0.024**	**-0.024**
Fixed $B\overline{B}$ A_{CP} and yield	+0.007	-0.007	+0.001	-0.001
Fixed PDF Params	+0.021	-0.021	+0.005	-0.005
Add $f_2(1270)$	+0.004	-0.004	+0.002	-0.002
Add $a_0^0(1450)$	**+0.049**	**-0.049**	**+0.018**	**-0.018**
Add $\phi(1680)$	+0.024	-0.024	+0.008	-0.008
Add $f_2(2010)$, $f_2(2300)$	**+0.034**	**-0.034**	**+0.013**	**-0.013**
DP PDF Stat.	**+0.040**	**-0.040**	**+0.013**	**-0.013**
Fit Bias	**+0.097**	**-0.097**	**+0.042**	**-0.042**
Detector Asym.	+0.000	-0.000	+0.000	-0.000
Total	+0.131	-0.129	+0.060	-0.059

Table D.7: $B^+ \to K^+K^-K^+$ systematics.

NR (S-wave)				
	FF $(+\sigma)$	FF $(-\sigma)$	$\mathcal{B}$ $(+\sigma)$	$\mathcal{B}$ $(-\sigma)$
$\phi(1020)$ Mass/Width	+3.282	-0.051	+1.137	-0.019
$f_0(1500)$ Mass/Width	+5.934	-3.481	+2.050	-1.201
$f_2'(1525)$ Mass/Width	+9.190	-5.923	+3.178	-2.050
$f_0(1710)$ Mass/Width	+6.569	-5.008	+2.266	-1.726
χ_{c0} Mass/Width	+0.562	-0.063	+0.196	-0.022
$\phi(1020)$ BW radius	**+34.557**	**-28.699**	**+11.973**	**-9.937**
$f_2'(1525)$ BW radius	+10.042	-0.000	+3.477	-0.000
$f_0(980)$ Mass	+1.989	-0.000	+0.689	-0.000
$f_0(980)$ g_π	+11.284	-11.079	+3.900	-3.835
$f_0(980)$ g_K	+4.430	-3.846	+1.532	-1.331
B-meson BW radius	+3.381	-3.381	+1.170	-1.170
Eff. map statistics	+2.030	-2.030	+0.708	-0.708
Tracking	+0.000	-0.000	+0.571	-0.571
$N_{B\overline{B}}$	+0.000	-0.000	+0.571	-0.571
PID	+4.389	-4.389	+0.532	-0.532
Fixed $B\overline{B}$ A_{CP} and yield	+0.489	-0.116	+0.170	-0.023
Fixed PDF Params	+0.882	-0.882	+0.249	-0.249
Add $f_2(1270)$	+13.196	-13.196	+4.617	-4.617
Add $a_0^0(1450)$	+8.476	-8.476	+3.039	-3.039
Add $\phi(1680)$	**+18.413**	**-18.413**	**+6.383**	**-6.383**
Add $f_2(2010)$, $f_2(2300)$	**+62.261**	**-62.261**	**+21.685**	**-21.685**
DP PDF Stat.	+5.785	-5.785	+2.050	-2.050
Fit Bias	+4.348	-4.348	+1.552	-1.552
Detector Asym.	+0.000	-0.000	+0.000	-0.000
Total	+78.546	-74.718	+27.300	-25.978

Table D.8: $B^+ \to K^+K^-K^+$ systematics.

NR (P-wave)				
	FF $(+\sigma)$	FF $(-\sigma)$	$\mathcal{B}$ $(+\sigma)$	$\mathcal{B}$ $(-\sigma)$
$\phi(1020)$ Mass/Width	+2.072	-0.101	+0.718	-0.036
$f_0(1500)$ Mass/Width	+4.257	-2.371	+1.472	-0.819
$f_2'(1525)$ Mass/Width	+9.171	-6.514	+3.174	-2.256
$f_0(1710)$ Mass/Width	+3.207	-2.256	+1.107	-0.778
χ_{c0} Mass/Width	+0.244	-0.002	+0.081	-0.000
$\phi(1020)$ BW radius	**+27.558**	**-22.716**	**+9.547**	**-7.866**
$f_2'(1525)$ BW radius	+7.704	-0.000	+2.668	-0.000
$f_0(980)$ Mass	+1.145	-0.000	+0.397	-0.000
$f_0(980)$ g_π	+6.815	-6.582	+2.357	-2.279
$f_0(980)$ g_K	+1.291	-1.098	+0.446	-0.380
B-meson BW radius	+2.071	-2.071	+0.717	-0.717
Eff. map statistics	+1.223	-1.223	+0.426	-0.426
Tracking	+0.000	-0.000	+0.261	-0.261
$N_{B\overline{B}}$	+0.000	-0.000	+0.261	-0.261
PID	+3.066	-3.066	+0.596	-0.596
Fixed $B\overline{B}$ A_{CP} and yield	+0.228	-0.040	+0.083	-0.019
Fixed PDF Params	+0.385	-0.385	+0.116	-0.116
Add $f_2(1270)$	+10.809	-10.809	+3.791	-3.791
Add $a_0^0(1450)$	**+46.610**	**-46.610**	**+16.253**	**-16.253**
Add $\phi(1680)$	+11.526	-11.526	+3.994	-3.994
Add $f_2(2010)$, $f_2(2300)$	**+50.782**	**-50.782**	**+17.661**	**-17.661**
DP PDF Stat.	+5.963	-5.963	+2.099	-2.099
Fit Bias	+9.492	-9.492	+3.076	-3.076
Detector Asym.	+0.000	-0.000	+0.000	-0.000
Total	+78.276	-75.866	+27.196	-26.364

Table D.9: $B^+ \to K^+K^-K^+$ systematics.

NR (Total)				
	FF $(+\sigma)$	FF $(-\sigma)$	$\mathcal{B}$ $(+\sigma)$	$\mathcal{B}$ $(-\sigma)$
$\phi(1020)$ Mass/Width	+0.130	-0.035	+0.045	-0.012
$f_0(1500)$ Mass/Width	+1.460	-1.572	+0.506	-0.545
$f_2'(1525)$ Mass/Width	+0.692	-0.742	+0.239	-0.258
$f_0(1710)$ Mass/Width	+1.037	-1.045	+0.355	-0.357
χ_{c0} Mass/Width	+0.142	-0.064	+0.050	-0.022
$\phi(1020)$ BW radius	+0.416	-0.560	+0.145	-0.192
$f_2'(1525)$ BW radius	+0.663	-0.978	+0.231	-0.340
$f_0(980)$ Mass	+1.056	-0.889	+0.366	-0.308
$f_0(980)$ g_π	+0.210	-0.190	+0.073	-0.069
$f_0(980)$ g_K	+1.906	-1.709	+0.659	-0.592
B-meson BW radius	+0.082	-0.082	+0.029	-0.029
Eff. map statistics	+0.343	-0.343	+0.117	-0.117
Tracking	+0.000	-0.000	+0.248	-0.248
$N_{B\overline{B}}$	+0.000	-0.000	+0.248	-0.248
PID	+0.096	-0.096	+0.374	-0.374
Fixed $B\overline{B}$ A_{CP} and yield	+0.180	-0.062	+0.071	-0.015
Fixed PDF Params	+0.258	-0.258	+0.096	-0.096
Add $f_2(1270)$	+0.572	-0.572	+0.210	-0.210
Add $a_0^0(1450)$	**+21.347**	**-21.347**	**+7.414**	**-7.414**
Add $\phi(1680)$	+0.179	-0.179	+0.059	-0.059
Add $f_2(2010)$, $f_2(2300)$	+2.102	-2.102	+0.696	-0.696
DP PDF Stat.	+0.498	-0.498	+0.171	-0.171
Fit Bias	+0.613	-0.613	+0.346	-0.346
Detector Asym.	+0.000	-0.000	+0.000	-0.000
Total	+21.690	-21.690	+7.552	-7.552

Table D.10: $B^+ \to K^+K^-K^+$ systematics.

	Total		Charmless	
	$\mathcal{B}$ $(+\sigma)$	$\mathcal{B}$ $(-\sigma)$	$\mathcal{B}$ $(+\sigma)$	$\mathcal{B}$ $(-\sigma)$
$\phi(1020)$ Mass/Width	+0.001	-0.001	+0.000	-0.001
$f_0(1500)$ Mass/Width	+0.003	-0.003	+0.003	-0.004
$f_2'(1525)$ Mass/Width	+0.002	-0.003	+0.006	-0.008
$f_0(1710)$ Mass/Width	+0.007	-0.007	+0.008	-0.008
χ_{c0} Mass/Width	+0.001	-0.000	+0.025	-0.024
$\phi(1020)$ BW radius	+0.003	-0.000	+0.001	-0.000
$f_2'(1525)$ BW radius	+0.002	-0.002	+0.001	-0.006
$f_0(980)$ Mass	+0.001	-0.000	+0.001	-0.002
$f_0(980)$ g_π	+0.001	-0.005	+0.005	-0.008
$f_0(980)$ g_K	+0.001	-0.001	+0.001	-0.002
B-meson BW radius	+0.001	-0.001	+0.001	-0.001
Eff. map statistics	+0.040	-0.040	+0.040	-0.040
Tracking	**+0.377**	**-0.377**	**+0.363**	**-0.363**
$N_{B\overline{B}}$	**+0.377**	**-0.377**	**+0.363**	**-0.363**
PID	**+0.617**	**-0.617**	**+0.589**	**-0.589**
Fixed $B\overline{B}$ A_{CP} and yield	+0.055	-0.052	+0.054	-0.052
Fixed PDF Params	**+0.183**	**-0.183**	**+0.182**	**-0.182**
Add $f_2(1270)$	+0.018	-0.018	+0.013	-0.013
Add $a_0^0(1450)$	+0.033	-0.033	+0.054	-0.054
Add $\phi(1680)$	+0.005	-0.005	+0.002	-0.002
Add $f_2(2010)$, $f_2(2300)$	+0.045	-0.045	+0.047	-0.047
DP PDF Stat.	+0.035	-0.035	+0.035	-0.035
Fit Bias	**+0.358**	**-0.358**	**+0.332**	**-0.332**
Detector Asym.	+0.000	-0.000	+0.000	-0.000
Total	+0.914	-0.914	+0.876	-0.875

Table D.11: $B^+ \to K^+K^-K^+$ systematics.

	$\phi(1020)$		$f_0(980)$	
	A_{CP} $(+\sigma)$	A_{CP} $(-\sigma)$	A_{CP} $(+\sigma)$	A_{CP} $(-\sigma)$
$\phi(1020)$ Mass/Width	+0.000	-0.000	+0.001	-0.000
$f_0(1500)$ Mass/Width	+0.000	-0.000	+0.006	-0.006
$f_2'(1525)$ Mass/Width	+0.001	-0.001	+0.004	-0.004
$f_0(1710)$ Mass/Width	+0.001	-0.001	+0.004	-0.004
χ_{c0} Mass/Width	+0.000	-0.000	+0.001	-0.000
$\phi(1020)$ BW radius	+0.000	-0.001	**+0.023**	**-0.024**
$f_2'(1525)$ BW radius	+0.001	-0.001	+0.006	**-0.009**
$f_0(980)$ Mass	+0.001	-0.000	+0.006	-0.003
$f_0(980)$ g_π	+0.000	-0.000	+0.005	-0.005
$f_0(980)$ g_K	+0.001	-0.001	+0.005	-0.004
B-meson BW radius	+0.000	-0.000	+0.002	-0.002
Eff. map statistics	+0.000	-0.000	+0.001	-0.001
Tracking	+0.000	-0.000	+0.000	-0.000
$N_{B\overline{B}}$	+0.000	-0.000	+0.000	-0.000
PID	+0.000	-0.000	+0.000	-0.000
Fixed $B\overline{B}$ A_{CP} and yield	+0.001	-0.001	+0.004	-0.003
Fixed PDF Params	+0.001	-0.001	+0.002	-0.002
Add $f_2(1270)$	+0.000	-0.000	+0.002	-0.002
Add $a_0^0(1450)$	**+0.003**	**-0.003**	**+0.022**	**-0.022**
Add $\phi(1680)$	+0.001	-0.001	+0.002	-0.002
Add $f_2(2010)$, $f_2(2300)$	+0.001	-0.001	+0.002	-0.002
DP PDF Stat.	+0.002	-0.002	+0.006	-0.006
Fit Bias	**+0.007**	**-0.007**	**+0.010**	**-0.010**
Detector Asym.	**+0.010**	**-0.010**	**+0.010**	**-0.010**
Total	+0.013	-0.013	+0.038	-0.039

Table D.12: $B^+ \to K^+K^-K^+$ systematics.

	$f_2'(1525)$		NR	
	A_{CP} $(+\sigma)$	A_{CP} $(-\sigma)$	A_{CP} $(+\sigma)$	A_{CP} $(-\sigma)$
$\phi(1020)$ Mass/Width	+0.000	-0.000	+0.000	-0.000
$f_0(1500)$ Mass/Width	+0.006	-0.006	+0.002	-0.001
$f_2'(1525)$ Mass/Width	+0.004	-0.005	+0.001	-0.001
$f_0(1710)$ Mass/Width	+0.002	-0.002	+0.002	-0.001
χ_{c0} Mass/Width	+0.000	-0.000	+0.000	-0.000
$\phi(1020)$ BW radius	**+0.008**	**-0.009**	**+0.010**	**-0.008**
$f_2'(1525)$ BW radius	+0.004	**-0.010**	+0.002	-0.002
$f_0(980)$ Mass	+0.000	-0.000	+0.003	-0.002
$f_0(980)$ g_π	+0.000	-0.001	+0.003	-0.003
$f_0(980)$ g_K	+0.001	-0.001	+0.003	-0.002
B-meson BW radius	+0.000	-0.000	+0.001	-0.001
Eff. map statistics	+0.001	-0.001	+0.000	-0.000
Tracking	+0.000	-0.000	+0.000	-0.000
$N_{B\overline{B}}$	+0.000	-0.000	+0.000	-0.000
PID	+0.001	-0.001	+0.000	-0.000
Fixed $B\overline{B}$ A_{CP} and yield	+0.005	-0.004	**+0.004**	-0.003
Fixed PDF Params	+0.003	-0.003	+0.001	-0.001
Add $f_2(1270)$	+0.003	-0.003	+0.001	-0.001
Add $a_0^0(1450)$	**+0.030**	**-0.030**	**+0.008**	**-0.008**
Add $\phi(1680)$	+0.001	-0.001	+0.000	-0.000
Add $f_2(2010)$, $f_2(2300)$	+0.007	-0.007	+0.002	-0.002
DP PDF Stat.	+0.005	-0.005	+0.002	-0.002
Fit Bias	**+0.013**	**-0.013**	**+0.007**	**-0.007**
Detector Asym.	**+0.010**	**-0.010**	**+0.010**	**-0.010**
Total	+0.038	-0.039	+0.019	-0.018

Table D.13: $B^+ \to K^+K^-K^+$ systematics.

	$\phi(1020)$		$f_0(980)$	
	δ $(+\sigma)$	δ $(-\sigma)$	δ $(+\sigma)$	δ $(-\sigma)$
$\phi(1020)$ Mass/Width	+0.001	-0.000	+0.000	-0.000
$f_0(1500)$ Mass/Width	+0.003	-0.002	+0.002	-0.001
$f_2'(1525)$ Mass/Width	+0.005	-0.005	+0.003	-0.003
$f_0(1710)$ Mass/Width	+0.005	-0.004	+0.003	-0.002
χ_{c0} Mass/Width	+0.001	-0.000	+0.000	-0.000
$\phi(1020)$ BW radius	**+0.012**	**-0.031**	**+0.012**	**-0.015**
$f_2'(1525)$ BW radius	**+0.009**	**-0.010**	+0.004	-0.006
$f_0(980)$ Mass	+0.006	-0.003	+0.005	-0.004
$f_0(980)$ g_π	+0.001	-0.000	+0.005	-0.003
$f_0(980)$ g_K	+0.001	-0.000	+0.001	-0.001
B-meson BW radius	+0.002	-0.002	+0.001	-0.001
Eff. map statistics	+0.002	-0.002	+0.001	-0.001
Tracking	+0.000	-0.000	+0.000	-0.000
$N_{B\bar{B}}$	+0.000	-0.000	+0.000	-0.000
PID	+0.000	-0.000	+0.000	-0.000
Fixed $B\overline{B}$ A_{CP} and yield	+0.003	-0.001	+0.002	-0.002
Fixed PDF Params	+0.004	-0.004	+0.001	-0.001
Add $f_2(1270)$	+0.002	-0.002	+0.002	-0.002
Add $a_0^0(1450)$	**+0.019**	**-0.019**	**+0.052**	**-0.052**
Add $\phi(1680)$	+0.002	-0.002	+0.001	-0.001
Add $f_2(2010)$, $f_2(2300)$	+0.003	-0.003	+0.002	-0.002
DP PDF Stat.	+0.006	-0.006	+0.004	-0.004
Fit Bias	**+0.015**	**-0.015**	+0.010	-0.010
Detector Asym.	+0.000	-0.000	+0.000	-0.000
Total	+0.031	-0.042	+0.055	-0.056

Table D.14: $B^+ \to K^+K^-K^+$ systematics.

	$f_2'(1525)$		χ_{c0}	
	δ $(+\sigma)$	δ $(-\sigma)$	δ $(+\sigma)$	δ $(-\sigma)$
$\phi(1020)$ Mass/Width	+0.000	-0.000	+0.000	-0.001
$f_0(1500)$ Mass/Width	+0.002	-0.001	+0.001	-0.001
$f_2'(1525)$ Mass/Width	+0.001	-0.002	+0.000	-0.001
$f_0(1710)$ Mass/Width	+0.001	-0.001	+0.001	-0.001
χ_{c0} Mass/Width	+0.000	-0.000	+0.002	-0.002
$\phi(1020)$ BW radius	**+0.009**	**-0.009**	+0.000	-0.002
$f_2'(1525)$ BW radius	+0.000	-0.002	+0.000	-0.003
$f_0(980)$ Mass	+0.001	-0.001	+0.001	-0.001
$f_0(980)$ g_π	+0.001	-0.001	+0.003	-0.002
$f_0(980)$ g_K	+0.001	-0.001	+0.001	-0.001
B-meson BW radius	+0.000	-0.000	+0.000	-0.000
Eff. map statistics	+0.000	-0.000	+0.000	-0.000
Tracking	+0.000	-0.000	+0.000	-0.000
$N_{B\overline{B}}$	+0.000	-0.000	+0.000	-0.000
PID	+0.001	-0.001	+0.000	-0.000
Fixed $B\overline{B}$ A_{CP} and yield	+0.002	-0.002	+0.001	-0.001
Fixed PDF Params	+0.001	-0.001	**+0.003**	**-0.003**
Add $f_2(1270)$	+0.001	-0.001	+0.003	-0.003
Add $a_0^0(1450)$	**+0.026**	**-0.026**	**+0.005**	**-0.005**
Add $\phi(1680)$	+0.001	-0.001	+0.001	-0.001
Add $f_2(2010)$, $f_2(2300)$	+0.003	-0.003	**+0.005**	**-0.005**
DP PDF Stat.	+0.003	-0.003	**+0.005**	**-0.005**
Fit Bias	**+0.009**	**-0.009**	**+0.010**	**-0.010**
Detector Asym.	+0.000	-0.000	+0.000	-0.000
Total	+0.029	-0.029	+0.015	-0.015

Table D.15: $B^+ \rightarrow K_S^0 K_S^0 K^+$ systematics.

$f_0(980)$				
	FF $(+\sigma)$	FF $(-\sigma)$	$\mathcal{B}$ $(+\sigma)$	$\mathcal{B}$ $(-\sigma)$
$f_0(1500)$ Mass/Width	+1.382	-1.677	+0.149	-0.179
$f_2'(1525)$ Mass/Width	+0.360	-0.331	+0.042	-0.038
$f_0(1710)$ Mass/Width	+0.781	-0.980	+0.085	-0.105
χ_{c0} Mass/Width	+0.223	-0.140	+0.024	-0.014
$f_2'(1525)$ BW radius	+0.000	-0.366	+0.000	-0.053
$f_0(980)$ Mass	+1.188	-0.341	+0.126	-0.036
$f_0(980)$ g_π	**+13.277**	**-12.847**	**+1.408**	**-1.364**
$f_0(980)$ g_K	+1.626	-2.057	+0.175	-0.219
B-meson BW radius	+0.122	-0.122	+0.020	-0.020
Eff. map statistics	+1.402	-1.402	+0.160	-0.160
Tracking	+0.000	-0.000	+0.110	-0.110
$N_{B\overline{B}}$	+0.000	-0.000	+0.088	-0.088
K_S^0 eff	+0.000	-0.000	+0.204	-0.204
PID	+0.011	-0.011	+0.076	-0.076
Fixed $B\overline{B}$ yields	+0.415	-0.446	+0.107	-0.108
Fixed $B\overline{B}$ A_{CP}	+0.052	-0.019	+0.006	-0.000
Fixed PDF Params	+0.899	-0.899	+0.192	-0.192
Signal NN Shape	+0.256	-0.256	+0.097	-0.097
Add Resonances	**+9.475**	**-9.475**	**+0.995**	**-0.995**
DP PDF Stat.	+2.242	-2.242	+0.228	-0.228
Detector Asym.	+0.000	-0.000	+0.000	-0.000
Fit Bias	**+3.559**	**-3.559**	**+0.383**	**-0.383**
Total	+17.133	-16.851	+1.844	-1.815

Table D.16: $B^+ \to K^0_S K^0_S K^+$ systematics.

$f_0(1500)$				
	FF ($+\sigma$)	FF ($-\sigma$)	$\mathcal{B}$ ($+\sigma$)	$\mathcal{B}$ ($-\sigma$)
$f_0(1500)$ Mass/Width	+0.178	-0.189	+0.019	-0.020
$f_2'(1525)$ Mass/Width	+0.045	-0.052	+0.005	-0.005
$f_0(1710)$ Mass/Width	+0.184	-0.197	+0.019	-0.021
χ_{c0} Mass/Width	+0.000	-0.011	+0.000	-0.001
$f_2'(1525)$ BW radius	+0.419	-0.077	+0.043	-0.008
$f_0(980)$ Mass	+0.045	-0.042	+0.005	-0.004
$f_0(980)$ g_π	+0.177	-0.176	+0.019	-0.019
$f_0(980)$ g_K	+0.007	-0.038	+0.001	-0.004
B-meson BW radius	+0.083	-0.083	+0.009	-0.009
Eff. map statistics	+0.094	-0.094	+0.010	-0.010
Tracking	+0.000	-0.000	+0.003	-0.003
$N_{B\overline{B}}$	+0.000	-0.000	+0.003	-0.003
K^0_S eff	+0.000	-0.000	+0.006	-0.006
PID	+0.000	-0.000	+0.002	-0.002
Fixed $B\overline{B}$ yields	+0.086	-0.103	+0.007	-0.009
Fixed $B\overline{B}$ A_{CP}	+0.002	-0.009	+0.000	-0.001
Fixed PDF Params	+0.105	-0.105	+0.007	-0.007
Signal NN Shape	+0.048	-0.048	+0.002	-0.002
Add Resonances	**+5.430**	**-5.430**	**+0.573**	**-0.573**
DP PDF Stat.	+0.226	-0.226	+0.023	-0.023
Detector Asym.	+0.000	-0.000	+0.000	-0.000
Fit Bias	+0.346	-0.346	+0.037	-0.037
Total	+5.474	-5.460	+0.578	-0.576

Table D.17: $B^+ \to K^0_S K^0_S K^+$ systematics.

$f'_2(1525)$				
	FF ($+\sigma$)	FF ($-\sigma$)	$\mathcal{B}$ ($+\sigma$)	$\mathcal{B}$ ($-\sigma$)
$f_0(1500)$ Mass/Width	+0.007	-0.017	+0.001	-0.002
$f'_2(1525)$ Mass/Width	**+0.362**	**-0.304**	**+0.038**	**-0.032**
$f_0(1710)$ Mass/Width	+0.024	-0.017	+0.003	-0.002
χ_{c0} Mass/Width	+0.000	-0.004	+0.000	-0.000
$f'_2(1525)$ BW radius	**+0.712**	-0.064	**+0.074**	-0.007
$f_0(980)$ Mass	+0.008	-0.010	+0.001	-0.001
$f_0(980)$ g_π	+0.032	-0.030	+0.003	-0.003
$f_0(980)$ g_K	+0.004	-0.000	+0.000	-0.000
B-meson BW radius	+0.180	**-0.180**	+0.019	**-0.019**
Eff. map statistics	+0.103	-0.103	+0.011	-0.011
Tracking	+0.000	-0.000	+0.005	-0.005
$N_{B\overline{B}}$	+0.000	-0.000	+0.004	-0.004
K^0_S eff	+0.000	-0.000	+0.008	-0.008
PID	+0.000	-0.000	+0.003	-0.003
Fixed $B\overline{B}$ yields	+0.140	-0.144	+0.012	-0.013
Fixed $B\overline{B}$ A_{CP}	+0.016	-0.019	+0.002	-0.002
Fixed PDF Params	+0.067	-0.067	+0.010	-0.010
Signal NN Shape	+0.044	-0.044	+0.000	-0.000
Add Resonances	**+0.678**	**-0.678**	**+0.071**	**-0.071**
DP PDF Stat.	+0.197	**-0.197**	+0.019	**-0.019**
Detector Asym.	+0.000	-0.000	+0.000	-0.000
Fit Bias	+0.209	**-0.209**	**+0.028**	**-0.028**
Total	+1.118	-0.843	+0.118	-0.090

Table D.18: $B^+ \to K^0_S K^0_S K^+$ systematics.

$f_0(1710)$				
	FF ($+\sigma$)	FF ($-\sigma$)	$\mathcal{B}$ ($+\sigma$)	$\mathcal{B}$ ($-\sigma$)
$f_0(1500)$ Mass/Width	**+0.325**	**-0.316**	**+0.035**	**-0.034**
$f'_2(1525)$ Mass/Width	+0.114	-0.107	+0.012	-0.011
$f_0(1710)$ Mass/Width	**+0.399**	**-0.387**	**+0.042**	**-0.041**
χ_{c0} Mass/Width	+0.003	-0.013	+0.000	-0.001
$f'_2(1525)$ BW radius	**+0.372**	-0.060	**+0.038**	-0.006
$f_0(980)$ Mass	+0.003	-0.000	+0.000	-0.000
$f_0(980)$ g_π	+0.168	-0.171	+0.018	-0.018
$f_0(980)$ g_K	+0.009	-0.019	+0.001	-0.002
B-meson BW radius	+0.041	-0.041	+0.004	-0.004
Eff. map statistics	+0.062	-0.062	+0.007	-0.007
Tracking	+0.000	-0.000	+0.004	-0.004
$N_{B\overline{B}}$	+0.000	-0.000	+0.003	-0.003
K^0_S eff	+0.000	-0.000	+0.007	-0.007
PID	+0.001	-0.001	+0.003	-0.003
Fixed $B\overline{B}$ yields	+0.079	-0.120	+0.007	-0.011
Fixed $B\overline{B}$ A_{CP}	+0.001	-0.004	+0.000	-0.000
Fixed PDF Params	+0.097	-0.097	+0.005	-0.005
Signal NN Shape	+0.048	-0.048	+0.009	-0.009
Add Resonances	**+0.229**	**-0.229**	**+0.025**	**-0.025**
DP PDF Stat.	**+0.341**	**-0.341**	**+0.035**	**-0.035**
Detector Asym.	+0.000	-0.000	+0.000	-0.000
Fit Bias	**+0.683**	**-0.683**	**+0.078**	**-0.078**
Total	+1.050	-0.980	+0.115	-0.108

Table D.19: $B^+ \rightarrow K_S^0 K_S^0 K^+$ systematics.

χ_{c0}				
	FF $(+\sigma)$	FF $(-\sigma)$	$\mathcal{B}$ $(+\sigma)$	$\mathcal{B}$ $(-\sigma)$
$f_0(1500)$ Mass/Width	+0.010	-0.018	+0.001	-0.002
$f_2'(1525)$ Mass/Width	+0.003	-0.005	+0.000	-0.000
$f_0(1710)$ Mass/Width	+0.002	-0.008	+0.000	-0.001
χ_{c0} Mass/Width	**+0.074**	**-0.071**	**+0.008**	**-0.007**
$f_2'(1525)$ BW radius	+0.000	-0.025	+0.000	-0.003
$f_0(980)$ Mass	+0.001	-0.013	+0.000	-0.001
$f_0(980)$ g_π	+0.008	-0.012	+0.001	-0.001
$f_0(980)$ g_K	+0.006	-0.000	+0.001	-0.000
B-meson BW radius	+0.011	-0.011	+0.001	-0.001
Eff. map statistics	+0.019	-0.019	+0.002	-0.002
Tracking	+0.000	-0.000	+0.004	-0.004
$N_{B\overline{B}}$	+0.000	-0.000	+0.003	-0.003
K_S^0 eff	+0.000	-0.000	**+0.007**	**-0.007**
PID	+0.001	-0.001	+0.003	-0.003
Fixed $B\overline{B}$ yields	+0.018	-0.032	+0.000	-0.001
Fixed $B\overline{B}$ A_{CP}	+0.004	-0.005	+0.000	-0.000
Fixed PDF Params	+0.036	-0.036	**+0.008**	**-0.008**
Signal NN Shape	+0.006	-0.006	+0.005	-0.005
Add Resonances	+0.050	-0.050	+0.003	-0.003
DP PDF Stat.	+0.043	-0.043	+0.005	-0.005
Detector Asym.	+0.000	-0.000	+0.000	-0.000
Fit Bias	**+0.298**	**-0.298**	**+0.032**	**-0.032**
Total	+0.318	-0.320	+0.037	-0.037

Table D.20: $B^+ \to K_S^0 K_S^0 K^+$ systematics.

NR (S-wave)				
	FF ($+\sigma$)	FF ($-\sigma$)	$\mathcal{B}$ ($+\sigma$)	$\mathcal{B}$ ($-\sigma$)
$f_0(1500)$ Mass/Width	+3.133	-3.701	+0.336	-0.394
$f_2'(1525)$ Mass/Width	+0.811	-0.741	+0.092	-0.083
$f_0(1710)$ Mass/Width	+2.049	-2.435	+0.220	-0.259
χ_{c0} Mass/Width	+0.141	-0.096	+0.015	-0.009
$f_2'(1525)$ BW radius	+0.091	-2.009	+0.017	-0.258
$f_0(980)$ Mass	**+4.631**	-3.849	+0.492	-0.408
$f_0(980)$ g_π	**+10.225**	**-9.909**	**+1.084**	**-1.052**
$f_0(980)$ g_K	+1.106	-1.364	+0.117	-0.142
B-meson BW radius	+0.619	-0.619	+0.075	-0.075
Eff. map statistics	+1.225	-1.225	+0.130	-0.130
Tracking	+0.000	-0.000	+0.148	-0.148
$N_{B\overline{B}}$	+0.000	-0.000	+0.118	-0.118
K_S^0 eff	+0.000	-0.000	+0.273	-0.273
PID	+0.010	-0.010	+0.101	-0.101
Fixed $B\overline{B}$ yields	+1.395	-1.485	+0.234	-0.240
Fixed $B\overline{B}$ A_{CP}	+0.089	-0.018	+0.009	-0.000
Fixed PDF Params	+1.315	-1.315	+0.284	-0.284
Signal NN Shape	+0.055	-0.055	+0.161	-0.161
Add Resonances	**+16.008**	**-16.008**	**+1.988**	**-1.988**
DP PDF Stat.	+3.712	-3.712	+0.378	-0.378
Detector Asym.	+0.000	-0.000	+0.000	-0.000
Fit Bias	+2.041	-2.041	+0.224	-0.224
Total	+20.535	-20.472	+2.460	-2.458

Table D.21: $B^+ \to K_S^0 K_S^0 K^+$ systematics.

	Total		Charmless	
	$\mathcal{B}$ $(+\sigma)$	$\mathcal{B}$ $(-\sigma)$	$\mathcal{B}$ $(+\sigma)$	$\mathcal{B}$ $(-\sigma)$
$f_0(1500)$ Mass/Width	+0.002	-0.001	+0.005	-0.006
$f_2'(1525)$ Mass/Width	+0.004	-0.003	+0.004	-0.003
$f_0(1710)$ Mass/Width	+0.002	-0.001	+0.003	-0.003
χ_{c0} Mass/Width	+0.001	-0.001	+0.006	-0.004
$f_2'(1525)$ BW radius	+0.004	-0.024	+0.005	-0.040
$f_0(980)$ Mass	+0.000	-0.000	+0.001	-0.002
$f_0(980)$ g_π	+0.000	-0.001	+0.002	-0.003
$f_0(980)$ g_K	+0.002	-0.000	+0.004	-0.002
B-meson BW radius	+0.005	-0.005	+0.008	-0.008
Eff. map statistics	+0.025	-0.025	+0.025	-0.025
Tracking	**+0.079**	**-0.079**	**+0.076**	**-0.076**
$N_{B\overline{B}}$	**+0.063**	**-0.063**	**+0.060**	**-0.060**
K_S^0 eff	**+0.146**	**-0.146**	**+0.140**	**-0.140**
PID	**+0.054**	**-0.054**	+0.051	-0.051
Fixed $B\overline{B}$ yields	+0.047	-0.046	+0.045	-0.045
Fixed $B\overline{B}$ A_{CP}	+0.001	-0.000	+0.001	-0.000
Fixed PDF Params	**+0.142**	**-0.142**	**+0.143**	**-0.143**
Signal NN Shape	**+0.089**	**-0.089**	**+0.092**	**-0.092**
Add Resonances	+0.027	-0.027	+0.043	-0.043
DP PDF Stat.	+0.039	-0.039	+0.040	-0.040
Detector Asym.	+0.000	-0.000	+0.000	-0.000
Fit Bias	+0.033	-0.033	+0.026	-0.026
Total	+0.263	-0.263	+0.260	-0.263

Table D.22: $B^+ \to K_S^0 K_S^0 K^+$ systematics.

	A_{CP} $(+\sigma)$	A_{CP} $(-\sigma)$	δ $(+\sigma)$	δ $(-\sigma)$
$f_0(1500)$ Mass/Width	+0.000	-0.000	+0.002	-0.003
$f_2'(1525)$ Mass/Width	+0.000	-0.000	+0.002	-0.001
$f_0(1710)$ Mass/Width	+0.000	-0.000	+0.001	-0.001
χ_{c0} Mass/Width	+0.000	-0.001	+0.015	-0.014
$f_2'(1525)$ BW radius	+0.000	-0.000	+0.000	-0.005
$f_0(980)$ Mass	+0.000	-0.000	+0.002	-0.002
$f_0(980)$ g_π	+0.000	-0.000	+0.001	-0.000
$f_0(980)$ g_K	+0.000	-0.000	+0.001	-0.000
B-meson BW radius	+0.000	-0.000	+0.004	-0.004
Eff. map statistics	+0.000	-0.000	+0.003	-0.003
Tracking	+0.000	-0.000	+0.000	-0.000
$N_{B\overline{B}}$	+0.000	-0.000	+0.000	-0.000
K_S^0 eff	+0.000	-0.000	+0.000	-0.000
PID	+0.000	-0.000	+0.000	-0.000
Fixed $B\overline{B}$ yields	+0.000	-0.001	+0.007	-0.006
Fixed $B\overline{B}$ A_{CP}	+0.002	-0.002	+0.006	-0.006
Fixed PDF Params	+0.002	-0.002	**+0.022**	**-0.022**
Signal NN Shape	+0.001	-0.001	+0.005	-0.005
Add Resonances	+0.001	-0.001	**+0.033**	**-0.033**
DP PDF Stat.	+0.002	-0.002	**+0.021**	**-0.021**
Detector Asym.	**+0.010**	**-0.010**	+0.000	-0.000
Fit Bias	**+0.011**	**-0.011**	**+0.086**	**-0.086**
Total	+0.015	-0.015	+0.099	-0.099

Table D.23: $B^0 \to K^+K^-K^0_S$ systematics.

$\phi(1020)$				
	FF $(+\sigma)$	FF $(-\sigma)$	$\mathcal{B}$ $(+\sigma)$	$\mathcal{B}$ $(-\sigma)$
$\phi(1020)$ Mass/Width	+0.026	-0.021	+0.007	-0.005
$f_0(1500)$ Mass/Width	+0.009	-0.004	+0.002	-0.001
$f_2'(1525)$ Mass/Width	+0.005	-0.000	+0.001	-0.000
$f_0(1710)$ Mass/Width	+0.015	-0.012	+0.004	-0.003
χ_{c0} Mass/Width	+0.003	-0.002	+0.001	-0.001
$\phi(1020)$ BW radius	**+0.681**	**-0.316**	**+0.180**	**-0.084**
$f_2'(1525)$ BW radius	+0.000	-0.002	+0.000	-0.001
$D, J/\psi$ Mass/Width	+0.011	-0.002	+0.002	-0.005
$f_0(980)$ Mass	+0.020	-0.024	+0.005	-0.006
$f_0(980)$ g_π, g_K	+0.059	-0.047	+0.015	-0.012
B-meson BW radius	+0.064	-0.064	+0.015	-0.015
Eff. map statistics	**+0.159**	**-0.159**	**+0.051**	**-0.051**
Tracking	+0.000	-0.000	+0.025	-0.025
$N_{B\overline{B}}$	+0.000	-0.000	+0.021	-0.021
K^0_S eff	+0.000	-0.000	+0.031	**-0.031**
PID	+0.117	**-0.117**	**+0.045**	**-0.045**
Fixed PDF Params (1)	+0.032	-0.019	+0.010	-0.004
Fixed PDF Params (2)	+0.060	-0.060	+0.020	-0.020
Signal NN Shape	+0.051	-0.051	+0.022	-0.022
Add $f_2(1270)$	+0.099	**-0.099**	+0.028	-0.028
Add $f_0(1370)$, $a_0^0(1450)$	+0.059	-0.059	+0.017	-0.017
Add $a_0^-(1450)$	+0.087	-0.087	+0.021	-0.021
Add $\phi(1680)$	+0.066	-0.066	+0.018	-0.018
Add $f_2(2010)$, $f_2(2300)$	+0.011	-0.011	+0.003	-0.003
Add $a_0^-(980)$	+0.067	-0.067	+0.016	-0.016
DP PDF Stat.	+0.126	**-0.126**	+0.038	**-0.038**
SVT/beamspot/DCS	+0.000	-0.000	+0.000	-0.000
Fit Bias	+0.057	-0.057	+0.030	**-0.030**
Total	+0.754	-0.449	+0.212	-0.140

Table D.24: $B^0 \to K^+K^-K^0_S$ systematics.

$f_0(980)$				
	FF $(+\sigma)$	FF $(-\sigma)$	$\mathcal{B}$ $(+\sigma)$	$\mathcal{B}$ $(-\sigma)$
$\phi(1020)$ Mass/Width	+0.031	-0.029	+0.008	-0.008
$f_0(1500)$ Mass/Width	+0.452	-0.521	+0.120	-0.138
$f'_2(1525)$ Mass/Width	+0.016	-0.042	+0.004	-0.011
$f_0(1710)$ Mass/Width	+0.353	-0.410	+0.094	-0.109
χ_{c0} Mass/Width	+0.007	-0.013	+0.002	-0.003
$\phi(1020)$ BW radius	+0.121	-0.029	+0.032	-0.008
$f'_2(1525)$ BW radius	+0.032	-0.130	+0.009	-0.036
$D, J/\psi$ Mass/Width	+0.035	-0.035	+0.008	-0.013
$f_0(980)$ Mass	**+2.660**	**-2.142**	**+0.705**	**-0.568**
$f_0(980)$ g_π, g_K	**+3.877**	**-3.856**	**+1.027**	**-1.021**
B-meson BW radius	**+1.843**	**-1.843**	**+0.493**	**-0.493**
Eff. map statistics	+0.396	-0.396	+0.112	-0.112
Tracking	+0.000	-0.000	+0.051	-0.051
$N_{B\bar{B}}$	+0.000	-0.000	+0.041	-0.041
K^0_S eff	+0.000	-0.000	+0.062	-0.062
PID	+0.489	-0.489	+0.025	-0.025
Fixed PDF Params (1)	+0.055	-0.147	+0.023	-0.050
Fixed PDF Params (2)	+0.200	-0.200	+0.080	-0.080
Signal NN Shape	+0.152	-0.152	+0.031	-0.031
Add $f_2(1270)$	+1.028	-1.028	+0.279	-0.279
Add $f_0(1370)$, $a^0_0(1450)$	**+7.224**	**-7.224**	**+1.928**	**-1.928**
Add $a^-_0(1450)$	+0.288	-0.288	+0.062	-0.062
Add $\phi(1680)$	+0.161	-0.161	+0.037	-0.037
Add $f_2(2010)$, $f_2(2300)$	+0.646	-0.646	+0.175	-0.175
Add $a^-_0(980)$	+0.069	-0.069	+0.017	-0.017
DP PDF Stat.	+1.066	-1.066	+0.275	-0.275
SVT/beamspot/DCS	+0.000	-0.000	+0.000	-0.000
Fit Bias	+0.383	-0.383	+0.111	-0.111
Total	+9.020	-8.880	+2.402	-2.365

Table D.25: $B^0 \to K^+K^-K_S^0$ systematics.

$f_0(1500)$				
	FF ($+\sigma$)	FF ($-\sigma$)	$\mathcal{B}$ ($+\sigma$)	$\mathcal{B}$ ($-\sigma$)
$\phi(1020)$ Mass/Width	+0.008	-0.003	+0.002	-0.001
$f_0(1500)$ Mass/Width	**+0.130**	**-0.124**	**+0.035**	**-0.033**
$f_2'(1525)$ Mass/Width	+0.019	-0.011	+0.005	-0.003
$f_0(1710)$ Mass/Width	+0.077	-0.061	+0.020	-0.016
χ_{c0} Mass/Width	+0.006	-0.000	+0.002	-0.000
$\phi(1020)$ BW radius	+0.013	-0.017	+0.003	-0.005
$f_2'(1525)$ BW radius	+0.009	-0.000	+0.002	-0.000
$D, J/\psi$ Mass/Width	+0.008	-0.000	+0.002	-0.000
$f_0(980)$ Mass	+0.007	-0.000	+0.002	-0.000
$f_0(980)$ g_π, g_K	+0.080	-0.073	+0.021	-0.019
B-meson BW radius	+0.011	-0.011	+0.003	-0.003
Eff. map statistics	+0.036	-0.036	+0.010	-0.010
Tracking	+0.000	-0.000	+0.004	-0.004
$N_{B\overline{B}}$	+0.000	-0.000	+0.003	-0.003
K_S^0 eff	+0.000	-0.000	+0.005	-0.005
PID	+0.013	-0.013	+0.009	-0.009
Fixed PDF Params (1)	+0.024	-0.013	+0.007	-0.004
Fixed PDF Params (2)	+0.026	-0.026	+0.010	-0.010
Signal NN Shape	+0.021	-0.021	+0.000	-0.000
Add $f_2(1270)$	**+0.145**	**-0.145**	**+0.038**	**-0.038**
Add $f_0(1370)$, $a_0^0(1450)$	**+0.378**	**-0.378**	**+0.089**	**-0.089**
Add $a_0^-(1450)$	+0.007	-0.007	+0.002	-0.002
Add $\phi(1680)$	**+0.119**	**-0.119**	**+0.028**	**-0.028**
Add $f_2(2010)$, $f_2(2300)$	+0.056	-0.056	+0.015	-0.015
Add $a_0^-(980)$	+0.008	-0.008	+0.002	-0.002
DP PDF Stat.	+0.082	-0.082	+0.022	-0.022
SVT/beamspot/DCS	+0.000	-0.000	+0.000	-0.000
Fit Bias	**+0.120**	**-0.120**	**+0.030**	**-0.030**
Total	+0.486	-0.480	+0.119	-0.118

Table D.26: $B^0 \to K^+K^-K^0_S$ systematics.

$f_2'(1525)$				
	FF $(+\sigma)$	FF $(-\sigma)$	$\mathcal{B}$ $(+\sigma)$	$\mathcal{B}$ $(-\sigma)$
$\phi(1020)$ Mass/Width	+0.001	-0.000	+0.000	-0.000
$f_0(1500)$ Mass/Width	+0.009	-0.009	+0.002	-0.002
$f_2'(1525)$ Mass/Width	+0.047	-0.053	+0.012	-0.014
$f_0(1710)$ Mass/Width	+0.010	-0.010	+0.003	-0.003
χ_{c0} Mass/Width	+0.000	-0.000	+0.000	-0.000
$\phi(1020)$ BW radius	+0.000	-0.003	+0.000	-0.001
$f_2'(1525)$ BW radius	+0.079	-0.033	+0.021	-0.009
$D, J/\psi$ Mass/Width	+0.001	-0.000	+0.000	-0.000
$f_0(980)$ Mass	+0.002	-0.001	+0.000	-0.000
$f_0(980)$ g_π, g_K	+0.005	-0.004	+0.001	-0.001
B-meson BW radius	+0.007	-0.007	+0.002	-0.002
Eff. map statistics	+0.017	-0.017	+0.005	-0.005
Tracking	+0.000	-0.000	+0.001	-0.001
$N_{B\bar{B}}$	+0.000	-0.000	+0.001	-0.001
K^0_S eff	+0.000	-0.000	+0.001	-0.001
PID	+0.009	-0.009	+0.001	-0.001
Fixed PDF Params (1)	+0.007	-0.006	+0.002	-0.001
Fixed PDF Params (2)	+0.010	-0.010	+0.002	-0.002
Signal NN Shape	+0.005	-0.005	+0.000	-0.000
Add $f_2(1270)$	**+0.594**	**-0.594**	**+0.152**	**-0.152**
Add $f_0(1370)$, $a_0^0(1450)$	+0.008	-0.008	+0.003	-0.003
Add $a_0^-(1450)$	+0.002	-0.002	+0.001	-0.001
Add $\phi(1680)$	+0.010	-0.010	+0.003	-0.003
Add $f_2(2010)$, $f_2(2300)$	+0.077	-0.077	+0.021	-0.021
Add $a_0^-(980)$	+0.003	-0.003	+0.001	-0.001
DP PDF Stat.	+0.034	-0.034	+0.009	-0.009
SVT/beamspot/DCS	+0.000	-0.000	+0.000	-0.000
Fit Bias	+0.076	-0.076	+0.019	-0.019
Total	+0.613	-0.609	+0.157	-0.156

Table D.27: $B^0 \to K^+K^-K^0_S$ systematics.

$f_0(1710)$				
	FF $(+\sigma)$	FF $(-\sigma)$	$\mathcal{B}$ $(+\sigma)$	$\mathcal{B}$ $(-\sigma)$
$\phi(1020)$ Mass/Width	+0.001	-0.023	+0.000	-0.006
$f_0(1500)$ Mass/Width	+0.144	-0.158	+0.038	-0.042
$f_2'(1525)$ Mass/Width	+0.006	-0.034	+0.002	-0.009
$f_0(1710)$ Mass/Width	**+1.127**	**-1.146**	**+0.298**	**-0.304**
χ_{c0} Mass/Width	+0.000	-0.019	+0.000	-0.005
$\phi(1020)$ BW radius	+0.067	-0.032	+0.017	-0.009
$f_2'(1525)$ BW radius	+0.011	-0.110	+0.003	-0.030
$D, J/\psi$ Mass/Width	+0.000	-0.028	+0.000	-0.011
$f_0(980)$ Mass	+0.052	-0.083	+0.013	-0.022
$f_0(980)$ g_π, g_K	+0.082	-0.106	+0.022	-0.029
B-meson BW radius	+0.024	-0.024	+0.010	-0.010
Eff. map statistics	+0.074	-0.074	+0.016	-0.016
Tracking	+0.000	-0.000	+0.032	-0.032
$N_{B\overline{B}}$	+0.000	-0.000	+0.026	-0.026
K^0_S eff	+0.000	-0.000	+0.039	-0.039
PID	+0.089	-0.089	**+0.117**	**-0.117**
Fixed PDF Params (1)	+0.025	-0.078	+0.001	-0.020
Fixed PDF Params (2)	+0.061	-0.061	+0.035	-0.035
Signal NN Shape	+0.007	-0.007	+0.044	-0.044
Add $f_2(1270)$	+0.290	-0.290	+0.079	-0.079
Add $f_0(1370)$, $a_0^0(1450)$	**+0.739**	**-0.739**	**+0.201**	**-0.201**
Add $a_0^-(1450)$	+0.215	-0.215	+0.052	-0.052
Add $\phi(1680)$	**+1.191**	**-1.191**	**+0.291**	**-0.291**
Add $f_2(2010)$, $f_2(2300)$	**+0.419**	**-0.419**	**+0.113**	**-0.113**
Add $a_0^-(980)$	+0.088	-0.088	+0.020	-0.020
DP PDF Stat.	+0.376	-0.376	+0.102	-0.102
SVT/beamspot/DCS	+0.000	-0.000	+0.000	-0.000
Fit Bias	**+0.537**	**-0.537**	**+0.125**	**-0.125**
Total	+2.008	-2.026	+0.535	-0.540

Table D.28: $B^0 \to K^+K^-K^0_S$ systematics.

χ_{c0}				
	FF ($+\sigma$)	FF ($-\sigma$)	$\mathcal{B}$ ($+\sigma$)	$\mathcal{B}$ ($-\sigma$)
$\phi(1020)$ Mass/Width	+0.003	-0.000	+0.001	-0.000
$f_0(1500)$ Mass/Width	+0.003	-0.000	+0.001	-0.000
$f_2'(1525)$ Mass/Width	+0.003	-0.000	+0.001	-0.000
$f_0(1710)$ Mass/Width	+0.003	-0.000	+0.001	-0.000
χ_{c0} Mass/Width	**+0.065**	**-0.060**	**+0.017**	**-0.016**
$\phi(1020)$ BW radius	+0.008	-0.006	+0.002	-0.002
$f_2'(1525)$ BW radius	+0.003	-0.000	+0.001	-0.000
$D, J/\psi$ Mass/Width	+0.008	-0.001	+0.002	-0.001
$f_0(980)$ Mass	+0.001	-0.000	+0.000	-0.000
$f_0(980)$ g_π, g_K	+0.004	-0.000	+0.001	-0.000
B-meson BW radius	+0.013	-0.013	+0.003	-0.003
Eff. map statistics	+0.016	-0.016	+0.004	-0.004
Tracking	+0.000	-0.000	+0.007	-0.007
$N_{B\overline{B}}$	+0.000	-0.000	+0.005	-0.005
K^0_S eff	+0.000	-0.000	+0.008	-0.008
PID	+0.006	-0.006	**+0.021**	**-0.021**
Fixed PDF Params (1)	+0.027	-0.009	+0.007	-0.003
Fixed PDF Params (2)	+0.015	-0.015	+0.008	-0.008
Signal NN Shape	+0.010	-0.010	+0.007	-0.007
Add $f_2(1270)$	+0.004	-0.004	+0.001	-0.001
Add $f_0(1370)$, $a_0^0(1450)$	+0.005	-0.005	+0.001	-0.001
Add $a_0^-(1450)$	**+0.047**	**-0.047**	**+0.012**	**-0.012**
Add $\phi(1680)$	+0.007	-0.007	+0.001	-0.001
Add $f_2(2010)$, $f_2(2300)$	+0.002	-0.002	+0.001	-0.001
Add $a_0^-(980)$	+0.028	-0.028	+0.007	-0.007
DP PDF Stat.	**+0.047**	**-0.047**	**+0.012**	**-0.012**
SVT/beamspot/DCS	+0.000	-0.000	+0.000	-0.000
Fit Bias	**+0.184**	**-0.184**	**+0.044**	**-0.044**
Total	+0.213	-0.209	+0.058	-0.057

Table D.29: $B^0 \to K^+K^-K^0_S$ systematics.

NR (S-wave)				
	FF ($+\sigma$)	FF ($-\sigma$)	$\mathcal{B}$ ($+\sigma$)	$\mathcal{B}$ ($-\sigma$)
$\phi(1020)$ Mass/Width	+0.000	-0.017	+0.000	-0.005
$f_0(1500)$ Mass/Width	+1.638	-1.844	+0.431	-0.487
$f_2'(1525)$ Mass/Width	+0.026	-0.063	+0.006	-0.017
$f_0(1710)$ Mass/Width	+0.214	-0.337	+0.056	-0.091
χ_{c0} Mass/Width	+0.075	-0.105	+0.018	-0.028
$\phi(1020)$ BW radius	+0.007	-0.136	+0.000	-0.019
$f_2'(1525)$ BW radius	+0.113	-0.656	+0.031	-0.181
$D, J/\psi$ Mass/Width	+0.112	-0.101	+0.024	-0.046
$f_0(980)$ Mass	+3.796	-3.028	+1.007	-0.805
$f_0(980)$ g_π, g_K	**+7.398**	**-7.768**	**+1.960**	**-2.057**
B-meson BW radius	+3.143	-3.143	+0.854	-0.854
Eff. map statistics	+0.524	-0.524	+0.146	-0.146
Tracking	+0.000	-0.000	+0.222	-0.222
$N_{B\overline{B}}$	+0.000	-0.000	+0.181	-0.181
K^0_S eff	+0.000	-0.000	+0.271	-0.271
PID	+0.322	-0.322	+0.568	-0.568
Fixed PDF Params (1)	+0.097	-0.309	+0.053	-0.107
Fixed PDF Params (2)	+0.476	-0.476	+0.206	-0.206
Signal NN Shape	+0.525	-0.525	+0.174	-0.174
Add $f_2(1270)$	+0.844	-0.844	+0.213	-0.213
Add $f_0(1370)$, $a_0^0(1450)$	**+28.915**	**-28.915**	**+7.970**	**-7.970**
Add $a_0^-(1450)$	+0.496	-0.496	+0.070	-0.070
Add $\phi(1680)$	+1.397	-1.397	+0.389	-0.389
Add $f_2(2010)$, $f_2(2300)$	+2.877	-2.877	+0.780	-0.780
Add $a_0^-(980)$	+0.386	-0.386	+0.087	-0.087
DP PDF Stat.	+2.847	-2.847	+0.694	-0.694
SVT/beamspot/DCS	+0.000	-0.000	+0.000	-0.000
Fit Bias	+1.732	-1.732	+0.624	-0.624
Total	+30.679	-30.706	+8.459	-8.467

Table D.30: $B^0 \to K^+K^-K^0_S$ systematics.

NR (P-wave)				
	FF $(+\sigma)$	FF $(-\sigma)$	$\mathcal{B}$ $(+\sigma)$	$\mathcal{B}$ $(-\sigma)$
$\phi(1020)$ Mass/Width	+0.013	-0.002	+0.003	-0.001
$f_0(1500)$ Mass/Width	+0.035	-0.010	+0.013	-0.003
$f_2'(1525)$ Mass/Width	+0.020	-0.007	+0.005	-0.002
$f_0(1710)$ Mass/Width	+0.078	-0.039	+0.020	-0.010
χ_{c0} Mass/Width	+0.027	-0.016	+0.007	-0.004
$\phi(1020)$ BW radius	+0.074	-0.000	+0.019	-0.000
$f_2'(1525)$ BW radius	+0.259	-0.035	+0.068	-0.009
$D, J/\psi$ Mass/Width	+0.035	-0.009	+0.010	-0.008
$f_0(980)$ Mass	+0.067	-0.045	+0.018	-0.012
$f_0(980)$ g_π, g_K	+0.020	-0.000	+0.005	-0.000
B-meson BW radius	**+0.505**	**-0.505**	**+0.136**	**-0.136**
Eff. map statistics	+0.057	-0.057	+0.016	-0.016
Tracking	+0.000	-0.000	+0.023	-0.023
$N_{B\overline{B}}$	+0.000	-0.000	+0.018	-0.018
K^0_S eff	+0.000	-0.000	+0.028	-0.028
PID	+0.071	-0.071	+0.048	-0.048
Fixed PDF Params (1)	+0.156	-0.072	+0.045	-0.024
Fixed PDF Params (2)	+0.113	-0.113	+0.047	-0.047
Signal NN Shape	+0.146	-0.146	+0.071	-0.071
Add $f_2(1270)$	+0.230	-0.230	+0.060	-0.060
Add $f_0(1370)$, $a_0^0(1450)$	+0.179	-0.179	+0.047	-0.047
Add $a_0^-(1450)$	**+0.984**	**-0.984**	**+0.266**	**-0.266**
Add $\phi(1680)$	+0.069	-0.069	+0.027	-0.027
Add $f_2(2010)$, $f_2(2300)$	**+0.535**	**-0.535**	**+0.142**	**-0.142**
Add $a_0^-(980)$	**+0.372**	**-0.372**	**+0.107**	**-0.107**
DP PDF Stat.	**+0.417**	**-0.417**	**+0.121**	**-0.121**
SVT/beamspot/DCS	+0.000	-0.000	+0.000	-0.000
Fit Bias	+0.149	-0.149	+0.053	-0.053
Total	+1.445	-1.410	+0.405	-0.397

Table D.31: $B^0 \rightarrow K^+K^-K^0_S$ systematics.

NR (Total)				
	FF ($+\sigma$)	FF ($-\sigma$)	$\mathcal{B}$ ($+\sigma$)	$\mathcal{B}$ ($-\sigma$)
$\phi(1020)$ Mass/Width	+0.000	-0.011	+0.000	-0.003
$f_0(1500)$ Mass/Width	+1.639	-1.808	+0.431	-0.477
$f_2'(1525)$ Mass/Width	+0.019	-0.044	+0.004	-0.012
$f_0(1710)$ Mass/Width	+0.186	-0.260	+0.048	-0.071
χ_{c0} Mass/Width	+0.101	-0.116	+0.025	-0.031
$\phi(1020)$ BW radius	+0.154	-0.135	+0.038	-0.037
$f_2'(1525)$ BW radius	+0.078	-0.397	+0.022	-0.113
$D, J/\psi$ Mass/Width	+0.070	-0.078	+0.029	-0.048
$f_0(980)$ Mass	+3.862	-3.073	+1.025	-0.817
$f_0(980)$ g_π, g_K	**+7.401**	**-7.751**	**+1.961**	**-2.052**
B-meson BW radius	+3.647	-3.647	+0.990	-0.990
Eff. map statistics	+0.516	-0.516	+0.145	-0.145
Tracking	+0.000	-0.000	+0.244	-0.244
$N_{B\overline{B}}$	+0.000	-0.000	+0.199	-0.199
K^0_S eff	+0.000	-0.000	+0.298	-0.298
PID	+0.393	-0.393	+0.616	-0.616
Fixed PDF Params (1)	+0.074	-0.211	+0.069	-0.106
Fixed PDF Params (2)	+0.351	-0.351	+0.257	-0.257
Signal NN Shape	+0.379	-0.379	+0.246	-0.246
Add $f_2(1270)$	+1.113	-1.113	+0.282	-0.282
Add $f_0(1370)$, $a_0^0(1450)$	**+30.155**	**-30.155**	**+8.038**	**-8.038**
Add $a_0^-(1450)$	+0.746	-0.746	+0.226	-0.226
Add $\phi(1680)$	+1.444	-1.444	+0.369	-0.369
Add $f_2(2010)$, $f_2(2300)$	+2.408	-2.408	+0.652	-0.652
Add $a_0^-(980)$	+0.261	-0.261	+0.090	-0.090
DP PDF Stat.	+2.695	-2.695	+0.659	-0.659
SVT/beamspot/DCS	+0.000	-0.000	+0.000	-0.000
Fit Bias	+1.943	-1.943	+0.646	-0.646
Total	+31.883	-31.893	+8.541	-8.544

Table D.32: $B^0 \to K^+K^-K^0_S$ systematics.

	Total		Charmless	
	$\mathcal{B}$ $(+\sigma)$	$\mathcal{B}$ $(-\sigma)$	$\mathcal{B}$ $(+\sigma)$	$\mathcal{B}$ $(-\sigma)$
$\phi(1020)$ Mass/Width	+0.000	-0.000	+0.000	-0.001
$f_0(1500)$ Mass/Width	+0.002	-0.003	+0.000	-0.002
$f_2'(1525)$ Mass/Width	+0.001	-0.002	+0.001	-0.003
$f_0(1710)$ Mass/Width	+0.001	-0.002	+0.001	-0.003
χ_{c0} Mass/Width	+0.002	-0.003	+0.020	-0.022
$\phi(1020)$ BW radius	+0.000	-0.002	+0.000	-0.004
$f_2'(1525)$ BW radius	+0.001	-0.006	+0.000	-0.006
$D, J/\psi$ Mass/Width	+0.016	-0.046	+0.014	-0.045
$f_0(980)$ Mass	+0.001	-0.002	+0.004	-0.005
$f_0(980)$ g_π, g_K	+0.003	-0.005	+0.007	-0.009
B-meson BW radius	+0.018	-0.018	+0.033	-0.033
Eff. map statistics	+0.084	-0.084	+0.084	-0.084
Tracking	**+0.194**	**-0.194**	**+0.186**	**-0.186**
$N_{B\overline{B}}$	**+0.158**	**-0.158**	+0.152	-0.152
K^0_S eff	**+0.236**	**-0.236**	**+0.227**	**-0.227**
PID	**+0.567**	**-0.567**	**+0.542**	**-0.542**
Fixed PDF Params (1)	+0.055	-0.055	+0.052	-0.054
Fixed PDF Params (2)	**+0.233**	**-0.233**	**+0.227**	**-0.227**
Signal NN Shape	**+0.275**	**-0.275**	**+0.268**	**-0.268**
Add $f_2(1270)$	+0.011	-0.011	+0.009	-0.009
Add $f_0(1370)$, $a_0^0(1450)$	+0.009	-0.009	+0.005	-0.005
Add $a_0^-(1450)$	+0.019	-0.019	+0.032	-0.032
Add $\phi(1680)$	+0.009	-0.009	+0.005	-0.005
Add $f_2(2010)$, $f_2(2300)$	+0.007	-0.007	+0.005	-0.005
Add $a_0^-(980)$	+0.015	-0.015	+0.021	-0.021
DP PDF Stat.	+0.121	-0.121	+0.118	-0.118
SVT/beamspot/DCS	+0.000	-0.000	+0.000	-0.000
Fit Bias	+0.149	-0.149	**+0.199**	**-0.199**
Total	+0.786	-0.787	+0.770	-0.771

Table D.33: $B^0 \to K^+K^-K^0_S$ systematics.

	$\phi(1020)$		$f_0(980)$	
	A_{CP} $(+\sigma)$	A_{CP} $(-\sigma)$	A_{CP} $(+\sigma)$	A_{CP} $(-\sigma)$
$\phi(1020)$ Mass/Width	+0.000	-0.001	+0.002	-0.000
$f_0(1500)$ Mass/Width	+0.000	-0.002	+0.005	-0.000
$f'_2(1525)$ Mass/Width	+0.000	-0.002	+0.003	-0.000
$f_0(1710)$ Mass/Width	+0.000	-0.002	+0.006	-0.000
χ_{c0} Mass/Width	+0.000	-0.002	+0.003	-0.000
$\phi(1020)$ BW radius	+0.006	-0.000	**+0.020**	**-0.059**
$f'_2(1525)$ BW radius	+0.000	-0.005	**+0.017**	-0.001
$D, J/\psi$ Mass/Width	+0.000	-0.002	+0.004	-0.000
$f_0(980)$ Mass	+0.003	-0.006	**+0.020**	-0.013
$f_0(980)$ g_π, g_K	+0.002	-0.005	+0.016	-0.011
B-meson BW radius	**+0.017**	**-0.017**	**+0.030**	**-0.030**
Eff. map statistics	+0.008	-0.008	+0.012	-0.012
Tracking	+0.000	-0.000	+0.000	-0.000
$N_{B\overline{B}}$	+0.000	-0.000	+0.000	-0.000
K^0_S eff	+0.000	-0.000	+0.000	-0.000
PID	+0.001	-0.001	+0.005	-0.005
Fixed PDF Params (1)	**+0.011**	**-0.021**	**+0.017**	-0.005
Fixed PDF Params (2)	+0.006	-0.006	+0.009	-0.009
Signal NN Shape	+0.004	-0.004	+0.011	-0.011
Add $f_2(1270)$	+0.002	-0.002	+0.011	-0.011
Add $f_0(1370)$, $a^0_0(1450)$	+0.002	-0.002	**+0.026**	**-0.026**
Add $a^-_0(1450)$	+0.001	-0.001	+0.002	-0.002
Add $\phi(1680)$	**+0.022**	**-0.022**	**+0.040**	**-0.040**
Add $f_2(2010)$, $f_2(2300)$	+0.000	-0.000	+0.004	-0.004
Add $a^-_0(980)$	+0.000	-0.000	+0.003	-0.003
DP PDF Stat.	+0.009	-0.009	**+0.022**	**-0.022**
SVT/beamspot/DCS	**+0.014**	**-0.014**	+0.014	-0.014
Fit Bias	**+0.028**	**-0.028**	**+0.024**	**-0.024**
Total	+0.046	-0.050	+0.082	-0.094

Table D.34: $B^0 \to K^+K^-K^0_S$ systematics.

	Other		$\phi(1020)$	
	A_{CP} $(+\sigma)$	A_{CP} $(-\sigma)$	β_{eff} $(+\sigma)$	β_{eff} $(-\sigma)$
$\phi(1020)$ Mass/Width	+0.001	-0.000	+0.000	-0.001
$f_0(1500)$ Mass/Width	+0.002	-0.000	+0.000	-0.002
$f_2'(1525)$ Mass/Width	+0.002	-0.000	+0.000	-0.001
$f_0(1710)$ Mass/Width	+0.003	-0.001	+0.000	-0.002
χ_{c0} Mass/Width	+0.001	-0.000	+0.000	-0.001
$\phi(1020)$ BW radius	+0.003	**-0.015**	**+0.033**	**-0.012**
$f_2'(1525)$ BW radius	+0.006	-0.000	+0.000	-0.002
$D, J/\psi$ Mass/Width	+0.001	-0.000	+0.000	-0.001
$f_0(980)$ Mass	+0.002	-0.000	+0.000	-0.003
$f_0(980)$ g_π, g_K	+0.003	-0.001	+0.000	-0.003
B-meson BW radius	**+0.007**	**-0.007**	**+0.012**	**-0.012**
Eff. map statistics	+0.003	-0.003	+0.003	-0.003
Tracking	+0.000	-0.000	+0.000	-0.000
$N_{B\bar{B}}$	+0.000	-0.000	+0.000	-0.000
K^0_S eff	+0.000	-0.000	+0.000	-0.000
PID	+0.001	-0.001	+0.002	-0.002
Fixed PDF Params (1)	**+0.008**	-0.005	+0.004	**-0.008**
Fixed PDF Params (2)	+0.005	-0.005	+0.003	-0.003
Signal NN Shape	+0.005	-0.005	+0.000	-0.000
Add $f_2(1270)$	+0.001	-0.001	+0.001	-0.001
Add $f_0(1370)$, $a_0^0(1450)$	+0.006	-0.006	+0.008	**-0.008**
Add $a_0^-(1450)$	+0.001	-0.001	+0.001	-0.001
Add $\phi(1680)$	**+0.018**	**-0.018**	**+0.030**	**-0.030**
Add $f_2(2010)$, $f_2(2300)$	+0.001	-0.001	+0.001	-0.001
Add $a_0^-(980)$	+0.001	-0.001	+0.000	-0.000
DP PDF Stat.	**+0.007**	**-0.007**	+0.006	-0.006
SVT/beamspot/DCS	**+0.014**	**-0.014**	+0.002	-0.002
Fit Bias	**+0.014**	**-0.014**	+0.006	-0.006
Total	+0.033	-0.034	+0.048	-0.038

Table D.35: $B^0 \to K^+K^-K^0_S$ systematics.

	$f_0(980)$		Other	
	β_{eff} $(+\sigma)$	β_{eff} $(-\sigma)$	β_{eff} $(+\sigma)$	β_{eff} $(-\sigma)$
$\phi(1020)$ Mass/Width	+0.000	-0.000	+0.000	-0.000
$f_0(1500)$ Mass/Width	+0.003	-0.003	+0.001	-0.000
$f_2'(1525)$ Mass/Width	+0.000	-0.001	+0.000	-0.000
$f_0(1710)$ Mass/Width	+0.005	-0.005	+0.002	-0.000
χ_{c0} Mass/Width	+0.001	-0.001	+0.001	-0.000
$\phi(1020)$ BW radius	+0.002	-0.003	**+0.005**	**-0.013**
$f_2'(1525)$ BW radius	+0.001	-0.001	+0.004	-0.000
$D, J/\psi$ Mass/Width	+0.000	-0.000	+0.000	-0.000
$f_0(980)$ Mass	+0.004	-0.005	+0.002	-0.001
$f_0(980)$ g_π, g_K	+0.004	-0.003	+0.002	-0.001
B-meson BW radius	+0.001	-0.001	**+0.006**	**-0.006**
Eff. map statistics	+0.002	-0.002	+0.001	-0.001
Tracking	+0.000	-0.000	+0.000	-0.000
$N_{B\overline{B}}$	+0.000	-0.000	+0.000	-0.000
K^0_S eff	+0.000	-0.000	+0.000	-0.000
PID	+0.000	-0.000	+0.001	-0.001
Fixed PDF Params (1)	+0.006	-0.004	**+0.005**	-0.003
Fixed PDF Params (2)	+0.003	-0.003	+0.002	-0.002
Signal NN Shape	+0.001	-0.001	+0.001	-0.001
Add $f_2(1270)$	+0.006	-0.006	**+0.005**	**-0.005**
Add $f_0(1370)$, $a_0^0(1450)$	**+0.067**	**-0.067**	**+0.013**	**-0.013**
Add $a_0^-(1450)$	+0.003	-0.003	+0.002	-0.002
Add $\phi(1680)$	**+0.022**	**-0.022**	+0.003	-0.003
Add $f_2(2010)$, $f_2(2300)$	+0.002	-0.002	+0.002	-0.002
Add $a_0^-(980)$	+0.001	-0.001	+0.000	-0.000
DP PDF Stat.	+0.012	-0.012	**+0.006**	**-0.006**
SVT/beamspot/DCS	+0.002	-0.002	+0.002	-0.002
Fit Bias	+0.006	-0.006	**+0.006**	**-0.006**
Total	+0.073	-0.073	+0.020	-0.023

Bibliography

[1] `http://resonaances.blogspot.com/2011/11/lhcb-has-evidence-of-new-physics-maybe.html`.

[2] C. Wu *et al.*, Phys. Rev. **105**, 1413 (1957).

[3] J. Christenson, J. Cronin, V. Fitch, and R. Turlay, Phys. Rev. Lett. **13**, 138 (1964).

[4] A. Sakharov, Pisma Zh. Eksp. Teor. Fiz. **5**, 32 (1967), [JETP Lett. **5**, 24 (1967)][Sov. Phys. Usp. **34**, 392 (1991)] [Usp. Fiz. Nauk **161**, 61 (1991)].

[5] B. Aubert *et al.*, Phys.Rev.Lett. **99**, 021603 (2007).

[6] S. Lin *et al.*, Nature **452**, 332 (2008).

[7] N. Cabibbo, Phys. Rev. Lett. **10**, 531 (1963).

[8] M. Kobayashi and T. Maskawa, Prog. Theor. Phys. **49**, 652 (1973).

[9] K. Nakamura *et al.*, J. Phys. **G37**, 075021 (2010).

[10] J. R. Ellis, M. K. Gaillard, D. V. Nanopoulos, and S. Rudaz, Nucl.Phys. **B131**, 285 (1977). Erratum Nucl. Phys. **B132**, 541 (1978).

[11] M. Beneke, Phys .Lett. **B620**, 143 (2005).

[12] H.-n. Li and S. Mishima, Phys. Rev. **D74**, 094020 (2006).

[13] H.-Y. Cheng, C.-K. Chua, and A. Soni, Phys. Rev. **D72**, 014006 (2005).

[14] M. Beneke and M. Neubert, Nucl. Phys. **B675**, 333 (2003).

[15] B. Aubert *et al.*, Phys. Rev. **D79**, 072009 (2009).

[16] G. N. Fleming, Phys. Rev. **135**, B551 (1964).

[17] D. Morgan, Phys. Rev. **166**, 1731 (1968).

[18] D. Herndon, P. Soding, and R. Cashmore, Phys. Rev. **D11**, 3165 (1975).

[19] M. Ablikim *et al.*, Phys. Lett. **B607**, 243 (2005).

[20] B. Aubert *et al.*, Phys. Rev. **D79**, 072006 (2009).

[21] A. Abele *et al.*, Phys. Rev. **D57**, 3860 (1998).

[22] C. Zemach, Phys. Rev. **133**, B1201 (1964).

[23] B. Aubert *et al.*, Phys. Rev. Lett. **99**, 161802 (2007).

[24] B. Aubert *et al.*, Phys. Rev. **D74**, 032003 (2006).

[25] J. Blatt and V. E. Weisskopf, *Theoretical Nuclear Physics* (J. Wiley, New York, 1952).

[26] S. M. Flatte, Phys. Lett. **B63**, 224 (1976).

[27] A. Garmash *et al.*, Phys. Rev. **D71**, 092003 (2005).

[28] Y. Nakahama *et al.*, Phys. Rev. **D82**, 073011 (2010).

[29] U. Wienands *et al.,* SLAC-PUB-12612.

[30] PEP-II: An Asymmetric B Factory. Conceptual Design Report. SLAC-R-418. June 1993.

[31] B. Aubert *et al.*, Nucl. Instrum. Meth. **A479**, 1 (2002).

[32] I. Adam *et al.*, Nucl. Instrum. Meth. **A538**, 281 (2005).

[33] W. a. Menges, IEEE Nucl. Sci. Symp. Conf. Rec. **5**, 1470 (2006).

[34] A. Dvoretskii, *BABAR* Analysis Document #643.

[35] B. Aubert *et al.*, Phys. Rev. Lett. **93**, 181805 (2004).

[36] J. Thompson and D. Dujmic, *BABAR* Analysis Document #769.

[37] D. Dujmic *et al., BABAR* Analysis Document #1396.

[38] A. Hoecker *et al.*, PoS **ACAT**, 040 (2007).

[39] J. Thompson *et al., BABAR* Analysis Document #1160.

[40] F. James and M. Roos, Comput. Phys. Commun. **10**, 343 (1975).

[41] `http://www.slac.stanford.edu/BFROOT/www/Physics/Tools/Tagging/Main/R24/tag08.html`.

[42] H. Albrecht *et al.*, Z. Phys. **C48**, 543 (1990).

[43] B. Aubert *et al.,* arXiv:0808.0700[hep-ex] (2008).

[44] M. Pivk and F. R. Le Diberder, Nucl. Instrum. Meth. **A555**, 356 (2005).

[45] P. del Amo Sanchez *et al.*, Phys. Rev. **D82**, 072004 (2010).

[46] J. Olsen *et al., BABAR* Analysis Document #1551.

[47] O. Long, M. Baak, R. N. Cahn, and D. P. Kirkby, Phys.Rev. **D68**, 034010 (2003).

[48] D. Acosta *et al.*, Phys. Rev. Lett. **95**, 031801 (2005).

[49] K. Chen *et al.*, Phys. Rev. Lett. **91**, 201801 (2003).